Lengthening the lifetime of roll-to-roll produced polymer solar cells

Madsen, Morten Vesterager; Krebs, Frederik C; Norrman, Kion

Publication date:
2013

Document Version
Publisher's PDF, also known as Version of record

Lengthening the lifetime of roll-to-roll produced polymer solar cells

PhD Thesis

Morten Vesterager Madsen

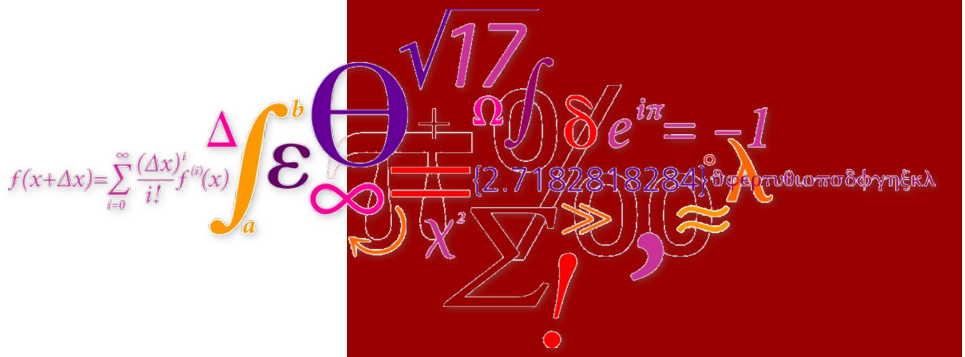

DTU Energy Conversion
Department of Energy Conversion and Storage

Lengthening the lifetime of roll-to-roll produced polymer solar cells

PhD Thesis

Morten Vesterager Madsen

Submitted July 2012

Department of Energy Conversion and Storage
Functional Organic Materials
Technical University of Denmark

Author: Morten Vesterager Madsen

Title: Lengthening the lifetime of roll-to-roll produced polymer solar cells

Report number:

ISSN:
ISBN:

Sponsorship: The project was financed through the Photovoltaic European Research Area Network (PV-ERA-NET), under the project acronym POLYSTAR.

Academic advisors:
Senior scientist Kion Norrman
Microstructures and Interfaces, Department of Energy Conversion and Storage

and

Professor Frederik C. Krebs
Functional Organic Materials, Department of Energy Conversion and Storage

Department of Energy Conversion and Storage
Technical University of Denmark
Frederiksborgvej 399
P.O.Box 49
DK-4000 Roskilde
Denmark
Telephone +45 46 77 58 00
Fax +45 46 77 5858

Table of contents

Chapter 4
Concentrated light for photo-degradation

Chapter 5
Applications of TOF-SIMS for polymer solar cells

Chapter 6

Appendix 1
Publications

Preface

This PhD thesis presents the main results of my work carried out at the Technical University of Denmark. The thesis represents three years of work initialized in August 2009 with focus on polymer solar cells. The project was financed through the Photovoltaic European Research Area Network (PV-ERA-NET), under the project acronym POLYSTAR. Senior scientist Kion Norrman was the supervisor of the project and Professor Frederik C. Krebs acted as the co-supervisor. The thesis is based on results published in a number of journals. The full list of publications is featured in Appendix 1 along with five included papers. The structure of the report is based on the included articles and split into four main chapters. While many of the results obtained throughout the three year period has been published, a number of project remained unfinished. While this was not the planned outcome, it definitely serves as a strong personal motivating factor to continue the work within the field, beyond the PhD.

The work carried out has relied on several people. Thomas Tromholt is a fellow PhD student whom I have closely collaborated with in connection with the photo degradation studies of polymers and building of equipment. I would like to thank you Thomas for our excellent collaborpation and our friendship. I would also like to thank our technician Torben Kjær and Kristian Larsen; you have been an invaluable resource allowing all the setups to be constructed. A special thank goes to Kristian O. Sylvester-Hvid who was an inspiration in the early part of my PhD and to Jens W. Andreasen who have been a solid support for me during the entire three years.

From my visits to the Johannes Kepler University I would like to thank Professor Kurt Hingerl and Babak Dastmalchi for valuable discussions, insights and hospitality.

I would also like to thank the entire group devoted to solar cells at DTU. Arvid, Birgit, Birgitta, Dechan, Emil, Eva, Hanne, Henrik, Jacob, Jon, Markus, Martin, Mikkel, Ole, Peter, Roar, Suren, Thomas, Thue, and Torben; thank you for having been a part of my experience here and for your support. Bente, Birgit, and Henrik I would also like to thank you for your invaluable help.

I would like to thank my family and friends for support throughout this three year period of my life. Lastly my girlfriend Katrine; I would like to thank you for your love and endless support.

List of abbreviations

DegradationMonitor	Software for post treatment of degradation data
EMA	Effective medium approximation
fmf	Full metadata format
HektoSun	Main acquisition software for photo-degradation
ITO	Indium tin oxide
IV-curve	Current-voltage curve
MDMO-PPV	Poly[2-methoxy-5-(3',7'-dimethyloctyloxy)-1-4-phenylene vinylene]
MSE	Mean Squared Error
NMR	Nuclear magnetic resonance
P3HT	Poly-3-hexyl-thiophene
PCBM	1-(3-methoxycarbonyl)propyl1-phenyl-[6,6]-methanolfullerene
PEDOT:PSS	Poly(3,4-ethylenedioxythiophene):poly(styrene sulfonate)
RR	Regio-regularity
TOF-SIMS	Time of Flight Secondary ion mass spectrometry
UV-vis	Ultraviolet-visible
XPS	X-ray photoelectron spectroscopy
ZnO	Zinc oxide

Abstract

The field of polymer solar cells is a field with an exponential growth in the number of published papers. It is a field defined by a set of challenges including; efficiency, stability and processability. Before all of these challenges have been addressed; polymer solar cells will not be a commercial success.

This dissertation is devoted primarily to the study of the stability of polymer solar cells, and more specifically to designing and verifying experimental techniques, procedures, and automated solutions to stability tests and characterization. The goal of the project was to expand the knowledge of the degradation mechanisms involved in roll-to-roll coated polymer solar cells. While only a part of the experiments have directly involved roll-to-roll coated devices, most of the work is applicable to coated devices.

The first part of the dissertation is devoted to the study of in-depth morphology of polymer solar cells using ellipsometry. It was demonstrated that ellipsometry can be used as a non destructive depth profiling technique to obtain compositional morphology of the active layer of roll-to-roll coated samples. The second and third part is devoted to the study of photo-chemical degradation of the active layer materials. The second part details the building of an automated setup for stability tests and presents results on thickness and absorbance dependence of the photo-chemical stability, acceptor stability, and the influence of intrinsic polymer parameters on stability. In the third part two light concentrating setups, built during the PhD, are detailed and results based on high intensity photo-degradation studies presented. In the last part of the dissertation the use of TOF-SIMS for polymer solar cell characterization is detailed and the results on intrinsic barrier effects and degradation patterns are summarized.

Danish abstract (Resume)

Feltet af plastsolceller er et felt med en eksponentiel vækst i antallet af publicerede artikler. Det er et område defineret ved et sæt af udfordringer, herunder effektivitet, stabilitet og bearbejdelighed. Før alle disse udfordringer er blevet løst, vil plastsolceller ikke blive en kommerciel succes.

Denne afhandling er helliget primært til undersøgelse af stabiliteten af plastsolceller, og mere specifikt til at designe og kontrollere eksperimentelle teknikker, procedurer og automatiserede løsninger til stabilitets test og karakterisering. Målet med projektet var at udvide kendskabet til nedbrydningsmekanismerne, som er involveret i rulle-til-rulle coatede plastsolceller. Mens kun en del af forsøgene er direkte er relateret til rulle-til-rulle coatede enheder, kan det meste af arbejdet anvendes hertil.

Den første del af afhandlingen omhandler studiet af dybde morfologi af plastsolceller ved hjælp ellipsometri. Det blev påvist, at ellipsometri kan anvendes som en ikke-destruktiv dybde profilering teknik til at forstå den morfologiske sammensætning af det aktive lag for rulle-til-rulle coatede prøver. Den anden og tredje del er afsat til undersøgelse af foto-kemisk nedbrydning af materialer, som indgår i det aktive lag. Den anden del indeholder detaljer om bygningen af et automatiseret setup til stabilitets test og præsenterer resultaterne for tykkelse og absorbans afhængighed af foto-kemisk stabilitet, acceptor stabilitet og indflydelsen af polymer parametre på stabilitet. I tredje del bliver to setups til koncentrering af lys, bygget iløbet af Ph.d.en, beskrevet i detaljer og resultater baseret på høj intensitet foto-nedbrydning præsenteret. I den sidste del af afhandlingen bliver brugen TOF-SIMS til plastsolcelle karakterisering detaljeret og resultaterne for barriere effekter og nedbrydnings mønstre sammenfattet.

Chapter 1

Introduction

The global energy future is arguably the most important subject undertaken by the scientific community. Without energy, our society of today will not function. Without energy we cannot find or administer medicine to cure disease, we cannot purify water, drive our cars, operate computers, or even study at night. The current energy need is roughly 15 TW and with an increasing world population this number is destined to increase. Professor of Physics and Astronomy at Rice University and Nobel laureate Richard E. Smalley coined the term the "Terawatt Challenge" based on this future energy deficit. Smalley defines the "Terawatt Challenge" as the challenge to provide the technology for accomplishing our energy goals An alternative that can act as a basis for energy prosperity in the 21st century, that is as enabling as oil and gas have been for the past century.[1] It seems inescapable that the world of the future must embrace alternative energies. The Oxford Dictionary defines alternative energy as "energy fuelled in ways that do not use up natural resources or harm the environment". The definition places emphasis on two key points: Firstly the use of natural resources, and secondly focus on the harm of the environment. It is clear that the term "alternative" presupposes a set of undesirable energy technologies against which alternative energies are contrasted; coal and oil must become a thing of the past. Renewable resources including, wind, photovoltaics, solar thermal, geothermal, marine, and tides still represents a minor fraction of the overall primary energy supply. With a total nameplate capacity of 93,957 MW as of end 2011 within Europe alone, wind is the leading alternative energy resource.[2] Several countries have high levels of penetration, such as 25.9% of electricity production in Denmark (2011), 15.6% in Spain (2011), 12% in Ireland (2011) and 10.6% in Germany (2011).[2] By comparison to all other energy sources the sun, however, is a vast resource. Taking the total solar irradiance of 1360.8 W/m^2 as the solar minimum outside the atmosphere the total energy eradiated from the sun at earth is roughly $1.25 \cdot 10^5$ TW .[3] This number exceeds our energy need by orders of magnitude, so even adjusting for losses in the atmosphere, inaccessible locations for solar harvesting, etc solar energy is an abundant resource.

The most direct use of solar energy is the conversion of photons to electricity by the photovoltaic effect. The photovoltaic effect as a phenomenon has been documented by many early experiments with the experiment of Alexandre-Edmond Becquerel in 1839 being the most well known.[4] However, it was not until the early 1950s that the photovoltaics developed into the solar cells of today. The first solar cell was made by Daryl Chapin, Calvin Fuller, and Gerald Pearson at Bell laboratories in 1954 utilizing a silicon p-n junction to achieve 6 % conversion efficiency.[5] With the space age, a market for solar cells emerged and the first American satellite Vanguard I launched in 1958 equipped with six solar cells mounted on the body. The use of solar cells on the satellite proved successful and the power-to-weight ratio of solar cells ensured their further success for space applications. For the initial history of solar cells their prices were dictated by the semiconductor industry, the price of silicon boules being the main cost factor. By 1971 the estimated price had reached $100 per watt. Since then progress have be massive. Solar cells are now part of a global industry with a multifaceted array of technologies competing. According to a study by EWEA photovoltaics accounted for the largest share of new installations within the energy sector in Europe. 21,000 MW worth of capacity was installed in 2011 accounting for 46.7% of the total installed capacity.[2]

A common distinction between solar technologies recognizes three generations of solar cells. The first generation is unsurprisingly represented by monocrystalline silicon solar cells. These solar cells, using silicon wafers, still account for the majority of the solar cell market. Their success is due to their high efficiency. 25 % conversion efficiency has been confirmed for laboratory cells, and typical installed efficiencies are around 15 %.[6] A major issue with monocrystalline solar cells, however, comes through their high manufacturing costs. Monocrystalline solar cells suffer from the fact that silicon has an indirect bandgap and thereby poor light absorbance. Therefore solar cells must be hundreds of microns in thickness to achieve good absorbance. Thin-film solar cells represent the second generation of solar cell technology and are typically made of direct band gap materials such as cadmium telluride (CdTe) and copper indium gallium selenide (CIGS) or amorphous silicon. Thin-film solar cells, are significantly cheaper to produce than first generation cells as the technology is based on the deposition of a thin semiconducting layer on a low cost substrate. The great advantage of second generation, thin-film solar cells, along with low cost, is their flexibility. The third generation of solar cell technology contains a wide range of potential solar innovations including dye-sensitized solar cells, nanocrystalline solar cells, and polymer solar cells. The third generation represents the cutting edge of solar technology and is likely to be divided into separate categories when further developed and produced.

Organic solar cells represent a successful technology within the third generation and also represent the main turning point of this thesis. The subject of polymer solar cells is actively researched by universities, national laboratories and several companies around the world.

1.1. Polymer solar cells

The potential advantages of polymer solar cells are numerous including flexibility, processability, low material cost, and independence on scarce resources. The flexibility as an advantage, is shared with thin-film photovoltaics, and is a feature allowing the solar cells to be incorporated into applications in an aesthetically pleasing manor. Solar panels that can be rolled out onto a roof or other surfaces are one option. Processability is another major selling point of polymer solar cells. Both first and second generation solar cells depend on vacuum deposition methods requiring massive amounts of energy. With polymer based organic solar cells, on the other hand, layers are processed from solution and complete solution processed cells are an option.[7] This allows for up-scaling the production and thus reducing the cost per area of polymer solar cells. Large rolls of substrate can be used on which the layers are deposited using printing or coating techniques, generally referred to as roll-to-roll coating.[8–10] The promise of low material cost and minimal use of scarce materials can be realized with polymer solar cells. Many second generation solar cells utilize materials that are scarce in nature. With polymer solar cells this can be avoided. Indium is, however, still used in most polymer solar cells, but demonstrations of indium free solar cells are available.[7,11–14]

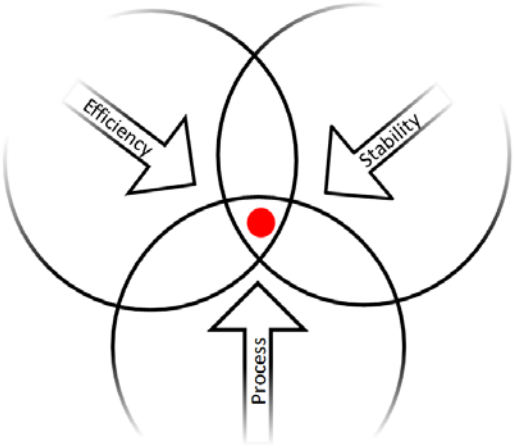

Figure 1.1. The unification challenge is defined as the challenge of unifying efficiency, stability and process for the same material.

Listing the advantages of polymer solar cells reveals a very enticing selling point; however, polymer solar cells have a number of drawbacks. Firstly while inorganic silicon-based solar cells may last on the order of 25 years; polymer based devices struggle to last a year. Efficiency has long remained the other major drawback of the technology. With polymer solar cell the efficiency is still behind more traditional technologies, but recent records exceeding 10% have been reported.[15,16] For polymer solar cells to mature to the market, the strong points of the technology will have to outmatch the weak points. However, it is still vital to optimize the weak points. Professor Fredrik C. Krebs have defined the unification challenge of polymer solar cells by stating that three issues share the same importance, see Figure 1.1.[17,18] These three issues were defined as; process, stability, and efficiency. The concept is very similar to the critical triangle for photovoltaics as presented by Professor Christoph J. Brabec, however substituting processability for cost.[19] While no issue can be argued more important than another, the efficiency of solar cells have long been given special attention. As an area of focus, the power conversion efficiency is important in order to compete with the more mature silicon technology and to justify research in the field of polymer solar cells. As long as focus of research is not on all of the areas, progress towards application of the technology will remain slow. Within recent years the number of reports on both processability and stability has increased significantly. Several reviews on stability have appeared plus one book.[17,20,21] Roll-to-roll deposition is becoming an established technique for producing polymer solar cells.[18,22,23]

1.2. The principle behind polymer solar cells

The use of polymer materials in solar cells is dependent upon their ability to transport electric current and to absorb light in the UV-visible spectra. The discovery and development of conductive polymers by Alan G. McDiarmid, Hideki Shirakawa and Alan Heeger was awarded the Nobel prize for chemistry in 2000, marking the importance of the discovery.[24] Conducting polymers depend on the delocalized nature of the π-electrons resulting in high electronic polarizability. Importantly in comparison with inorganic semiconducting materials, organic semiconductors exhibit generally poor charge carrier mobility (lower by orders of magnitude).[25] On the other hand organic semiconductors have strong absorption coefficients partly balancing the mobility as thin layer (~100 nm) can show high absorbance. Another major difference to crystalline inorganic semiconductors is the comparably small diffusion length of excitons. Excitons further exhibit strong binding energies and strong internal electric fields are therefore needed to separate them into free charge carriers. The first organic solar cells employed single organic layers between two metals of different work functions. Later implementations

employed a bi-layer heterojunction geometry, in which two organic layers with specific electrons and hole transporting properties were sandwiched between the electrodes.[26] This developed into bi-layer heterojunctions of polymer-fullerene structures introduced in 1993 as photoinduced electron transfer between the optically excited polymer to the fullerene molecule was observed.[27–29] The realization of the bulk heterojunction based polymer solar cells in 1995 by Yu et al. introduced further improvements in power conversion efficiency.[30] The bulk heterojunction has since become the most successful and most implemented version of a polymer solar cell that comprise a mixture of a polymer acting as a donor, and a soluble fullerene derivative acting as the acceptor material. The role of the bulk heterojunction is several-fold. The layer must absorb light, generate and separate excitons, and transport charge carriers to their respective electrodes. The morphology of the bulk heterojunction affects all of these processes. Excitons are generated at electron donor and acceptor phase interfaces and the morphology optimally should ensure that the interface area is maximized so charge separation can take place. Conduction of charge carriers requires connected regions of donor and acceptor phases respectively.

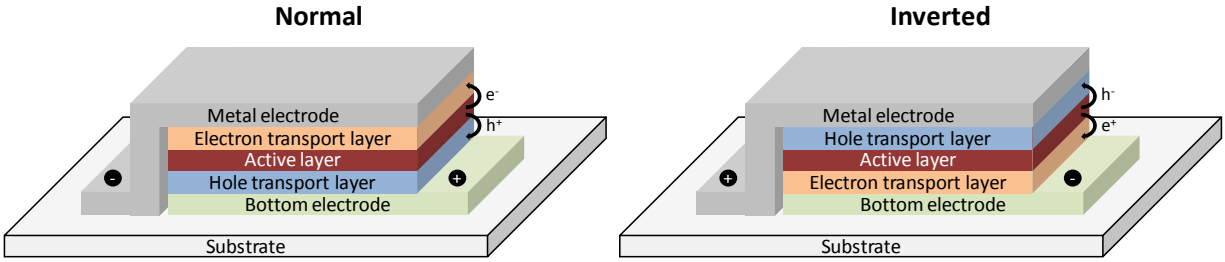

Figure 1.2. Normal (left) and inverted (right) device geometries.

Currently two device geometries almost exclusively describe the majority of polymer solar cells. These are: the normal and the inverted geometry represented in Figure 1.2, both using a bulk heterojunction active layer. For a normal geometry stack the device is typically built upon a semitransparent transparent conductive electrode, most often indium tin oxide (ITO). Following the electrode layer is a hole transport layer PEDOT:PSS, the active layer, an optional electron transport layer (e.g. LiF), and a low workfunction metal electrode on top. The metal electrode acts as the cathode in the normal geometry while the ITO layer acts as the anode. This geometry achieves the built-in electric field since the top electrode is a low-work-function metal serving as the negative electrode. In the inverted geometry electrons and holes exit the device in the opposite direction. This is typically accomplished using zinc oxide (ZnO) as a hole-blocking layer and PEDOT:PSS as hole transport layer.[31] The main advantages of the inverted type geometry is related to the fact the high-workfunction metals can be

deposited onto polymer layers via non-vacuum techniques and that avoiding the low-workfunction metal removes a weak point in terms of stability.[31,32]

1.3. Stability of polymer solar cells

When discussing the stability of any photovoltaic device the source of instability in the device must be uncovered. Polymer solar cells generally present significant degradation when operated.[17,20] The degradation is of course linked to both intrinsic and extrinsic stability. Examples of extrinsic stability deficiencies relate to corrosion of interconnections, yellowing of the encapsulation material or similar; typically traits shared between different solar cell technologies. Intrinsic stability relate to the stability of the materials, the interfaces within the solar cell, etc. The intrinsic stability of the solar cell is in many ways the most interesting from a scientific viewpoint. If a material is not intrinsically stable, the final device will suffer or strong measures must be taken to circumvent the problems of the material.

As a generalization organic materials are not inert. They are naturally more susceptible to chemical degradation from e.g. oxygen and water than inorganic materials.[33–35] In contrast the pn-junction of the monocrystalline silicon solar cells is very stable and 25 years of lifetime is the norm. Polymer materials are dynamic and reactive, and prone to attack by a range of agents. When organic matter is illuminated, the materials react via photochemical and photolytic processes.[36–39] The materials are also not heat stable and can suffer heat or sunlight-induced morphology changes or interfacial degradation over their operating lifetime. The bulk heterojunction with a specific morphology of interconnected domains do not necessarily represent the most thermodynamically stable configuration and growth of PCBM acceptor crystallites altering the optimal morphology has been observed.[40–43] Polymer solar cells can also sustain damage to the top electrode, often made from a low-work-function metal that is reactive and easily oxidized in ambient air.[44,45] All in all the stability of organic solar cells are on a different playing field compared to inorganic solar cells.

There are measures that can be taken to improve stability of polymer solar cells. Encapsulation technology can protect materials from environmental factors; minimize the availability of oxygen and water, thereby prolonging the life of the device. Organic semiconductors can be made more resistant to oxidation by appropriate tuning of their electronic levels, and they can be made “harder” by tuning their glass-transition temperature or with cross-linking. Using thermo-cleavable polymers is an approach in which side chains are eliminated post deposition, making otherwise unprocessable but stable materials available.[46–48] Electrodes can be made more stable by capping the reactive metal with

a less reactive one.[49] There is no doubt that an improved understanding of degradation mechanisms will result in better solar cells if the constituent materials can be improved. A stable device prime for production will result from a compromise of optimizing the individual materials and by utilizing all available methods of improvement on device level including encapsulation.

1.4. Project goals

The stated goal of this PhD project is the identification of degradation mechanisms in roll-to-roll produced polymer solar cells. This is a challenging task compared to laboratory cells that are typically constructed on a plane glass substrate using spin coating and evaporative techniques. Throughout the project various model systems have been used to study aspects of polymer solar cells relating to degradation. The first major chapter in the report is focused on the application of ellipsometry on polymer solar cells. While none of these efforts were directly related to degradation of polymer solar cells, the work has advanced the potential for using ellipsometry to study polymer solar cells on flexible substrates especially for morphology studies. The second chapter revolves around the study of photo-oxidation of polymer materials and the efforts to build an automated system for evaluating photo-stability of the polymers. The fourth chapter is devoted to the application of concentrated light to photo-degradation of polymer materials. The last chapter details the use of chemical analysis towards polymer solar cells. The appendix includes a full publication list plus five selected articles.

1.5. References

(1) Smalley, R. E.; Bush, W.; Mansfield, S. Future Global Energy Prosperity : The Terawatt Challenge. *MRS Bulletin* **2004**.

(2) EWEA Wind in Power - 2011 European Statistics. *http://www.ewea.org/fileadmin/ewea_documents/documents/publications/statistics/Stats_2011.pdf, accesssed 5/6-12* **2011**.

(3) Kopp, G.; Lean, J. L. A new, lower value of total solar irradiance: Evidence and climate significance. *Geophysical Research Letters* **2011**, *38*, 01706-1-7.

(4) Becquerel, A. E. Mémoire sur les effets électriques produits sous l'influence des rayons solaires. *Comptes Rendus* **1839**, *9*, 561-567.

(5) Chapin, D. M.; Fuller, C. S.; Pearson, G. L. A New Silicon p-n Junction Photocell for Converting Solar Radiation into Electrical Power. *Journal of Applied Physics* **1954**, *25*, 676-677.

(6) Green, M. A.; Emery, K.; Hishikawa, Y.; Warta, W.; Dunlop, E. D. Solar cell efficiency tables (version 39). *Progress in Photovoltaics: Research and Applications* **2012**, *20*, 12-20.

(7) Krebs, F. C. All solution roll-to-roll processed polymer solar cells free from indium-tin-oxide and vacuum coating steps. *Organic Electronics* **2009**, *10*, 761-768.

(8) Blankenburg, L.; Schultheis, K.; Schache, H.; Sensfuss, S.; Schrödner, M. Reel-to-reel wet coating as an efficient up-scaling technique for the production of bulk-heterojunction polymer solar cells. *Solar Energy Materials and Solar Cells* **2009**, *93*, 476-483.

(9) Krebs, F. C.; Gevorgyan, S. A.; Alstrup, J. A roll-to-roll process to flexible polymer solar cells: model studies, manufacture and operational stability studies. *Journal of Materials Chemistry* **2009**, *19*, 5442-5451.

(10) Krebs, F. C. Polymer solar cell modules prepared using roll-to-roll methods: Knife-over-edge coating, slot-die coating and screen printing. *Solar Energy Materials and Solar Cells* **2009**, *93*, 465-475.

(11) Krebs, F. C. Air stable polymer photovoltaics based on a process free from vacuum steps and fullerenes. *Solar Energy Materials and Solar Cells* **2008**, *92*, 715-726.

(12) Zimmermann, B.; Glatthaar, M.; Niggemann, M.; Riede, M. K.; Hinsch, a.; Gombert, a. ITO-free wrap through organic solar cells—A module concept for cost-efficient reel-to-reel production. *Solar Energy Materials and Solar Cells* **2007**, *91*, 374-378.

(13) Zimmermann, B.; Würfel, U.; Niggemann, M. Longterm stability of efficient inverted P3HT:PCBM solar cells. *Solar Energy Materials and Solar Cells* **2009**, *93*, 491-496.

(14) Manceau, M.; Angmo, D.; Jørgensen, M.; Krebs, F. C. ITO-free flexible polymer solar cells: From small model devices to roll-to-roll processed large modules. *Organic Electronics* **2011**, *12*, 566-574.

(15) UCLA UCLA engineers create tandem polymer solar cells that set record for energy-conversion. *http://newsroom.ucla.edu/portal/ucla/ucla-engineers-create-tandem-polymer-228468.aspx, accesssed 5/5-12* **2012**.

(16) Heliatek Heliatek sets new record efficiency of 10.7% for its organic tandem cell. *http://www.heliatek.com/?p=1923&lang=en, accessed 5/5-12* **2012**.

(17) Jørgensen, M.; Norrman, K.; Krebs, F. C. Stability/degradation of polymer solar cells. *Solar Energy Materials and Solar Cells* **2008**, *92*, 686-714.

(18) Krebs, F. C. Fabrication and processing of polymer solar cells: A review of printing and coating techniques. *Solar Energy Materials and Solar Cells* **2009**, *93*, 394-412.

(19) Brabec, C. J. Organic photovoltaics: technology and market. *Solar Energy Materials and Solar Cells* **2004**, *83*, 273-292.

(20) Jørgensen, M.; Norrman, K.; Gevorgyan, S. A.; Tromholt, T.; Andreasen, B.; Krebs, F. C. Stability of polymer solar cells. *Advanced materials* **2012**, *24*, 580-612.

(21) Krebs, F. C. *Stability and Degradation of Organic and Polymer Solar Cells*; John Wiley & Sons, 2012.

(22) Krebs, F. C. *Polymeric Solar Cells: Materials, Design, Manufacture*; DEStech Publications, 2010.

(23) Søndergaard, R.; Hösel, M.; Angmo, D.; Larsen-Olsen, T. T.; Krebs, F. C. Roll-to-roll fabrication of polymer solar cells As the performance in terms of power conversion efficiency and operational. **2012**, *15*, 36-49.

(24) Shirakawa, H.; Louis, E. J.; Macdiarmid, A. G.; Chaing, C. K.; Heeger, A. J. Synthesis of Electrically Conducting Organic Polymers : Halogen Derivatives of Polyacetylene, (CH)x. *Journal of the Chemical Society Chemical Comminication* **1977**, 578-580.

(25) Scharber, M. C.; Mühlbacher, D.; Koppe, M.; Denk, P.; Waldauf, C.; Heeger, a. J.; Brabec, C. J. Design Rules for Donors in Bulk-Heterojunction Solar Cells—Towards 10 % Energy-Conversion Efficiency. *Advanced Materials* **2006**, *18*, 789-794.

(26) Tang, C. W. Two-layer organic photovoltaic cell. *Applied Physics Letters* **1986**, *48*, 183.

(27) Sariciftci, N. S.; Braun, D.; Zhang, C.; Srdanov, V. I.; Heeger, A. J.; Stucky, G.; Wudl, F. Semiconducting polymer-buckminsterfullerene heterojunctions: Diodes, photodiodes, and photovoltaic cells. *Applied Physics Letters* **1993**, *62*, 585-587.

(28) Sariciftci, N. S.; Smilowitz, L.; Heeger, a. J.; Wudl, F. Semiconducting polymers (as donors) and buckminsterfullerene (as acceptor): photoinduced electron transfer and heterojunction devices. *Synthetic Metals* **1993**, *59*, 333-352.

(29) Sariciftci, N. S.; Smilowitz, L.; Heeger, A. J.; Wudl, F. Photoinduced Electron Transfer from a Conducting Polymer to Buckminsterfullerene. *Science* **1992**, *258*, 1474-1476.

(30) Yu, G.; Gao, J.; Hummelen, J. C.; Wudl, F.; Heeger, A. J. Polymer Photovoltaic Cells: Enhanced Efficiencies via a Network of Internal Donor-Acceptor Heterojunctions. *Science* **1995**, *270*, 1789-1791.

(31) White, M. S.; Olson, D. C.; Shaheen, S. E.; Kopidakis, N.; Ginley, D. S. Inverted bulk-heterojunction organic photovoltaic device using a solution-derived ZnO underlayer. *Applied Physics Letters* **2006**, *89*, 143517.

(32) Lee, T.-W.; Zaumseil, J.; Bao, Z.; Hsu, J. W. P.; Rogers, J. a Organic light-emitting diodes formed by soft contact lamination. *Proceedings of the National Academy of Sciences of the United States of America* **2004**, *101*, 429-33.

(33) Norrman, K.; Krebs, F. C. Lifetimes of organic photovoltaics: Using TOF-SIMS and 18O2 isotopic labelling to characterise chemical degradation mechanisms. *Solar Energy Materials and Solar Cells* **2006**, *90*, 213-227.

(34) Norrman, K.; Gevorgyan, S. a; Krebs, F. C. Water-induced degradation of polymer solar cells studied by H2(18)O labeling. *ACS applied materials & interfaces* **2009**, *1*, 102-12.

(35) Madsen, M. V.; Norrman, K.; Krebs, F. C. Oxygen- and water-induced degradation of an inverted polymer solar cell: the barrier effect. *Journal of Photonics for Energy* **2011**, *1*, 011104 1-6.

(36) Manceau, M.; Rivaton, A.; Gardette, J.-L.; Guillerez, S.; Lemaître, N. Light-induced degradation of the P3HT-based solar cells active layer. *Solar Energy Materials and Solar Cells* **2010**, *95*, 1315-1325.

(37) Manceau, M.; Rivaton, A.; Gardette, J.-L.; Guillerez, S.; Lemaître, N. The mechanism of photo- and thermooxidation of poly(3-hexylthiophene) (P3HT) reconsidered. *Polymer Degradation and Stability* **2009**, *94*, 898-907.

(38) Tromholt, T.; Madsen, M. V.; Carlé, J. E.; Helgesen, M.; Krebs, F. C. Photochemical stability of conjugated polymers, electron acceptors and blends for polymer solar cells resolved in terms of film thickness and absorbance. *Journal of Materials Chemistry* **2012**, *22*, 7592-7601.

(39) Madsen, M. V.; Tromholt, T.; Böttiger, A.; Andreasen, J. W.; Norrman, K.; Krebs, F. C. Influence of processing and intrinsic polymer parameters on photochemical stability of polythiophene thin films. *Polymer Degradation and Stability* **2012**.

(40) Zhang, Y.; Yip, H.-L.; Acton, O.; Hau, S. K.; Huang, F.; Jen, A. K.-Y. A Simple and Effective Way of Achieving Highly Efficient and Thermally Stable Bulk-Heterojunction Polymer Solar Cells Using

Amorphous Fullerene Derivatives as Electron Acceptor. *Chemistry of Materials* **2009**, *21*, 2598-2600.

(41) Swinnen, a.; Haeldermans, I.; vande Ven, M.; D'Haen, J.; Vanhoyland, G.; Aresu, S.; D'Olieslaeger, M.; Manca, J. Tuning the Dimensions of C60-Based Needlelike Crystals in Blended Thin Films. *Advanced Functional Materials* **2006**, *16*, 760-765.

(42) Bertho, S.; Janssen, G.; Cleij, T. J.; Conings, B.; Moons, W.; Gadisa, A.; D'Haen, J.; Goovaerts, E.; Lutsen, L.; Manca, J.; Vanderzande, D. Effect of temperature on the morphological and photovoltaic stability of bulk heterojunction polymer:fullerene solar cells. *Solar Energy Materials and Solar Cells* **2008**, *92*, 753-760.

(43) Drees, M.; Hoppe, H.; Winder, C.; Neugebauer, H.; Sariciftci, N. S.; Schwinger, W.; Schäffler, F.; Topf, C.; Scharber, M. C.; Zhu, Z.; Gaudiana, R. Stabilization of the nanomorphology of polymer–fullerene "bulk heterojunction" blends using a novel polymerizable fullerene derivative. *Journal of Materials Chemistry* **2005**, *15*, 5158.

(44) Reese, M. O.; Morfa, A. J.; White, M. S.; Kopidakis, N.; Shaheen, S. E.; Rumbles, G.; Ginley, D. S. Pathways for the degradation of organic photovoltaic P3HT:PCBM based devices. *Solar Energy Materials and Solar Cells* **2008**, *92*, 746-752.

(45) Lira-Cantu, M.; Norrman, K.; Andreasen, J. W.; Casan-Pastor, N.; Krebs, F. C. Detrimental Effect of Inert Atmospheres on Hybrid Solar Cells Based on Semiconductor Oxides. *Journal of The Electrochemical Society* **2007**, *154*, 508-513.

(46) Liu, J.; Kadnikova, E. N.; Liu, Y.; McGehee, M. D.; Fréchet, J. M. J. Polythiophene containing thermally removable solubilizing groups enhances the interface and the performance of polymer-titania hybrid solar cells. *Journal of the American Chemical Society* **2004**, *126*, 9486-7.

(47) Krebs, F. C.; Spanggaard, H. Significant Improvement of Polymer Solar Cell. *Journal of Materials Chemistry* **2005**, *17*, 5235-5237.

(48) Helgesen, M.; Madsen, M. V.; Andreasen, B.; Tromholt, T.; Andreasen, J. W.; Krebs, F. C. Thermally reactive Thiazolo[5,4-d]thiazole based copolymers for high photochemical stability in polymer solar cells. *Polymer Chemistry* **2011**, *2*, 2536-2542.

(49) Reese, M. O.; White, M. S.; Rumbles, G.; Ginley, D. S.; Shaheen, S. E. Optimal negative electrodes for poly(3-hexylthiophene): [6,6]-phenyl C61-butyric acid methyl ester bulk heterojunction photovoltaic devices. *Applied Physics Letters* **2008**, *92*, 053307.

Chapter 2

Applications of ellipsometry for polymer solar cells

Ellipsometry is a sensitive optical method proposed by Paul Drude (1863 - 1906) and has thus been used for over a hundred years to derive information about surface and bulk properties.[1] It makes use of the fact that the polarization state of light changes when the light beam is reflected from a surface and the technique makes it possible to deduce information about the film properties, especially the film thickness. Generally optical measurement techniques are of great interest since they under normal circumstances are non-invasive and non-destructive. Ellipsometry is no exception. The basic principle of ellipsometry is, as mentioned, that upon reflection the polarization changes. The exact nature of the polarization change is determined by the properties of the sample including thickness and complex refractive index. The main advantage of ellipsometry is that, in opposition to other optical techniques that are inherently diffraction limited, ellipsometry exploits phase information and the polarization state of light, and can achieve angstrom resolution. In its simplest form, the technique is applicable to thin films with thickness less than a nanometer and up to thicknesses of several micrometers. An obvious application of ellipsometry is the use in the semiconductor industry, where thin layers of silicon dioxide are a central element throughout production. Ellipsometry enables process engineers to keep track of the thickness of the film.

In the field of organic solar cells several reports exist on applications of ellipsometry for determining optical constants and thickness, surface roughness, and morphology. While determination of thicknesses and optical constants are an important application of ellipsometry, this application is mostly used to augment other measurement and to optimize processes.[2,3] A more advanced use of ellipsometry is the use of ellipsometry to study the morphology of the bulk hetero junction. A number of approached to this exists in literature. Campoy-Quiles et al. have demonstrated work modeling the vertical composition profile of P3HT:PCBM films and reported a composition gradient varying from PCBM-rich near the PEDOT:PSS layer to P3HT-rich at the air interface.[4] This result is important in the understanding of the performance of solar cells made by spin coating. Germack et. al. have

substantiated the results and proposed that changes in the surface energy significantly affects the vertical composition profile.[5] Their analysis was based spectroscopic ellipsometry and near-edge X-ray absorption fine structure spectra.

The main work regarding ellipsometry conducted during my PhD revolved around a similar principle of determining in-depth morphology studies using ellipsometry applied for flexible substrates. I have further employed ellipsometry to generate thickness profile scans and surface scans of roll-to-roll coated samples as a quality control measure. At Risø DTU I had access to a Sopra Labs GES51 Spectroscopic ellipsomter. This particular ellipsometer was a rotating analyzer ellipsometer equipped with a translational stage, microspot optics, and an auto focus feature. The instrument was flawed when delivered from the manufacturer and a large amount of work went into solving issues relating to hardware limits, constructing sample holders, identifying and reporting software bugs, etc. The instrument was eventually sold back to the company. The results obtained with the Sopra instrument was limited to measurement of thickness and determination of optical constants and has resulted in two non co-authored contributions in peer reviewed journals in the articles entitled: “Non-destructive lateral mapping of the thickness of the photoactive layer in polymer based solar cells”[3] and “A solution process for inverted tandem solar cells”[6]. During three one week sessions the remaining parts of the measurements was done at the Johannes Kepler University (JKU) of Linz at the Zentrum für Oberflächen- und Nanoanalytik (ZONA) under Professor Kurt Hingerl. At JKU a Woollam Co. M-2000 Variable Angle Spectroscopic Ellipsometer, with a spectral range of 0.75 to 6.5 eV was available and was used to measure the data presented in the article: “Ellipsometry as a nondestructive depth profiling tool for roll-to-roll manufactured flexible solar cells” (Appendix 1.1)[7] and also data presented solely in this thesis. The Woolam ellipsometer had no translation stage or autofocus option. However, being a rotating compensator ellipsometer the instrument was far more suited to conduct measurements on organic samples. The details of the differences between a rotating analyzer and a rotating compensator ellipsometer will be explained in the following sections along with an introduction to the field of ellipsometry and the most important theoretical aspects. The last part of the chapter is devoted to the specific work carried out during the PhD.

2.1. Ellipsometry theory

Ellipsometry, as mentioned, is designed to measure the change of polarization upon reflection or transmission. Calculations of the polarization state are therefore tied to the electric field vector,

defining the direction of the polarization of the light wave. The electric field vector is decomposed into two components named *p* and *s* respectively, a tradition originating from their German names Parallel and Senkrect. Ellipsometry is primarily interested in how *p*- and *s*- components change upon reflection or transmission in relation to each other. The change in polarization is commonly written as

$$\frac{r_p}{r_s} = \tan(\Psi) e^{i\Delta}. \qquad \text{Eq. 2.1}$$

The right side of the equation is describing the measurement with $\tan(\Psi)$ representing the amplitude ratio upon reflection, and $e^{i\Delta}$ the phase shift. The left side of the equation describes the sample with r_p and r_s being the two components of the reflection coefficient. As ellipsometry measures a ratio of two values rather than an absolute value of either, the measurement is robust, accurate, and reproducible. For instance, ellipsometry is relatively insensitive to scattering and fluctuations, and requires no standard sample or reference beam. However, as ellipsometry is an indirect method, where the measured Ψ and Δ cannot be converted directly into the optical constants of the sample, a model analysis must be performed. Direct conversion into real data is only possible in simple cases of isotropic, homogeneous and infinitely thick films. In all other cases a layer model must be established, which considers the optical constant and thickness parameters of all individual layers of the sample including the correct layer sequence. Then using an iterative procedure unknown optical constants and / or thickness parameters are varied, and the right side of Equation 2.1 is calculated using the Fresnel equations for r_s and r_p. The best match provides the optical constants and thickness parameters of the sample. Roughness for example can be included in the model by using a effective medium approximation; effectively changing the optical constants in the model.[8]

Ellipsometry measurements

Obtaining Ψ and Δ from the ellipsometric measurement is very dependent on the type of ellipsometer used. Rotating analyzer ellipsometry is probably the most widespread technique, but the technique has a weakness in that it is not capable of determining the phase Δ, but rather $\cos(\Delta)$. A rotating compensator ellipsometer is capable of overcoming this issue.

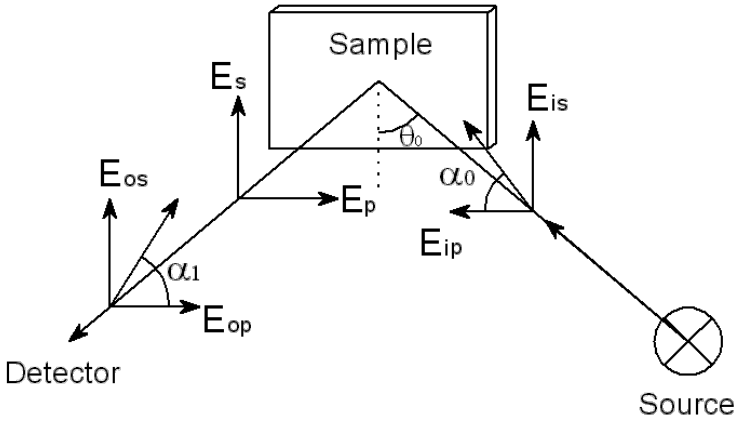

Figure 2.1. A simple ellipsometry system consisting of a light source, a polarizer, a sample, an analyzer, and a detector.

Rotating analyzer or rotating polarizer ellipsometry is a simple form of ellipsometry employed by many manufactures including the instrument at Risø DTU. See Figure 2.1 for a schematic representation of a rotating analyzer setup. The setup is based on an electromagnetic radiation emitted by a light source and linearly polarized by a polarizer. After reflection from the sample the radiation passes a second polarizer, used to analyze the polarization, and then falls into the detector. Using the Jones matrix formalism it is possible to describe the light passage through a rotating analyzer ellipsometer. Polarized light is represented by a Jones vector, and linear optical elements are represented by Jones matrices. When light crosses an optical element the resulting polarization of the emerging light is found by taking the product of the Jones matrix of the optical element and the Jones vector of the incident light

$$\vec{E}_0 = T_A \ddot{R}(\alpha_1)\ddot{T}_s\vec{E}_i = \begin{bmatrix} 1 & 0 \\ 0 & 0 \end{bmatrix}\begin{bmatrix} \cos(\alpha_1) & \sin(\alpha_1) \\ -\sin(\alpha_1) & \cos(\alpha_1) \end{bmatrix}\begin{bmatrix} r_p & 0 \\ 0 & r_s \end{bmatrix}\begin{bmatrix} E_i\cos(\alpha_0) \\ E_i\sin(\alpha_0) \end{bmatrix}. \quad (9)$$

$\vec{E}_i$ is the Jones vector representation of the incident electric field after a linear polarizer. $\ddot{T}$ is the sample reflection, $\ddot{R}(\alpha_1)$ is the rotation to match the coordinate system of the analyzer, and T_A represents the analyzer. For a rotating analyzer ellipsometer α_1 is changed to get several intensity readings. A rotating polarizer ellipsometer instead rotates the polarization of the incoming light. The intensity at the detector is the absolute value of the outgoing electric field $I_0 = \vec{E}_0 \cdot \vec{E}_0^*$. By introducing the stokes parameters; $s_0 = |E_p|^2 + |E_s|^2$, $s_1 = |E_p|^2 - |E_s|^2$, and $s_2 = E_p E_s^* + E_s E_p^*$ the intensity can be written as

$$I_0(\alpha_1) = \frac{1}{2}\left[s_0 + s_1\cos(2\alpha_1) + s_2\sin(2\alpha_1)\right].$$

The value of the Stokes parameters can be determined experimentally by conducting measurements of the intensity at a minimum of three rotations of the polarizer (α_1). Hereby three equations for I_0 is introduced with the three Stokes parameters as the only unknowns. It is possible to express the elliptical parameters by the Stokes parameters

$$\Psi = \frac{1}{2}\cos^{-1}\left[-\frac{I_0(0°) - I_0(90°)}{I_0(0°) + I_0(90°)}\right],$$

and

$$\Delta = \cos^{-1}\left[\frac{2I_0(45°)}{(I_0(0°) + I_0(90°))\sin(\Psi')} - \frac{1}{\sin(\Psi')}\right].$$[9]

In the above example it was assumed that measurements of the intensity were conducted at 0°, 45°, and 90°. The value of Δ is an inverse cosine function. This means that the precision and accuracy is poor when Δ is near 0° or 180°. For applications not requiring several angles of incident to be measured this is not a big issue. It will then be possible to conduct the measurements near the Brewster angle and maintain good accuracy of Δ. If several angles of incident is necessary in order to fit the model, poor accuracy in Δ can be problematic. This condition is encountered as an example when trying to model in-depth morphology; since multiple angles of incidence yields measurements at different optical path lengths providing valuable information. It is possible to install a compensator element into the beam path either before or after the sample. The compensator can convert the near linear polarization state near Δ = 0° or 180° to a near circular polarization state (Δ=90°), optimizing sensitivity for Δ. Hereby both Ψ and Δ can be accurately measured over their full ranges. However, a perfectly ideal spectroscopic compensator element does not exist and compensator elements which can be used spectroscopically are not achromatic.[10] This means that the retardance of the compensator must be calibrated throughout the entire spectral range. Otherwise the accuracy of the ellipsometric data will be degraded by the introduction of the compensator element.

An alternative approach to introduce a compensator into the ellipsometer beam path is to implement the rotating compensator ellipsometer configuration. This setup is not restricted to measuring only $\cos(\Delta)$, since the rotating-compensator instrument provides all four Stokes vector components for the light beam reflected from the sample surface.[10] In contrast, the rotating-polarizer instrument provides only three such components. This also means that this configuration is capable of measuring the depolarization which occurs from samples with non-uniform film thickness, roughness and other sample inhomoginities.

Data analysis

After a sample is measured and the right side of Equation 2.1 has been determined, a model must be constructed to describe the sample. The model is used to calculate the response from the Fresnel equations which describe each material with thickness and optical constants. When the values are not known they become fitting parameters for which a preliminary guess is applied. The calculated values from the left side of equation 1 are then compared to the experimental data. Any unknown parameter can be varied to improve the match between experiment and calculation. The best match between the model and the experiment is found through regression, where an estimator, like the Mean Squared Error (MSE), is used to quantify the difference between curves. The unknown parameters are allowed to change until the minimum MSE is reached. It important at this point to notice that the process of fitting can be complicated, and that many local minima may exist. It is very possible for the regression algorithm fall into a local minimum depending on the initial parameter guess.

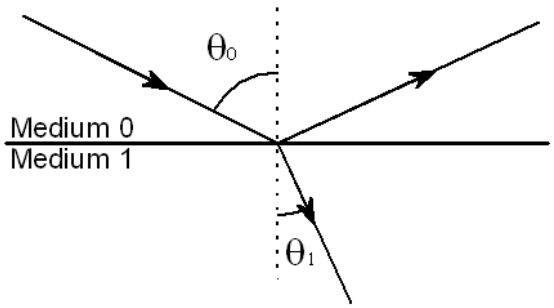

Figure 2.2. Reflection and transmission of an incident light wave at a surface boundary or a infinite film.

The simplest example of an ellipsometry model comes in the form of a bulk sample (infinite film), see Figure 2.2. Following Equation 2.1 the model must describe the ratio of r_p and r_s. For the infinite film approximation r_p and r_s are simply given by the Fresnel reflection coefficients

$$r_s = \frac{n_0\cos(\theta_0) - n_1\cos(\theta_1)}{n_0\cos(\theta_0) + n_1\cos(\theta_1)} \quad \text{and} \quad r_p = \frac{n_0\cos(\theta_1) - n_1\cos(\theta_0)}{n_0\cos(\theta_1) + n_1\cos(\theta_0)},$$

where n_0 and n_1 is the index of refraction for medium 0 and 1 respectively.[11] The refracted angle (θ_1) is related by Snells law to n_0, n_1, and θ_0. Thereby the index of refraction for medium 1 remains the only unknown. Solving Equation 2.1 with the simple Fresnel coefficients yields

$$n_1 = n_0\sin(\theta_0)\left[\left(\frac{\tan(\Psi)\exp(i\Delta) - 1}{1 + \tan(\Psi)\exp(i\Delta)}\right)^2 \tan^2(\theta_0) + 1\right]^{\frac{1}{2}} \qquad \text{Eq. 2.2}$$

A negative solution for the equation also exist, however, since the refractive index cannot be negative this solution is not shown. It follows that refractive index can directly be calculated from the ellipsometric parameters. No fitting is therefore necessary in this case.

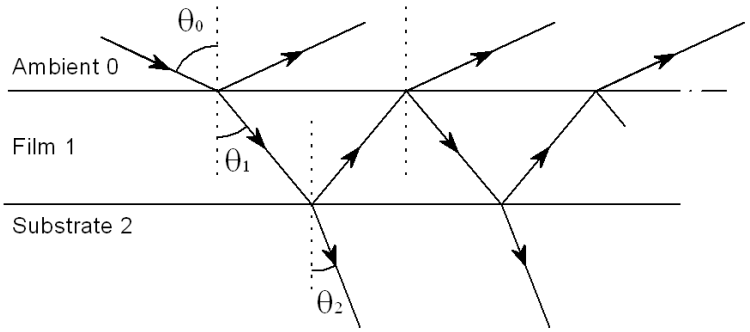

Figure 2.3. Illustration of a film substrate optical system. The system consists of three parts; the ambient environment, the film, and the sample.

A case of importance in ellipsometry is an optical system consisting of an ambient-film-substrate system as shown in Figure 2.3. When the refractive index of the film and the substrate is known it is possible to determine the thickness of the film in such a system by utilizing the Fresnel coefficients. For the single layer ontop of a substrate the coefficients are given by the Airy formula

$$R_p = \frac{r_{01,p} + r_{12,p}\exp(-i2\beta)}{1 + r_{01,p}r_{12,p}\exp(-i2\beta)} \quad \text{and} \quad R_s = \frac{r_{01,s} + r_{12,s}\exp(-i2\beta)}{1 + r_{01,s}r_{12,s}\exp(-i2\beta)},$$

where r_{01} and r_{12} are the reflection parameters for the ambient-film and the film-substrate system respectively.[10] β is the phase angle containing the thickness of the film and is given by

$$\beta = 2\pi d/\lambda n_1 \cos(\theta_1),$$

where *d* is the thickness, and λ the wavelength. Inserting R_p and R_s into Equation 2.1 yields a complex quadratic equation for $\exp(-i2\beta)$ which can be solved as

$$\exp(-i2\beta) = \frac{-\left(\frac{R_p}{R_s}E - B\right) \pm \left[\left(\frac{R_p}{R_s}E - B\right)^2 - 4\left(\frac{R_p}{R_s}D - A\right)\left(\frac{R_p}{R_s}F - C\right)\right]^{\frac{1}{2}}}{2\left(\frac{R_p}{R_s}D - A\right)},$$

where $A = r_{01,s}r_{12,s}r_{12,p}$, $B = r_{12,p} + r_{01,p}r_{01,s}r_{12,s}$, $C = r_{01,p}$, $A = r_{01,p}r_{12,p}r_{12,s}$, $E = r_{12,s} + r_{01,s}r_{01,p}r_{12,p}$, and $F = r_{01,s}$. This allows the thickness d to be calculated since the thickness is only represented in β. However, since the thickness is given in a complex exponential no single solution for the thickness exists. The thin film approximation deals with this issue by assuming that the lowest positive thickness value is the correct thickness. To determine the thickness for thicker films it is possible to conduct measurements for several wavelengths and thereby introduce more equations. For multiple isotropic layers, the calculation of the complex reflection coefficients is more complicated and performed using a matrix representation, where each layer is represented by two 2 X 2 complex matrices, one for the pp polarization and the other for the ss polarization.[10]

Optical coefficient parameterization

With ellipsometry the most typical situation with an ambient-film-substrate system is to know the complex refractive index of the substrate (either by previous measurement or from a table value), but not the thickness nor the complex refractive index of the film. In this case it is never possible to directly calculate all three unknowns. With spectroscopic ellipsometry the situation is better. However, since the refractive index is wavelength dependent the introduction of more wavelength add as many unknowns as equations. It is therefore necessary to model the optical dispersion by a simplified model to determine both optical constants and thickness. This parameterization of the optical components is done though a dispersion law simulating the optical indices and their variation according to the

wavelength. A very common optical dispersion is the Cauchy optical dispersion where six parameters are used

$$n = A + \frac{B}{\lambda^2} + \frac{C}{\lambda^4} \text{ and } k = \frac{D}{\lambda} + \frac{E}{\lambda^3} + \frac{F}{\lambda^5}.$$

By using the dispersion relation the system becomes over determined making the fitting of the parameters more robust. The Cauchy dispersion is often used as a simple approach to determine the thickness of a film. If a wavelength range exist where the film has zero absorbance the *k* component vanishes and only three fitting parameters remains beyond the thickness.

Another dispersion model often used is the the Tauc Lorentz model. This is typically used for the parameterization of the optical functions for amorphous semiconductors and insulators for which the imaginary part of the dielectric function ε_i is determined by multiplying the Tauc joint density of states by the ε_i, as obtained from the Lorentz oscillator model. The real part of the dielectric function ε_r is calculated from ε_i using Kramers-Kronig integration, making the model Kramers-Kronig consistent.

Effective medium approximation

Using an effective medium approximation (EMA), mixtures of materials with known refractive can be described. The EMA is a physical model that describes the macroscopic properties of a medium based on the properties and the relative fractions of its components. Based on the additive character of the polarizability, a generalization of the Claussius-Mossotti formula can be written as

$$\frac{\langle\varepsilon\rangle - \varepsilon_h}{\langle\varepsilon\rangle + 2\varepsilon_h} = (1-f)\frac{\varepsilon_1 - \varepsilon_h}{\varepsilon_1 + 2\varepsilon_h} + f\frac{\varepsilon_2 - \varepsilon_h}{\varepsilon_2 + 2\varepsilon_h},$$

where $\langle\varepsilon\rangle$ is the effective dielectric function, ε_1 and ε_2 are the dielectric functions of the two media subject to mixing, ε_k the dielectric function of the host medium with the inclusions, and *f* the volume ratio of material 2.[12] The underlying assumptions of the equation are that it applies for spherical inclusions and dipole interactions only. In the Bruggeman model the effective medium itself act as the host material, so $\langle\varepsilon\rangle = \varepsilon_h$.[12] The model is then self-consistent and the two phases play exactly the same role. The effective dielectric function of the mixture is given by the second order equation

$$0 = (1-f)\frac{\varepsilon_1 - \langle\varepsilon\rangle}{\varepsilon_1 + 2\langle\varepsilon\rangle} + f\frac{\varepsilon_2 - \langle\varepsilon\rangle}{\varepsilon_2 + 2\langle\varepsilon\rangle}. \qquad \text{Eq. 2.3}$$

The validity of the Bruggeman effective medium approximation requires the sizes of the phases (dielectrics) in a composite material to be sufficiently greater than atomic sizes, but smaller than 1/10 of the wavelength, which indeed is true for the bulk heterojunction films. The effective medium approximation cannot represent non-additive features of the dielectric function, such as charge transfer absorption bands. Lastly the dielectric functions of the phases must be independent of size and shape.

Practical considerations

There are a number of practical considerations to be familiar with in connection with ellipsometry measurements. The first major hurdle is backside reflections. Backside reflections occur when front surface and back surface reflections overlap and enter the detector. This happens for transparent substrates which are polished on both sides. This was the case for the glass substrates used during this thesis for modeling work. These unwanted backside reflections are incoherent with the desired reflection from the front side and can either be accounted for in the model or suppressed by experimental means. One approach is to roughen the backside so the light is effectively scattered.

Another effect encountered in connection with ellipsometry is depolarization. Depolarization occurs when totally polarized light used as a probe in ellipsometry is transformed into partially polarized light. The effect of depolarization is especially severe for a rotating angle ellipsometer as the instrument assumes that reflected light is totally polarized. Imagine a case where the reflected light of linear polarization is overlapped with circular polarization. For a rotating angle ellipsometer the polarization state of this reflected light will be interpreted as elliptical polarization, since this instrument assumes totally polarized light for reflected light. With a rotating compensator ellipsometer the depolarization can be measured and included in the model. The physical phenomena that generate partially polarized light upon light reflection are; surface light scattering caused by a large surface roughness, incident angle variation originating from the weak collimation of probe light, wavelength variation, thickness inhomogeneity in the film, and backside reflection.[13] The measurement of the depolarization therefore gives a good indication of the quality of the sample.

2.2. Model system and validation

The main results using ellipsometry conducted during this thesis has been determining the in-depth morphology of P3HT:PCBM on flexible substrates (Appendix 2.1)[7], conducting thickness and composition linescans on flexible substrates (Appendix 2.1) [7], and doing surface thickness scans on flexible substrates (previously unpublished). In order to achieve this, model work was conducted on glass substrates and validated. Firstly the optical constants of the substrate was determined, secondly the optical constants of the constituent materials (P3HT and PCBM) were measured. A model system was established using an effective medium approximation to describe the layer both including and excluding morphology and validated by complementary techniques. Lastly the model system was applied to the flexible substrate samples.

The solar cell geometry chosen as the basis for the main ellipsometry work was a modified Fraunhofer type solar cell fabricated by a full roll-to-roll process, with a Kapton/Al/Cr/P3HT:PCBM/PEDOT:PSS/Ag structure.[14] The active layer was the layer of interest. For this specific geometry efficiencies up to 3.1% had been reported on lab scale cells and 0.5 % efficiency for roll-to-roll processed cells.[14–16] This specific geometry was chosen because of the bottom aluminum electrode. The typical flexible substrate material such as biaxially-oriented polyethylene terephthalate (PET), is made by stretching the polymer materials. The stretching is achieved through a series of sequential processes, in which the film is first drawn in the machine direction using heated rollers and subsequently drawn in the transverse direction in a heated oven. Once the drawing is completed, the film is crystallized under tension in the oven at temperatures typically above 200 °C, preventing the film from shrinking. The disadvantage with this process from an ellipsometry point of view is that the process induces optical anisotropy in the material. This anisotropy is difficult but not impossible to model, making ellipsometry more complicated. With a rotating angle ellipsometer this type of substrate will never work since the anisotropy induces a mixed polarization state that cannot be correctly described. Additional problems with the substrate occur in connection with mounting the substrate. Since tension will twist the optical axis changing the anisotropy, the sample must be mounted without any tension. A simple approach to conducting ellipsometry on PET involves using only the UV part of the spectrum. This will work due to the absorbance of the PET material, making it possible to make determinations about film thickness and perhaps roughness. For the studies conducted here a simpler system with aluminum on top of a Kapton film was chosen. This system is favorable since only the aluminum must be included in the model.

Substrate optical constant

The use of a flexible substrate presents a number of challenges. Primarily the production of several samples with different thicknesses and compositions was not viable on the Kapton / Aluminum substrate. Additionally the optical constants of the material were not well described. A model system was therefore needed with a well described substrate. The first step in dealing with a model system is to find a suitable substrate to work on. One option was to choose a silicon wafer. The advantage of silicon is that the surface roughness is minimal, the optical constants are well known and described, and the material is optically homogeneous. Additionally since silicon has an index of refraction at 3.96 at 590 nm the ellipsometric measurement will be very precise since the refractive index of most polymer materials are in the range 1.2 – 1.7. Hereby good resolution of both Ψ and Δ can be expected even with a rotating angle ellipsometer. The drawbacks of this substrate are that silicon has a vastly different surface energy than glass, making spin coating of the materials more cumbersome. Secondly since no solar cell geometry at Risø DTU is based on silicon, this substrate option was abandoned. Instead glass was chosen as the model substrate material.

Optically there are a number of complications using glass. Firstly since glass is transparent in the visible spectrum backside reflections must be mitigated. This was done by roughening the backside with a diamond scribe. The second issue was that the index of refraction is not well known for all types of glass. This, however, could easily be overcome by measuring the refractive index. However, thirdly; there are many types of glass available and not all are optically homogeneous. The most commonly used type of glass is float glass. Float glass is made by floating molten glass on a bed of molten metal, typically tin. This induces a gradient of tin into the glass on both sides. The bottom gradient stems from direct contact with the molten tin, and the top side from tin vapors. Hereby this type of glass has two dissimilar sides both featuring an optical gradient. To obtain a workable optical model for this type of substrate, attempts were made to remove the top micrometers of glass by grinding and polishing. This allowed bulk values of the refractive index to be measured and calculated using Equation 2.2 in Matlab. Then this value could be used to introduce an ambient-film-substrate system as shown in Figure 2.3, where a tin layer was included as the film layer. While moderately successful this approach was later dropped as a better substrate was indentified.

The alternative glass chosen was objective glass manufactured by Menzel-Gläser. This specific glass is especially suitable for ellipsometry since it is drawn according to the Fourcault-method. Hereby it does not exhibit the tin-rich layer from the typical float glass. This type of glass is also characterized by low

surface roughness. All the data presented here for the model system is measured based on this substrate glass. The optical index was measured by direct conversion using Equation 2.2 with the backside roughened for the measurements.

Optical constant of constituent materials

To obtain the optical constants for the constituent materials; namely P3HT and PCBM a generalized oscillator model was set up. The procedure began, in the case of P3HT, by determining the thickness by fitting a Cauchy model using the zero absorbance approximation. With the thickness locked the complex refractive index could be obtained from point-by-point calculation. These values are, however, directly affected by the noise in the measurement since the system is not overdetermined. A model for the optical constants therefore needed to be introduced. A generalized oscillator model, using Tauc Lorentz oscillators was employed for this. Using the complex refractive index obtained by point-by-point calculation each oscillator could be introduced and roughly fitted by hand. After that a fitting routine was initiated with a range established for each fitting parameter. Measurements of P3HT were conducted at both Risø DTU on the Sopra rotating angle ellipsometer and at JKU on the Woolam rotating compensator ellipsometer, with similar results. The results shown here was obtained at JKU. Following the same procedure the optical constants of PCBM were determined.

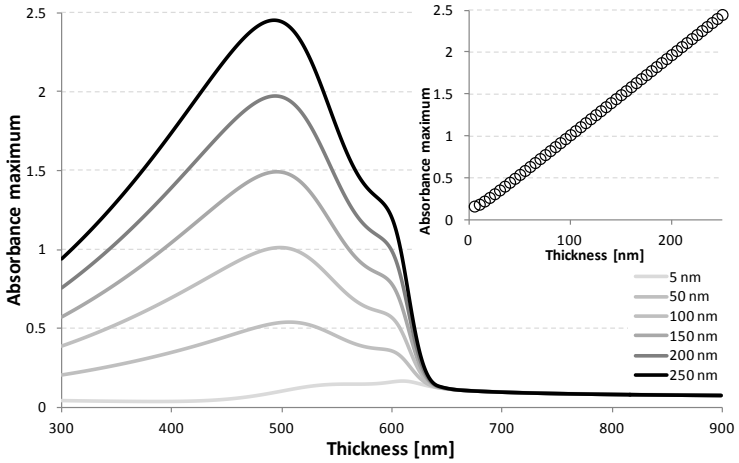

Figure 2.4. A simulation of the absorption based on the optical constants measured by ellipsometry. The insert shows the absorption maximum as a function of thickness.

An example of the direct application of these measurements is featured in the article: "Photochemical stability of conjugated polymers, electron acceptors and blends for polymer solar cells resolved in terms of film thickness and absorbance" (Appendix 2.2)[17] where a fit of the absorption spectrum of P3HT and PCBM is used to validate a model to determine the thickness of a film of P3HT on a glass

substrate by the maximum absorbance value only. Thickness measurements obtained by atomic force microscopy showed a linear relation between thickness and absorption maximum value. The simulation based on the optical constants, see Figure 2.4, validated this linear relation. This model was also used in the articles: "Influence of processing and intrinsic polymer parameters on photochemical stability of polythiophene thin films" (Appendix 2.3)[18] and "Concentrated light for accelerated photo degradation of polymer materials" (Appendix 2.3)[19].

Model system

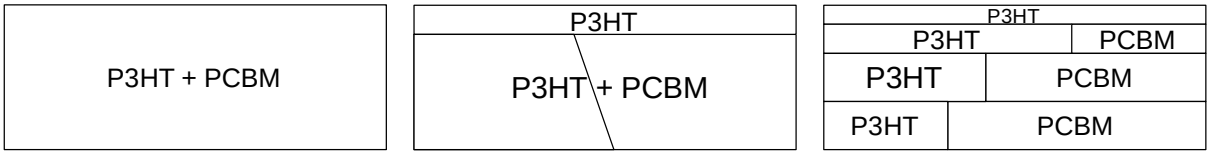

Figure 2.5. A single layer EMA mix (left) of the two components, this model is labeled simple EMA. A more complex model (middel) featuring a phase separated top part of P3HT of varying thickness, labeled as the linear gradient model. A four phase model (right).

In order to model a blended system of P3HT and PCBM an effective medium approximation based on Equation 2.3 was introduced. The effective medium approximation allows the effective dielectric function to be calculated based on the volume fraction of the constituent materials. A blended layer of P3HT and PCBM can hereby be modeled as depicted in the left of Figure 2.5. Using this model it is possible to combine the complex refractive index of P3HT and PCBM as seen in Figure 2.6. In the figure peaks are assigned to P3HT and PCBM respectively.

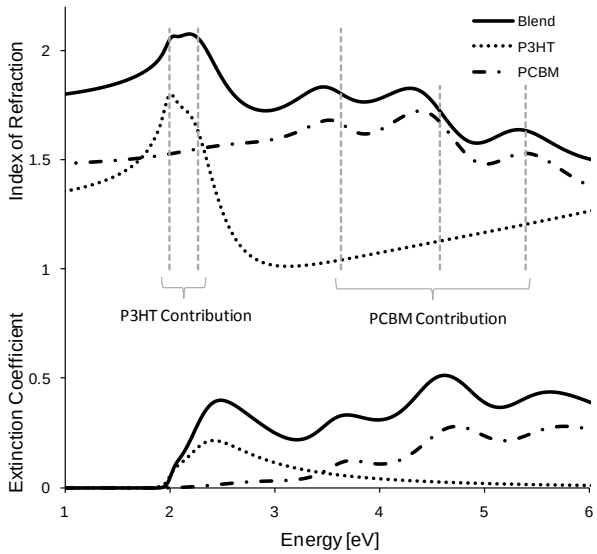

Figure 2.6. Optical dispersions with peaks assigned are shown for both the index of refraction (top) and the extinction coefficient (bottom). The solid line is the dispersions of the BHJ layer and the dotted lines are the dispersions for the pure phases. Reprinted with permission from the American Chemical Society.[7]

In order to model more advanced features using the effective medium approximation an expansion is introduced. The right part of Figure 2.5 depicts a model where a stack of four layers represents the entire film. This way each level represents a part of the in-depth morphology. Various degrees of freedom can be introduced by locking different aspects of the model such as the ratio of a given layer or the thickness. An even more advanced model, such as the one depicted in the middle of Figure 2.5, can be achieved. The gradient is described by introducing a high number of layers and locking their composition to follow a function. In this case a linear function has been chosen for the composition, but all types of mathematical functions are possible.

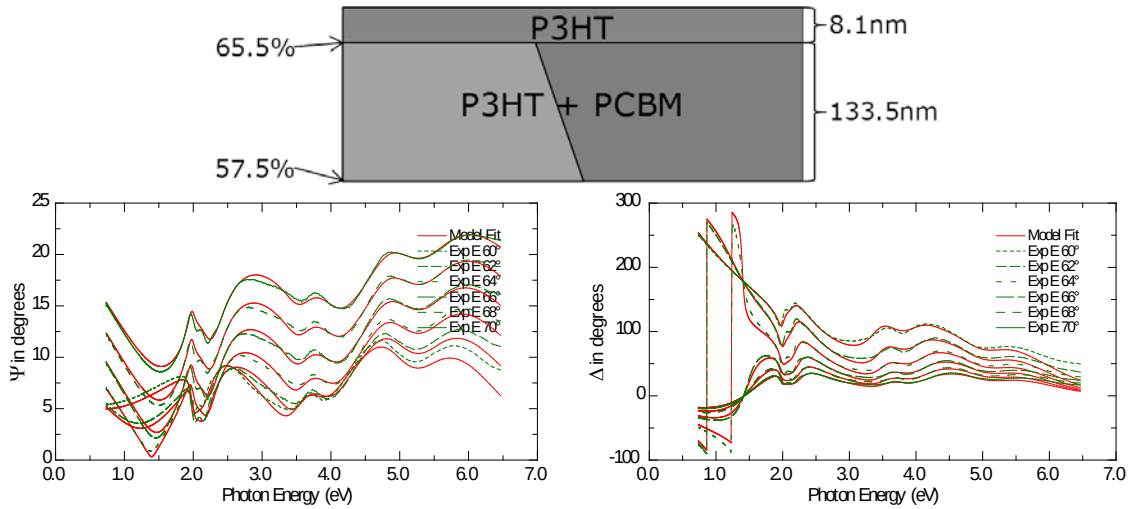

Figure 2.7. The phase gradient model (top) shows the result of the fitting procedure. The fit of Ψ (bottom right) and Δ (bottom left) shows the quality of the fit (MSE = 20.59), where red lines represents the model and green the experimental values.

In order to establish the correct in-depth morphology of the sample a large number of samples were made at different thicknesses and concentrations. These were comprised of a series of samples made at different spin speeds (500, 1000, 2000, 4000 rpm) and concentrations (1:1, 1:0.7). By using the four phase model seen in Figure 2.5, fitting was carried out using a random global fit algorithm running within reasonable physical limits. The idea of the random global fit is that each fitting parameter is restricted to a certain range. Then the computer generates a large number of starting guesses to be run in the fitting algorithm. These were given such that the composition of P3HT and PCBM could not be negative and that the total thickness stayed within ±20 percent of the thickness as determined by a zero absorption Cauchy model. The model was subject to a fitting process were the compositions of the four layers were set to values from 0 and 100 percent composition in steps of 25 percent. The combined thickness was set at values between 20% less than the expected thickness and 20 % above the expected thickness with five evenly spaced guesses. The thicknesses of the sublayers were treated as free parameters set to the value from the previous fit. Hereby 2500 different starting guesses were established. These were fitted in a random order as the randomness prevents the fit from falling back into the previous local minimum. The overall best set of parameters was saved. By repeating this procedure for all eight samples with different thickness and composition it was established that a linear vertical composition gradient combined with a top phase separation would yield the simplest model capable of describing all thicknesses and compositions with a low minimum square error for all samples. The linear model with the phase separation only has four fitting parameters, see the middle

of Figure 2.5. Two examples of the four phase fitting can be seen in Figure 2.9 and Figure 2.10 respectively. The linear gradient model yielded generally fits with low mean square error and one example of this model for a glass substrate can be seen in Figure 2.7 along with the fits of Ψ and Δ.

Model system validation

Generally it is very difficult to prove a model used for ellipsometry. In this work it is important to notice that the ellipsometry model so far, has not been based on anything beyond the ellipsometry measurement. The random global fitting procedure allowed a prediction of the in-depth morphology. When a range of samples had been evaluated a simplified model was chosen to represent the in-depth morphology. The linear model with phase separation, see Figure 2.5, was also chosen to be the simplest model describing the in depth morphology. It is therefore perhaps not the best model to describe all details of the in depth morphology, but rather a model giving good consistent fits with less tendency for the model to fall into local minima during the fitting. This is the case since this model represents a large decrease in the number of free parameters (four phase model = 8 parameters and linear model with phase separation = 4 parameters).

In order to validate the model a number of measures were introduced. The first leg in the validation procedure was validating the total thicknesses determined by the ellipsometry model. This was done by measuring the thickness of all samples using AFM. All thicknesses were within the uncertainty of the AFM values, thereby validating that the model is capable of determining the thickness.

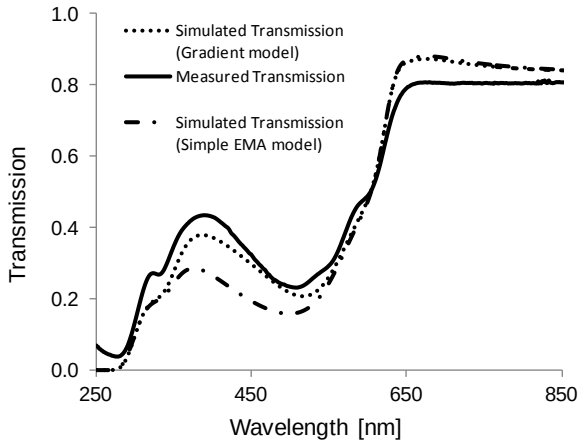

Figure 2.8. Transmission simulation Good fit between simulated transmission and measured transmission.

The second leg in the validation is related to the transmission of the sample. Since the transmission spectrum can be calculated from the optical constants and the thickness; the model can be validated

by comparing the simulated transmission spectrum to a measured transmission spectrum. Figure 2.8 shows the simulated transmission spectrum for both the one layer effective medium and for the linear gradient model along with the measured transmission spectrum. Generally it must be noted that the simulation of the absorption is based on the pure phase optical spectra of P3HT and PCBM respectively. A perfect fit can therefore not be expected as for example vibronic features cannot be modeled within that restraint. However, it is clear that the fit of the linear model is an improvement over the fit of the single layer effective medium. Reasonable fits of the transmission was observed for all samples.

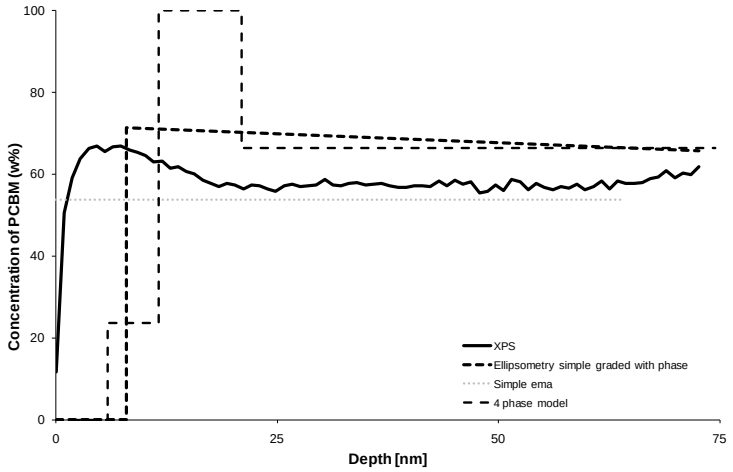

Figure 2.9. Three different models represented by the dashed lines (simple EMA model, four phase model, and linear model with phase separation, see figure 2) detailing the in-depth morphology of a P3HT:PCBM 1:1 blend spin-coated on glass at 4000 rpm.

The last leg in the validation procedure was to determine the in-depth morphology directly using a complementary technique. This was done by X-ray photoelectron spectroscopy (XPS) depth profiling using a K-alpha XPS (Thermo Electron Limited, Winsford, UK) with a monochromated Al-K_α X-ray source. The composition of P3HT and PCBM was calculated by measuring the content of carbon and sulfur and then calculating the distribution of the two phases by considering the molecular formulas of P3HT and PCBM respectively. This was possible since only P3HT contains sulfur. Atomic compositions were determined from surface spectra, and were calculated by determining the integral peak intensities using a Shirley type background removing the inelastically scattered electron contribution. A comparison of the XPS depth profile and the ellipsometrically determined profile is depicted in Figure 2.9 and Figure 2.10. By comparing the XPS and ellipsometry data it is observed that the XPS depth profile does not feature an as distinct phase separation as the ellipsometry model suggests. Since the

probe depth of the XPS is 5-12 nm the real gradient will be a convolution of the real vertical gradient and the probe depth, smoothening out the result. Therefore the XPS data supports the ellipsometry model. The pileup of PCBM in the beginning of the XPS profile and the later more linear slope is described well within the linear gradient restriction.

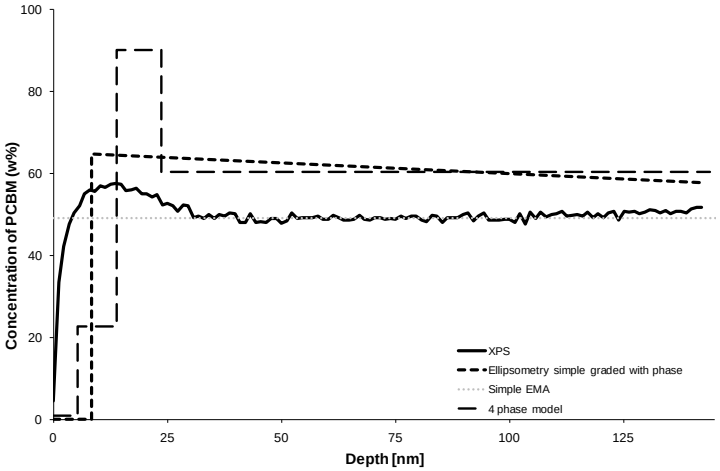

Figure 2.10. Three different models represented by the dashed lines (simple EMA model, four phase model, and linear model with phase separation, see figure 2) detailing the in-depth morphology of a P3HT:PCBM 1:0.7 blend spin-coated on glass at 500 rpm.

2.3. Results

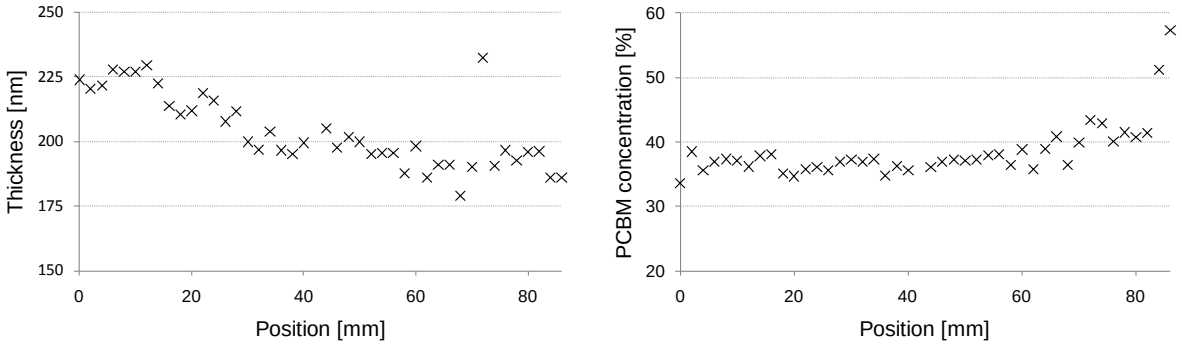

Figure 2.11. Line scan depicting (left) thickness and (right) composition distribution over the width of the printed stripe. Reprinted with permission from the American Chemical Society.[7]

Having established a sound model to describe the in-depth morphology and also the blend ratio it was possible to shift from the model substrate to the flexible substrate. Laminating the substrates onto a piece of glass introduced rigidity to the sample and ensured that the samples were flat. It was found necessary to use micro-spot for acceptable measurements to be conducted. For each measurement the depolarization factor was measured to evaluate the degree of partially polarized light caused by

curvature of the sample. Thus only measurements exhibiting low depolarization were considered. The optical dispersion of the substrate was determined by point by point fitting procedure solving the ellipsometric equations analytically (Equation 2.2) and making the best fit for multiple angles. Using the simple EMA model for the BHJ layer (Figure 2.5 left) fits of the thickness and composition of constituents could be made. This was employed to conduct a line scans across the width of the slot-die coated stripe (8 cm wide) on the Woolam ellipsometer at JKU. As this ellipsometer did not have a translation stage the line scans had to be made by hand. The spatial resolution of the micro spot optics was roughly 0.1 mm. Figure 2.11 depicts a linscan made with 50 points. The sample is a P3HT coated piece of Kapton with an aluminum / chrome electrode. The linescans are presented in full in the article entitled "Ellipsometry as a Nondestructive Depth Profiling Tool for Roll-to-Roll Manufactured Flexible Solar Cells", Appendix 2.1[7]. The model showed that the thickness had a slope in the distribution of BHJ layer over the observed sample. The composition at the macroscopic level is determined by the composition of the solution and the results confirmed that no real composition change is visible across the sample.

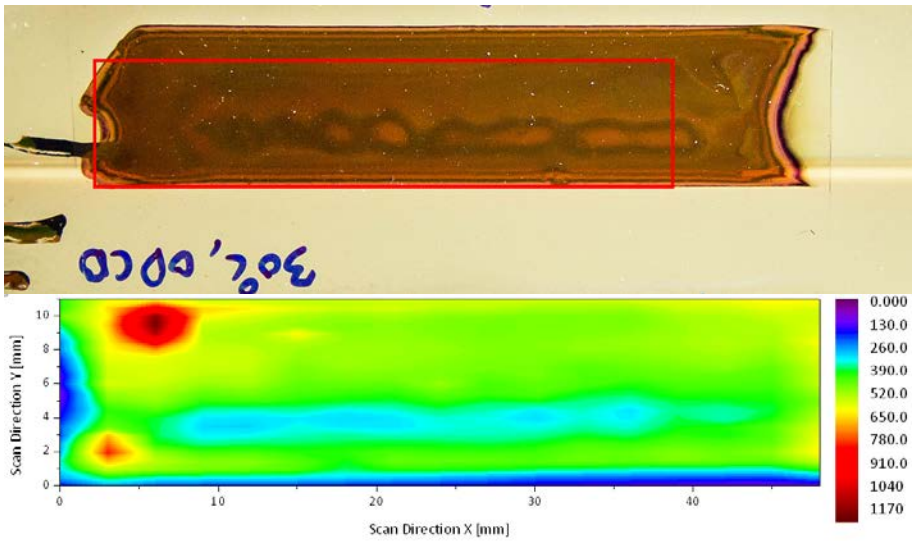

Figure 2.12.Photograph of the roll coated sample (top) and thickness map (bottom).

Using a motorized translation stage, measurements can be carried out with small translation overhead, however, doing the measurements by hand meant only a few linescans could be conducted. Even with a motorized stage and setting the translation overhead to 5 seconds and using only one angle, the complete acquisition, would take 400 seconds. It is hereby becomes clear that ellipsometry in this form is not appropriate for real time roll-to-roll characteristics, but rather constitutes a means of off-line quality control and process optimization.

The idea of the linescan can easily be evolved into conducting a surface scan. This is simply done by doing multiple linescans. Figure 2.12 shows a surface scan of a sample made on a roll coating setup. Features are clearly recognizable from the photograph of the sample. It is surprising that the sample exhibits thickness variations in the range from 100 nm to 1 µm and suggests that the coating in this case was very unstable. This data has not previously been published.

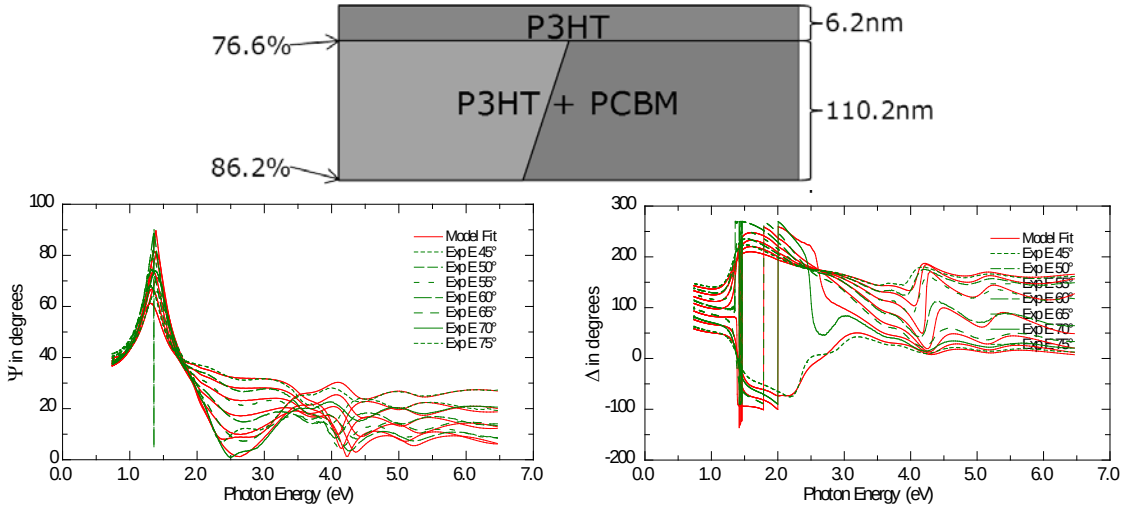

Figure 2.13. Flexible chrome Kapton substrate spin-coated with P3HT:PCBM. The model is shown on top and the fits of Ψ and Δ is shown in the bottom.

Fitting of the ellipsometric data for spin-coated flexible substrates revealed that the vertical gradient could be modeled within the same framework used for the samples based on glass substrates, see Figure 2.13. The behavior of a phase separated P3HT layer remained, but the linear gradient had reversed. In these cases more PCBM was found at the substrate interface as compared to the glass substrates. For a roll-to-roll coated sample a similar in-depth morphology could be shown, see Figure 2.14. These results were presented in the article entitled: "Ellipsometry as a Nondestructive Depth Profiling Tool for Roll-to-Roll Manufactured Flexible Solar Cells", (Appendix 2.1)[7].

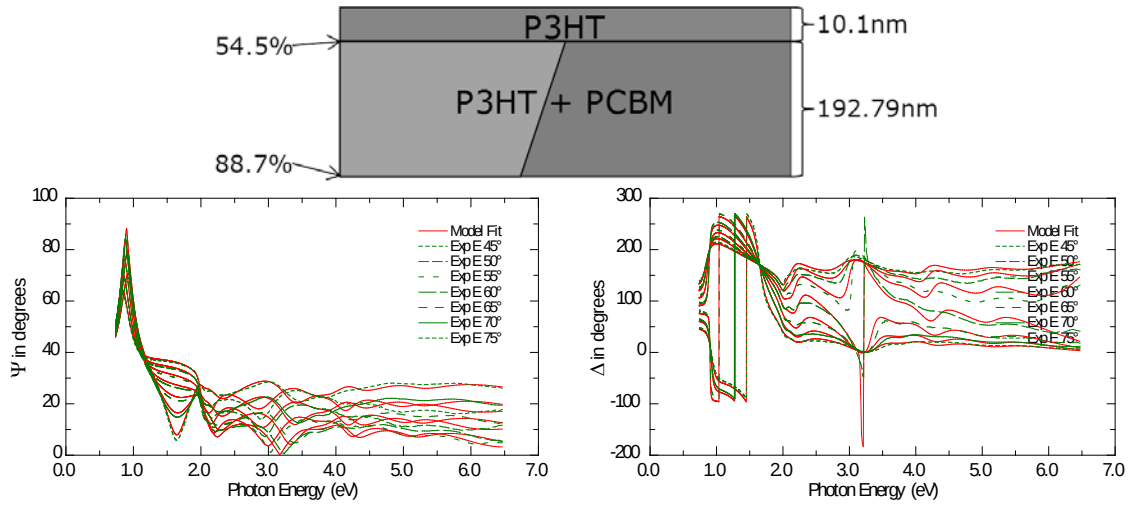

Figure 2.14. Flexible chrome Kapton substrate coated with P3HT:PCBM. The model is shown on top and the fits of Ψ and Δ is shown in the bottom.

2.4. Conclusions

From the work presented in this chapter it is evident that the implementation of ellipsometry in the organic photovoltaic processing technology presents a series of challenges. Some challenges are related to the application of ellipsometry to organic materials on glass substrates. Other challenges are unique when working on flexible substrates. It has been demonstrated that variable angle spectroscopic ellipsometry can be employed to determine optical constants of the organic materials involved. The use of a rotating compensator ellipsometer for this application is by far preferable. This is mainly due to the fact that the refractive index of the polymer materials almost matches that of glass. It has also been demonstrated that ellipsometry can be a useful technique to evaluate the quality of roll or roll-to-roll coated samples. For this thickness and composition linescans have been carried out as well as thickness maps.

The composition gradients in the bulk heterojunction layer of polymer solar cells can be determined by ellipsometry. This has been demonstrated by studying various model systems and confirming results with transmission measurements and XPS depth profiles. It was concluded that samples manufactured by spin coating and slot-die coating exhibit similar vertical composition gradient on equal substrates. It is important to stress that great care must been taken when using ellipsometry to test the model. Reasonable means of confirming the model include checking the thickness by complementary techniques such as AFM and comparing simulations to optical transmission spectra. In addition is important to stress that ellipsometry can act as a predictive technique. In the case presented here; the

models are based on a model with randomly assigned parameters, with no preconceived knowledge of the in-depth morphology necessary.

It is well known that thermal annealing leads to a dramatic increase in the PCE with respect to as-spun devices.[20] This leads to a non-thermodynamically stable situation.[21–24] Ellipsometry with the models described in this thesis will be able to monitor the change in morphology using the technique presented.

2.5. References

(1) Drude, P. Ueber Oberflächenschichten. I. Theil. *Annalen der Physik* **1889**, *272*, 532-560.

(2) Hoppe, H.; Sariciftci, N. S.; Meissner, D. Molecular Crystals and Liquid Crystals Optical constants of conjugated polymer / fullerene based bulk- heterojunction organic solar cells. *Molecular Crystals and Liquid Crystals* **2002**, *385*, 37-41.

(3) Sylvester-Hvid, K. O.; Tromholt, T.; Jørgensen, M.; Krebs, F. C.; Zimmermann, K.; Liehr, A. Non-destructive lateral mapping of the thickness of the photoactive layer in polymer based solar cells. *Progress in Photovoltaics: Research and Applications* **2011**.

(4) Campoy-quiles, M.; Ferenczi, T.; Agostinelli, T.; Etchegoin, P. G.; Kim, Y.; Anthopoulos, T. D.; Stavrinou, P. N.; Bradley, D. D. C.; Nelson, J. Morphology evolution via self-organization and lateral and vertical diffusion in polymer : fullerene solar cell blends. *Nature Materials* **2008**, *7*, 158-164.

(5) Germack, D. S.; Chan, C. K.; Kline, R. J.; Fischer, D. A.; Gundlach, D. J.; Toney, M. F.; Richter, L. J.; Delongchamp, D. M. Interfacial Segregation in Polymer / Fullerene Blend Films for Photovoltaic Devices. *Macromolecules* **2010**, *43*, 3828-3836.

(6) Larsen-Olsen, T. T.; Bundgaard, E.; Sylvester-Hvid, K. O.; Krebs, F. C. A solution process for inverted tandem solar cells. *Organic Electronics* **2011**, *12*, 364-371.

(7) Madsen, M. V.; Sylvester-Hvid, K. O.; Dastmalchi, B.; Hingerl, K.; Norrman, K.; Tromholt, T.; Manceau, M.; Angmo, D.; Krebs, F. C. Ellipsometry as a Nondestructive Depth Profiling Tool for Roll-to-Roll Manufactured Flexible Solar Cells. *Journal of Physical Chemistry C* **2011**, *115*, 10817-10822.

(8) Aspnes, D. E.; Theeten, J. B.; Hottier, F. Investigation of effective-medium models of microscopic surface roughness by spectroscopic ellipsometry. *Physical Review B* **1979**, *20*, 3292-3302.

(9) Azzam, R. M. A.; Bashara, N. M. *Ellipsometry and Polarized Light*; North Holland, 1988.

(10) Tompkins, H. G.; Irene, E. A.; Hill, C.; Carolina, N. *Handbook of Ellipsometry*; 2005.

(11) Klein, M. V.; Furtak, T. E. *Optics*; Edition, S., Ed.; Wiley, 1986.

(12) Bruggeman, D. A. G. Berechnung verschiedener physikalischer Konstanten von heterogenen Substanzen. *Annalen der Physika* **1935**, *24*, 636-679.

(13) Fujiwara, H. *Spectroscopic Ellipsometry - Principles and Applications*; Wiley, 2003.

(14) Manceau, M.; Angmo, D.; Jørgensen, M.; Krebs, F. C. ITO-free flexible polymer solar cells: From small model devices to roll-to-roll processed large modules. *Organic Electronics* **2011**, *12*, 566-574.

(15) Zimmermann, B.; Glatthaar, M.; Niggemann, M.; Riede, M. K.; Hinsch, a.; Gombert, a. ITO-free wrap through organic solar cells—A module concept for cost-efficient reel-to-reel production. *Solar Energy Materials and Solar Cells* **2007**, *91*, 374-378.

(16) Zimmermann, B.; Würfel, U.; Niggemann, M. Longterm stability of efficient inverted P3HT:PCBM solar cells. *Solar Energy Materials and Solar Cells* **2009**, *93*, 491-496.

(17) Tromholt, T.; Madsen, M. V.; Carlé, J. E.; Helgesen, M.; Krebs, F. C. Photochemical stability of conjugated polymers, electron acceptors and blends for polymer solar cells resolved in terms of film thickness and absorbance. *Journal of Materials Chemistry* **2012**, *22*, 7592-7601.

(18) Madsen, M. V.; Tromholt, T.; Böttiger, A.; Andreasen, J. W.; Norrman, K.; Krebs, F. C. Influence of processing and intrinsic polymer parameters on photochemical stability of polythiophene thin films. *Polymer Degradation and Stability* **2012**.

(19) Madsen, M. V.; Tromholt, T.; Norrman, K.; Krebs, F. C. Concentrated light for accelerated photo degradation of polymer materials. *Submitted to Advanced Energy Materials* **2012**.

(20) Padinger, F.; Rittberger, R. S.; Sariciftci, N. S. Effects of Postproduction Treatment on Plastic Solar Cells. *Advanced Functional Materials* **2003**, *13*, 85-88.

(21) Zhang, Y.; Yip, H.-L.; Acton, O.; Hau, S. K.; Huang, F.; Jen, A. K.-Y. A Simple and Effective Way of Achieving Highly Efficient and Thermally Stable Bulk-Heterojunction Polymer Solar Cells Using Amorphous Fullerene Derivatives as Electron Acceptor. *Chemistry of Materials* **2009**, *21*, 2598-2600.

(22) Swinnen, a.; Haeldermans, I.; vande Ven, M.; D'Haen, J.; Vanhoyland, G.; Aresu, S.; D'Olieslaeger, M.; Manca, J. Tuning the Dimensions of C60-Based Needlelike Crystals in Blended Thin Films. *Advanced Functional Materials* **2006**, *16*, 760-765.

(23) Bertho, S.; Janssen, G.; Cleij, T. J.; Conings, B.; Moons, W.; Gadisa, A.; D'Haen, J.; Goovaerts, E.; Lutsen, L.; Manca, J.; Vanderzande, D. Effect of temperature on the morphological and photovoltaic stability of bulk heterojunction polymer:fullerene solar cells. *Solar Energy Materials and Solar Cells* **2008**, *92*, 753-760.

(24) Drees, M.; Hoppe, H.; Winder, C.; Neugebauer, H.; Sariciftci, N. S.; Schwinger, W.; Schäffler, F.; Topf, C.; Scharber, M. C.; Zhu, Z.; Gaudiana, R. Stabilization of the nanomorphology of polymer–fullerene "bulk heterojunction" blends using a novel polymerizable fullerene derivative. *Journal of Materials Chemistry* **2005**, *15*, 5158.

Chapter 3

Automated photo-degradation

Performing photo-degradation of both complete solar cells and single polymer layers is a necessary step in obtaining knowledge of the degradation mechanisms. Once degraded the cells or the materials can be probed by relevant techniques and be further degraded. The photo-degradation itself is typically achieved by illuminating the sample under a solar simulator and the sample can then be manually transferred to and from the instrument intended for characterization. One primary method of following the degradation is by optical transmission measurements. A large number of publications exits in literature with this exact approach.[1–8] A main focus during this PhD has been in the automation of the trivial task of performing photo-degradation. By removing the element of an operator from the process the number of errors in an experiment is reduced significantly. Secondly time intervals of measurements can be reduced and lag time almost completely removed. Lastly since an automated system can work day and night a much larger number of samples can be evaluated, increasing the statistics. By operating a sample exchanger robot equipped with a spectrometer setup for transmission measurements this was achieved. The design and construction of this degradation environment along with acquisition and post treatment software is the focus of this chapter. The setup has been used in connection with four articles entitled; “Photochemical stability of conjugated polymers, electron acceptors and blends for polymer solar cells resolved in terms of film thickness and absorbance” (Appendix 2.2)[9], “Influence of processing and intrinsic polymer parameters on photochemical stability of polythiophene thin films” (Appendix 2.3)[10], “Comparative Studies of Photo Chemical Cross-linking Methods for Stabilizing the Bulk Hetero-Junction Morphology in Polymer Solar Cells” (not included in the thesis)[11], and ”Concentrated light for accelerated photo degradation of polymer materials” (Appendix 2.4)[12]. The work has solely focused on the degradation of the active layer materials.

3.1. Light induced degradation of polymer materials

While large efforts are put into describing the degradation and stability of solar cells, focusing purely on the stability of the polymer itself can yield valuable insight into the degradation mechanisms. Using

UV-visible spectroscopy to study the rate of polymer degradation is a straight forward technique. It makes sense since the absorption is vital for solar cell operation as only absorbed photons can generate excitons. The technique of monitoring the gradual absorbance loss was first presented by Holdcroft in 1991, studying photo-chemical stability of P3HT.[13] Describing photo-stability can be done either in solution[14] or as thin films.[15,16] Chemical properties such as conjugation length and crystallinity can be qualitatively discussed based on the absorption measurements. Using degradation rates based on loss of absorbance directly allows for correlating the degradation state to the number of intact monomer units. The number of monomers scales directly with the absorbance, and thus the degradation state can be written as

$$D_{state} = \frac{N_{Monomer}}{N_{initial}} = \frac{A}{A_{initial}},$$

where $N_{initial}$ is the initial number of monomers, $A_{initial}$ and A is the initial and current absorbance respectively. The number of monomers at a given time during degradation can be expressed by

$$N_{Monomer} = \frac{N_A \rho}{M} t \cdot D_{state}$$

,

where N_A is Avogadro's number, ρ is the polymer density, M is the molar mass, and t is the film thickness. According to the Lambert-Beer law, the thickness of the film scales with the absorbance. The reciprocal rate of monomer loss yields the degradation event interval,

$$\tau = \left(\frac{dN_{Monomer}}{dt} \right)^{-1}.$$

It is hereby evident that the use of UV-visible spectroscopy is a direct approach for obtaining information on the rate of photo-degradation. This can directly be used to compare polymers, but also to compare effects of barrier materials, temperature, atmosphere and more. Using this technique Manceau et al. has created a rule of thumb for photo-stability of a range of polymers.[1]

The most used polymer in polymer solar cells is arguably P3HT. Degradation of P3HT is well documented and can be facilitated by exposure to light and molecular oxygen that destroys the π–

conjugation and consequently induces loss of absorption. P3HT is degraded under these conditions in solution as well as a solid (e.g. a film). The consequence of degradation is well established but the mechanism responsible for it has been subject to discussion. Whereas singlet oxygen is known to be the cause of degradation in solution,[17] the degradation mechanism in the solid state is believed to be different. Manceau et al. have proposed a degradation mechanism based on a radical process beginning from an abstraction of an allylic hydrogen, leading to side-chain and sulfur oxidation.[8,18] This process is responsible for breaking the macromolecular backbone resulting in loss of conjugation and consequent bleaching of the sample. This mechanism occurs under both photo- and thermo-oxidation enforcing the notion that singlet oxygen is not the main intermediate in the degradation process. Hintz *et al.* have conjectured that the polymer is mainly attacked at the terminal thiophene rings under photo-oxidation.[2] The authors concluded this from observing the kinetics of the blueshift in the optical absorption. They observed that the blueshift, indicating loss of conjugation (observed for oligomers with less than 20 thiophene units), is not observed until the end of the degradation of the polymer. Hintz et al. have also demonstrated that a strong increase in photon effectiveness is observed for photo-degradation of P3HT films for decreasing irradiation wavelengths.[3] Changing the illumination wavelength from 554 to 335 nm lead to an increase by a factor of 50 in effectiveness of the P3HT photo-oxidation. This observation supports the radical chain mechanism driven by photo-generation of radicals by the photo-lysis of precursors absorbing in the ultraviolet region.

3.2. Degradation setup

In order to be able to produce reliable data on photo-degradation automatically at a fast rate, a framework needed to be established. This included:

- A sample exchange robot to handle samples during illumination and measurement
- An acquisition software solution
- A post treatment software solution

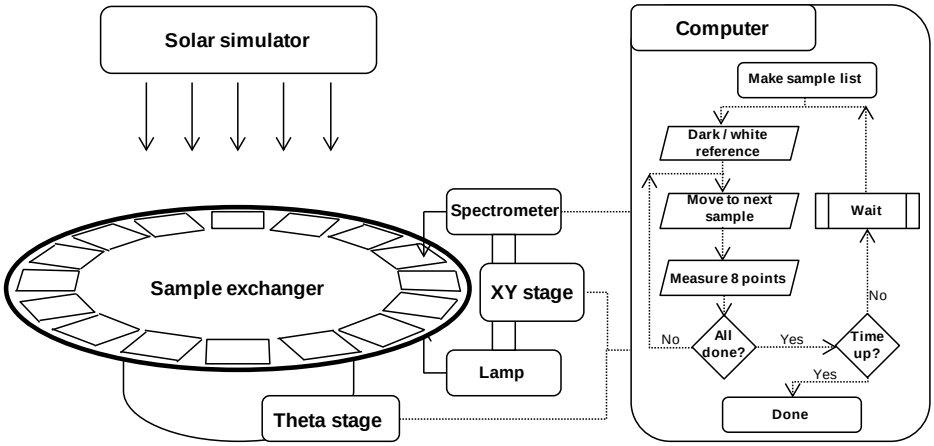

Figure 3.1 Schematic drawing of the workflow of the photo degradation setup.

The workflow of the system designed, is shown in Figure 3.1. The sample exchanger robot is responsible for moving samples to and from the spectrometer. A computer program is constantly running to make sure samples are measured according to the sample list. The entire software system including the post treatment software is designed from the ground up and written in the C# language and compiled using Microsoft Visual Studio.

Sample exchange robot

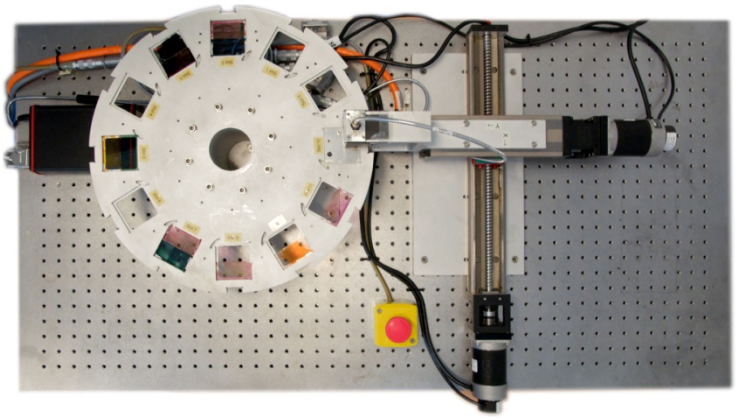

Figure 3.2. Top view of the sample exchanger robot assembly.

The sample exchanger robot had the purpose to automate the process of recording transmission spectra. The setup consists of a rotational stage mounted with a sample holder, and a two axis motorized arm mounted with a spectrometer setup, see Figure 3.2. The sample exchanger has a circular aluminum disc of outer diameter 36 cm mounted, into which 12 sample slots of 50.5 x 50.5 mm had been milled. Each of these sample slots could either house a 50 x 50 mm substrate or alternatively two 50 x 25 mm samples. Springs ensured that the samples when mounted would not

move inside the slots. The spectroscopy light source was fixed in the bottom part of a fork type arm and light was collected from the top part of the arm. The arm was mounted on the x-y stage allowing motion in the table plane. The rotation of the sample exchanger was performed by a rotational stage (HIWIN TMS32-A00) and the x-y axis was driven by two server motors (MCG 9500188/A). Both the server motors and the rotational stage were controlled via a Galil motor driver (Galil DMC-430) with a RS232 interface for computer control and programming. The setup features an emergency button mounted centrally for quick and easy access.

Spectrometer

The spectrometer setup used consisted of a broad-band light source illuminating the sample along with a spectrometer for detection of the transmitted light. Assuming negligible scattering in the system, the absorption at normal light incidence is expressed by

$$Abs = 1 - R - T \,,$$

where R is the intensity of the reflected light from the sample and T is the transmitted light intensity. The studies are typically conducted with polymers deposited on glass substrates. Using a clean glass substrate as a reference sample, the transmission of a single layer deposited on the substrate is expressed by

$$Abs = \frac{I_R - I_0}{I_D - I_0},$$

where I_R is the intensity of a reference substrate, I_D is the dark intensity and I_0 is the intensity for the polymer-glass sample. The absorption of a polymer film is typically given in units of absorbance A, which is defined by $A = \log(Abs)$. Absorbance is a unit-less quantity, which scales with the thickness of the polymer film according to Lamberts -Beer law.

The actual spectroscopic setup is based on a fiber based probe mounted on the fork arm of the sample exchanger robot. An optical fiber-based CCD spectrometer (Avantes AvaSpec 1024 with a 400 µm quartz fiber) and a halogen/deuterium light source (Avantes AvaLight-DHc) are used to record the absorption spectrum in transmission geometry in the range of 300 to 900 nm at set intervals. The light source optical fiber is mounted in the bottom part of the fork and at the top part light was collected into the spectrometer fiber. Collimating lenses (Avantes - COL-UV/VIS) ensured a parallel light beam

through the sample with a circular area of 3 mm. The spectrometer has a USB interface allowing computer control and the light source had a built-in shutter mechanism operated by a TTL signal. The data output from the spectrometer was used to control this shutter for dark intensity measurements via the computer software.

Light source

A Steuernagel SolarConstant solar simulator custom fitted with an Osram 1200 W Hydrargyrum medium-arc iodide (HMI) lamp providing an AM1.5G spectrum was used for all degradation experiments. The solar intensity was adjusted to 1 kW m^{-2} according to a ThorLabs thermopile (S314C). The light was not filtered and therefore a UV rich spectrum was obtained with a cut-off at 280 nm. Fans were employed to cool samples during the experiments and the temperature was kept at 30 °C. All degradations were performed in a lab with humidity and thermal control to ensure a constant degradation environment.

Sample layout

During degradation, the entire surface of each sample was degraded. Thus multiple areas of the samples could be monitored, by which more data was recorded for the same sample. Different numbers of points of degradation on the samples were used, referred to as degradation points. Different distributions and densities of degradation points could be used to either perform temporally dense measurements or to measure a larger number of degradation points to maximize statistics. The maximum number of degradation points was obtained with a grid pattern (7 x 4) in which 28 degradation points were distributed. An alternative layout focused on obtaining the most uniform thickness of degradation points were layered out in an arc around the spin coating center. This layout could thereby decrease the influence of the thickness inhomogeneity as seen for spin coated samples. It was in fact quickly realized that the grid pattern had the great advantage that a rather broad thickness range could be covered by a single sample and therefore this layout was commonly used when thickness plots were required.

Acquisition software

This section will detail the most important aspects of the software including considerations for the main file format, multi file format compatibility, interaction surface, instrument modules, and control modules. All the software was written in the C# programming language. Before the start of the project a main goal was that the software solution must be as modular as possible. This means that a number of choices on how the program was split into classes and solutions were taken at an early stage. A

solution represents a collection of classes included in a single namespace. Classes are constructs used to create instances of itself. Two main solutions were created for generic data handling and instrument handling. A large amount of work was put into designing and programming the software platform that was expandable and useable for a wide range of applications. Therefore everything was made as generic as possible. Beyond the main software programs discussed in this chapter programs to evaluate mass spectra from TOF-SIMS, from ellipsometry, and more was written based on the generic solutions. For the project a total of approximately 15,000 lines of code have been written and over 100 iterations of the software were given a version number during the development. The code lines were distributed as follows:

- 3,300 lines for data handling including file formats, plot functionality, data interaction functionality.
- 4,500 lines for instrument communication and data pre-treatment.
- 3,000 lines for the main acquisition software dubbed: “HektoSun”.
- 1,700 lines for the data treatment software dubbed “DegradationMonitor”.
- 2,500 lines for various smaller software implementations.

The main design criteria before beginning the task of programming included identifying a file format suitable for the column based data widely used for spectrometer data, mass spectra, IV-curves, etc. The file format chosen was the Full-Metadata format (fmf) as defined by Riede *et al.*[19] The format is based on four principles: readable self-documentation, flexible structure, fail-safe compatibility, and searchability. The basic idea of the format is that all metadata required to interpret the tabular data are stored in the file itself, allowing for the automated generation of publication-ready tables and graphs. A large effort was put into developing a representation of the fmf format as a C# class. This allowed instances of the data to be handled within the program. The data class contains methods to access data based on either indexes or data values, interpolate data points, find minimum / maximum points, calculate running averages, etc. The data class contains a metadata class element containing a representation of the metadata from the file. Via this the data class knows the names of the columns and the units of the data. An extensive input / output class was written to convert the data class into a file or to open a file into a data class instance. The input / output class ensures that a large list of file formats can be interpreted as data classes. This way the input / output class can directly convert files between different formats via the data class. The implemented file formats include various

ellipsometry formats, mass spectra formats, IV data formats, spectroscopy formats, etc. A generic importer was also implemented, allowing arbitrary column based data to be imported. Within the data handling set of classes a plot class and a class allowing interaction with the data in a grid based tabular format was implemented. The plot class allowed the data to be plotted and includes zoom functionality, plot layout controls, export functionalities, range selection tools, etc. The class enabling the data to be displayed as a data grid automatically ensures binding between multiple open data grids and plots, data search options, column sorting, and more. In summary the data handling class is responsible for all data in the program including the visualization and interaction with the data and is generically written to work with any column based data sets.

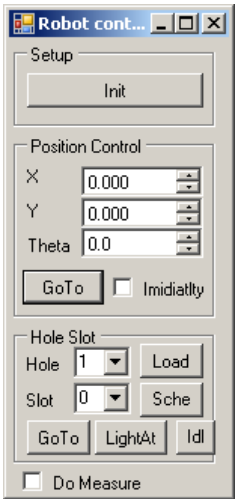

Figure 3.3. Robot controller class for the x-y-theta stage.

The second major solution was written for the instruments. Firstly all instruments were represented by their own class. For similar instruments it was prioritized that the instruments were switchable at runtime. For example three different “robots” were used; one was a two axis stage, one a rotational stage, and the last a rotational stage with a two axis stage. An example of a use for the robots was as sample exchangers. For the main software no distinction between the stages was needed as long as the program could uniquely identify the sample and move to the sample by an identifier. For this reason a layer of interfaces was implemented between the main program and the instrument classes. In programming an interface is a reference type object with no implementation, it allows for communication with classes inheriting from the interface. The use of interfaces allows easier maintainability and makes code reuse much more accessible because implementation is separated from the interface. In the case of the robots five interfaces were defined; a common interface, an

interface for an x-stage, an x-y-stage, a theta-stage, and an x-y-theta-stage. The common interface includes methods such as a home function, a reset function, and a move-to function implementing a sample identifier. The remaining interfaces include the move to functions for their respective modes. Using inheritance the instrument classes inherits from the respective interfaces. In this way the communication is handled via the interfaces and the code becomes independent on the choice of the specific robot. A screenshot of the robot controller form for the x-y-theta stage is shown in Figure 3.3. Each instrument class has its own form, primarily used for debugging. The program form for the spectrometer is shown in Figure 3.4. This class contains controls for controlling the lamp shutter of the light source. When dark measurements are carried out the shutter is automatically applied. It is possible to record transmission, absorbance, and irradiance measurements in the form directly. The data recorded is stored as a data class instance and can be saved to the disk by using the export option.

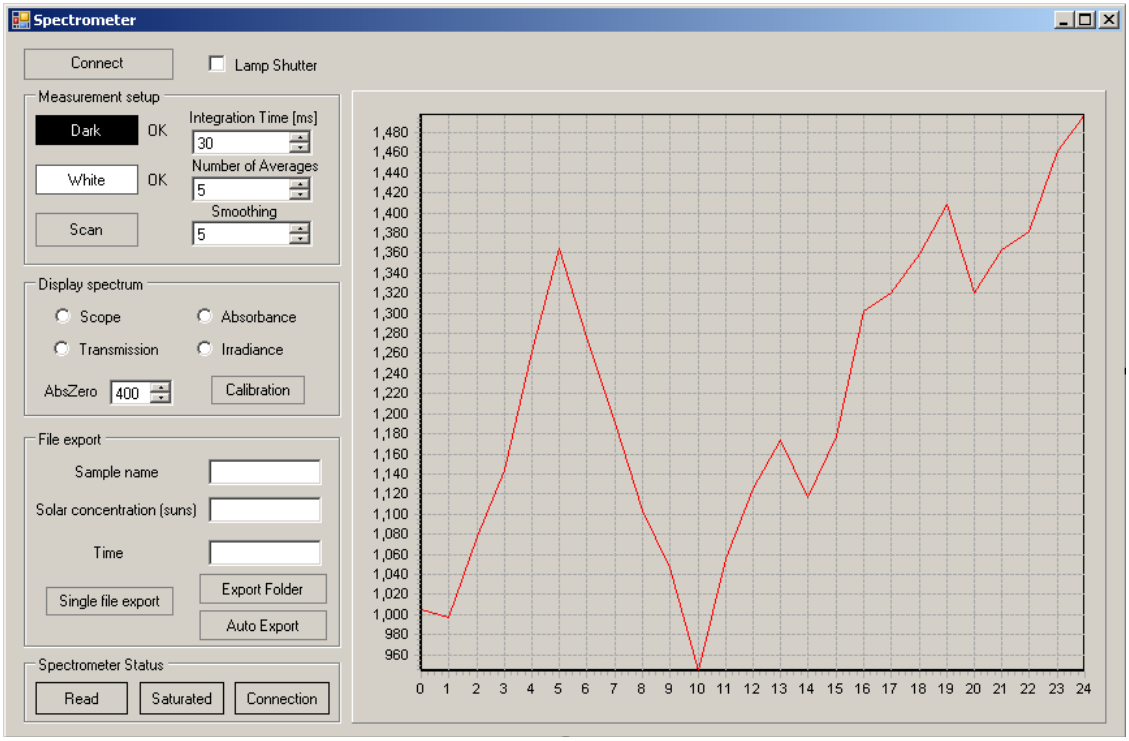

Figure 3.4. Spectrometer class. The program form contains functionality for recording and storing single measurements.

The program used for the data acquisition was dubbed “HektoSun” and a screenshot can be seen in Figure 3.5. The program can generally access all instrument interfaces which can be activated in the right side. After activation the forms for each instrument can be accessed for debugging and test

purposes. Through the tabs in the top of the program the different functionalities can be accessed. “UVvis” is the most important tab, since it is used for all photo-degradation using transmission measurements. The “Cell Test” and the “Conc Cell Test” tabs are used for solar cell measurements using a Keithley source meter (compatiple with either a Keithley 2400 or 2401). With the “Cell Test” tab cells can be tested using a multiplexer and up to 36 cells can be monitored in parallel. The mapping tab holds functionality for mapping either the transmission from the spectrometer or the readout of a photodiode to map light distribution. The LightGradient tab holds some advanced functions, “R&D” and “Setup” is mainly used for debugging. The status panel in the bottom left corner tracks the progress of the currently running function. Via the Tools menu the post treatment software can be accessed along with various smaller programs including a file conversion tool.

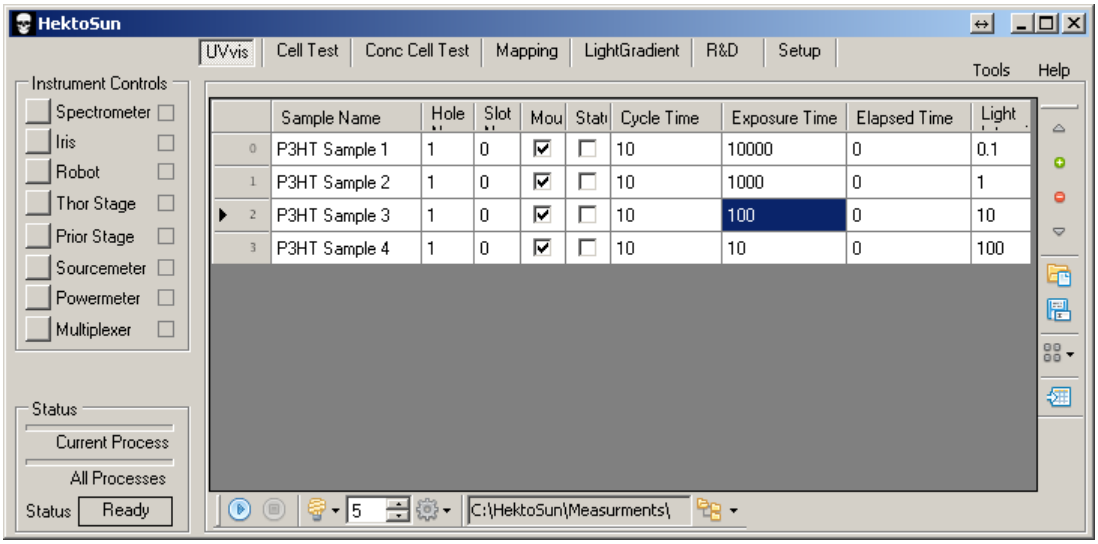

Figure 3.5. Main window of the acquisition software dubbed “HektoSun”.

The basic operation of the “UVvis” tab is based on the sample list. This data grid is used directly from the data handling solution as described earlier. Within this list, all the relevant data for the sample can be typed in. This includes the sample name, the hole, and slot number identifying the placement of the sample. The first checkbox tells if the sample is mounted or not and the second checkbox becomes checked when the measurement is done. The cycle time indicates the time span between measurements; the exposure is time the total time before the measurement is terminated, and the elapsed time is the time expired. Lastly the light intensity can be given in number of suns. With a solar simulator the light intensity must be equal for all samples and set accordingly to the intensity of the light source. The right toolbox allows sample priority to be changed, samples to be deleted or added, preset sample lists to be loaded, and the list to be saved or existing lists to be opened. Keyboard

shortcuts for all these functionalities are also implemented. The bottom toolbox controls the experiment with a play button starting the experiment, a pause button, and a stop button. The light source and the specific robot can be selected as well. Lastly the export folder can be defined.

Post treatment software

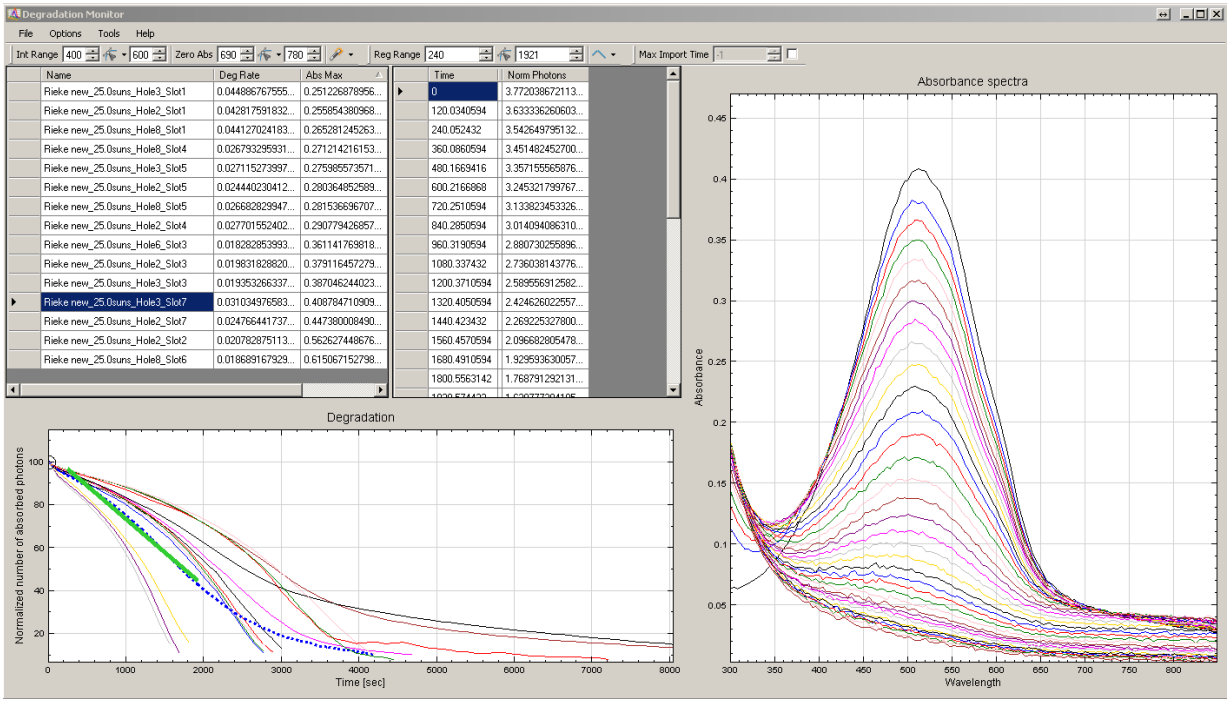

Figure 3.6. Screenshot of the program dubbed "DegradationMonitor".

The software responsible for the post data treatment was dubbed "Degradation Monitor", see Figure 3.6. The absorbance files generated during the measurement can either be opened from the menu or dropped directly into the left data grid. The left data grid represents the samples; the right grid is a list of the absorbance measurements for the selected sample. The right plot shows the selected absorption spectrum and the left plot shows a generated degradation profile based on the calculation method selected. The data is handled directly within the data handling solution, so the data grids are generated directly and bound together, so that when a data set is selected in the right grid the left grid is updated automatically. The plots are also bound so they update according to the selections made in the data grids. In the top toolbar integration ranges can be set, along with various other parameters. All the parameters can be set individually for each sample or be applied for all samples. The software is capable of handling a couple of gigabyte of data depending on the amount of ram in the computer. If the number of data files is too large various data compression tools are available. The spectra can be

imported with lower resolution, a speed mode selecting a representative set of data can be used, and data can be imported until a given maximum degradation time. Another important aspect of the post treatment software is the implemented filters. The software employs a modified median filter to remove odd measurements from the data sets. The software is generally well functioning and has been used exclusively for the treatment of degradation data during this PhD.

Validation

With the photo-degradation environment completed a validation phase was needed. During this validation phase a long list of small improvements was made and a number of hardware and software bugs were identified and corrected. The process became ever more important as the setup was required to run unattended for longer and longer periods. At the last part of the PhD the setup was running almost without interruption with samples being exchanged at runtime. This meant that the software had to be stable enough to be run indefinitely without encountering errors. Examples of errors included variables overflowing, unknown hardware exceptions, etc. With time the software began to run smoothly as corrections were made and counter measures implemented. One example of a problem encountered was that roughly 1 in 100 recorded spectra was extremely noise filled. This happened at the hardware level were the measurement was done at a too low integration time despite the preset setting. To encounter this problem a check of all recorded spectra was implemented, and if the noise threshold was superseded the measurement was repeated automatically.

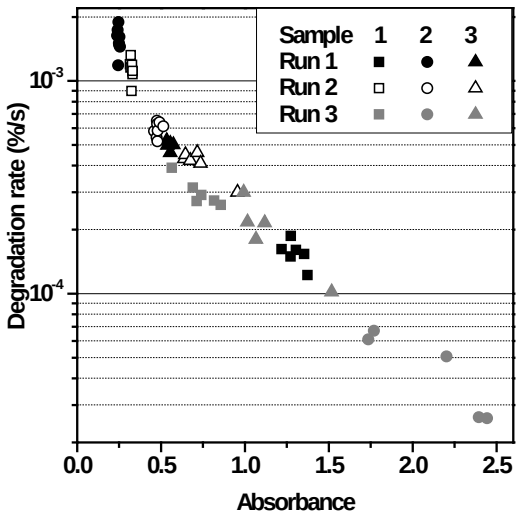

Figure 3.7. Validation test of the degradation setup where three degradation tests were performed where three P3HT samples where degraded.

To validate the entire system a small test was established; three different degradation experiments were performed on three different days, see Figure 3.7 Each experiment comprised three samples of P3HT of different thicknesses with eight degradation points on each sample, and all degradation points were plotted together. No grouping between the samples or between the degradation experiments was observed and the precision of the evaluated degradation rates was considered high.

3.3. Results

With the photo-degradation environment working, a lot of data was produced. The first scientific contribution was reported in the article entitled: "Photochemical stability of conjugated polymers, electron acceptors and blends for polymer solar cells resolved in terms of film thickness and absorbance" (Appendix 2.2)[9] When making comparative studies of polymer stabilities, many different parameters influence the experimental conditions. Some may be outside the control of the experimenter. Parameters such as the temperature, light spectrum, and light intensity are typically kept constant. The focus of the article was to expand the knowledge of the parameter room comprising the simple system of a thin polymer film on a substrate. The main question before the work of this article regarded the influence of thickness on stability. Further since it is common to use the initial absorption to compare polymer stability[1], it is important to known if this indeed yields a fair comparison between stabilities or if the thickness directly is a better basis of comparison. The effect of varying optical density / thickness on material stability was not studied systematically before the article and therefore the uncertainty introduced by thickness variation was unknown. By comparing stabilities without knowing the influence of the thickness of the film, wrong conclusions can be drawn in the worst case.

In the article photochemical stabilities of six different polymers were studied, see Figure 3.8. Clear initial absorbance / thickness dependence was visible for all polymers. By plotting the relative stabilities of the polymers to the stability of regio-regular P3HT, revealed that reasonably flat lines were obtained when plotted against the initial absorbance, see Figure 3.9 (left). This indicated that the absorbance provides a relatively fair basis for comparison. However, as is evident from the figure, intersections between different polymers are present. Hereby comparing polymers at low initial absorption can yield the opposite conclusion when comparing polymers at high initial absorbance. This is extremely important to comparative studies, where the absorbance has to be kept constant for all materials to provide a basis for valid conclusions on relative stabilities. Still the validity of estimating a

material stability based on a single measurement at a single absorbance is considered doubtful. Only by studying a wide thickness range for all studied samples, a sound estimation of relative stabilities can be obtained. Consequently it was concluded that relative stabilities cannot be given in factors less than five if only a single degradation of each material has been performed.

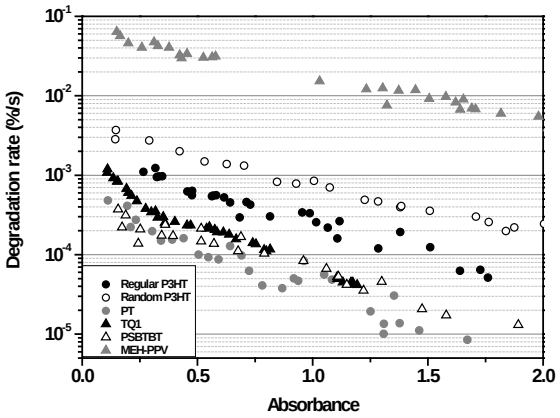

Figure 3.8. Absorbance resolved degradation rates for six different polymers. Reprinted with permission from the Royal Society of Chemistry.[9]

While the relative stability estimation was not perfect in the initial absorbance basis, thickness as a basis can also be considered. It is far more cumbersome to use thickness as the basis of comparison as the thickness must be measured externally. Using AFM; thickness / initial absorbance relations were established for all the polymers and blends. The linear relation used was confirmed with simulations based on ellipsometry measurements as described in Chapter 2. This allowed the degradation rates to be plotted in terms of thickness. This plot is different from the absorbance based plot since the materials have vastly different extinction coefficients. The relative stabilities with P3HT as a basis, is plotted in Figure 3.9 (right) with thickness as a basis. It is clearly evident that this basis is inferior to the absorbance basis. It was therefore concluded that using initial absorbance as the basis of comparison was the best choice.

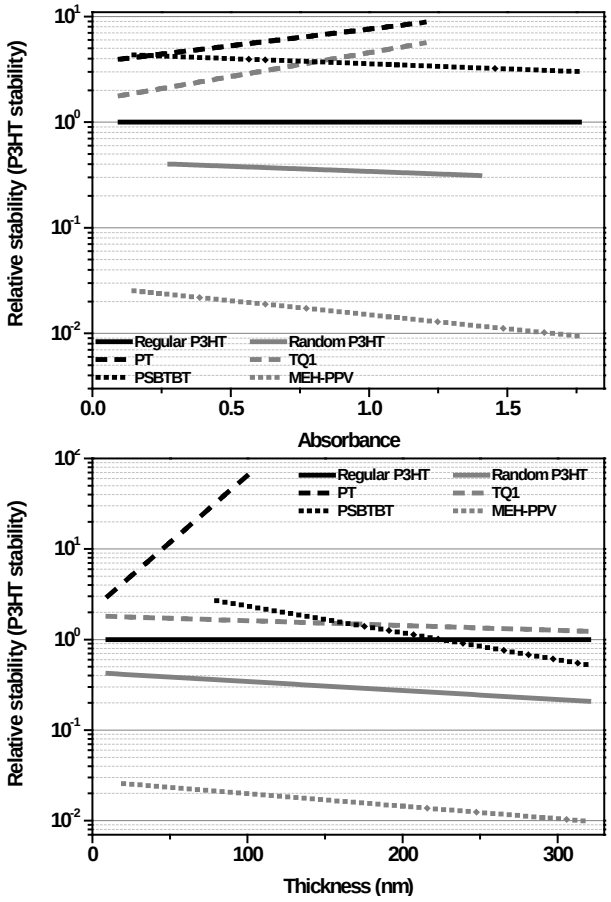

Figure 3.9. Absorbance resolved stabilities (right) and thickness resolved stabilities (left) in units of P3HT stability for the studied polymers. Reprinted with permission from the Royal Society of Chemistry.[9]

The effect of adding a fullerene derivative to the polymers was studied extensively within the article. For each of the studied polymers, their respective blends in a ratio of 1:1 with PCBM were studied and the blends of P3HT with 5 different electron acceptors were documented. It was shown that the absorbance basis remained the better choice as compared to the thickness basis (see Figure s9-s11 in Appendix 2.2 (supporting materials))[9].

The photochemical stability of blends of conjugated polymers and electron acceptors is a topic that has only been briefly discussed in the literature. Rivaton et al. evaluated the stabilities of regio-regular P3HT and P3HT:PC60BM (1:1 ratio) and reported a stabilization factor of 8. They used a thickness basis, where films of approximately 200 nm were compared.[7] The observed degradation rates were in good correlation with the results observed at Risø DTU for the similar blend. The degradation rates were observed to vary with an order of magnitude between the most unstable blend, P3HT:ICBA, and the most stable blend, P3HT:C_{60}. Significant variations in relative stabilities were observed for the different

electron acceptors with C_{60} stabilizing by a factor of approximately 10 while ICBA was observed to destabilize the blend by a factor of 2. The magnitude of the stabilization of P3HT by the electron acceptor was observed to correlate well with the LUMO–LUMO gap in the low absorbance range. A ranking of decreasing stabilization of C_{60}, $PC_{60}BM$, $PC_{70}BM$, bisPCBM, and ICBA was found, which is in clear correspondence with a decreasing LUMO–LUMO gap or increasing open circuit voltage of the corresponding solar cells. Overall, this result demonstrated the increasing thermodynamic tendency of increasing the population of excited states on the P3HT relative to the acceptor, thus implying a higher degradation rate. For this reason, the application of ICBA in polymer solar cells to obtain 6.5% efficiency[20] introduces a significant decrease in photochemical stability that will affect the operational device lifetime negatively.

Studying the different polymers blended with PCBM the general expectation was that a highly unstable material should benefit highly from being blended with $PC_{60}BM$, since each excitation has a large possibility of leading to a degradation event. For a highly stable material this effect would be less pronounced. This exact tendency was observed as the unstable MEH-PPV was highly stabilized by a factor of around 15, while the stable PT was only stabilized by a factor 3. Additionally, PSBTBT was found to destabilize slightly by a factor of 0.3. A destabilization is expected if the polymer is comparable to or more photo-chemically stable than the electron acceptor. This was the case for PSBTBT, where for an absorbance above 1, the polymer stability even exceeds the stability of $PC_{60}BM$. For this material combination a charge transfer to $PC_{60}BM$ will induce a larger degradation rate than by keeping the excited electron on the pure polymer.

The second scientific contribution using the photo-degradation framework came with the article entitled: “Influence of processing and intrinsic polymer parameters on photochemical stability of polythiophene thin films” (Appendix 2.3)[10]. This article expanded upon the work of the previous article by investigating the influence of processing and intrinsic parameters on the photo-degradation of P3HT. As was done in the previous article, it is generally common to express stability in units of stability of a reference material of well-known stability, typically P3HT. This assumes that P3HT presents an intrinsic, constant stability that is independent of synthesis routes, regio-regularity (RR), molecular weight, molecular weight distribution, crystallinity etc if the relative stabilities are compared across different experiments. The overall effect is that the material stabilities expressed in units of P3HT stability as reported in the literature may be associated with significant uncertainty and cannot

be compared directly. Furthermore, until this article, development of stable conjugated polymers for polymer solar cells has been focused on the stability of the different functional groups used for the synthesis. However, understanding the influence of the above described intrinsic polymer properties on the photo-chemical stability is highly appealing, since it will provide a new set of tools when designing novel materials for polymer solar cells. In the article 18 different batches of P3HT from different manufacturers and batches made in house were tested and compared. By studying films of different thicknesses insight into oxygen availability in the film and effects of light shielding could be discussed. Assuming that oxygen diffusion is not limited and that light shielding from the top layer of the film is insignificant, the concentration of oxidized thiophene rings is independent of film thickness. Figure 3.10 shows a plot of degradation event interval against film thickness and a plot of total film lifetime. The existence of a constant lifetime region implied that the degradation took place in parallel for the entire depth of the film. This means that for this region light shielding is negligible and oxygen is equally available for all depths in accordance with the findings of Hintz *et al*.[3] For films thicker than 175 nm, either light shielding or lack of oxygen sets the bottom part of the film apart from rest of the film with a lower degradation rate. The event interval was therefore observed to stabilize in this region. The conclusion was consistent with observations of the blueshift kinetics. For films in the stable region of 125–175 nm, the blueshift of the absorbance occurred late near the last 20% of the degradation. For films thicker than 175 nm the blueshift appeared earlier. This was consistent with the fact that parts of the film degraded later than the top part of the film, thereby extending the degradation. The fast blueshift for thin films (<75 nm) indicates that another mechanism was involved in this region. A candidate for the increase in reaction rate is the higher surface to volume ratio. If the reactions are more likely on the surface the rate may easily be different. The polymers in the top layer can be expected to have a higher density of kinks, introducing more attack points for the reaction and explaining the fast blueshift observed for thin films.

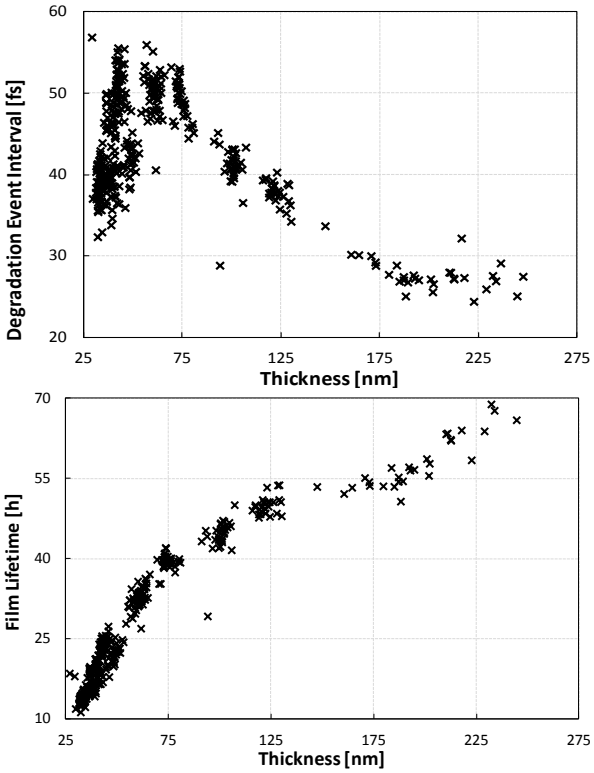

Figure 3.10. Degradation event interval (left) plotted against the thickness of a film of R1 polymer. The film lifetime (right) as calculated from the time between degradation events and the initial number of monomers. Reprinted with permission from Elsevier.[10]

P3HT polymers with significantly different molecular weight and regio-regularity were included in the study. The first observation was that while the molecular weight did not seem to play an important role. The regio-regularity did. This is consistent with work presented by Hintz *et al.*[3] and Dupuis *et al.*[21] A hypothesis was established that in accordance with observations by Hintz *et al.*[3]the polymer is attacked only at terminal thiophene units. Assuming that each breach of regularity introduces two new attack points, it was possible to model the degradation rate as a function of regio-regularity. The relative number of attack points was written as

$$N_{ap} = \frac{2\left(1 - RR_x\right)}{2\left(1 - RR_{R1}\right)},$$

where N_{ap} is the number of attack points relative to R1, RR_X is the regio-regularity of the specific polymer, and $RR_{R1}$is the regio-regularity of polymer R1 used for normalization. Figure 3.11 shows a plot of the normalized degradation rate as a function of regio-regularity and relative number of attack points. The dotted line in the graph represents the theoretical value of degradation rate, calculated

from the degradation rate of R1. It is evident that the simple model is capable of explaining the behavior in a convincing manner, suggesting that each breach of regularity induces new attack points that weaken the system. The conjugation length is proportional to the regio-regularity since the conjugation breaks when the polymer is not planar and the π electrons are not in the same plane.

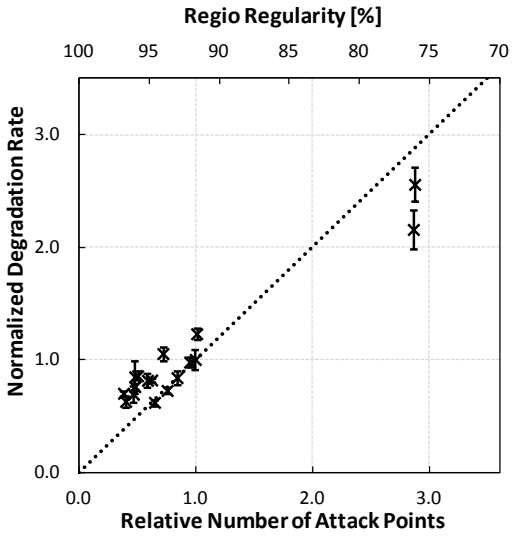

Figure 3.11. Normalized degradation rate plotted against the calculated relative conjugation length / regio-regularity. The dotted line represents the predicted degradation rate. Reprinted with permission from Elsevier.[10]

In the article it was demonstrated that annealing the films of P3HT increased the stability, see Figure 3.12. While it was documented that the crystallinity of the films increased for regio-regular films, it was also shown that regio-random films increased in stability. It was therefore concluded that the crystallinity plays a minor role in the stability. The effect of the stabilization was instead ascribed to the relaxation of the polymer leading to fewer high energy kinks.

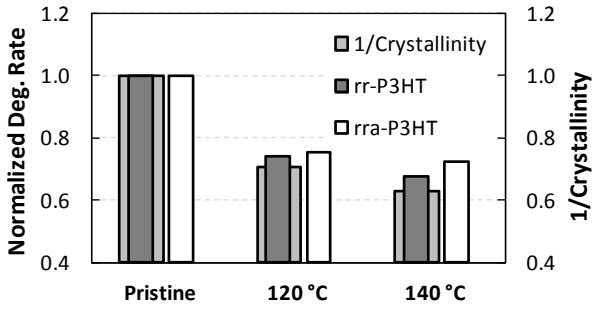

Figure 3.12. (Left scale) Degradation rate of (dark grey) regio-regular and (white) regio-random P3HT normalized to their respective pristine degradation rates. (Right scale) Reciprocal crystallinity as deduced from X-ray diffraction studies. Reprinted with permission from Elsevier.[10]

3.4. Conclusions

The automated degradation setup was in general a great success. As an example the total workload for degradation of 22 samples with a total of 176 degradation points can be estimated to: spin coating (22 minutes), sample loading and sample registration in the software (10 minutes), and evaluation of absorbance resolved degradation rates (3 minutes). Thus a total of around 40 minutes workload for a degradation experiment results in a workload per degradation point of around 14 seconds or roughly 2 minutes per sample. This can be contrasted to a manual setup where samples are degraded under a solar simulator and frequently brought to a spectrometer for absorbance measurements. A skilled operator can degrade 20 samples in parallel, and thus the work load would imply: spin coating (20 min), 10 absorbance measurements for acceptable statistics of all samples (10 x 40 minutes) and a final degradation rate evaluation based on manual, serial data processing in *e.g.* a spread sheet (20 minutes). A total of 440 minutes would be required for 20 parallel degradations and thus on the average each degradation point would demand 22 minutes of work. This gain in operator efficiency has allowed a series of experiments to be conducted with high statistical validity. In excess of 5,000 glass slides were used for degradation experiments during this PhD project. Additionally, the precision of the automated setup outperforms any manual handling since measurements are performed with higher frequency, non interrupted illumination, and with a fixed geometry during the entire degradation as opposed to the manual handling where samples are removed from the degradation setup and transported to and from the spectrometer. Finally, in terms of the reliability of the automated setup the timing of the data point acquisition is computer controlled (data is stored with millisecond accuracy), while manual handling involves an attentive operator keeping track of time, introducing a multitude of risks to the data acquisition.

With the automated degradation system photo-chemical degradation at 1 sun was performed both for a range of conjugated polymers and electron acceptors. These results allowed a wide range of thicknesses to be investigated leading to recommendations about the experimental procedure for photodegradation based on absorbance loss. Firstly it was recommended that samples are compared based on initial absorbance value rather than their thickness. The stability ranking between the materials of the pure polymers was found to be similar to the ranking for their respective blends, implying that the photochemical stability of a pure polymer is a good measure of its associated blend stability. Different electron acceptors were found to stabilize P3HT decreasingly with decreasing donor-acceptor LUMO-LUMO gap. Destabilization of P3HT was observed in the case of the electron

acceptor ICBA. Thereby, the decreased stabilization of P3HT by high LUMO electron acceptors poses a challenge if these materials are to be of commercial interest. By studying the influence of processing and intrinsic polymer parameters on photochemical stability it was shown to be evident that the polymer degradation follows strict 0^{th} order degradation kinetics for the initial part of degradation. Stability was found to increase with regio-regularity following the ratio of head-to-tail connected thiophene units, demonstrating that the polymer is attacked at points of broken conjugation. Annealing was shown to relax the films and increase conjugation length and in turn, increases stability and delay spectral blueshift. For films of different thickness, the interval between degradation events was observed to scale linearly with the initial number of thiophene rings for medium thick films (75–175 nm) indicating that oxygen diffusion and light shielding effects had negligible or no effect for medium thick films.

The results demonstrated that photochemical degradation of conjugated polymers is a powerful tool to polymer stability assessment if the results are interpreted correctly. The use of an automated system is necessary in order to conduct hundreds or thousands of degradation experiments which will provide sufficient data for solid conclusions.

3.5. References

(1) Manceau, M.; Bundgaard, E.; Carlé, J. E.; Hagemann, O.; Helgesen, M.; Roar, S.; Jørgensen, M.; Krebs, F. C. Photochemical stability of π-conjugated polymers for polymer solar cells a rule of thumb. *Journal of Materials Chemistry* **2011**, *21*, 4132-4141.

(2) Hintz, H.; Egelhaaf, H.-J.; Peisert, H.; Chassé, T. Photo-oxidation and ozonization of poly(3-hexylthiophene) thin films as studied by UV/VIS and photoelectron spectroscopy. *Polymer Degradation and Stability* **2010**, *95*, 818-825.

(3) Hintz, H.; Egelhaaf, H.-J.; Lüer, L.; Hauch, J.; Peisert, H.; Chassé, T. Photodegradation of P3HT–A Systematic Study of Environmental Factors. *Chemistry of Materials* **2010**, *23*, 145-154.

(4) Manceau, M.; Helgesen, M.; Krebs, F. C. Thermo-cleavable polymers: Materials with enhanced photochemical stability. *Polymer Degradation and Stability* **2010**, *95*, 2666-2669.

(5) Rivaton, A.; Chambon, S.; Manceau, M.; Gardette, J.-L.; Firon, M.; Lemaitre, N.; Guillerez, S.; Cros, S. Impact of light on organic solar cells: evolution of the chemical structure, morphology, and photophysical properties of the active layer. *Proceedings of SPIE* **2008**, *7002*, 70020I-70020I-12.

(6) Manceau, M.; Chambon, S.; Rivaton, A.; Gardette, J.-L.; Guillerez, S.; Lemaître, N. Effects of long-term UV–visible light irradiation in the absence of oxygen on P3HT and P3HT:PCBM blend. *Solar Energy Materials and Solar Cells* **2010**, *94*, 1572-1577.

(7) Rivaton, A.; Chambon, S.; Manceau, M.; Gardette, J.-L.; Lemaître, N.; Guillerez, S. Light-induced degradation of the active layer of polymer-based solar cells. *Polymer Degradation and Stability* **2010**, *95*, 278-284.

(8) Manceau, M.; Rivaton, A.; Gardette, J.-L. Involvement of Singlet Oxygen in the Solid-State Photochemistry of P3HT. *Macromolecular Rapid Communications* **2008**, *29*, 1823-1827.

(9) Tromholt, T.; Madsen, M. V.; Carlé, J. E.; Helgesen, M.; Krebs, F. C. Photochemical stability of conjugated polymers, electron acceptors and blends for polymer solar cells resolved in terms of film thickness and absorbance. *Journal of Materials Chemistry* **2012**, *22*, 7592-7601.

(10) Madsen, M. V.; Tromholt, T.; Böttiger, A.; Andreasen, J. W.; Norrman, K.; Krebs, F. C. Influence of processing and intrinsic polymer parameters on photochemical stability of polythiophene thin films. *Polymer Degradation and Stability* **2012**.

(11) Carlé, J. E.; Andreassen, B.; Tromholt, T.; Madsen, M. V.; Jørgensen, M.; Krebs, F. C. Comparative Studies of Photo Chemical Cross-linking Methods for Stabilizing the Bulk Hetero-Junction Morphology in Polymer Solar Cells. *Submitted to Journal of Materials Chemistry* **2012**.

(12) Madsen, M. V.; Tromholt, T.; Norrman, K.; Krebs, F. C. Concentrated light for accelerated photo degradation of polymer materials. *Submitted to Advanced Energy Materials* **2012**.

(13) Holdcroft, S. A photochemical study of poly(3-hexylthiophene). *Macromolecules* **1991**, *24*, 4834-4838.

(14) Goutam, P. J.; Singh, D. K.; Giri, P. K.; Iyer, P. K. Enhancing the photostability of poly(3-hexylthiophene) by preparing composites with multiwalled carbon nanotubes. *Journal of Physical Chemistry B* **2011**, *115*, 919-24.

(15) Hintz, H.; Egelhaaf, H.-J.; Lüer, L.; Hauch, J.; Peisert, H.; Chassé, T. Photodegradation of P3HT−A Systematic Study of Environmental Factors. *Chemistry of Materials* **2010**, *23*, 145-154.

(16) Manceau, M.; Bundgaard, E.; Carlé, J. E.; Hagemann, O.; Helgesen, M.; Søndergaard, R. Photochemical stability of π-conjugated polymers for polymer solar cells: a rule of thumb. *J. Mater. Chem.* **2011**, *21*, 4132-4141.

(17) Koch, M.; Nicolaescu, R.; Kamat, P. V. Photodegradation of Polythiophene-Based Polymers : Excited State Properties and Radical. *Journal of Physical Chemistry C* **2009**, *113*, 11507-11513.

(18) Manceau, M.; Rivaton, A.; Gardette, J.-L.; Guillerez, S.; Lemaître, N. The mechanism of photo- and thermooxidation of poly(3-hexylthiophene) (P3HT) reconsidered. *Polymer Degradation and Stability* **2009**, *94*, 898-907.

(19) Riede, M.; Schueppel, R.; Sylvester-Hvid, K. O.; Kühne, M.; Röttger, M. C.; Zimmermann, K.; Liehr, A. W. On the communication of scientific data: The Full-Metadata Format. *Computer Physics Communications* **2010**, *181*, 651-662.

(20) Zhao, G.; He, Y.; Li, Y. 6.5% Efficiency of polymer solar cells based on poly(3-hexylthiophene) and indene-C(60) bisadduct by device optimization. *Advanced materials* **2010**, *22*, 4355-4358.

(21) Dupuis, A.; Wong-Wah-Chung, P.; Rivaton, A.; Gardette, J.-L. Influence of the microstructure on the photooxidative degradation of poly(3-hexylthiophene). *Polymer Degradation and Stability* **2012**, *97*, 366-374.

Chapter 4

Concentrated light for photo-degradation

Advancements in research has pushed the stability of polymer solar cells. Outdoor tests of polymer solar cells with lifetime exceeding one year have been demonstrated.[1,2] Assuming an average of 1,000 h of nominal sunlight exposure per year about 500 kWh m^{-2} of absorbed light is expected for a solar cell (if only 50 % is absorbed by the cells). This means that running such a solar cell under an AM1.5 solar simulator continually, reduces the test time to 1,000 hours (42 days and nights) to be equivalent with the influx of light from one year. Materials such as polythiophene (PT) have been shown to have degradation rates of 0.029% / h under ambient 1 sun conditions.[3] With this level of stability, fast material screening under accelerated conditions is an appealing prospect. Acceleration methods utilizing atmosphere and temperature control have been demonstrated to increase degradation rates by a factor of 20.[4] Temperature has typically been used to accelerate the degradation of polymer solar cells. Concentrated light, on the other hand, has not generally been applied within the field of polymer solar cells. During this PhD a large amount of work has gone into optimizing and perfecting the use of concentrated light for degradation experiments. Two setups have been constructed to enable extremely high concentrations to be reached and used comfortably for degradation studies. One setup is based on an artificial light source and is advantageous since it can be run nonstop without breaks. The other setup is based on concentration of real sunlight as opposed to simulated sunlight. This setup can achieve very high concentration (~2000 suns), but is limited to times of clear skies. The article entitled “Thermally reactive Thiazolo[5,4-d]thiazole based copolymers for high photochemical stability in polymer solar cells” describes the use of the artificial concentrated light source to compare the photo stability of novel polymers and the article: “Concentrated light for accelerated photo degradation of polymer materials” (Appendix 2.5)[5] is a verification of the technique and establishes the acceleration factor for concentrated sunlight. No publication has yet been made using the solar concentrator.

4.1. Acceleration methodologies

Doing accelerated testing of polymer solar cells have become an almost near common practice. A general review of the concept of accelerated testing of organic solar cells has been written by Haillant describing concepts such as; increased irradiation, increased temperature, increased humidity and time compression.[6] The main acceleration parameter used for accelerated studies is temperature, however many other parameters affect the lifetime of the solar cell. Therefore a wide variety of accelerated test conditions can be imagined. Time compression is one in which the solar cell is tested by rapidly cycling test parameters. Herby daily cycles of environmental parameters are compressed to within a few hours. Compressed cycles generate mechanical stress of thermal origin due to the fast change in temperature.

Using temperature as an acceleration parameter is attractive since the temperature is easily controlled and easily reported. The rationale behind using the temperature as an acceleration parameter is that the decay process, which may be chemical in nature follows an Arrhenius-type model. Assuming this model the temperature dependence of the reaction can be described by an exponential function

$$k_{\text{deg}} = Ae^{\frac{E_A}{RT'}},$$

where R is the gas constant, E_A is the activation energy, and A is the reaction dependent pre-factor. Alternatively the rate constant can be expressed in terms of the Boltzmann constant. Hereby the energy will be expressed directly instead of energy per mol as $k_B = R/N_A$. From the exponential behavior the reaction rate is clearly extremely temperature dependent. An acceleration factor can be defined as the ratio of two reaction rates at different temperature

$$K = Ae^{\frac{E_A}{RT'}} \Big/ Ae^{\frac{E_A}{RT}} = e^{\frac{E_A}{R}\left(\frac{1}{T}-\frac{1}{T'}\right)}.$$

The prefactor is the same for both equations and is therefore eliminated in the equation. Accelerated testing was applied to MDMO-PPV/PCBM solar cells by Schuller *et al.* determining the acceleration factor in the temperature range of 40–105 °C[4]. They observed a roughly linear behavior of log(K) versus 1/T with a more than ten-fold increase in the rate of degradation from 40 to 105 °C. They concluded that the activation energy was in the range of 300–350 meV. Using temperature as an acceleration factor seems simple with the Arrhenius formula and the model has been used to predict

lifetimes of solar cells.[7] The main problem with the model is that it assumes that only the activation energy of one decay mechanism is needed to describe the entire system. As demonstrated by Gevorgyan *et al.* the acceleration factor may change during the lifetime of the device.[8] In addition temperature independent processes can take place, further invalidating the model. UV light at 400 nm has an energy of 3 eV, which is a high energy compared even with the thermal energy at room temperature. Heating the sample by an additional 50–60 °C does not necessarily affect processes much. Degradation limited by diffusion depends directly on the diffusion coefficient of the chemical species responsible for the decay. In this case temperature can play an important role since this diffusion coefficient is temperature dependent according to an Arrhenius-type exponential equation. So in theory, at low temperature, the UV degradation processes may dominate, while the diffusion process could take over at higher temperatures. If this is the case, accelerated testing would give false temperature dependence for the stability. If increasing the temperature causes thermo-oxidative processes to become the main degradation pathway and altering the chemical evolution observed without acceleration, the test is invalid. Therefore it is important to understand the degradation mechanisms involved when designing acceleration conditions.

As an alternative to the above described acceleration methodologies the use of concentrated light is perhaps the conceptually simplest type of accelerated studies. Sunlight concentration setups within the field of inorganic photovoltaics, has been developed for high performance solar cells with increased power output as the main goal.[9] The goal is to effectively increase the active area of high price multijunction solar cells by relatively cheap concentrator systems. Within the field of polymer solar cells concentrated light has been scarcely used to study degradation. It is, however clear that with the multitude of degradation mechanisms that are accelerated by concentrated light, the polymer solar cell response is complex, and even effects such as reversible degradation have been observed.[10] Conventional stability assessments of organic solar cells are performed by studying the decrease of power conversion efficiency during the degradation time. However, a multitude of parameters including the polymer, the electron and hole transport layers, the electrodes, and the interfaces influence the device performance. As a result the interplay between many different parameters is probed making single parameters such as the stability of the polymer itself rather inconclusive. To focus on the actual stability of the polymer, degradations under 1 sun illumination of the polymer have demonstrated the intrinsic stability of polymers directly as described in the previous chapter.[3,11] The exact same approach have been use to expose pure polymers to concentrated light. Tromholt *et al.*

performed such accelerated degradations of conjugated polymer up to 200 suns.[12] For both MEH-PPV and P3HT the acceleration factors were found to increase linearly with solar intensity and at 200 suns a complete degradation of MEH-PPV took place within 80 seconds. This study demonstrated that degradation of polymers can be highly accelerated by concentrated light, and that the approach has the potential to serve as a standard tool for rapid polymer stability evaluation. As the field of concentrated light is still new, a rigorous analysis of degradation rates observed at 1 sun and concentrated light has been needed.

4.2. Indoor artificial concentrator

An indoor artificial light concentrator can potentially have many advantages. In a country like Denmark where the number of sunshine hours can be few and far between using artificial lighting greatly increases the usability of a setup as compared to a solar concentrating setup. Prior to the construction of the indoor concentrator a number of design criteria were established. Firstly the system needed to have a constant spectrum with a spectral distribution approximately like AM1.5. Light intensity regulation between 0.1 to 100 suns over a 1 cm^2 illuminated area was a design goal. The system must feature a built-in shutter mechanism and be completely computer operated.

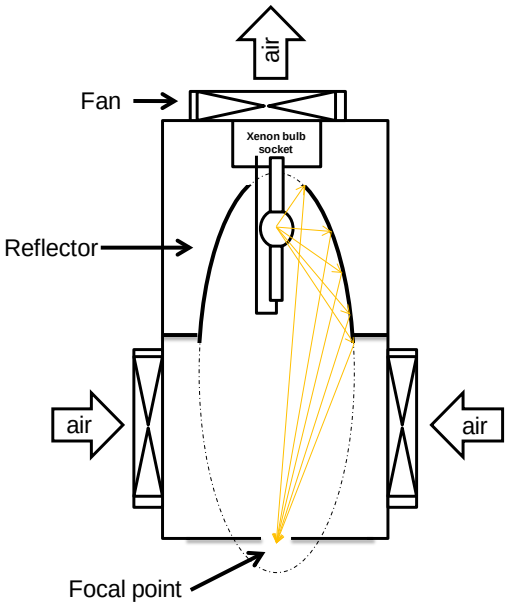

Figure 4.1. Schematic of the artificial light concentrating setup.

To meet the design criteria; the design of the concentrator was based on an elliptical reflector to refocus the light from a light bulb into the second focal point of the ellipse, as shown in Figure 4.2. This

way high light intensity could be achieved at the exit of the system. By selecting a 1200 W hydrargyrum medium-arc iodide (HMI) light bulb, the spectrum of the concentrator was set (the bulb is identical to the one used in the solar simulator, as described in Chapter 3). This type of lamp is commonly used in solar simulators with reasonable spectral match with natural sunlight. Since the HMI bulb requires a constant correction of the voltage to ensure constant current flow and an ignition spark of several kV; a ballast and igniter system was specified and installed up as well.

Intensity regulation was accomplished with an iris. The initial design featured a camera like iris with a diameter of 50 mm (ThorLabs D50S). The iris was controlled by a linear actuator (Firgelli M12-100mm). The first iris employed had a dark coating and was not able to withstand the heat generated from the incoming light. The second generation iris (Edmound optics NT53-913) was larger at 70 mm diameter and had highly polished steel iris blades to circumvent the heating issue. However, after prolonged use the iris blades warped out of shape in the heat. Lastly a custom iris with two blades of 1 mm sheet aluminum was constructed, see Figure 4.2 (right). This iris was driven by two stepper motors through a gear reduction.

Figure 4.2. The iris (right) is an aluminum plate, moved by a stepper motor with a gear reduction. The shutter plate (left) is operated by a rotary solenoid.

The shutter mechanism was based on a rotary solenoid with a 1 mm aluminum blocking plate, see Figure 4.2 (left). Both the iris and the shutter mechanism were controlled through an Arduino derived controller called a Netduino. The Netduino is an open source electronics platform using the .Net micro framework and can therefore be programmed and debugged within the Microsoft Visual Studio environment.

Lamp assembly

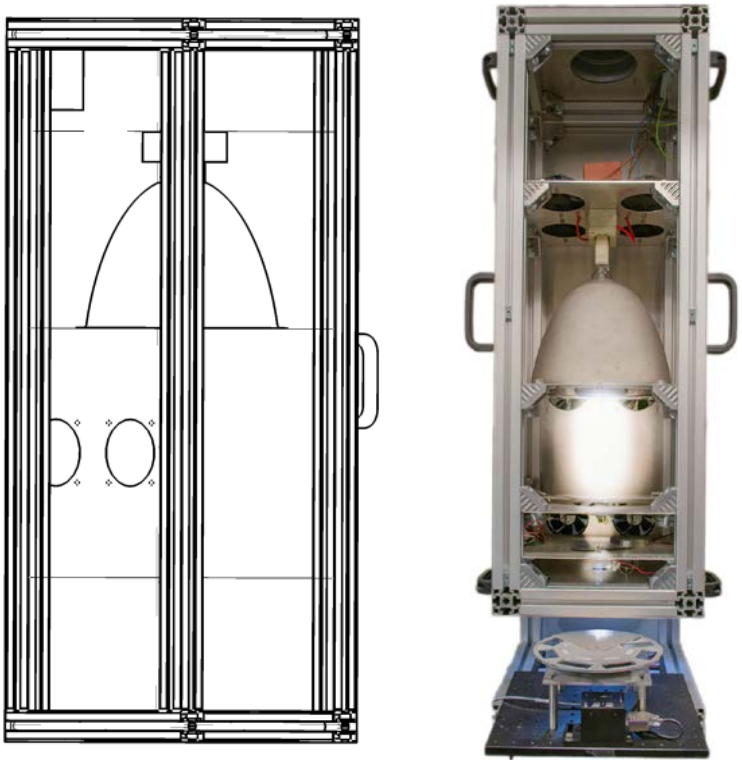

Figure 4.3. A drawing of the concentrator assembly (left) with elliptical reflector, Rexroth aluminum chassis, and HMI bulb. A picture of the finished setup (right) featuring the sample exchanger at the bottom.

To assemble the lamp a chassis was created using Rexroth aluminum profiles. The design was meant to be as adjustment friendly as possible and was laid out in AutoCad Inventor prior to construction, see Figure 4.3. The width of the total system was 350 mm and the height 1200 mm. All optical components were mounted on vertical mounting plates fixed onto the main frame. The top mounting plate featured a 7 kV igniter (Schiederwerk, Germany, model 18-7) along with the lamp socket (Osram socket G-38). The 1200 W HMI bulb (Osram) was inserted in the socket and fixed with tensing screws on each pin, fixating the bulb even when facing down. The lamp was powered by an external power supply based on an electronic ballast from Schiederwerk (PVG, 12-12 AC SL). Beneath the lamp plate a rhodium coated elliptical reflector made by Optiforms (focal length 509 mm, diameter 260 mm, height 206 mm) was mounted. The second focal point of the ellipse was adjusted to be 30 mm above the bottom of the lamp chassis. A fused silica kaleidoscope (10 x 10 x 75 mm) made by Quartz Plus was positioned at the exit of the chassis, homogenizing the spatial light distribution of the outgoing light and providing a square 1 cm^2 high intensity illuminated area. Two mounting plates were inserted

between the ellipse and the kaleidoscope. The top plate featured the iris mechanism and the bottom plate the shutter mechanism. At the underside of the iris plate the Netduino controller, a relay controlling the rotary solenoid, plus two stepper motor drivers for the iris stepper motors were placed. The iris mechanism employs electronic hard limits allowing the setup to reinitialize the stepper motor positions. To control the iris and shutter a software class was created. The visual appearance of this class is seen in Figure 4.4. The sides of the chassis were covered with sheet aluminum and handles were fitted to ensure easy handling of the device. The lamp assembly was wall mounted in two vertical aluminum profiles for easy high adjustment. In the top of the chassis a ventilation pipe connected to the central ventilation system of the building was placed. This was needed since the lamp generated ozone. Cooling of the setup during operation was achieved through eight fans. Air is mainly sucked in from the bottom of the setup and removed at the top. By this, cooling of the light bulb and the embedded electronics was ensured.

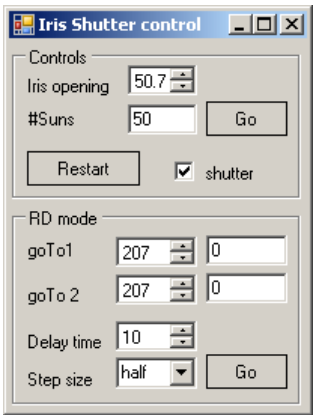

Figure 4.4. Screen capture from iris and shutter control module.

Sample exchange robot

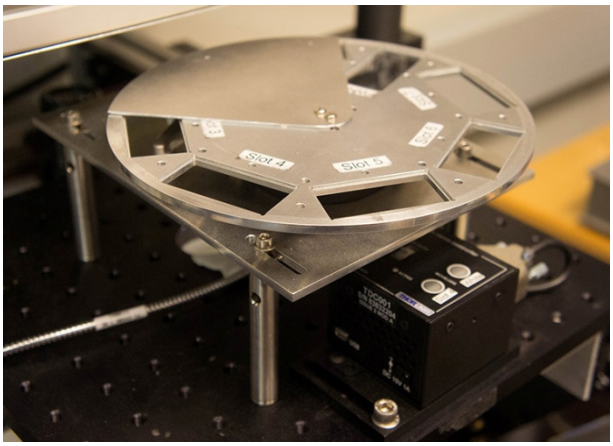

Figure 4.5. Sample exchanger robot.

A custom sample exchange robot was designed for the concentrator setup. The design of the sample exchanger is similar to the one described in Chapter 3, but smaller and tailor made for the concentrator. The sample exchange robot is seen in Figure 4.5 and in the bottom of Figure 4.3 right. The sample holder plate is designed to hold seven samples plus one reference sample. The rotation is achieved with a ThorLabs rotation stage (PRM1Z8) and controller (apt-dc servo controller TDC001). A 1 mm aluminum mask plate with two 3 mm circular aperture was positioned on the sample holder plate. The first aperture positioned under the light exit and the second in the path of the optical transmission measurement system. The positions for light and transmission were then mapped in the software controlling the stage. As the implementation of the instrument classes in the software discussed in Chapter 3 was done through interfaces, the class controlling this stage could directly be used in the existing software. It is even possible to change the sample exchanger robot during runtime. The entire sample exchanger with optical fibers attached was mounted on an optical breadboard, which again was mounted on drawer rails. Hereby the sample exchanger could easily slide underneath the lamp assembly and be pulled out for samples to be exchanged.

Atmosphere chamber

Two atmosphere chambers were constructed with double quartz windows to allow absorption spectra to be recorded without the need of removing samples from the chamber. Both chambers were designed to be mounted on the sample exchanger robot and thereby measurements of four samples under controlled atmospheres could be conducted simultaneously under one sun conditions and serially under concentrated light. One of the atmosphere chambers can be seen in Figure 4.6.

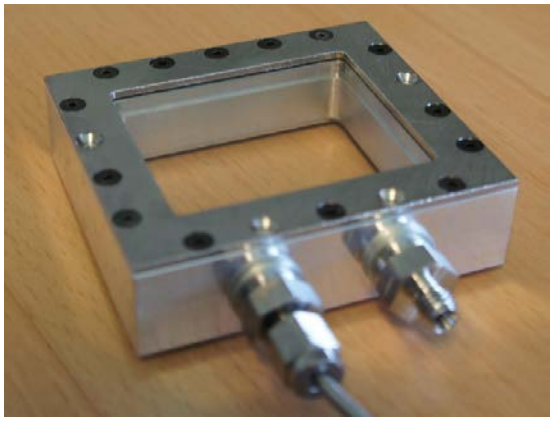

Figure 4.6. The atmosphere chamber is designed with dual windows to allow transmission measurements to be carried out, without removing the sample from the chamber.

UV-visible absorbance measurements

UV-visible absorbance spectra were recorded in transmission mode with an Avantes Avaspec-3648 CCD fiber spectrometer in connection with an Avantes deuterium-halogen light source (AvaLight-DHc). The system is nearly identical to the one described in Chapter 3 using a newer spectrometer and a compact light source. For the software different control classes were needed for each spectrometer, but using an interface each class interacted with the general software seamlessly.

Acquisition and post treatment software

The acquisition software used for the concentrator setup is the exact same piece of software used for the one sun photo-degradation studies, as described in Chapter 3. Two modes of operation were allowed within the software; one for one sun degradation and one for concentrated work. The major difference in operation is that while using a one sun solar simulator all samples are illuminated in parallel. With the solar concentrator the mode of operation is limited to degrading a single sample point at the time. This means that a total degradation time must be typed in prior to the experiment as each sample is degraded individually. A feature allowing automatic termination was implemented allowing a stop condition to be selected. The most common stop condition was observing when the integrated absorption, within a certain range, reached a predetermined value. The mode of operation is selected at run time and both sample exchanger robots will work in either mode.

Setup validation

With the artificial concentrator system built; a validation was needed to ensure that all design criteria had been meet. These criteria included the ability to generate light concentrations in the range from 0.1 to 100+ suns, have uniform light distribution, and spectral invariance for all intensities.

The light intensity was measured with a S314C thermopile from Thorlabs. It was determined that a maximum of 200 suns was achieved at full iris opening. At low intensities a limited resolution was available, but 1 sun could easily be achieved. By inserting a blocking plate under the light bulb the intensity was lowered, however, this avoided direct light from the light bulb greatly increasing low intensity resolution. With this blocking plate the light intensity was reduced to 150 suns, but fine sub 1 sun resolution could be achieved.

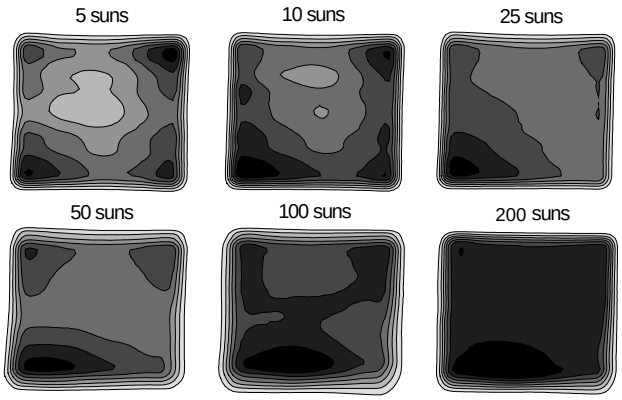

Figure 4.7. Spatial intensity maps of different solar intensities. At 200 suns a fairly homogeneous light distribution is obtained, while at lower solar intensities the spatial inhomogeneity increases.

The blocking plate had a dual purpose. In addition to improving the light intensity resolution; it also vastly improved the light distribution. The spatial light intensity distribution as shown in Figure 4.7 was mapped with a Hamamatsu S5971 photodiode with a 50 µm pinhole raster scanned by an x-y-stage (Prior microscope stage, H128V3). The outgoing light from the kaleidoscope was found to be slightly diverging, implying that the distance between sample and kaleidoscope had to be kept constant for all experiments. All experiments were therefore conducted with a distance of 5 mm, which was also utilized for the mapping of the intensity distributions. Figure 4.7 shows the light distribution measured for 6 different iris openings without the blocking plate. It was found that a higher degree of light blocking by the iris introduced a higher inhomogeneity of the light intensity. Going from a free light passage at 200 suns to higher degrees of blocking, a higher intensity was observed in the corners of the kaleidoscope. At all intensities symmetry around the center of the kaleidoscope was observed, which indicated a good alignment of the optical elements in the setup in terms of projection of the light onto the kaleidoscope. The increasing center intensity was a result of direct light from the light bulb. With the blocking plate in place a pronounced improvement in light intensity distribution was obtained.

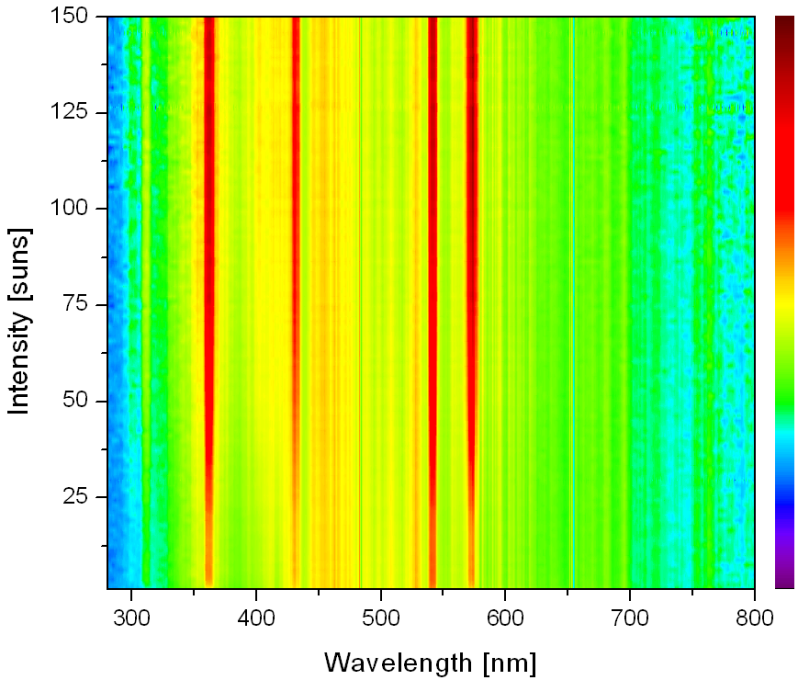

Figure 4.8. Scan of the irradiance from the concentrator as a function of intensity. The color bar represents the normalized irradiance with violet as minimum and dark red as maximum.

The spectral variance of the setup for different intensities, shown in Figure 4.8, was mapped in integral intensity steps from 1 to 150 suns. The figure shows a representation of the normalized irradiance as a function of wavelength and intensity. Clear vertical lines are observed both for peaks (green) and local minima (red) indicating a complete conservation of the spectral features. A minor narrowing of the features combined with a minor decrease of UV content at low intensities was observed. However, this is not believed to have an observable influence on the degradation data.

In short the concentrator fulfilled or exceeded the design criteria by having a constant spectrum and light intensity regulation from 0.1 to 150 suns over a 1 cm^2 illuminated area.

4.3. Solar concentrator

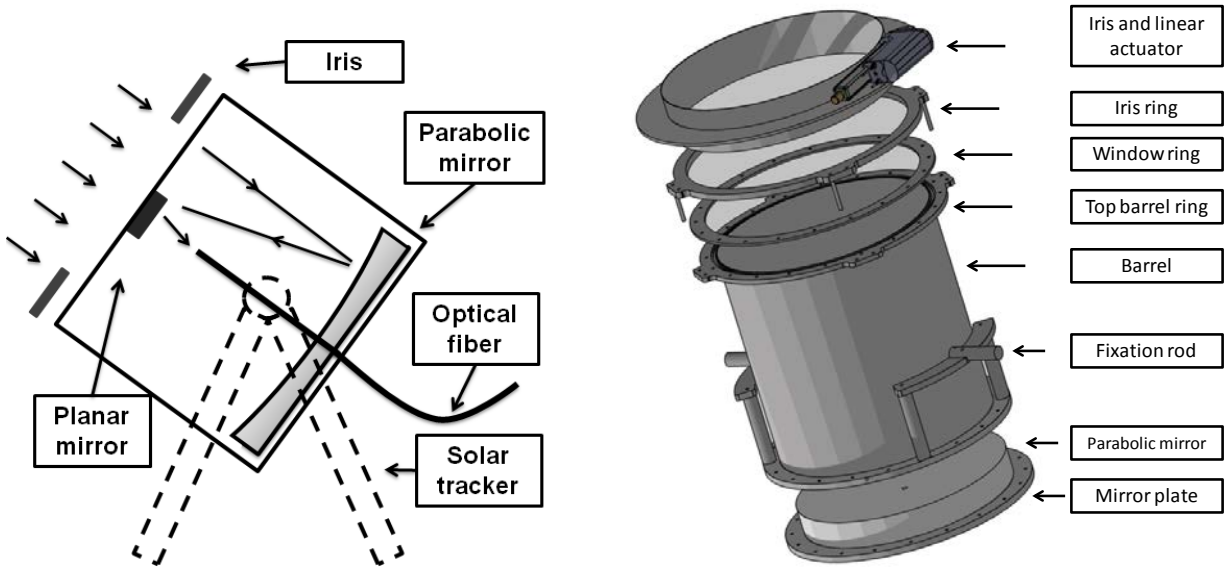

Figure 4.9. Schematic of the solar concentrator (right). Autodesk Inventor rendering of the cylinder (left).

The basic principle behind the solar concentrator is that a Cassegrain reflective system with a parabolic mirror reflects sunlight onto a planar mirror, from which the light is coupled into an optical fiber, see Figure 4.9. Inside a laboratory the fiber exit can be used to conduct experiments with concentrated sunlight. As compared to the artificial concentrator, the solar concentrator setup constructed was based on very different design principles with intended specifications deviating significantly in key areas. The artificial light concentrator was designed to be stable and capable of delivering 150 suns on a 1 cm^2 area. The solar concentrator on the other hand would, by using the sun as the light source, not be able to be stable for operation over more than the sunny hours of the day. The intensity of the light, however, was intended to far exceed the artificial light concentrator. In Figure 4.10 a picture of the mounted functional setup is seen along with a picture of the fiber inside the concentrator.

Figure 4.10. Solar concentrator (left) and close-up of fiber (right).

The design of the solar concentrator was based on a 600 mm diameter diamond turned solid aluminum parabola obtained from LT-ultra, Germany. The reflector was mounted inside a 580 mm high aluminum barrel tightly fitting around the mirror. Enclosed with a glass front window mounted with an o-ring, the barrel was effectively shielded air tight, to exclude humidity, snow, rain etc. The window further provided the fixation point for a planar aluminum mirror (Edmund Optics NT47-113, diameter 5.4 mm) reflecting the light into the fiber inserted from the back of the barrel and through the main reflector. As normal irradiation from the sun is required to couple the light a solar tracking system was needed. Due partly to the size (>100 kg) of the reflector and partly to the design criteria of high temporal stability a custom tracking system was constructed for the concentrator. High precision of the solar tracking is needed since a minor deviation from normal incidence would result in the focus moving outside the optical fibers with an associated decrease of coupled light intensity. Two triangles mounted on a supporting plate was used to hang the barrel in two ball bearings. The barrel was mounted in its vertical center of gravity to keep the stresses on the fixation rods to a minimum. With all parts designed using the Autodesk Inventor software the overall center of gravity could be estimated in the design phase. Hereby, the height of the pillars supporting the fixation rods could be adjusted accordingly. Two slewing drives were used to control the rotation and the inclination of the setup. A large 14” drive with 6.5 kNm of torque was selected for the rotation and a smaller 3” with 0.4 kNm of output torque was used for the inclination. Both were driven by 24 V DC motors with a gear

ratio of 234:1. With these drives the tracking precision of the system was estimated to be less than 0.10° for the rotation and less than 0.15° for the inclination.

Controlling the solar tracking two options were possible. Firstly the solar position can be calculated based on the position of the setup and the exact time. The advantage of this system is that the concentrator will always point directly at the sun, since the system will not be disturbed by external factors such as clouds, reflections, etc. The other solution is tracking based on the incoming light. This system in opposition to the calculation based system does not require fine adjustments of the initial position of the system. Such a system relies on 4 photodiodes mounted at different angles. At any given detector position, the current generated in the photodiodes will be different since some are more exposed. When the intensity of all four photo diodes match the system has perfectly tracked the sun. Compared to calculation based tracking, this system is cruder since the system must constantly corrects its position. The calculation based system allows for fewer movements or even one single continuous movement following the sun. Based on cost and ease of use a detector based tracking system was obtained from the company HelioTrack. The entire concentrator system was mounted on top of an office building with a flat roof on top of a 3.5 x 3.5 m wooden platform, see Figure 4.10. The laboratory was located in a adjacent building. Thereby signal and power cables plus the optical fibers were dug into the ground to insure minimum disturbance to the surroundings.

To control the intensity of light impinging on the parabolic mirror, an iris was used. Due to the large dimensions of the setup a ventilation shaft damper from the ventilation company Lindab was used. The damper is a large iris capable of being adjusted from 100% to approx. 20%. A LA36 linear actuator from Linak was mounted to remotely control the iris. A shutter mechanism was implemented by driving the tracker off the sun. Optical fibers with a numerical aperture of 0.48 and a high transmissivity (Thorlabs BFH48-1000) were chosen and 7 fibers were bundled together. The diameter of the bundle was 3.0 mm with each fiber having a 1 mm diameter. The focus spot in turn had a 6 mm diameter consequently, only 20 % of the light in the focal point was coupled into the fibers. While this large loss may seem unnecessary it served the purpose of increasing temporal stability of the output power. This works since small variations in incidence angle will not take the fiber bundle outside the focus. Because of the intense photon flux the fibers had to be stripped of their protective jackets at both ends. The fiber bundle was guided through the outer wall into the laboratory. The total length of the fiber bundle was 35 meters and 3 meters extended into in the laboratory.

The maximum power output from the fibers was recorded to 12 W with the Thorlabs thermopile. With each fiber opening being 0.785 mm^2 the output area becomes 3.39 mm^2. With this power density the solar concentrator is capable of approximately 2150 suns equivalent intensity.

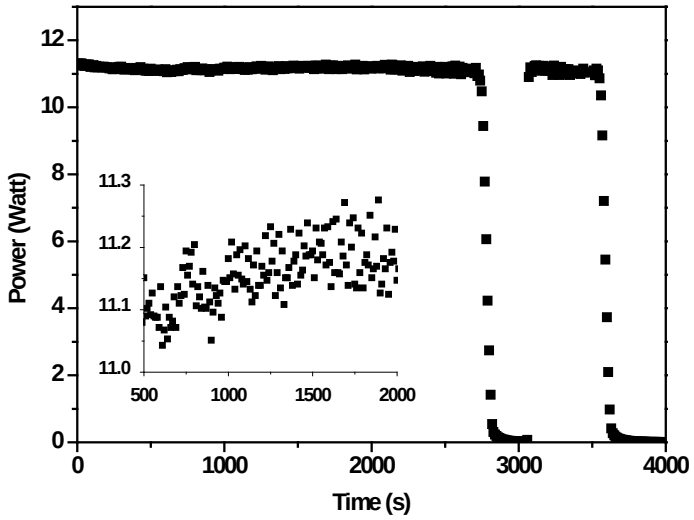

Figure 4.11. Intensity monitoring during 4000 seconds. The shutter is applied twice at 2800 and 3600 seconds.

The power stability during solar tracking was monitored by recording the power every 10 seconds with the thermopile, see Figure 4.11. The power was observed to be constant around 11 W at the given day. At 2,800 and 3,600 seconds the shutter was applied to demonstrate the speed of closing and recovery. The inset shows the variations in the power in the range of 500 to 2000 seconds with increased contrast. Fluctuations in the range of 0.1 W were observed due to the solar tracking, corresponding to approximately 1 % fluctuations.

4.4. Results

In the work described in the article entitled: "Thermally reactive thiazolo[5,4-d]thiazole based copolymers for high photochemical stability in polymer solar cells"[13] the first use of the artificial light concentrator is featured. In that work novel thermally reactive thiazolo[5,4-d]thiazole based copolymers were synthesized. Thermolytic elimination of the ester groups allowed the solubilizing groups to be eliminated around 200 °C. The solubilizing groups are required in order to process polymer materials into thin films, but they are also a part of the reason why the polymers degrade as they allow for both morphologic changes along with chemical transformations caused by diffusion of small molecules and constituents. In order to overcome this, polymer materials with thermally

cleavable solubilizing groups were investigated. To confirm that the elimination of the solubilizing groups improved the durability of the materials the photo-chemical stability was estimated using concentrated light, see Figure 4.12. It is evident that the pristine films are the most unstable under the given conditions. While the photo-chemical stability observed at 100 suns could not be directly converted into an expected stability at 1 sun, the measurements provided good estimate of the relative stabilities between different polymers. The stability of PhxSDT-DTZ was observed to be more than twice that of the P3HT reference (at T50). The thermocleaving was found to introduce a considerable stability improvement of the polymer PhxSDT-DTZ. The T50 is 12 min which increases with 50% for the thermocleaved polymer PhxSDT-DTZ* to a T50 of 18 min. The introduction of PCBM creating a 1 : 2 PhxSDT-DTZ:PCBM blend approximately doubled the T50 both in the case of the pristine and the annealed films consistent with the discussion in Chapter 3.

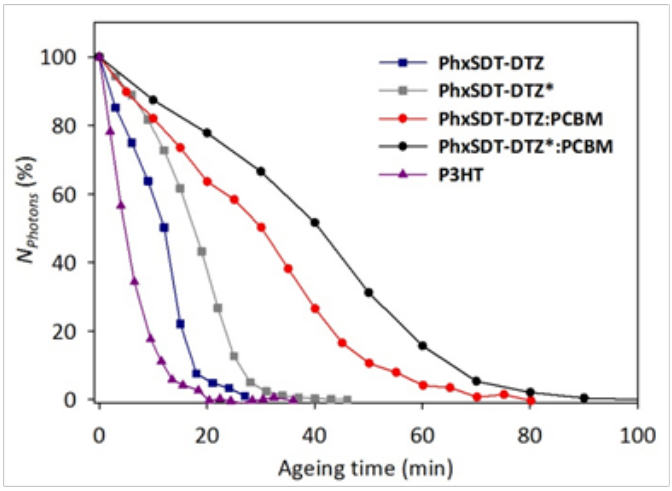

Figure 4.12. Evolution of the normalized absorption during accelerated photochemical ageing in ambient air under 100 solar intensities. The asterix marks the thermally treated samples.

In the article: "Concentrated light for accelerated photo degradation of polymer materials" (Appendix 1.4)[5] the connection between degradation rates and mechanisms at 1 sun and high intensity is presented and discussed. As nothing conclusive could be said about the 1 sun degradation rate in the previous article based on accelerated studies, the value of the technique is limited. As long as it is not clear whether or not the degradation mechanisms remains constant and if other mechanisms comes into play, the use of concentrated light remains a quantitative technique. From the literature it is known that a strong increase in photon effectiveness is observed for photo degradation of P3HT films for decreasing irradiation wavelengths, and it has been demonstrated that oxygen diffusion is not a rate limiting factor under 1 sun conditions.[11,14] For concentrated light conditions it is unknown if this

remains true. Concentrated light might introduce degradation mechanisms that are not observed at 1 sun, which could change the degradation rates. The thermal equilibrium of the sample is expected to change with intensity convoluting the degradation rates. A single study by Tromholt *et al.* reports accelerated photochemical degradation by concentrated sunlight. They observed an acceleration factor of 55 for P3HT by comparing the degradation rate at 1 sun and at 100 suns.[15] This suggests that at 100 suns, each photon has roughly half the effectiveness that a photon has at 1 sun. A bit depressingly the authors compared five different polymers (MEH-PPV, P3HT, JC1, PCPDTBT, and MH76) and reached different acceleration factors for each. If true, this means that the photochemical stability measured at high intensities cannot be compared even to each other. In their study, however, the spectrum at 1 sun was an artificial light source, while the 100 sun spectrum was natural sunlight focused through a concentrator lens setup. The spectra thus had vastly different UV content and a decrease in photon effectiveness was consequently expected explaining the sub 100 acceleration factor. The differences in acceleration factor between the different polymers can be explained by their different absorbance. Thereby different response to the two different spectra is expected. The question, however, remains: are the photons equally destructive at all intensities or do some higher order degradation mechanisms become prevalent at higher intensities.

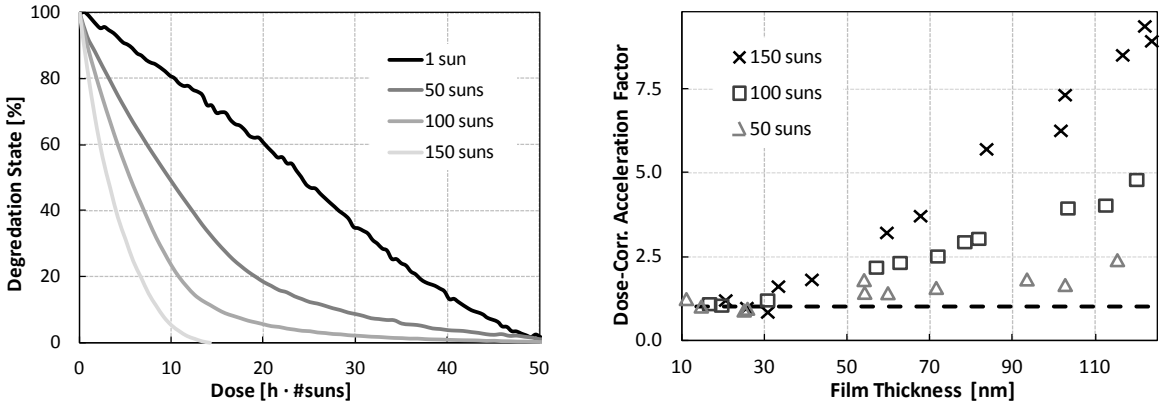

Figure 4.13 Degradation state versus dose for 110 nm P3HT films performed at 1, 50, 100, and 150 suns (left). Dose-corrected acceleration factors for films degraded at 50, 100, and 150 suns as a function of film thickness (right).

By studying degradation of P3HT under highly concentrated light (50 – 150 suns) a significant behavior was observed, see Figure 4.13. While the gradual decrease of absorbance during degradation of P3HT is linear at 1 sun, the linearity is observed to be lost for concentrated light conditions. The degradation rate is decelerating with time, making it impossible to establish a single degradation rate for polymers degraded under concentrated light. It was further observed that the dose-corrected degradation rate

were always higher for concentrated conditions. By determining degradation rates for the initial 10 percent of the degradation process; 1 sun conditions could be compared to concentrated conditions. The dose-corrected acceleration factor, calculated by the ratio of the dose-corrected degradation rates for concentrated light (50, 100, and 150 suns) and the corresponding value for 1 sun, for film thicknesses between 10 and 115 nm is compared in Figure 4.13 (right). The degradation rate corresponding to 1 sun, depicted as the dashed line represents a polynomial fit of 526 separate degradation experiments covering the entire film thickness range. The dose-corrected acceleration factor of 8 observed for 150 suns at the largest film thickness indicates an absolute acceleration factor of 1,200. It is evident that increasing light intensity implies increasing dose-corrected degradation rates when compared to the 1 sun data. Additionally, the effect is observed to increase with film thickness, suggesting that the photon effectiveness increases with higher light intensity and film thickness. In the article it was hypothesized that the rise in effectiveness observed was purely a consequence of the induced temperature increase during experiments. It is expected that the temperature will increase during illumination and that the extent of the induced temperature increase depends both on the absorption of the sample and the light intensity. Thus the hypothesis explains the decelerating degradation rates observed in Figure 4.13 (right). Since it was technically not possible to measure the temperature in the material during light exposure an estimate was needed. By assuming that the temperature could be modeled by the absorbed energy, a radiative loss, and a loss associated with the thermal conductivity through the glass, the steady state temperature was calculated in the article. For a film of 100 nm, a temperature of 65 °C was predicted for 150 suns. It is important to emphasize that this temperature represented a lower limit estimate since the model assumes an instant thermalisation between the polymer and the glass substrate and the model assumes that the substrate is coupled to a perfect heat reservoir. An upper limit was obtained by measuring the temperature of a model system comprising a glass / polymer / silver stack under illumination. At 150 suns a temperature of 175 °C was measured. Consequently, a film with a thickness of 100 nm was predicted to have a temperature in the range between 65 °C and 175 °C. In this temperature range acceleration factors from 3 to 30 is expected with an acceleration determined by an Arrhenius type behavior. The observed acceleration is clearly within the limits, and at the measured acceleration factor for 150 suns / 100 nm a temperature of 105 °C would account for the acceleration. As the hypothesis implies that materials with different activation energies will yield different acceleration factors; PT with an activation energy of E_A = 16.0 *kJ* was tested.[16] By assuming that the temperature of PT is equal to the temperature of

P3HT at equal absorption PT was predicted to have a dose-corrected acceleration factor of 2.2 at an optical density of 0.5. The experimentally determined dose-corrected acceleration factor for PT was 2.0 in excellent agreement with the prediction.

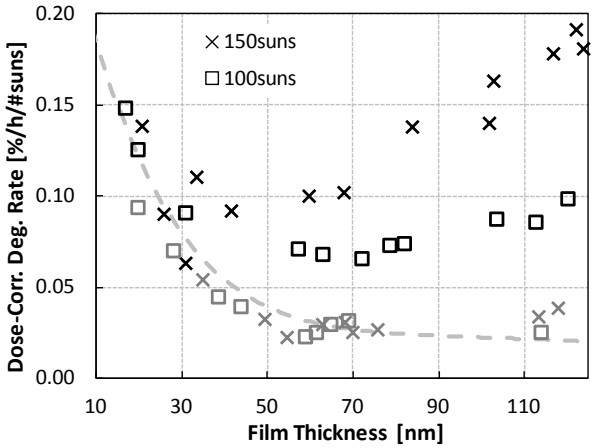

Figure 4.14. Dose-corrected degradation rates for cooled (grey markers) and non-cooled samples (black markers). The dotted grey line represents the 1 sun degradation rate.

In an attempt to prevent or at least minimize heating of the samples, an air ventilation setup was installed. The samples were continuously ventilated by a dry air flow at a rate of 25 liters per minute at ambient temperature directed at the polymer surface, which effectively cooled the samples. As is evident from Figure 4.14 the degradation rates from the cooled samples overlay the 1 sun degradation rates. This confirmed the hypothesis that temperature is the only difference between 1 sun and concentrated degradation. It also implies that concentrated light can be used to determine the degradation rates for polymer films with proper cooling, leading to the opportunity of using concentrated light as a rapid evaluation tool in the pursuit of stable materials. Further since the degradation is accelerated based on an Arrhenius behavior the degradation rates at increased temperature and light intensity is deterministic, given the activation energy.

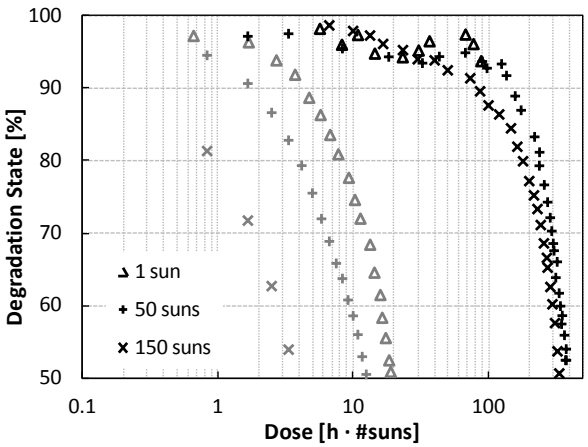

Figure 4.15. Degradation of P3HT in nitrogen atmosphere (black markers) and degradation in ambient atmosphere (grey markers).

As the thermal activation is expected only for samples where photo-oxidation is dominant, no thermal activation is expected for samples in a nitrogen atmosphere. This is shown in Figure 4.15. The increased energy associated with the temperature increase is insignificant in comparison to the energy of the light. At 100 °C, the thermal energy equates to 32 meV, which is significantly lower than the photon energy (1 - 4.5 eV). From Figure 4.15 it is evident that the photo-lysis of P3HT is not thermally activated as the degradation at 1 sun, 50 suns, and 150 suns overlap in degradation time. It thus follows that for all practical purposes thermal activation only occurs when oxygen is present.

4.5. Conclusions

As demonstrated; the use of concentrated light can accelerate degradation studies by extremely high factors enabling rapid routine studies to be conducted for even very air-stable polymers that consequently can be studied within minutes. Concentrated light is clearly an effective tool for screening polymer stability and thus a valuable tool for the development of competitive polymer solar cells.

By studying degradation rates at different light intensities of conjugated polymers, it has been clearly established that the degradation rate scales linearly with light intensity. Any observed deviations from this behavior can be ascribed to an induced temperature increase leading to a thermal acceleration factor. With the induced temperature extremely high acceleration factors can be achieved. An acceleration factor of 1,200 was reported, which is the highest reported in literature. With proper cooling the relative acceleration factor vanished demonstrating that the degradation mechanism and kinetic remained unchanged in the range between 1 and 150 suns. This documents that the photon effectiveness towards degradation is fundamentally independent of the light intensity for films of

P3HT. If the temperature of the sample and activation energy is known, it is further possible to compensate for the temperature induced acceleration and use concentrated studies deterministically.

4.6. References

(1) Hauch, J. A.; Schilinsky, P.; Choulis, S. A.; Childers, R.; Biele, M.; Brabec, C. J. Flexible organic P3HT:PCBM bulk-heterojunction modules with more than 1 year outdoor lifetime. *Solar Energy Materials and Solar Cells* **2008**, *92*, 727-731.

(2) Krebs, F. C.; Norrman, K. Analysis of the Failure Mechanism for a Stable Organic Photovoltaic During 10 000 h of Testing. *Progress in Photovoltaics: Research and Applications* **2007**, *15*, 697-712.

(3) Tromholt, T.; Madsen, M. V.; Carlé, J. E.; Helgesen, M.; Krebs, F. C. Photochemical stability of conjugated polymers, electron acceptors and blends for polymer solar cells resolved in terms of film thickness and absorbance. *Journal of Materials Chemistry* **2012**, *22*, 7592-7601.

(4) Schuller, S.; Schilinsky, P.; Hauch, J.; Brabec, C. J. Determination of the degradation constant of bulk heterojunction solar cells by accelerated lifetime measurements. *Applied Physics A: Materials Science & Processing* **2004**, *79*, 37-40.

(5) Madsen, M. V.; Tromholt, T.; Norrman, K.; Krebs, F. C. Concentrated light for accelerated photo degradation of polymer materials. *Submitted to Advanced Energy Materials* **2012**.

(6) Haillant, O. Accelerated weathering testing principles to estimate the service life of organic PV modules. *Solar Energy Materials and Solar Cells* **2011**, *95*, 1284-1292.

(7) De Bettignies, R.; Leroy, J.; Firon, M.; Sentein, C. Accelerated lifetime measurements of P3HT:PCBM solar cells. *Synthetic Metals* **2006**, *156*, 510-513.

(8) Gevorgyan, S. A.; Jørgensen, M.; Krebs, F. C. A setup for studying stability and degradation of polymer solar cells. *Solar Energy Materials and Solar Cells* **2008**, *92*, 736-745.

(9) Chemisana, D. Building Integrated Concentrating Photovoltaics: A review. *Renewable and Sustainable Energy Reviews* **2011**, *15*, 603-611.

(10) Tromholt, T.; Manor, A.; Katz, E. A.; Krebs, F. C. Reversible degradation of inverted organic solar cells by concentrated sunlight. *Nanotechnology* **2011**, *22*, 225401.

(11) Madsen, M. V.; Tromholt, T.; Böttiger, A.; Andreasen, J. W.; Norrman, K.; Krebs, F. C. Influence of processing and intrinsic polymer parameters on photochemical stability of polythiophene thin films. *Polymer Degradation and Stability* **2012**.

(12) Tromholt, T.; Katz, E. A.; Hirsch, B.; Vossier, A.; Krebs, F. C. Effects of concentrated sunlight on organic photovoltaics. *Applied Physics Letters* **2010**, *96*, 073501.

(13) Helgesen, M.; Madsen, M. V.; Andreasen, B.; Tromholt, T.; Andreasen, J. W.; Krebs, F. C. Thermally reactive Thiazolo[5,4-d]thiazole based copolymers for high photochemical stability in polymer solar cells. *Polymer Chemistry* **2011**, *2*, 2536-2542.

(14) Hintz, H.; Egelhaaf, H.-J.; Lüer, L.; Hauch, J.; Peisert, H.; Chassé, T. Photodegradation of P3HT−A Systematic Study of Environmental Factors. *Chemistry of Materials* **2010**, *23*, 145-154.

(15) Tromholt, T.; Manceau, M.; Helgesen, M.; Carlé, J. E.; Krebs, F. C. Degradation of semiconducting polymers by concentrated sunlight. *Solar Energy Materials and Solar Cells* **2010**, *95*, 1308-1314.

(16) Otero, T. F.; Santos, F. Polythiophene oxidation: Rate coefficients, activation energy and conformational energies. *Electrochimica Acta* **2008**, *53*, 3166-3174.

Chapter 5

Applications of TOF-SIMS for polymer solar cells

Time-of-flight secondary ion mass spectrometry (TOF-SIMS) is a technique used primarily for the study of surfaces of solids. In simple terms secondary ion mass spectrometry is the mass spectrometry of ionized particles emitted when a surface is bombarded by energetic primary particles. Beyond positively and negatively charged ions, neutral particles are emitted. The ions are typically a mixture of atomic ions molecular fragment ions, cluster ions, and molecular ions (if sufficiently small). This allows for a detailed chemical analysis of the surface by providing a mass spectrum. The TOF-SIMS variant of the technique works by assessing the time-of-flight of the secondary ions and thereby achieving a high resolution of the mass of the ions. The usefulness of the method depends on the precision of the time-of-flight analyzers and on the properties of the primary ion used. With modern equipment differentiation of different chemicals and isotopes is standard.

TOF-SIMS has been applied to characterize polymer solar cells mainly to study degradation. Examples of this include; characterization of oxygen and water induced degradation, pinhole effects and more. Diffusion of indium into the PEDOT:PSS layer was demonstrated by Bulle-Lieuwma *et al*. using depth profiling TOF-SIMS.[1] Van Duren et al. have demonstrated that nanoscale phase separation occurs in active layers comprising MDMO-PPV and PCBM.[2] The phase separation was not observed up to 50 *wt.* % PCBM, but at 67 *wt.* % PCBM almost pure PCBM domains in a surrounding matrix of MDMO-PPV was observed. The data was based on AFM, TEM, and TOF-SIMS depth profiling. By standard solar cell characterization a connection with the phase separation and the device performance was established. By studying TOF-SIMS images Norrman *et al.* demonstrated that oxygen diffuses through pinholes in the aluminum electrode of a normal geometry device structure.[3] Using $^{18}O_2$ isotopic labeling in conjunction with TOF-SIMS Norrman *et al.* also demonstrated that oxygen-containing species were generated throughout the active layer. It was demonstrated that the oxygen came from the atmosphere and diffused through the aluminum electrode and into the device.[4] As related to the results presented in Chapter 2 Jo *et al.* have reported that upon solvent annealing, PCBM molecules

migrate or diffuse toward the top surface of the BHJ composite films, which induce a new vertical composition. They used TOF-SIMS measurements of the top surface of the composite films to confirm this change in vertical composition.[5]

As is evident from the examples of the use of TOF-SIMS for the study of organic solar cells; TOF-SIMS can be an extremely useful technique for elucidating information from devices. During this PhD study work with TOF-SIMS has been presented in three journal articles entitled; "The effect of post-processing treatments on inflection points in current–voltage curves of roll-to-roll processed polymer photovoltaics"[6], "Degradation patterns in water and oxygen of an inverted polymer solar cell"[7], and "Oxygen- and water-induced degradation of an inverted polymer solar cell: the barrier effect" (Appendix 2.2)[8].

5.1. TOF-SIMS theory and principles

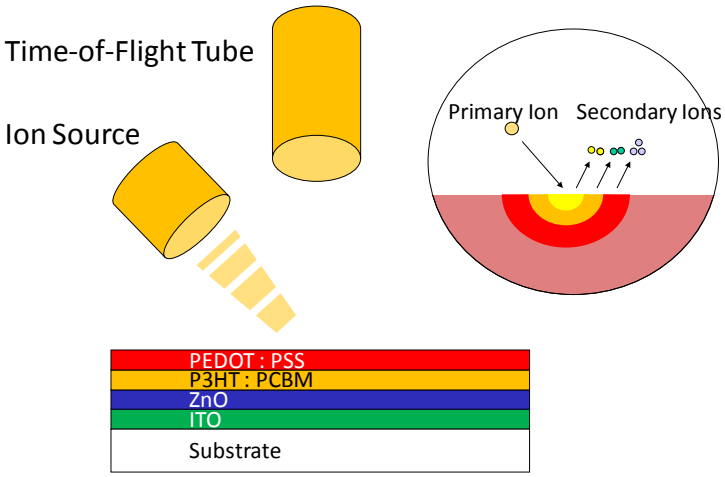

Figure 5.1. Schematic of the TOF-SIMS system featuring primary ion source and time-of-flight tube.

The basic operation of TOF-SIMS is that upon bombarded by energetic primary particles a collision cascade is initiated from the sample surface, see Figure 5.1 for a schematic of the TOF-SIMS operation. Since the ion source is pulsed, using short pulses of < 1 ns, accurate time-of-flight measurements can be conducted. This is done as the emitted secondary ions are extracted into the time-of-flight analyzer by applying a high voltage potential, V_0, between the sample surface and the mass analyzer. Secondary ions travel through the time-of-flight analyzer with different velocities, depending on their mass to charge ratio. For each primary ion pulse, a full mass spectrum is obtained by measuring the arrival times of the secondary ions at the detector and performing a time-to-mass conversion. The generated

secondary ions are electrostatically accelerated into a field-free drift region with a nominal kinetic energy of

$$E_k = zV_0 = \frac{1}{2}mv^2 ,$$

where *m* the mass of ion, *v* the flight velocity of the ion, and *z* is the ion charge. As ions with lower mass have higher flight velocity than ones with higher mass, they will reach the secondary-ion detector earlier. As a result, the mass separation is obtained in the flight time t_{TOF} from the sample to the detector. The flight time is expressed by

$$t_{TOF} = L\left(\frac{2zV_0}{m}\right)^{-\frac{1}{2}},$$

as $v = L/t_{TOF}$, where *L* is the length of the flight tube and t_{TOF} is the time-of-flight. Since *L* and V_0 are instrument parameters a simplification of the equation for the time of flight can be written as

$$t_{TOF} = a\left(\frac{m}{z}\right)^{\frac{1}{2}} + b .$$

a and *b* are constants based upon the instrument parameters, and m/z is the mass-to-charge ratio of the ion. The equation is valid as long as the initial ion velocity is zero.[9] A calibration of the measurement is necessary as electronic delays in the time measurement system must be taken into account. During this calibration the constants *a* and *b* are extracted from a least square fit using known calibration peaks in the spectrum. This calibration must be preformed for all obtained spectra. The equation can alternatively be written as

$$\frac{m}{z} = a' \cdot t_{TOF}{}^2 + b' .$$

It is hereby clear that the mass spectrometry is not in fact determining the mass, but rather the mass to charge ratio. The mass spectrum is drawn as a histogram of counts for each time interval converted into mass per charge.

Mass spectrum analysis

Mass spectra have several distinct sets of peaks, which include the molecular ion (if detected), isotope peaks, fragmentation peaks, and meta stable peaks. Different types of ion sources result in different arrays of fragments produced from the original molecules. It is therefore important that care is put into the correct assignment of mass peaks in the spectrum. Usually the first strategy for identifying an unknown compound is to compare its experimental mass spectrum against a library of mass spectra. With knowledge of expected signals it is possible to assign mass markers to a range of the peaks. Mass spectrometers work in either negative or positive ion mode as a result of the value of the acceleration potential. It is very important to know whether the observed ions are negatively or positively charged. Many molecules/fragments/atoms are only observed in either negative or positive mode.

One major disadvantage of TOF-SIMS is that it is not a qualitative technique. This problem is caused by the matrix effect as secondary ion formation is strongly influenced by electron exchange processes between departing spices and the surface. Thus the electronic state of the surface is critical and the surrounding material becomes highly influential on the ion yield. To circumvent this problem complementary measurement techniques can be used, one example is X-ray photoelectron spectroscopy (XPS). TOF-SIMS data can empirically be calibrated against XPS data resulting in a transformation of qualitative TOF-SIMS data into quantitative data, which is especially useful when studying low levels of photo-oxidation in materials used in organic solar cells.

Practical considerations

Being a destructive technique certain experiments are not possible using TOF-SIMS. It is not possible to take a working solar cell, degrade it, do a measurement and then degrade it again. After the analysis the solar cell will no longer function. Therefore experiments must be carefully planned.

Contaminants can be a major problem when conducting chemical analysis using surface sensitive (~1 nm) techniques such as TOF-SIMS. Silicone is a common contaminant on surfaces, and it is easily introduced by various materials such as oils, greases, heater transfer fluid, sealants, adhesives, surfactant, and medical devices. The typical silicone is polydimethylsiloxane (PDMS), which has a very low surface tension and thus preferentially segregates on the surface of samples. The silicone contaminant on the surface will induce strong signals and the mass spectra will be filled with peaks from the silicone rather than the real sample. Silicone results in the characteristic peaks including m/z 28, 43, 73, 133, 147, 207, 221, and 281.[10] Likely sources for silicone are latex gloves as some latex

gloves contain silicones. It is therefore extremely important to handle samples carefully and avoid contamination. A preferable option is to use polyethylene gloves that contain no additives.

Gaining access to layers of interest

Gaining access to the layers of interest is an important part of doing mass spectral analysis of solar cell devices. To achieve this two different approaches are available. The first is doing depth profiling and the second is physically removing the layers (if possible).

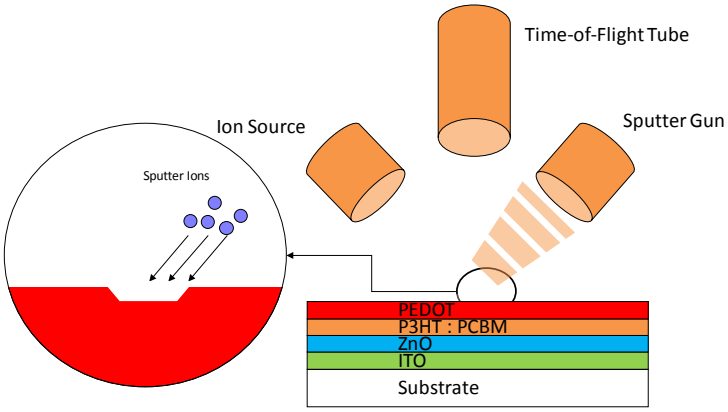

Figure 5.2. Schematic of the depth profiling procedure. An alternative ion source is used to remove material.

Depth profiling is achieved by introducing a constant ion sputter phase in between the pulsed mode acquisition phase in order to remove material. Successive removal of each layer in the multilayer device thus exposing the interfaces, which can then be analyzed. The process is then repeated until the desired depth has been reached. The sputter process is achieved via a secondary gun, see Figure 5.2. This sputter mode depth profiling by TOF-SIMS allows monitoring of all species of interest simultaneously, and with high mass resolution. As a consequence of differences in the sputter efficiencies through different materials the depth profile is not normally displayed as a function of depth, but rather as a function of sputter time. It is not straightforward to perform a TOF-SIMS depth profile on multilayered thin-film devices. Problems include interlayer mixing caused by the sputter process, in which small amounts of the sputtered material will tend to be pushed further into the next layer. This complicates the analysis of diffusion phenomena in the sputter direction. Bulle-Lieuwma *et al.* have reported an increasing bottom crater roughness when starting from the aluminum top layer, resulting in a loss of depth resolution.[1] Another problem with TOF-SIMS depth profiling is the significant charge build-up in the sample surface caused by the sputter ion bombardment, which in many cases is too extensive for the electron bombardment to be able to fully compensate for the

effect. Charge build-up will decrease the intensity of secondary ions resulting in loss of sensitivity. Despite the short comings depth profiling is a valuable tool allowing information to be obtained from the entire stack including the interfaces and the bulk.

The other option of gaining access to the buried interfaces is to physically remove material. This can be done in either of two ways; by delamination or by exploiting solubility of the layers. Since the layers comprised in a polymer solar cell is often solution processed, the organic layers can subsequently be re-dissolved and removed. This is done by gently swiping the surface with a cotton stick soaked in a solvent capable of dissolving the layer and without dissolving the next layer. The process is repeated until the layer is completely removed. Delamination is possible with encapsulated devices, since peeling the encapsulation off typically reveals a buried interface. The method can also be used on non encapsulated devices with tape substituted for the encapsulation material. When performing delamination it is critical to determine if the delamination occurred as expected. This can typically be tested by acquiring ion images on both exposed surfaces.

Isotopic labeling

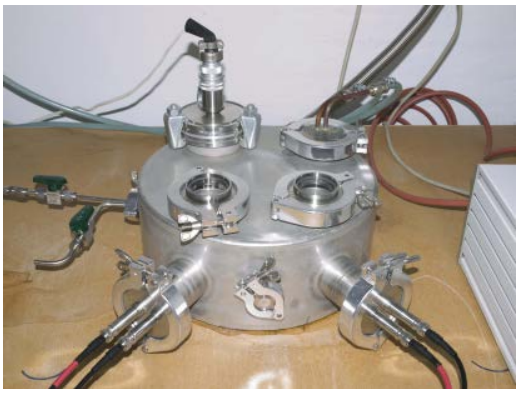

Figure 5.3. Atmosphere chamber used for controlled atmosphere degradation.

Since TOF-SIMS is not a quantitative technique it is desirable to have uniquely identifiable markers. One way of achieving this is to use an isotopically labeled atmosphere. This allows incorporation from the atmosphere to be monitored. Since the natural ratio of isotopes is well known it is possible to identify the amount introduced under the labeled atmosphere. For this an atmosphere chamber is used, see Figure 5.3.[11] Typical isotopically labeled atmospheres consist of $^{18}O_2$ or $H_2{}^{18}O$ (often mixed with N_2 in order to simulate ambient conditions).

5.2. Results

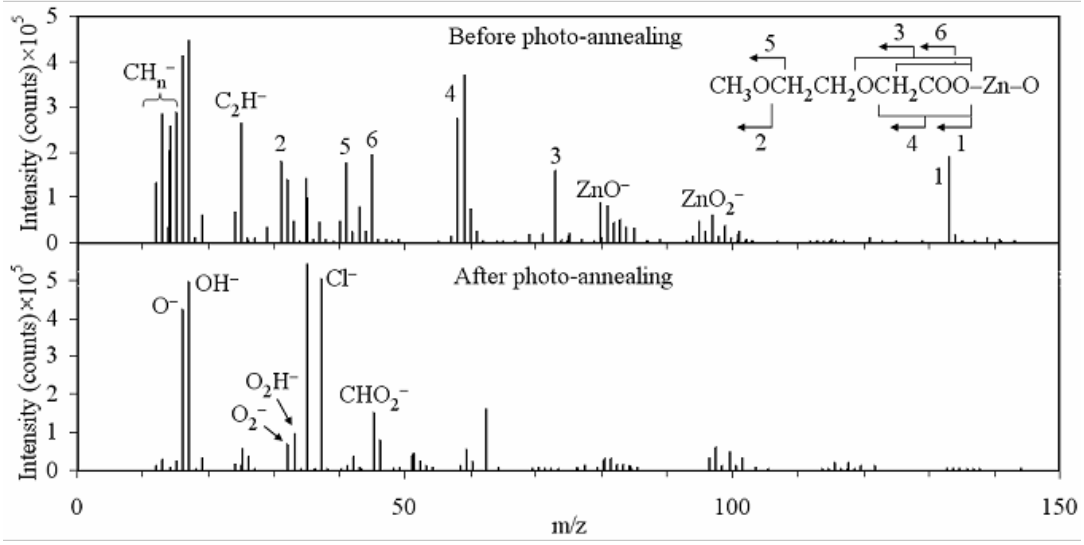

Figure 5.4. TOF-SIMS mass spectra of a ZnO surface before and after 22 h of photo-annealing. Reprinted with permission from Elsevier.[6]

The first contribution is described in the article entitled "The effect of post-processing treatments on inflection points in current–voltage curves of roll-to-roll processed polymer photovoltaics"[6] (not included in the thesis). In this work an investigation of an observed inflection point in roll-to-roll coated inverted polymer solar cells was studied. The inflection point was shown to be removed after continuous current-voltage sweeps during illumination (1000 W m^{-2}) at 80 ˚C for 15–30 minutes. In addition to classical IV testing under various conditions, devices were analyzed using XPS and TOF-SIMS in order to ascertain a possible relationship between photo-annealing and chemical changes in the devices. The chemical composition of the ZnO layer was observed to change significantly as a result of photo-annealing, see Figure 5.4. A possible mechanism based on ZnO photo-conductivity, photo-oxidation and redistribution of oxygen inside the device as proposed by Verbakel was used to explain the observed inflection point.[12] Re-distribution of oxygen within the cell was thus responsible for the reversible inflection point behavior. The oxygen was present as a result of photo-desorption from ZnO and/or decreased oxygen solubility in the encapsulation layers (at elevated temperatures). It was concluded that devices employing ZnO will likely require some pre-treatments and/or chemical doping in order to optimize performance. In the article it was demonstrated that photo-annealing removes the remains of methoxyethoxy-acetate used to make the ZnO nano-particles soluble, see the peak marked 1 in Figure 5.4. The observation of characteristic fragment ions from the ionization process confirms the identity of the methoxyethoxy-acetate. The presence of an O_2H^- peak that increases in

intensity after photo-annealing was also observed. This is an indicator ion for the superoxide ion, known to form during photo-excitation of ZnO in the presence of oxygen, and contributes to the degradation of organic materials including P3HT.

The second contribution comes in the form of the article entitled "Oxygen- and water-induced degradation of an inverted polymer solar cell: the barrier effect" (Appendix 2.2)[8]. In this work the difference between the stability of normal and inverted geometry devices was investigated. While cells of normal geometry have demonstrate high stability when subjected to oxygen and low stability when subjected to a water atmosphere the opposite is true for inverted device geometry cells, see Figure 5.5. It was observed that both atmospheres lead to fast degradation of the initial response for the non-encapsulated devices (black). The oxygen atmosphere led to complete degradation of the device in roughly 20 hours with all parameters showing fast decay. The comparable cell exposed to a humid atmosphere remained functional after the 480 hour time frame of the experiment. The encapsulated devices (grey) generally showed little degradation.

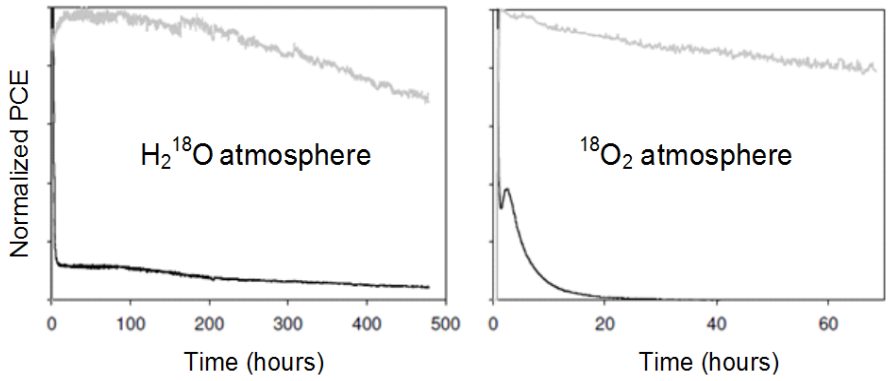

Figure 5.5. Normalized PCE describing the degradation in performance of encapsulated (grey) and Non-encapsulated (black) devices under continuous illumination (330 W m^{-2}, AM1.5G, 65 ± 2 °C). Reprinted with permission from SPIE.[8]

The mechanism for the diffusion of water into the normal geometry device is fairly well described by primarily diffusion of oxygen through pinholes in the metal electrode.[3] As a possible explanation of the difference in the behavior for normal and inverted cells it was hypothesized that the different layers act as a barrier toward both water and oxygen. If this barrier effect is different for oxygen and water the hypothesis can explain the observed behavior. The aim of the work presented was to determine the effect of each layer in the inverted geometry stack as a barrier material. A series of four partial solar cells were prepared for both atmospheres (molecular oxygen and water), see Figure 5.6. This

allowed the barrier effect of the layers from the active layer and up to be tested. The experiment was based on the uptake of isotopically labeled oxygen ($^{18}O_2$) and water ($H_2{}^{18}O$). The influence of the atmosphere was established by illumination of the samples at 330 Wm^{-2} at 65 °C in a chamber with controlled atmosphere. The chamber, see Figure 5.3, was equipped with a quartz window allowing illumination. Prior to the experiment a pressure of $\sim 10^{-4}$ mbar was established inside the chamber and the entire system was purged with nitrogen (99.9%) and pumped back down to $\sim 10^{-4}$ mbar. For the water atmosphere condition the chamber was then injected via a septum with $H_2{}^{18}O$ (97%, 5 mL, ~20 mmol). The entire system had a volume of 2.5 L resulting in a saturated isotopically labeled atmosphere. For the oxygen atmosphere the chamber was filled with 1 atm of $^{18}O_2$ and N_2 in a ratio of 20 to 80. For both atmosphere conditions the samples were exposed for a period of 14 days.

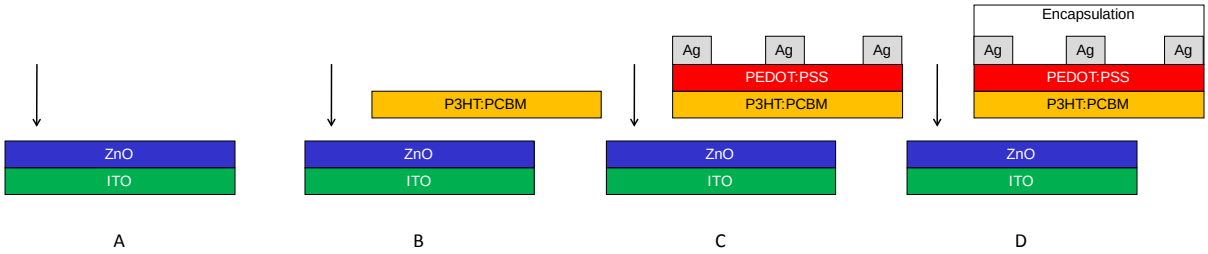

Figure 5.6. Schematic illustration of partial (a)–(c) and complete (d) solar cell devices.

Information on where and to what extent oxygen uptake took place was investigated by analyzing the ZnO surfaces by TOF-SIMS. In order to obtain access to the ZnO surface delamination was used in the case of the encapsulated device. The delamination was shown to take place at the P3HT:PCBM / PEDOT:PSS interface. For the remaining sample layers the PEDOT:PSS layer was removed by gently swiping the surface with a cotton stick soaked in pure water. The underlying P3HT:PCBM layer was removed using the same procedure by substituting water with chloroform. Having exposed the entire ZnO interface for all partial devices TOF-SIMS surface analysis was carried out. Figure 5.7 shows the incorporation of ^{18}O at the ZnO surface in each of the given cases. In the oxygen atmosphere a clear barrier effect is seen for all layers (blue bars). It is seen that each layer has a distinctive effect as a barrier. In the humid atmosphere (red bars) it is seen that the active layer has a profound effect on the oxygen uptake. In fact the barrier effect of the active layer effectively shields the effect of the preceding layers as the difference between B and C lies within the error bars. The elevated incorporation of oxygen seen for the encapsulated devise (D) is somewhat puzzling. The explanation given in the article was that the binder used for the Alcan encapsulation is hygroscopic and acted as a reservoir for water. The observations that the uptake of oxygen is more pronounced in an dry oxygen

atmosphere as compared to a humid atmosphere is in good correlation with the lifetime study demonstrating superior lifetime for cells in a humid atmosphere for inverted geometry devices.

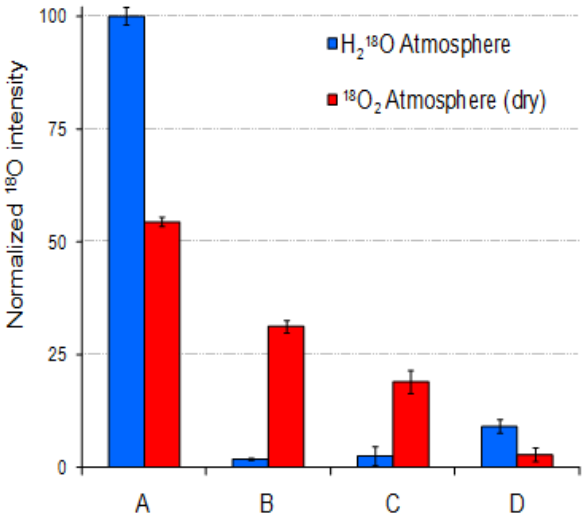

Figure 5.7. Normalized ^{18}O intensities for partial (a)–(c) and complete (d) solar cells. The values was normalized to the largest degree of oxygen exchange seen in the oxygen-free humid atmosphere. (c) The functional cell without encapsulation, (d) the same cell with encapsulation, and (a) and (b) partial device.

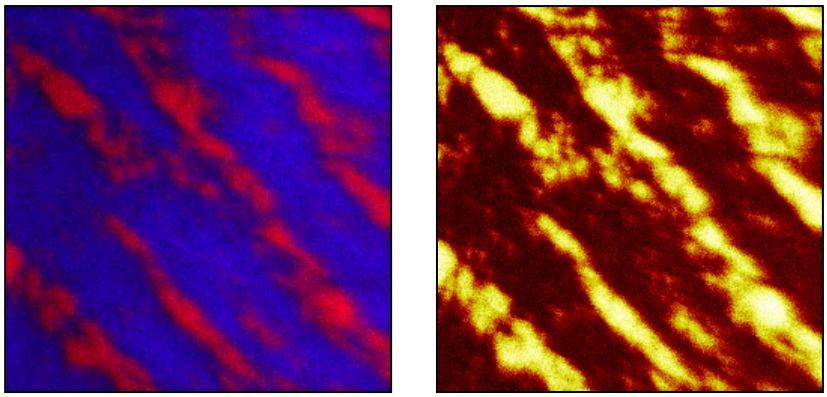

Figure 5.8. Contrast image (left) of the PEDOT phase marker (red) and the PSS markers (blue). The markers are PEDOT: S, ^{34}S, C_2S, C_2HS, $C_6H_5O_2S$, $C_6H_6O_2S$ and PSS: SO_2, SO_3, $C_8H_7SO_3$. $^{18}O^-$ marker shown for the same data set (right). The sample was exposed to an $^{18}O_2$ rich atmosphere.

In the article entitled "Degradation patterns in water and oxygen of an inverted polymer solar cell"[7] (not included in this thesis), the spatial distribution of induced reaction products in multilayer polymer solar cells was mapped. The geometry studied was an inverted geometry device with a layer sequence starting with an ITO coated glass slide. On top of this a ZnO layer followed by a P3HT:PCBM active layer and a PEDOT:PSS acting as a hole transporting layer. The top electrode was a printed silver electrode. By using labeled atmospheres ($H_2{}^{18}O$ and $^{18}O_2$) detailed information on where and to what extent

uptake took place was obtained. A combined XPS and TOF-SIMS analysis then enabled degradation patterns and failure mechanisms to be elucidated. It was concluded that the reactions taking place at the interface between the active layer and the PEDOT:PSS were the major cause of device failure. Phase separation in the PEDOT:PSS was observed, with the PEDOT-rich phase being responsible for most of the interface degradation in oxygen atmospheres. TOF-SIMS images displaying the distribution of $^{18}O^-$ demonstrated that oxygen preferentially reacted with the PEDOT phase, see Figure 5.8. This observed phase separation affects the barrier properties of the layers as a result. It was observed that the reaction pattern of $^{18}O^-$ was persistent through the sublayers suggesting that oxygen diffuses more efficiently through the PEDOT as compared to the PSS phase. In the water atmospheres, little chemically induced degradation was observed as seen in Figure 5.9 where no contrast in the $^{18}O^-$ image can be seen in relation to the PEDOT:PSS contrast image.

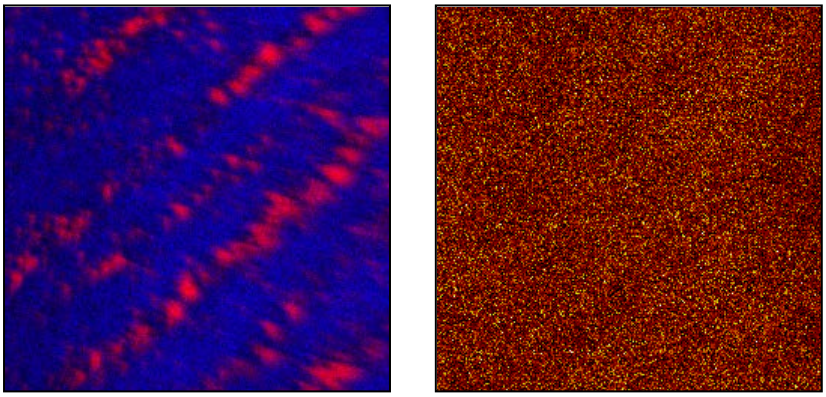

Figure 5.9. The left image represents a contrast image of the PEDOT phase marker (red) and the PSS markers (blue). The markers are PEDOT: S, ^{34}S, C_2S, C_2HS, $C_6H_5O_2S$, $C_6H_6O_2S$ and PSS: SO_2, SO_3, $C_8H_7SO_3$. The right image represents the same data set, but shows the $^{18}O^-$ marker. The sample was exposed to a humid $H_2{}^{18}O$ atmosphere.

5.3. Conclusions

With the results presented it is clear that TOF-SIMS is a powerful technique for doing chemical analysis of solar cells and materials. The technique becomes useful for polymer solar cells partly because it is capable of extracting information from buried interfaces and from the bulk. Access to these interfaces can be gained either using depth profiling, but also by delamination and redesolving layers.

It has been demonstrated that the individual layer offer a barrier effects against molecular oxygen and water in an inverted geometry polymer solar cell. In an oxygen-free humid atmosphere the barrier effect of the active layer (P3HT:PCBM) is demonstrated to be very pronounced. The barrier effect of

the active layer effectively overshadows the effect of the preceding layers. While these results cannot be related to the relative lifetime of the device in molecular oxygen and water, they are useful when designing encapsulation materials.

5.4. References

(1) Bulle-Lieuwma, C. W. T.; Gennip, W. J. H. V.; Duren, J. K. J. V.; Jonkheijm, P.; Janssen, R. A. J.; Niemantsverdriet, J. W. Characterization of polymer solar cells by TOF-SIMS depth proling. *Applied Surface Science* **2003**, *204*, 547-550.

(2) Duren, J. K. J. V.; Yang, X.; Loos, J.; Bulle-Lieuwma, C. W. T.; Sieval, a. B.; Hummelen, J. C.; Janssen, R. a. J. Relating the Morphology of Poly(p-phenylene vinylene)/Methanofullerene Blends to Solar-Cell Performance. *Advanced Functional Materials* **2004**, *14*, 425-434.

(3) Norrman, K.; Larsen, N. B.; Krebs, F. C. Lifetimes of organic photovoltaics: Combining chemical and physical characterisation techniques to study degradation mechanisms. *Solar Energy Materials and Solar Cells* **2006**, *90*, 2793-2814.

(4) Norrman, K.; Krebs, F. C. Lifetimes of organic photovoltaics: Using TOF-SIMS and 18O2 isotopic labelling to characterise chemical degradation mechanisms. *Solar Energy Materials and Solar Cells* **2006**, *90*, 213-227.

(5) Jo, J.; Na, S.-I.; Kim, S.-S.; Lee, T.-W.; Chung, Y.; Kang, S.-J.; Vak, D.; Kim, D.-Y. Three-Dimensional Bulk Heterojunction Morphology for Achieving High Internal Quantum Efficiency in Polymer Solar Cells. *Advanced Functional Materials* **2009**, *19*, 2398-2406.

(6) Lilliedal, M. R.; Medford, A. J.; Madsen, M. V.; Norrman, K.; Krebs, F. C. The effect of post-processing treatments on inflection points in current–voltage curves of roll-to-roll processed polymer photovoltaics. *Solar Energy Materials and Solar Cells* **2010**, *94*, 2018-2031.

(7) Norrman, K.; Madsen, M. V.; Gevorgyan, S. A.; Krebs, F. C. Degradation patterns in water and oxygen of an inverted polymer solar cell. *Journal of the American Chemical Society* **2010**, *132*, 16883-16892.

(8) Madsen, M. V.; Norrman, K.; Krebs, F. C. Oxygen- and water-induced degradation of an inverted polymer solar cell: the barrier effect. *Journal of Photonics for Energy* **2011**, *1*, 011104 1-6.

(9) Cotter, R. J. Time-of-Flight Mass Spectrometry Basic Prinsicpes and Current State. *ACS Symposium Series* **1994**, *549*, 16-48.

(10) Vickerman, J. C.; Briggs, D. *Tof-SIMS: Surface Analysis by Mass Spectrometry*; IM Publications, 2001.

(11) Gevorgyan, S. A.; Jørgensen, M.; Krebs, F. C. A setup for studying stability and degradation of polymer solar cells. *Solar Energy Materials and Solar Cells* **2008**, *92*, 736-745.

(12) Verbakel, F.; Meskers, S. C. J.; Janssen, R. A. J. Electronic memory effects in diodes from a zinc oxide nanoparticle-polystyrene hybrid material. *Applied Physics Letters2* **2006**, *89*, 102103 1-3.

Chapter 6

Summary and Future Challenges

The main goal of the project was identification of degradation mechanisms in roll-to-roll produced polymer solar cells. While the work described in the dissertation has revolved around this subject most work has been on model systems.

Through the study of in-depth morphology of polymer solar cells using ellipsometry, it was revealed that ellipsometry can be used to study advanced aspects of the solar cell composition. While the results presented did not deal with the stability or degradation of solar cells, the technique can potentially be used for this. It is well known that the morphology of the active layer is not thermodynamically stable and ellipsometry could serve as a non-destructive technique for monitoring the evolution of the morphology.

The two following chapters of the dissertation were devoted to the study of photo-chemical degradation of the active layer materials. The second part detailed the building of an automated setup for stability testing and presented results on thickness and absorbance dependence of the photo-chemical stability, acceptor stability, and the influence of intrinsic polymer parameters on stability. In the third part two light concentrating setups, built during the PhD, were detailed and results based on high intensity photo-degradation studies presented. The results of these two chapters, while being generic, can be directly applied to roll-to-roll coated polymer solar cells. Especially the automated aspect of the degradation setups will allow degradation experiments to keep the pace of the coating process and be a rapid evaluation tool.

In the last part of the dissertation the use of TOF-SIMS for polymer solar cell characterization was detailed and the results on intrinsic barrier effects and degradation patterns were summarized. TOF-SIMS is a characterization technique very suited for roll-to-roll coated devices since it is not directly affected by the substrate choice.

Appendix 1

Publications

Full publication list

(1) Lilliedal, M. R.; Medford, A. J.; Madsen, M. V.; Norrman, K.; Krebs, F. C. The effect of post-processing treatments on inflection points in current–voltage curves of roll-to-roll processed polymer photovoltaics. *Solar Energy Materials and Solar Cells* **2010**, *94*, 2018-2031.

(2) Norrman, K.; Madsen, M. V.; Gevorgyan, S. A.; Krebs, F. C. Degradation patterns in water and oxygen of an inverted polymer solar cell. *Journal of the American Chemical Society* **2010**, *132*, 16883-16892.

(3) Madsen, M. V.; Norrman, K.; Krebs, F. C. Oxygen- and water-induced degradation of an inverted polymer solar cell: the barrier effect. *Journal of Photonics for Energy* **2011**, *1*, 011104 1-6.

(4) Madsen, M. V.; Sylvester-Hvid, K. O.; Dastmalchi, B.; Hingerl, K.; Norrman, K.; Tromholt, T.; Manceau, M.; Angmo, D.; Krebs, F. C. Ellipsometry as a Nondestructive Depth Profiling Tool for Roll-to-Roll Manufactured Flexible Solar Cells. *Journal of Physical Chemistry C* **2011**, *115*, 10817-10822.

(5) Helgesen, M.; Madsen, M. V.; Andreasen, B.; Tromholt, T.; Andreasen, J. W.; Krebs, F. C. Thermally reactive Thiazolo[5,4-d]thiazole based copolymers for high photochemical stability in polymer solar cells. *Polymer Chemistry* **2011**, *2*, 2536-2542.

(6) Tanenbaum, D. M.; Hermenau, M.; Voroshazi, E.; Lloyd, M. T.; Galagan, Y.; Zimmermann, B.; Hösel, M.; Dam, H. F.; Jørgensen, M.; Gevorgyan, S. a.; Kudret, S.; Maes, W.; Lutsen, L.; Vanderzande, D.; Würfel, U.; Andriessen, R.; Rösch, R.; Hoppe, H.; Teran-Escobar, G.; Lira-Cantu, M.; Rivaton, A.; Uzunoğlu, G. Y.; Germack, D.; Andreasen, B.; Madsen, M. V.; Norrman, K.; Krebs, F. C. The ISOS-3 inter-laboratory collaboration focused on the stability of a variety of organic photovoltaic devices. *RSC Advances* **2012**, *2*, 882.

(7) Rösch, R.; Tanenbaum, D. M.; Jørgensen, M.; Seeland, M.; Bärenklau, M.; Hermenau, M.; Voroshazi, E.; Lloyd, M. T.; Galagan, Y.; Zimmermann, B.; Würfel, U.; Hösel, M.; Dam, H. F.; Gevorgyan, S. a.; Kudret, S.; Maes, W.; Lutsen, L.; Vanderzande, D.; Andriessen, R.; Teran-Escobar, G.; Lira-Cantu, M.; Rivaton, A.; Uzunoğlu, G. Y.; Germack, D.; Andreasen, B.; Madsen, M. V.; Norrman, K.; Hoppe, H.; Krebs, F. C. Investigation of the degradation mechanisms of a variety of organic photovoltaic devices by combination of imaging techniques—the ISOS-3 inter-laboratory collaboration. *Energy & Environmental Science* **2012**, 6521-6540.

(8) Tromholt, T.; Madsen, M. V.; Carlé, J. E.; Helgesen, M.; Krebs, F. C. Photochemical stability of conjugated polymers, electron acceptors and blends for polymer solar cells resolved in terms of film thickness and absorbance. *Journal of Materials Chemistry* **2012**, *22*, 7592-7601.

(9) Madsen, M. V.; Tromholt, T.; Böttiger, A.; Andreasen, J. W.; Norrman, K.; Krebs, F. C. Influence of processing and intrinsic polymer parameters on photochemical stability of polythiophene thin films. *Polymer Degradation and Stability* **2012**.

(10) Madsen, M. V.; Tromholt, T.; Norrman, K.; Krebs, F. C. Concentrated light for accelerated photo degradation of polymer materials. *Submitted to Advanced Energy Materials* **2012**.

(11) Teran-Escobar, G.; Tanenbaum, D. M.; Voroshazi, E.; Hermenau, M.; Norrman, K.; Lloyd, M. T.; Galagan, Y.; Zimmermann, B.; Hösel, M.; Dam, H. F.; Jørgensen, M.; Gevorgyan, S.; Kudret, S.; Maes, W.; Lutsen, L.; Vanderzande, D.; Würfel, U.; Andriessen, R.; Rösch, R.; Hoppe, H.; Rivaton, A.; Uzunoğlu, G. Y.; Germack, D.; Andreasen, B.; Madsen, M. V.; Bundgaard, E.; Krebs, F. C.; Lira-Cantu, M. On the stability of a variety of organic photovoltaic devices by IPCE and in-situ IPCE analyses - The ISOS-3 inter-laboratory collaboration. *Physical Chemistry Chemical Physics* **2012**.

(12) Andreasen, B.; Tanenbaum, D. M.; Hermenau, M.; Voroshazi, E.; Lloyd, M. T.; Galagan, Y.; Zimmernann, B.; Kudret, S.; Maes, W.; Lutsen, L.; Vanderzande, D.; Würfel, U.; Andriessen, R.; Rösch, R.; Hoppe, H.; Teran-escobar, G.; Lira-cantu, M.; Rivaton, A.; Uzunoğlu, G. Y.; Germack, D. S.; Hösel, M.; Dam, H. F.; Jørgensen, M.; Gevorgyan, S. A.; Madsen, M. V.; Bundgaard, E.; Krebs, F. C.; Norrman, K. TOF-SIMS investigation of degradation pathways occurring in a variety of organic photovoltaic devices – the ISOS-3 inter-laboratory collaboration. *Submitted to Physical Chemistry Chemical Physics* **2012**.

(13) Carlé, J. E.; Andreassen, B.; Tromholt, T.; Madsen, M. V.; Jørgensen, M.; Krebs, F. C. Comparative Studies of Photo Chemical Cross-linking Methods for Stabilizing the Bulk Hetero-Junction Morphology in Polymer Solar Cells. *Submitted to Journal of Materials Chemistry* **2012**.

Included publications

Appendix 1.1 (p 107-120)

Ellipsometry as a Nondestructive Depth Profiling Tool for Roll-to-Roll Manufactured Flexible Solar Cells

Morten V. Madsen, Kristian O. Sylvester-Hvid, Babak Dastmalchi, Kurt Hingerl, Kion Norrman, Thomas Tromholt, Matthieu Manceau, Dechan Angmo, and Frederik C. Krebs, *Journal of Physical Chemistry C* **2011**, 115 (21), 10817-10822

Appendix 1.2 (p 121-138)

Photochemical stability of conjugated polymers, electron acceptors and blends for polymer solar cells resolved in terms of film thickness and absorbance

Thomas Tromholt , Morten V. Madsen , Jon E. Carlé , Martin Helgesen and Frederik C. Krebs, *Journal of Materials Chemistry C* **2012**, 22, 7592-7601

Appendix 1.3 (p 139-152)

Influence of processing and intrinsic polymer parameters on photochemical stability of polythiophene thin films

Morten V. Madsen, Thomas Tromholt, Arvid Böttiger, Jens W. Andreasen, Kion Norrman and Frederik C. Krebs, *Journal of Polymer Degradation and Stability* **2012**, DOI: 10.1016/j.polymdegradstab.2012.07.021

Appendix 1.4 (p 153-168)

Concentrated light for accelerated photo degradation of polymer materials

Morten V. Madsen, Thomas Tromholt, Kion Norrman, and Frederik C. Krebs, *Submitted to Advanced Energy Materials* **2012**

Appendix 1.5 (p 169-174)

Oxygen- and water-induced degradation of an inverted polymer solar cell: the barrier effect

Morten V. Madsen, Kion Norrman, and Frederik C. Krebs, *Journal of Photons for Energy* **2011**, 1, 011104 1-4

THE JOURNAL OF PHYSICAL CHEMISTRY C

ARTICLE

pubs.acs.org/JPCC

Ellipsometry as a Nondestructive Depth Profiling Tool for Roll-to-Roll Manufactured Flexible Solar Cells

Morten V. Madsen,*[,†] Kristian O. Sylvester-Hvid,[†] Babak Dastmalchi,[‡] Kurt Hingerl,[‡] Kion Norrman,[†] Thomas Tromholt,[†] Matthieu Manceau,[†] Dechan Angmo,[†] and Frederik C. Krebs[†]

[†]Solar Energy Programme, Risø National Laboratory for Sustainable Energy, Technical University of Denmark, Frederikborgsvej 399, DK-4000 Roskilde, Denmark

[‡]Zentrum für Oberflächen- und Nanoanalytik, Johannes Kepler University, Altenberger Strasse 69, AT-4040 Linz, Austria

Supporting Information

ABSTRACT: We show that it is possible to perform ellipsometry on large area roll-to-roll (R2R) coated solar cells on flexible substrates and further demonstrate that the slot-die coating technique employed yields the same bulk heterojunction (BHJ) film morphology and vertical phase separation as laboratory samples prepared by the spin coating technique. The solar cell device geometry was Kapton/Al/Cr/P3HT:PCBM/PEDOT:PSS/Ag. Variable angle ellipsometry was used to determine the optical dispersions of the pure phases of P3HT and PCBM allowing an effective medium approximation model to be employed. It was found that a top layer phase separation of P3HT and a vertical linear gradient of P3HT and PCBM best described the BHJ layer. The model was tested for samples of varying thickness and blend composition, model parameters including thickness (AFM), vertical composition (XPS depth profiling), and optical transmission (optical simulation and UV−visible spectroscopy comparisons) was confirmed to comply with the model. A means of quality testing and optimization of the coating procedure line scans across a R2R slot-die-coated sample over large distances (8 cm) was made giving insight into thickness and composition uniformity.

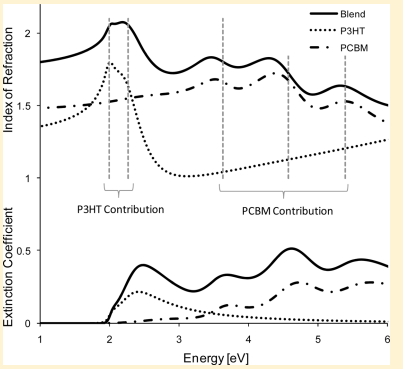

1. INTRODUCTION

The realization of bulk heterojunction (BHJ)-based organic solar cells in 1995 by Yu et al.[1] introduced significant improvements in power conversion efficiency. BHJ-based solar cells have been reported with efficiencies as high as 8.3% as demonstrated by Konarka[2] and 8.5% by Mitsubishi Chemical Corp.[3] However, even at >8% efficiency, organic solar cells cannot compete with inorganic solar cell devices. Amorphous silicon solar cells easily outmatch organic solar cells in efficiency as well as cover many of the same unique aspects, such as flexibility and low weight of the final device. The real unique advantage of polymer solar cells is the relative ease of production, the prospect of no material shortages, and the potential low cost. Several examples of roll-to-roll (R2R) manufacturing of polymer solar cells can be found in literature, both including and excluding vacuum steps for electrode deposition.[4,5] As the inverted type solar cell geometry allows for the use of a solution processed back electrode, most R2R solar cell devices are based on this geometry.[6] Solution-processed back electrodes are an advantage since vacuum steps are undesirable, as they both increase the time and energy consumption associated with production. The role of the BHJ is several-fold. The layer must absorb light, generate and separate excitons, and transport charge carriers to their respective electrodes. The morphology of the BHJ affects all of these processes. Excitons are separated at electron donor and acceptor phase interfaces, and the morphology optimally should ensure that the interface area is maximized. Conduction of charge carriers requires connected regions of donor and acceptor phases, respectively. Literature shows examples where surface energy effects cause segregation in the BHJ layer of the most described material combination poly-3-hexylthiophene:phenyl-C_{61}-butyric acid methyl ester (P3HT:PCBM). Using variable angle spectroscopic ellipsometry (VASE), Campoy-Quiles et al.[7] modeled the vertical composition profile of P3HT:PCBM films and reported a composition gradient varying from PCBM-rich near the poly(3,4-ethylenedioxythiophene):poly(styrenesulfonate) (PEDOT:PSS) layer to P3HT-rich at the air interface. Consequently, the normal device geometry is inferior to the inverted geometry since P3HT acts as a hole-transporting phase and PCBM acts as an electron transporting phase. Yang and coworkers[8,9] reported P3HT:PCBM BHJ devices with an inverted geometry, where devices showed increased power conversion efficiency over the conventional architecture. This enhanced performance was ascribed to the segregation of blend components as observed with X-ray photoelectron spectroscopy (XPS) depth profiling. It was demonstrated in agreement with

Received: January 14, 2011
Revised: March 18, 2011
Published: May 10, 2011

dx.doi.org/10.1021/jp2004002 | J. Phys. Chem. C 2011, 115, 10817–10822

Campoy-Quiles et al.[7] that the air interface of the blend film was P3HT-rich, whereas the buried interface was PCBM-rich. Recently, studies by Germack et al. substantiated the hypothesis that changes in the surface energy significantly affects the vertical composition profile by casting BHJ layers on two hole transport layers (HTLs) with significantly different surface energies and characterizing them using spectroscopic ellipsometry and near-edge X-ray absorption fine structure spectroscopy. Using three-dimensional reconstructions by transmission electron microtomography Bavel et al.[10,11] presented data suggesting enrichment of P3HT at the lower part of the BHJ layer and, correspondingly, enrichment of PCBM close to the surface. Their findings differ from the results presented by Germack et al.[12] and Yang et al.[8,9] The authors suggest that the underlying substrate surface energy is not important for the formation of vertical gradients, as different morphologies can be observed on equal substrates. Rather the thermodynamic aspects of the interacting components, in particular the kinetic aspect involved during film and morphology formation, is believed to be central in the formation of vertical gradients.

All of the above-described results have been reported on rigid substrates, with the films deposited by spin coating. R2R manufacturing techniques are becoming more prevalent, and the nanomorphology induced by this technique is of general interest. The influence of the deposition technique itself as compared to the surface energy contribution becomes highly interesting. In this work, VASE is applied to determine thickness, composition of constituents, vertical composition gradients in R2R slot-die-coated P3HT:PCBM BHJ layers. The solar cell geometry targeted for this research is a modified Fraunhofer-type solar cell fabricated by a full R2R process, with a Kapton/Al/Cr/P3HT:PCBM/PEDOT:PSS/Ag structure, and described in detail by Manceau et al.[13] Efficiencies up to 3.1% and excellent stability have been obtained by Zimmerman et al.[14,15] Using this geometry in a lab-scale test, 1.4% efficiencies for printed electrode lab-scale cells and 0.5% efficiency for R2R processed cells have been demonstrated by Manceau et al.[13]

2. EXPERIMENTAL SECTION

2.1. Model Device Preparation. Objective glass model devices were prepared by spin coating the BHJ layer. The objective glass is manufactured by Menzel-Gläser and is especially suited as substrates for ellipsometry, as the glass is drawn according to the Fourcault-method; thereby it does not exhibit the tin-rich top layer associated with the widely used Pilkington process. The BHJ layer was spin coated at speeds of 500, 1000, 2000, and 4000 rpm at two concentrations: 1:1 and 1:0.7. A blend solution consisting of 10 mg mL^{-1} P3HT (Rieke Metals Lot: BS16−24) and 10 mg mL^{-1} PCBM (Solenne BV, 99% purity) in chlorobenzene was used for all model devices. The solution was stirred at 40 °C overnight, after which it was brought to room temperature and was ready to use. Samples were also prepared by doctor-blading using a solution of 10 mg mL^{-1} P3HT (BASF, Sepiolid P200) and 10 mg mL^{-1} PCBM (Solenne BV, 99% purity) in chlorobenzene.

2.2. R2R Processing. Deposition of the Cr, Al/Cr stack was performed using magnetron sputtering at Polyteknik A/S (Denmark) on the Kapton foil as purchased from Skultuna Flexibles AB (Sweden) and trimmed to a web of 290 mm. The bare foil was introduced into a R2R sputtering system employing two DC magnetrons with two different targets (Al and Cr). After pumping down overnight, either 100 nm of Cr or 100 nm of Al followed by 15 nm of Cr was deposited in two 8 cm wide stripes. The web speed was 1 cm min^{-1}. R2R slot-die coating was performed on a BC30 basecoater from Solarcoating Machinery GmbH (Germany) from a chlorobenzene solution of 21 mg mL^{-1} P3HT and 18.5 mg mL^{-1} PCBM.[16] P3HT was purchased from BASF as Sepiolid P200, labeled P3HT(Sepiolid) and [60]PCBM was purchased from Solenne BV (purity of 99%). The typical coating speed was 2 m min^{-1}, and the active layer was subsequently dried at 90 °C with a residence time in the oven of around 30 s. The dry layer thickness was estimated to be 260 nm, based on manufacturing parameters and material dry density considerations. The principles, details, and solar cell test results of the R2R processing can be found in the work by Manceau et al.[13]

2.3. Ellipsometry. Variable angle spectroscopic ellipsometry measurements were carried out using a Woollam Co. M-2000 Variable Angle Spectroscopic Ellipsometer, with a spectral range of 0.75 to 6.5 eV. All measurements were done for angles between 45 and 75 degrees with 5 degree steps. When noted, focusing optics were used to minimize the spot size of the measurement spot, referred to as the microspot. All ellipsometry measurements were carried out at the Johannes Kepler University of Linz at the Zentrum für Oberflächen- and Nanoanalytik.

2.4. XPS. XPS depth profiling analysis were performed on a Kα (Thermo Electron Limited, Winsford, UK) using a monochromated Al−K_α X-ray source, a 400 μm spot size, and a takeoff angle of 90° from the surface plane. Surface spectra (100−600 eV, 200 eV detector pass energy) were evaluated at discrete depths. Sputtering was performed over a 1 mm^2 area using 1000 eV Ar^+ with an ion current of 2.7 μA.

3. RESULTS AND DISCUSSION

The devices studied in this work were based on flexible Kapton substrates with either Cr coating (100 nm Cr/Kapton) or Cr/Al coating (15 nm Cr/100 nm Al/Kapton). To test and verify the measurement and data fitting procedure, a model system was employed. In this case, a glass substrate was chosen as a substrate, and the BHJ layer (P3HT (Rieke):PCBM) was spin coated on top. This substrate allows for transmission measurements to be made as a means of testing the ellipsometric model; additionally XPS depth profiles were made to verify the procedure. For slot-die-coated and spin-coated samples, two different polymers were used: P3HT (Rieke) was used for spin-coated samples, and P3HT (Sepiolid) was used for slot-die-coated and doctor-bladed samples due to different solubility properties of the polymers.

3.1. The VASE Approach. VASE is used as the primary tool to determine the vertical composition gradient in the BHJ layer. The complex ratio between the reflection amplitude of the polarized light with the electric field in the plane of incidence (r_p) and perpendicular to the plane of incidence (r_s) is expressed in terms of the ellipsometric parameters Ψ and Δ.

$$\frac{r_p}{r_s} = \tan(\Psi)e^{i\Delta} \quad (1)$$

The ellipsometric parameters are measured accurately, allowing measurements to be fitted to a complex model including spatial effects such as a vertical composition profile. To further ensure quality of the fit, measurements are carried out at variable angles, thus supplying data at different optical path lengths. Using an effective medium approximation (EMA) ascribed to

Bruggeman,[17] mixtures of materials with known n and k can be described. The EMA is a physical model that describes the macroscopic properties of a medium based on the properties and the relative fractions of its components. On the basis of the additive character of the polarizability, a generalization of the Claussius−Mossotti formula can be written as

$$\frac{\langle\varepsilon\rangle - \varepsilon_h}{\langle\varepsilon\rangle + 2\varepsilon_h} = (1-f)\frac{\varepsilon_1 - \varepsilon_h}{\varepsilon_1 + 2\varepsilon_h} + f\frac{\varepsilon_2 - \varepsilon_h}{\varepsilon_2 + 2\varepsilon_h} \quad (2)$$

where $\langle\varepsilon\rangle$ is the effective dielectric function, ε_1 and ε_2 are the dielectric functions of the two media subject to mixing, ε_k the dielectric function of the host medium with the inclusions, and f is the volume ratio of material 2. The underlying assumptions of the equation are that it applies for spherical inclusions and dipole interactions only. Neither is strictly true for the BHJ layer, but the model is still applicable as the dipole interaction is a standard first order approximation giving good results, and because changing the depolarization factor from the spherical value of 1/3 is not generally significant.[18] In the Bruggeman model, $\langle\varepsilon\rangle = \varepsilon_h$, thereby letting the effective medium itself act as the host material.[17] The model is then self-consistent, and the two phases play exactly the same role. The effective dielectric function of the mixture is given by the second-order equation

$$0 = (1-f)\frac{\varepsilon_1 - \langle\varepsilon\rangle}{\varepsilon_1 + 2\langle\varepsilon\rangle} + f\frac{\varepsilon_2 - \langle\varepsilon\rangle}{\varepsilon_2 + 2\langle\varepsilon\rangle} \quad (3)$$

Since f is given as the volume fraction, a conversion is necessary to calculate the mass fraction given for the blends. By considering the basic formula for the volume fraction with the volumes expressed as mass per density, the following relation between mass fraction and volume fraction can be found:

$$f_{mf} = \frac{1}{1 + (f_{vf}^{-1} - 1)\frac{\rho_{PCBM}}{\rho_{P3HT}}} \quad (4)$$

where f_{mf} is the mass fraction, and f_{vf} is the volume fraction. ρ_{PCBM} and ρ_{P3HT} are the dry densities of the respective phases. The dry densities have been found in literature to be 1.33 g cm^{-3} and 1.5 g cm^{-3} for P3HT and PCBM, respectively.[19,20] The validity of the Bruggeman effective medium approximation requires the sizes of the phases (dielectrics) in a composite material to be sufficiently greater than atomic sizes, but smaller than 1/10 of the wavelength, which indeed is true for the BHJ films. The EMA cannot represent nonadditive features of the dielectric function, such as charge transfer absorption bands. This is, however, not a problem since such features seems to be weak in all recorded spectra. Vibronic features originating from crystallization of the P3HT is also neglected in the model. Lastly, the dielectric functions of the phases must be independent of size and shape; this is expected to be the case based on the success of the implementation of the model to samples with varying thickness and composition.

3.2. Pure Phase Optical Dispersions. The dielectric function of both phases, P3HT and PCBM, must be known for the EMA model to be used for a blended system. Glass substrates with spin-coated P3HT (Rieke) and PCBM, respectively, were measured using VASE. The optical dispersion of the pure phases was derived from a generalized oscillator model, using Tauc Lorentz oscillators[21] (see Figure 1). The Tauc Lorentz model is typically used for the parametrization of the optical functions for amorphous semiconductors and insulators for which the imaginary part of the dielectric function ε_i is determined by multiplying the Tauc joint density of states by the ε_i, as obtained from the Lorentz oscillator model. The real part of the dielectric function ε_r is calculated from ε_i using Kramers−Kronig integration, making the model Kramers−Kronig consistent. The Supporting Information contains the fits of the ellipsometry parameters for both P3HT and PCBM in Figures s13 and s14, respectively.

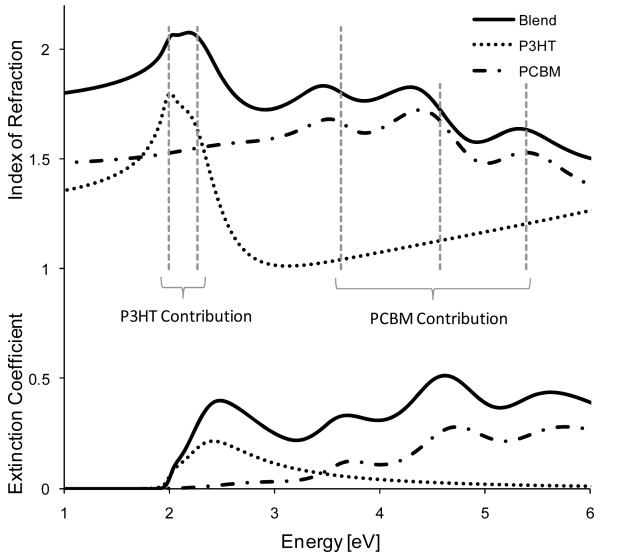

Figure 1. Optical dispersions with peaks assigned are shown for both the index of refraction (top) and the extinction coefficient (bottom). The solid line is the dispersions of the BHJ layer and the dotted lines are the dispersions for the pure phases. The blend optical dispersion is calculated from the pure phase dispersions, using an EMA model as depicted in Figure 2a.

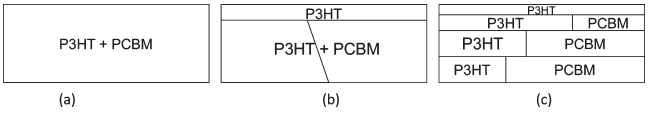

Figure 2. (a) Single layer EMA mix of the two components; this model is labeled simple EMA. (b) More complex model featuring a phase separated top part of P3HT of varying thickness; the bulk of the layer is comprised of a P3HT/PCBM mix described by a linear gradient, labeled as the linear gradient model. (c) Four phase model used for initial fitting.

3.3. Model System Fitting. A series of samples were spin coated on glass substrate at different speeds (500, 1000, 2000, and 4000 rpm) employing two blend concentrations (1:1 and 1:0.7) and measured using VASE. Using the EMA three different models were proposed to describe the optical dispersion, all depicted in figure 2. The four phase model seen in Figure 2c is intended as a general model used to determine the shape of the vertical gradient. Fitting to this model was carried out for samples with layer thicknesses varying from 50 to 200 nm, using a random global fit algorithm running within reasonable physical limits. These were given such that the composition of P3HT and PCBM could not be negative and that the total thickness must stay within ±20% of the thickness determined with ellipsometry using a Cauchy model (with k assumed zero). These latter thicknesses were further supported by atomic force microscopy (AFM)-based thickness measurements. The model was subject to a fitting process where the compositions of the four layers were

dx.doi.org/10.1021/jp2004002 |J. Phys. Chem. C 2011, 115, 10817–10822

set to values from 0 and 100% composition in steps of 25%. The combined thickness was set at values between 20% less than the expected thickness and 20% above the expected thickness with five evenly spaced guesses. The thicknesses of the sublayers were treated as free parameters set to the value from the previous fit. Hereby 2500 different starting guesses were established. These were fitted in a random order (randomness prevents the fit to fall back into the previous local minimum). The overall best set of fit parameters for the 2500 guesses was saved. By repeating this procedure for eight samples with different thickness and composition, it was established that a linear vertical composition gradient combined with a top phase separation would yield the simplest model capable of describing all thicknesses and compositions with a low minimum square error for all samples with only four fitting parameters (see Figure 3b; the four phase model has eight fitting parameters). In the Supporting Information, all four models are shown with XPS depth profiles for two samples (Figures s1 and s6). In Figures s3−s5 and s8−s10, the ellipsometry fits are shown for the different models, and Figures s2 and s7 show simulated transmission spectra for all models along with the measured transmission spectra. The linear gradient model, seen in Figure 2b, gave consistent fits with thicknesses as verified by fitting a Cauchy model in the wavelength range 650−1690 nm. The average deviation between the Cauchy model and the gradient model is 1.8% as documented in Table s1 in the Supporting Information. The linear gradient model is furthermore capable of producing simulated transmission spectra comparing well to measurements, as seen in Figure 3 and in the Supporting Information.

Further verification of the proposed gradient profile is achieved through XPS depth profiling. The composition of P3HT and PCBM is calculated by measuring the content of carbon and sulfur and then calculating the distribution of the two phases by considering the molecular formulas of P3HT and PCBM, respectively (only P3HT contains sulfur). Atomic compositions were determined from surface spectra, and were calculated by determining the integral peak intensities using a Shirley type background, removing the inelastically scattered electron contribution. A comparison of the XPS depth profile and the ellipsometrically determined vertical profile is depicted in Figure 4. By comparing the XPS and ellipsometry data, it is observed that the XPS depth profile does not feature a phase separation as distinct as the one the ellipsometry model suggests. Since the probe depth of the XPS is 5−12 nm, the real vertical gradient will be a convolution of the real vertical gradient and the probe depth, smoothening out the result. Therefore the XPS data supports the ellipsometry model. The pileup of PCBM in the beginning of the XPS profile and the later more linear slope is described well within the linear gradient restriction.

3.4. Flexible Substrate Fitting. Using flexible substrates for ellipsometry introduces a number of complications. First, one must ensure that the substrates are flat. This was achieved by laminating the substrates onto a piece of glass, thereby inducing rigidity to the sample. However, microspot optics was still found necessary for acceptable measurements to be conducted. For each measurement, the depolarization factor was measured to evaluate the degree of partially polarized light caused by curvature of the sample. Thus only measurements exhibiting low depolarization were considered. The substrate used was a Kapton/Al/Cr substrate, which in itself is a multilayer substrate consisting of several highly absorbing layers. The Cr layer is expected to oxidize as the layer is freely exposed to the atmo-

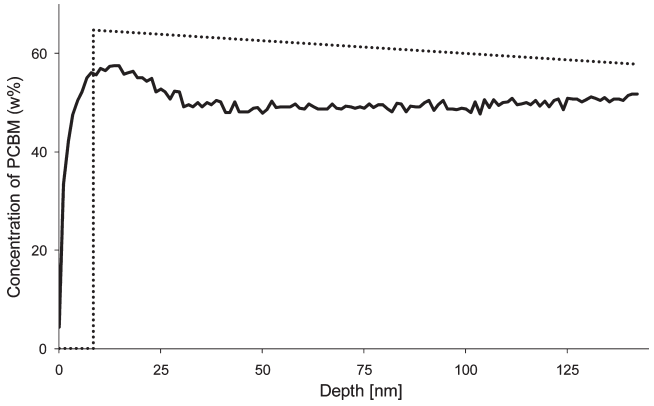

Figure 4. An XPS depth profile compared to the ellipsometrically determined gradient model. The dotted line is the gradient profile from the ellipsometry model. The solid curve is the XPS depth profile.

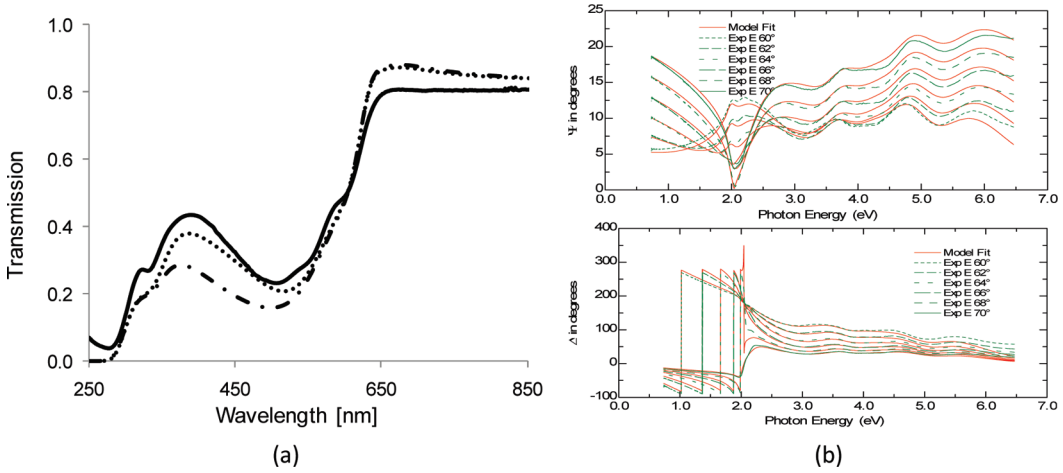

Figure 3. (a) The simulated transmission spectrum (dotted line) shows a good fit for the vertical profile as compared to the measured transmission spectrum (solid line). The dashed dot line represents a simple EMA model, as seen in panel b in Figure 2, which does not reproduce the transmission as convincingly as the more advanced model. (b) Fitted ellipsometric parameters with red lines displaying measured values and green lines representing simulated values.

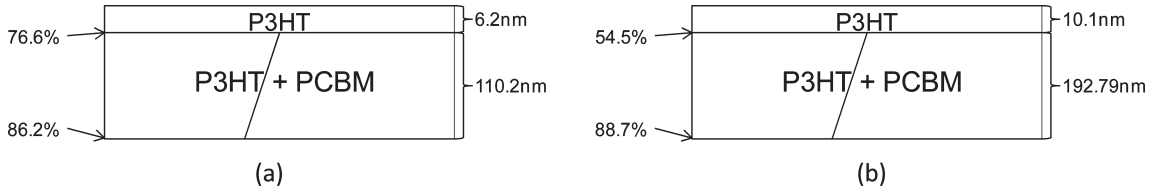

Figure 5. (a) Vertical composition gradient for the P3HT:PCBM/Cr/Kapton spin-coated sample. The mixture is 1:1. (b) Vertical composition gradient as determined for the P3HT:PCBM/Cr/Al/Kapton slot-die-coated sample. The mixture is 1:0.85. In the Supporting Information, Figures s11 and s12 show the fitted and measured ellipsometric parameters.

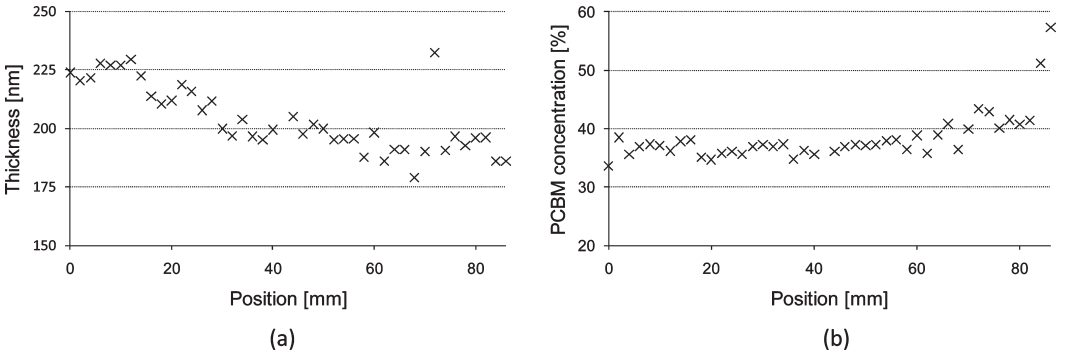

Figure 6. Line scan depicting (a) thickness and (b) composition distribution over the width of the printed stripe.

sphere. The aluminum layer is protected under the Cr layer and the sputtering processes of Al and Cr is completed without breaking the vacuum. However, when chromium oxide is heated with aluminum, it is reduced to chromium metal and aluminum oxide. The layer is therefore quite complicated and modeling and determination of sublayer distribution, thicknesses of sublayers etc., is difficult. Bare Kapton/Al and Kapton/Cr substrates were therefore evaluated in an attempt to build a useful model. However, a monolayer model with infinite absorption (infinite thickness) was chosen as the model resulting in the best fits. The optical dispersions were determined by a point-by-point fitting procedure solving the ellipsometric equations analytically and making the best fit for multiple angles. The Kapton/Cr substrate was fitted using the same procedure. The difference between the Kapton/Cr and the Kapton/Al/Cr is primarily the efficiency of the resulting solar cells as the Al layer increases the conductivity considerably. For ellipsometry it is desirable to have the simplest substrates. Therefore the Kapton/Cr substrate was used for all model work, and the Kapton/Al/Cr were used in the slot-die coating, as slot-die-coated cells were also meant for a solar cell production run.

3.5. Flexible Substrate Results. Fitting of the ellipsometric data for spin-coated Kapton/Cr substrates revealed that the vertical gradient could be modeled within the same framework used for the samples based on glass substrates (see Figure 5a). The behavior of a phase-separated P3HT layer remained, but the linear gradient had reversed. In these cases, more PCBM was found at the substrate interface as compared to the glass substrates. Again, fitting of the c-type model found in Figure 2 was carried out to ensure that the model was in fact valid. For these samples, the P3HT (Rieke) was used.

For the slot-die-coated samples, the P3HT (Sepiolod) was used. It was not possible to spin coat this polymer neither alone nor blended with PCBM. Therefore doctor-bladed samples with P3HT (Sepiolid) were made with both pure P3HT and blended with PCBM on both glass substrates and Cr/Kapton substrates. The optical dispersion determined for P3HT (Rieke) turned out to be applicable for the P3HT (Sepiolid) in the doctor-bladed samples with similar vertical distributions. Therefore the same gradient model was applied to the slot-die-coated substrates. Figure 5b shows the fitted parameters for the slot-die-coated sample. It can be seen that the vertical composition gradient is similar to the spin-coated sample on the Cr/Kapton substrate, shown in Figure 5a. The results show that the slot-die coating process does not lead to a change in the vertical distribution of the constituents as compared to spin-coated samples, meaning that the phase-separated top layer remains as well as the gradient of P3HT and PCBM. It is therefore concluded that the manufacturing technique in the present case plays a minor role in the formation of the vertical composition gradient in the BHJ layer. The surface energy of the substrate appears to be the important factor in this case. Even though the substrates used for slot-die coating and spin coating are not identical, the surface energy is not changed, as the top layer is identical.

3.6. Ellipsometry for Process Control. A line scan was conducted over the width of the slot-die-coated stripe (8 cm wide). Using the simple EMA model for the BHJ layer (Figure 1a) fits of the thickness and composition of constituents were made along the line scan (see Figure 6). The model shows that the thickness has a slope in the distribution of BHJ layer over the observed sample. Outliers in the graph are not to be considered since they have very high minimum square error, especially the measurements near the edges of the sample. The decrease in the fit quality is associated with the curvature of the sample which could not be compensated for by using the microspot objectives and correcting the stage tilt. This is also supported by a high degree of depolarization observed near the edges. The thickness was also fitted using the Cauchy model in the wavelength range 650−1690 nm under assumption of zero absorption, and yielded thicknesses within ±3% of the

thicknesses found for the EMA model. The composition at the macroscopic level is determined by the composition of the solution, and Figure 6b confirms that no real composition change is visible across the sample.

The spatial resolution of the micro spot optics is roughly 0.1 mm. The speed of line scans is determined by the speed of translating the sample. In the case presented, the sample is translated manually. However, using a motorized stage translation, measurements can be carried out with small translation overhead. The speed of the measurement is high for ellipsometry employing a CCD-based spectrometer, giving an acquisition time with adequate integration time of roughly 60 s including seven angles. Restricting measurements to one angle, the acquisition time is reduced to about 5 s. Setting the translation overhead to 5 s and using only one angle, the complete acquisition, shown in Figure 6, can be completed in 400 s. It is hereby clear that ellipsometry in this form is not appropriate for real time R2R characteristics, but rather constitutes a means of off-line quality control and process optimization.

4. CONCLUSIONS

The implementation of ellipsometry in the organic photovoltaic processing technology presents a series of challenges. It has been demonstrated that VASE can be employed to determine composition gradients in the BHJ layer of polymer solar cells with flexible substrates. Overfitting of data is a general concern when dealing with ellipsometry. In this work, great care has been taken by testing the model on samples of varying thickness and composition, as well as confirming model parameters including thickness (simplified Cauchy model and AFM), vertical composition (XPS depth profiling), and optical transmission (optical simulation and UV−visible spectroscopy). It was concluded that samples manufactured by spin coating and slot-die coating exhibit similar vertical composition gradient on equal substrates. A technique for fabrication optimization has been demonstrated by implementations of line scans across a coated sample giving insight into thickness and composition variations over the width of a R2R slot-die coated sample.

■ ASSOCIATED CONTENT

Supporting Information. Additional figures and tables as described in the text. This information is available free of charge via the Internet at http://pubs.acs.org.

■ AUTHOR INFORMATION

Corresponding Author
*E-mail: mves@risoe.dtu.dk.

■ ACKNOWLEDGMENT

This work was supported by the Photovoltaic European Research Area Network (PV-ERA-NET), under the project acronym POLYSTAR and by the European Commission through the Seventh Framework Programme for Research and Technological Development under the Information and Communication Technologies (ICT) project acronym HIFLEX (Grant Number 248678). The authors thank Dr. Birger Zimmermann (Fraunhofer ISE, Germany) for fruitful discussions about the Kapton/Al/Cr concept.

■ REFERENCES

(1) Yu, G.; Gao, J.; Hummelen, J.; Wudl, F.; Heeger, A. *Science* **1995**, *270*, 1789.
(2) Konarka Technologies Homepage.http://www.konarka.com/index.php/site/pressreleasedetail/konarkas_power_plastic_achieves_world_record_83_efficiency_certification_fr (accessed Jan 11, 2011).
(3) Mitsubishi Chemical Corporation Homepage. http://www.mitsubishichem-hd.co.jp/english/news_release/index.html (accessed Mar 15, 2011).
(4) Krebs, F. C. *Org. Electron.* **2009**, *10*, 761–768.
(5) Krebs, F. C.; Jørgensen, M.; Norrman, K.; Hagemann, O.; Alstrup, J.; Nielsen, T. D.; Fyenbo, J.; Larsen, K.; Kristensen, J. *Sol. Energy Mater. Sol. Cells* **2009**, *93*, 422–441.
(6) Krebs, F. C.; Alstrup, J.; Spanggaard, H.; Larsen, K.; Kold, E. *Sol. Energy Mater. Sol. Cells* **2004**, *83*, 293–300.
(7) Campoy-Quiles, M.; Ferenczi, T.; Agostinelli, T.; Etchegoin, P. G.; Kim, Y.; Anthopoulos, T. D.; Stavrinou, P. N.; Bradley, D. D. C.; Nelson, J. *Nat. Mater.* **2008**, *7*, 158–164.
(8) Liao, H. H.; Chen, L. M.; Xu, Z.; Li, G.; Yang, Y. *Appl. Phys. Lett.* **2009**, *92*, 173303.
(9) Xu, Z.; Chen, L. M.; Yang, G.; Huang, C. H.; Hou, J.; Wu, Y.; Li, G.; Hsu, C. S.; Yang, Y. *Adv. Funct. Mater.* **2009**, *19*, 1227–1234.
(10) van Bavel, S.; Sourty, E.; Veenstra, S.; Loos, J. *J. Mater. Chem.* **2009**, *19*, 5388–5393.
(11) Loos, J. *Mater. Today* **2010**, *13*, 14–20.
(12) Germack, D. S.; Chan, C. K.; Kline, R. J.; Fischer, D. A.; Gundlach, D. J.; Toney, M. F.; Richter, L. J.; DeLongchamp, D. M. *Macromolecules* **2010**, *43*, 3828–3836.
(13) Manceau, M.; Angmo, D.; Jørgensen, M.; Krebs, F. C. *Org. Electron.* **2010**10.1016/j.orgel.2011.01.009.
(14) Zimmermann, B.; Glatthaar, M.; Niggemann, M.; Riede, M.; Hinsch, A.; Gombert, A. *Sol. Energy Mater. Sol. Cells* **2007**, *91*, 374–378.
(15) Zimmermann, B.; Würfel, U.; Niggemann, M. *Sol. Energy Mater. Sol. Cells* **2009**, *93*, 491–496.
(16) Krebs, F. C. *Sol. Energy Mater. Sol. Cells* **2009**, *93*, 465–475.
(17) Bruggeman, D. *Ann. Phys.* **1935**, *416*, 665–679.
(18) Aspnes, D.; Theeten, J.; Hottier, F. *Phys. Rev. B* **1979**, *20* 3292–3302.
(19) Erwin, M. M.; McBride, J.; Kadavanich, A. V.; Rosenthal, S. J. *Thin Solid Films* **2002**, *409*, 198–205.
(20) Geens, W.; Martens, T.; Poortmans, J.; Aernouts, T.; Manca, J.; Lutsen, L.; Heremans, P.; Borghs, S.; Mertens, R.; Vanderzande, D. *Thin Solid Films* **2004**, *451*, 498–502.
(21) Jellison, G.; Modine, F. *Appl. Phys. Lett.* **2009**, *69*, 371–373.

Supporting materials section for
Ellipsometry as a nondestructive depth profiling tool for R2R manufactured flexible solar cells

Morten V. Madsen[1*], Kristian O. Sylvester-Hvid[1], Babak Dastmalchi[2], Kurt Hingerl[2], Kion Norrman[1], Thomas Tromholt[1], Matthieu Manceau[1], Dechan Angmo[1] and Frederik C. Krebs[1]

[1]Solar Energy Programme, Risø National Laboratory for Sustainable Energy, Technical University of Denmark, Frederikborgsvej 399, DK-4000 Roskilde, Denmark

[2]Zentrum für Oberflächen- und Nanoanalytik, Johannes Kepler University, Altenberger Strasse 69, AT-4040 Linz, Austria

[*]mves@risoe.dtu.dk

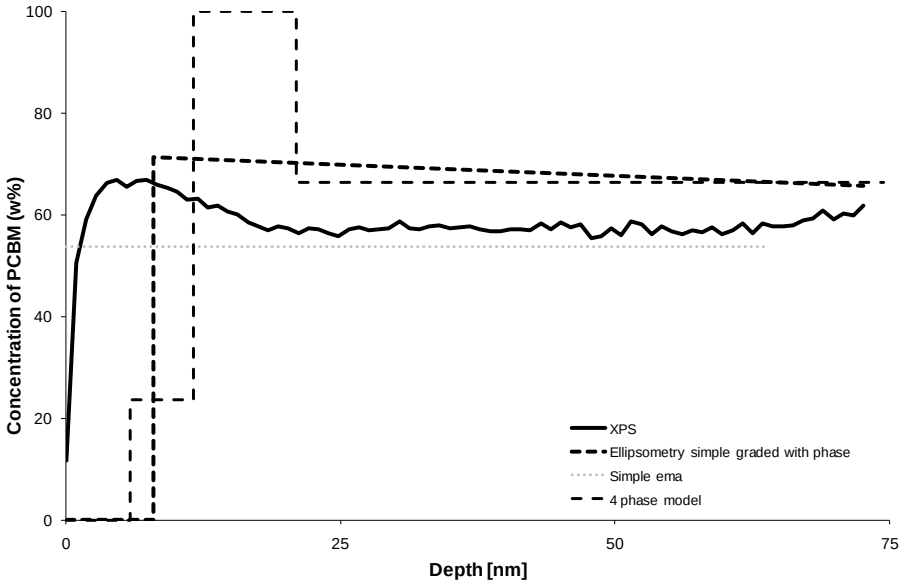

Figure s1. Three different models (simple EMA model, four phase model, and linear model with phase separation, see figure 2) detailing the in-depth morphology of a P3HT:PCBM 1:1 blend spincoated on glass at 4000 rpm. Thicknesses; simple EMA: 63.7 nm, four phase model: 74.4 nm, thickness for linear gradient with phase separation: 72.7 nm, Cauchy model based thickness: 70.6 nm.

1

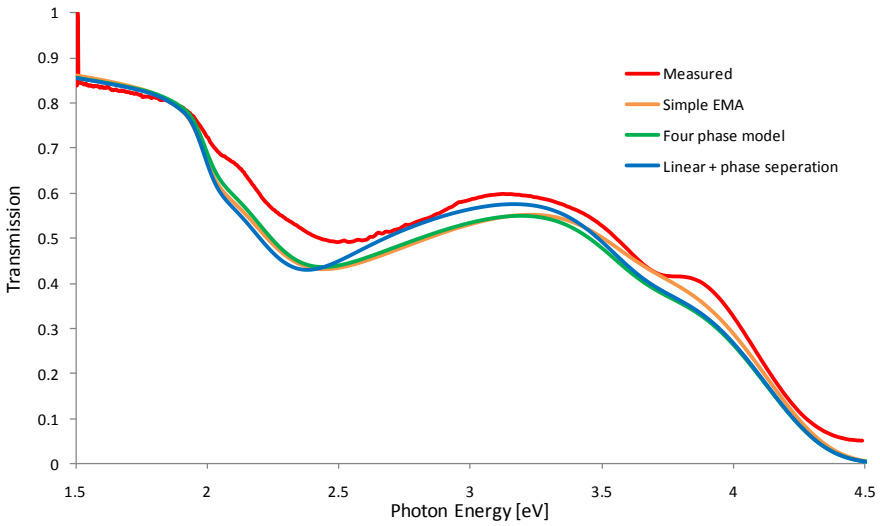

Figure s2. Measured and simulated transmission spectra for the simple EMA model (orange), four phase model (green), and linear model with phase separation (blue), and the measured transmission (red). The data are made to the models shown in figure s1.

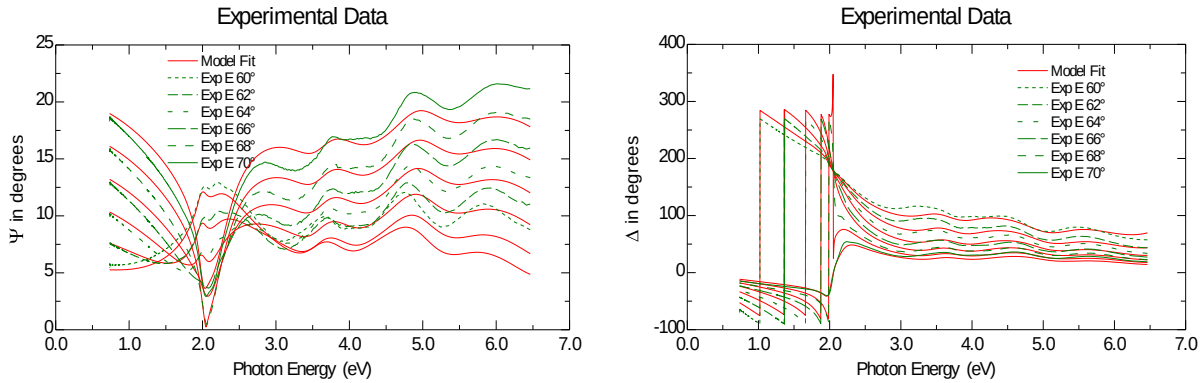

Figure s3. Ellipsometry fit for the simple EMA model associated with figure s1. The thickness was found to be 63.7 nm with a minimum square error of 41.67.

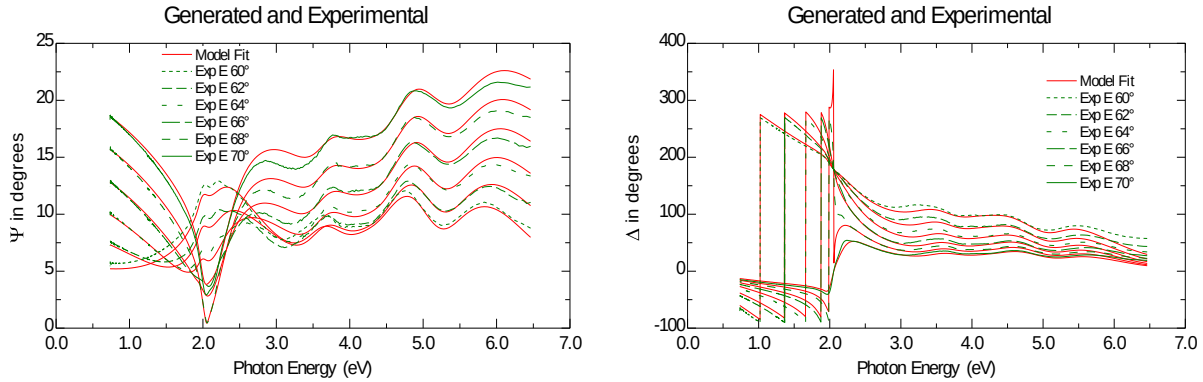

2

Figure s4. Ellipsometry fits for the four phase model associated with figure s1. The thickness was found to be 74.4 nm with a minimum square error of 23.22.

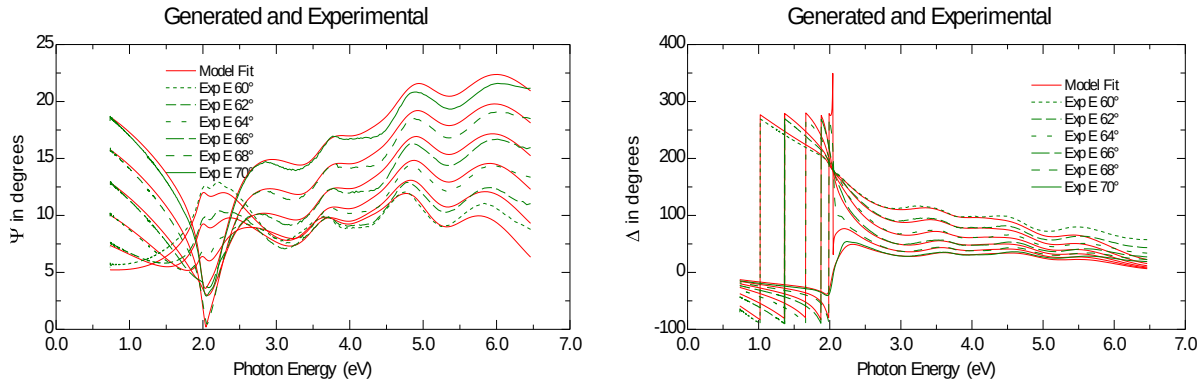

Figure s5. Ellipsometry fits for the linear gradient with phase separation model associated with figure s1. The thickness was found to be 72.7 nm with a minimum square error of 26.41.

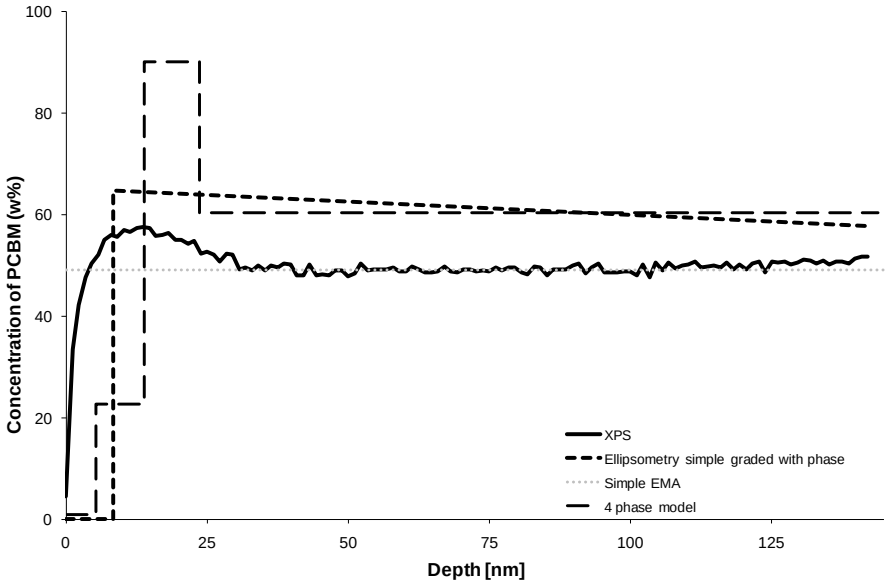

Figure s6. Three different models (simple EMA model, four phase model, and linear model with phase separation, see figure 2) detailing the in-depth morphology of a P3HT:PCBM 1:0.7 blend spincoated on glass at 500 rpm. Thicknesses; simple EMA: 147.1 nm, four phase model: 143.9 nm, thickness for linear gradient with phase separation: 142.2 nm, Cauchy model based thickness: 141.5 nm.

3

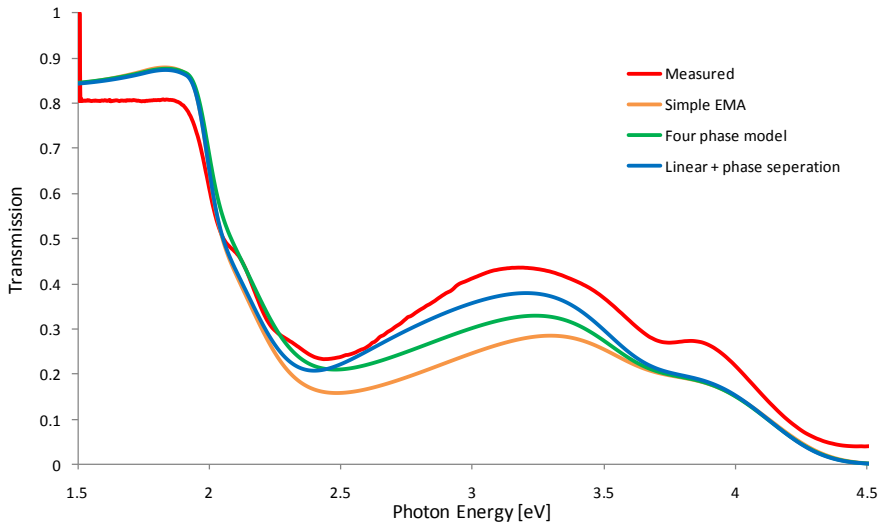

Figure s7. Measured and simulated transmission spectra for the simple EMA model (orange), four phase model (green), and linear model with phase separation (blue), and the measured transmission (red). The data are made to the models shown in figure s2.

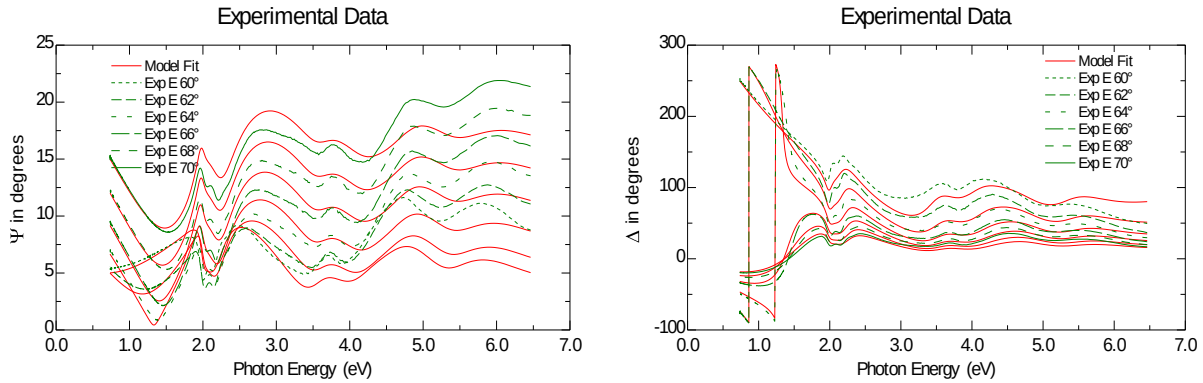

Figure s8. Ellipsometry fit for the simple EMA model associated with figure s2. The thickness was found to be 147.1 nm with a minimum square error of 55.3.

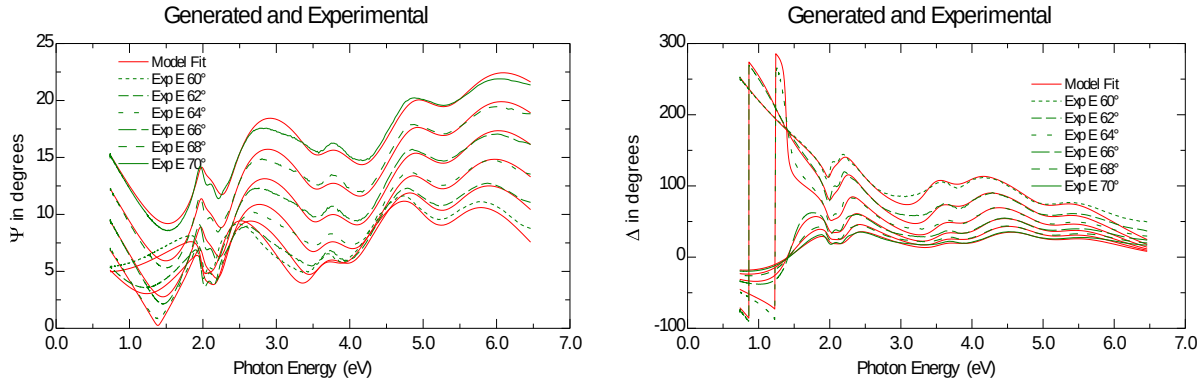

4

Figure s9. *Ellipsometry fits for the four phase model associated with figure s2. The thickness was found to be 143.9 nm with a minimum square error of* 17.84.

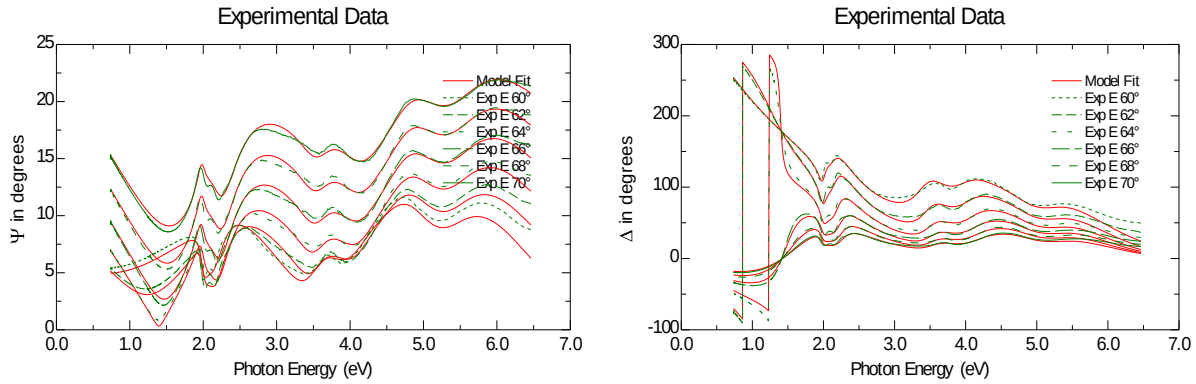

Figure s10. Ellipsometry fits for the linear gradient with phase separation model associated with figure s2. The thickness was found to be 142.2nm with a minimum square error of 20.59

Mix	Spin speed	T total* (Cauchy)	T total (Cauchy)	T main layer	T top layer	T ratio
1:1	4000	72	70.6	64.7	8.0	1.03
1:1	2000	103	101.7	88.9	9.0	0.96
1:1	1000	143	140.8	134.5	7.3	1.01
1:1	500	202	202.7	189.1	11.5	0.99
1:0.7	4000	53	52.4	44.8	7.5	1.00
1:0.7	2000	72	71.9	61.8	7.8	0.97
1:0.7	1000	99	99.4	86.5	11.3	0.98
1:0.7	500	139	141.5	133.7	8.5	1.00

Table s1. The table shows comparisons of the thicknesses determined with the linear gradient model with thicknesses determined with a Cauchy model in the wavelength range 650 – 1690 nm with k assumed zero. The T ratio is the ratio between the Cauchy thickness and the layer thickness from the linear model with phase separation.

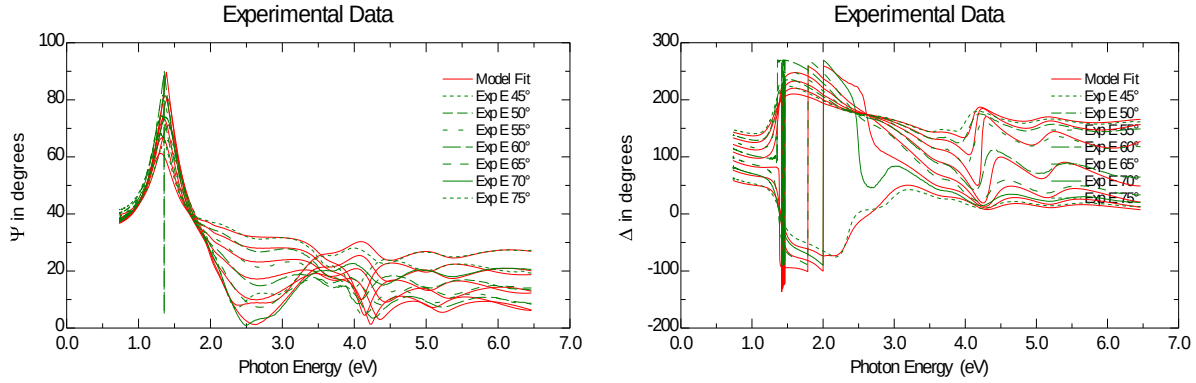

5

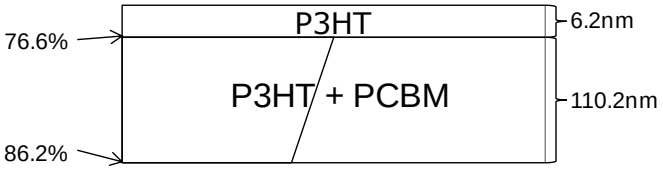

Figure s11. Shows data for spin coated sample on Chrome Kapton substrate. The minimum square error is 82.21.

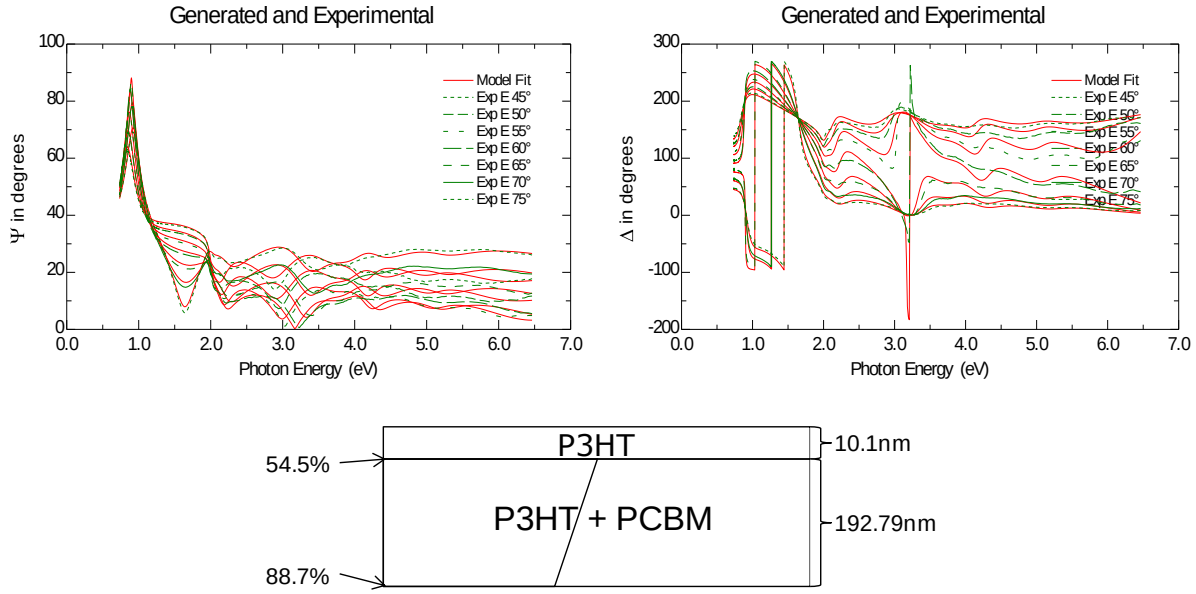

Figure s12. Shows data for slot die coated sample on Chrome Aluminum Kapton substrate. The minimum square error is 48.79.

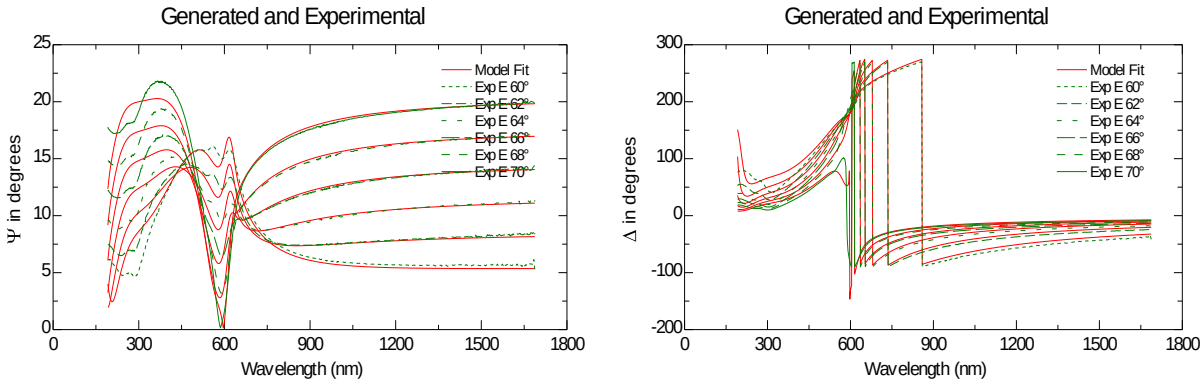

Figure s13. Ellipsometry fit for P3HT on glass spin coated at 4000 rpm. The thickness was measured to be 38.2 nm and the minimum square error is 44.3.

6

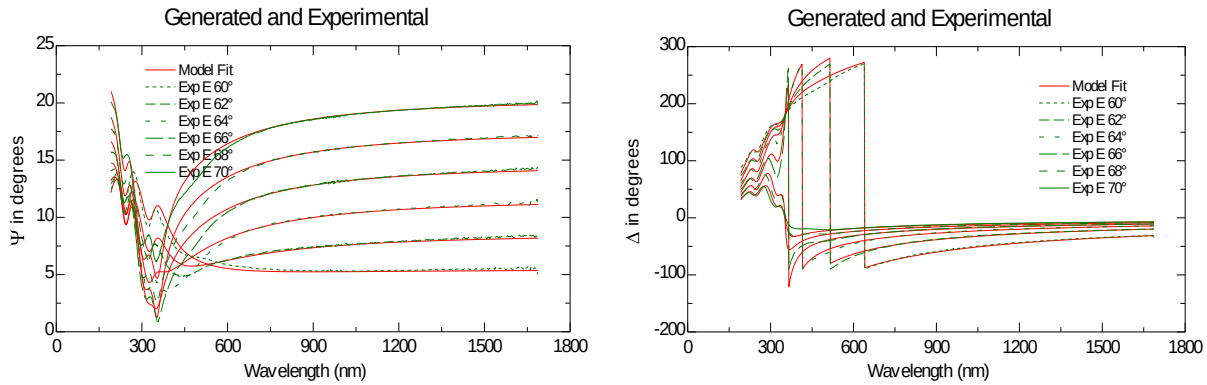

Figure s14. Ellipsometry fit for PCBM on glass spin coated at 4000 rpm. The thickness was measured to be 37.6 nm and the minimum square error is 22.6.

7

Journal of Materials Chemistry

Appendix 1.2

Cite this: *J. Mater. Chem.*, 2012, **22**, 7592

www.rsc.org/materials

PAPER

Photochemical stability of conjugated polymers, electron acceptors and blends for polymer solar cells resolved in terms of film thickness and absorbance†

Thomas Tromholt,* Morten Vesterager Madsen, Jon E. Carlé, Martin Helgesen and Frederik C. Krebs

Received 4th December 2011, Accepted 7th February 2012
DOI: 10.1039/c2jm16340c

Photochemical degradation at 1 sun under AM1.5G illumination was performed on six conjugated polymers and five different electron acceptors. Additionally, the respective polymer:$PC_{60}BM$ and P3HT:electron acceptor blends were studied, and all degradations were resolved in terms of film thickness and absorbance. A fully automated degradation setup allowed for inclusion of in excess of 1000 degradations in this study to enable a discussion of reliability of the technique. Degradation rates were found to increase exponentially with decreasing film absorbance for all materials. The relative stabilities within each material group were found to vary for both the pure polymers and the blends. The stability ranking between the materials of the pure polymers was found to be similar to the ranking for their respective blends, implying that the photochemical stability of a pure polymer is a good measure of its associated blend stability. Different electron acceptors were found to stabilize P3HT decreasingly with decreasing donor–acceptor LUMO–LUMO gap. Destabilization of P3HT was observed in the case of the electron acceptor ICBA. Additionally, the decreased stabilization of P3HT by high LUMO electron acceptors poses a challenge to solar cell encapsulation if these materials are to be of commercial interest. The presented method is generally applicable to all types of organic materials to assess photochemical stabilities. The presented results of conjugated polymers demonstrate that this is a powerful tool for conjugated polymer stability assessment if the results are interpreted correctly.

Introduction

With the increasing attention polymer solar cells (PSCs) are receiving on the basis of potential ease of processing, low cost and light weight,[1–3] solving the stability issue is becoming increasingly urgent. While the efficiency of devices has rapidly risen to exceed 8%,[4] stability is still a major limitation to the technology.[5] A multitude of new polymers have been developed and their performances in PSCs have been studied.[6,7] However, the stability of the polymers is only rarely discussed and therefore their practical potential in actual commercial solar cells is not obvious if they cannot combine high performance with high stability.

A general complication regarding stability assessment of the conjugated polymer in PSCs is the influence of several degradation mechanisms external to the polymer, *e.g.* diffusion of water and oxygen into the cell,[8] hole and electron transport layer degradation,[9,10] morphology and phase changes of the active layer.[11] An alternative method is to focus only on the stability of the polymer itself by degrading only the polymer, either in solution[12] or as thin films.[13,14] By this the photochemical stability of a large number of different material classes has been established.[14] Consequently, this knowledge has been used as a practical guide to direct polymer synthesis and development in the direction of higher stabilities.

Photochemical stability of polymers is normally studied by monitoring the UV-visible photo-bleaching as a function of degradation time.[14] However, the photochemical stability of polymers is known to be highly dependent on several different parameters, *e.g.* oxygen concentration, humidity, temperature, light intensity, film optical density (thickness), UV content, ozone concentration and molecular weight.[13,15] As a result, when making comparative studies of polymer stabilities, many different parameters influence the experimental conditions, which may be outside the control of the experimenter. The majority of the above mentioned parameters are normally approximately constant within an experimental study if not actively changed. Parameters such as the temperature, light spectrum, and light intensity are typically kept constant. Contrary to this, the optical density (thickness) of the sample is more prone to variation and great attention must be given to keep this parameter constant for all samples. Furthermore, the effect of varying optical density (thickness) on material stability has not been studied systematically and therefore the uncertainty introduced by thickness variation is unknown. Degradation of

Risø National Laboratory for Sustainable Energy, Technical University of Denmark, Frederiksborgvej 399, DK-4000 Roskilde, Denmark. E-mail: ttro@risoe.dtu.dk

† Electronic supplementary information (ESI) available. See DOI: 10.1039/c2jm16340c

conjugated polymers in the ambient is highly dominated by the concentration of light and oxygen.[5] In general, due to the limited penetration depth of both light and oxygen, a thick film is expected to be more stable than a thin film. In the literature, examples of this effect can be found by comparison of different P3HT stabilities, where the time frame for a complete degradation with the same light source was found to increase ten-fold when the film absorbance was increased from 0.2 to 0.6‡.[14,16] Additionally, when performing comparative stability studies between different materials, the effect of the optical density (thickness) on the stability for different materials is unknown. The overall effect is that the photochemical stabilities obtained for thin films are not necessarily consistent with the stabilities obtained for thick films.

This study presents a rigorous analysis of the influence of the optical density (thickness) on the photochemical stability of different materials and material combinations relevant to PSCs. However, the presented method is applicable as a stability assessment tool to all types of organic materials. To allow for a thorough analysis of the parameter space, a fully automated degradation setup was constructed. By this a high number of degradation studies could be performed while keeping the workload for the experimenter to a minimum. This study therefore presents in excess of 1000 degradations, providing a sound basis for all conclusions. Six different conjugated polymers were studies as well as five different electron acceptors to establish their individual stabilities and the dependence of these on optical density (thickness). To study the actual chemical context of conjugated polymers in PSCs, the impact of blending P3HT with the five different electron acceptors is studied. This studies the consequence of application of high LUMO level acceptors to PSCs. Finally, the stability of blends consisting of the six studied polymers and $PC_{60}BM$ is assessed. This allows for a general discussion of the correlation between photochemical stability of the single polymers and their associated blends, which is essential for making sound predictions of the stability of different polymers in PSCs.

Experimental

Sample preparation

Six different polymers were studied, which contain different chemical moieties (Fig. 1). 90–94% regio-regular poly[3-hexylthiophene] (P3HT) was obtained from Rieke metals. Synthetic procedures and characterization data for poly[2,3-bis-(3-octyloxyphenyl)quinoxaline-5,8-diyl-*alt*-thiophene-2,5-diyl] (TQ1), regio-random P3HT, and poly[(4,4′-bis(2-ethylhexyl)dithieno[3,2-b:2′,3′-d]silole)-2,6-diyl-*alt*-(2,1,3-benzothiadiazole)-4,7-diyl] (PSBTBT) are documented elsewhere.[17–19] A thermocleavable polymer poly[3-(2-methylhexan-2-yl)-oxy-carbonyldithiophene] allowed for the preparation of solid polythiophene (PT) film from solution[20] by cleaving the polymer on a hot plate in the ambient at 300 °C for 10 seconds after spin coating.[21] Molecular weights for all polymers are given in Table S1†. Photochemical stabilities of all polymers of a single thickness have already been established.[13,14,16,22] All polymers and blends were spin coated on

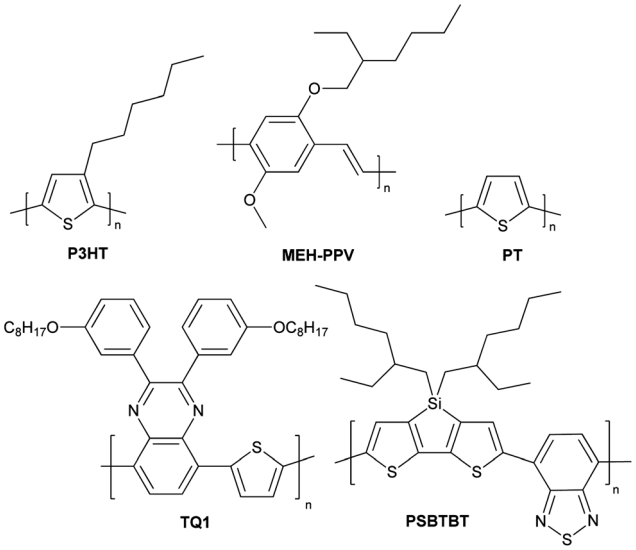

Fig. 1 Schematic illustrations of the polymers studied.

glass substrates from chlorobenzene in the ambient at room temperature in concentrations ranging from 5 to 30 mg mL^{-1} to obtain a wide range of layer thicknesses. Absorbance spectra of all polymers are shown in Fig. S1a†.

Five different electron acceptors were studied of which four are functionalizations of C_{60} Buckminster fullerenes (Fig. 2). Phenyl-[6,6]-C61-butyric acid methyl ester ($PC_{60}BM$), bis$PC_{60}BM$ and $PC_{70}BM$ were obtained from Solenne, C_{60} was obtained from Aldrich, while the indene-C_{60} bis-adduct (ICBA) was obtained from Plextronics. Absorbance spectra of electron acceptors are shown in Fig. S1b†.

Degradation setup

A Steuernagel solar simulator with an Osram 1200 W HMI lamp providing an AM1.5G spectrum was used for all degradations.

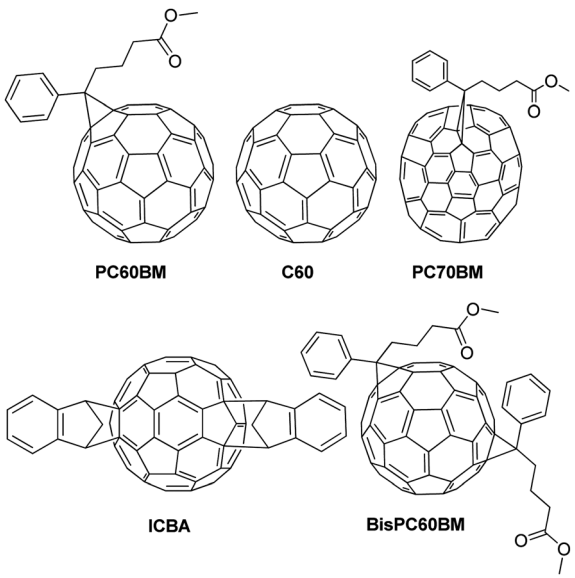

Fig. 2 Schematic illustrations of the studied electron acceptors.

‡ Corrected value in accordance with the article author.

A power meter was used to adjust the solar intensity to 1 kW m^{-2}. The light was not filtered and therefore a UV rich spectrum was obtained with a cut-off at 280 nm (Fig. S2†). All degradations were performed in a laboratory with humidity (20% relative humidity) and thermal control (23 °C room temperature) to ensure a constant degradation environment. The temperature during all degradation experiments of the samples was 32 °C. The ozone generated by the light bulb was removed with a fan, and the samples were thus exposed to the ozone concentration of the laboratory, which was slightly higher than outdoor ozone levels. A fully automated sample exchanger with a capacity of 24 different samples was employed to perform multiple degradations in parallel (Fig. 3A–C). The distance to the center was identical for all samples avoiding effects of spatial inhomogeneities of the illumination. An optical fiber-based CCD spectrometer (Avantes AvaSpec 1024 with a 400 μm quartz fiber) and a halogen/deuterium light source (Avantes AvaLight-DHc) were used to record the absorption spectra in a transmission geometry in the range of 300 to 900 nm at set intervals based on the approach described in ref. 23. By using collimating lenses adjusted normal to the sample, a parallel light probe was obtained by which a circular area of Ø 3 mm was probed. The flowchart in Fig. 3C shows the operation procedure of the degradation setup. During each run 22 samples were mounted in the sample exchanger and eight degradation points were measured on each sample and thus 176 parallel degradations were monitored in parallel to increase the statistic significance. After the recording of the absorbances, the samples were allowed to degrade for a customized interval with no rotation of the exchanger, typically 5 minutes.

Stability evaluation

The degradation rates were extracted from the decrease of the calculated *total number of absorbed photons* (N_{photon}) per second as absorbed by the polymer, when the recorded absorption spectrum is folded with a theoretical AM1.5G solar spectrum as described in ref. 24. 30–500 absorption spectra were recorded for each individual sample point. A strictly linear decrease of N_{photon} was observed for all polymers during the entire degradation. The slope of the decrease of N_{photon} over time allowed for the evaluation of the degradation rate. Only few percent of degradation allowed a precise estimation of the degradation rate due to the high density of recorded absorption spectra. A C# based automated software infrastructure was established to handle the high number of data files generated. This software showed the N_{photon} evolution for all 176 samples as well as the respective absorption spectra. If an erroneous absorption spectrum was recorded, this was clearly observed when processing the data and the data point could thus be dismissed. In total, this study presents in excess of 1000 degradations each including an average of 50 absorption measurements. Invalid data points have been filtered from the data where effects of particles, bad film coverage, inhomogeneous film thickness *etc.* clearly influenced the degradation rates. The reliability of the method is demonstrated by comparison of evaluated degradation rates for P3HT on the same sample, for different samples and different separate experiments, which are all found to strictly follow the same correlation (Fig. 3D).

When neglecting the significant time invested in setting up the apparatus and the time required for its validation, the total operator workload for all the degradation data reported here is

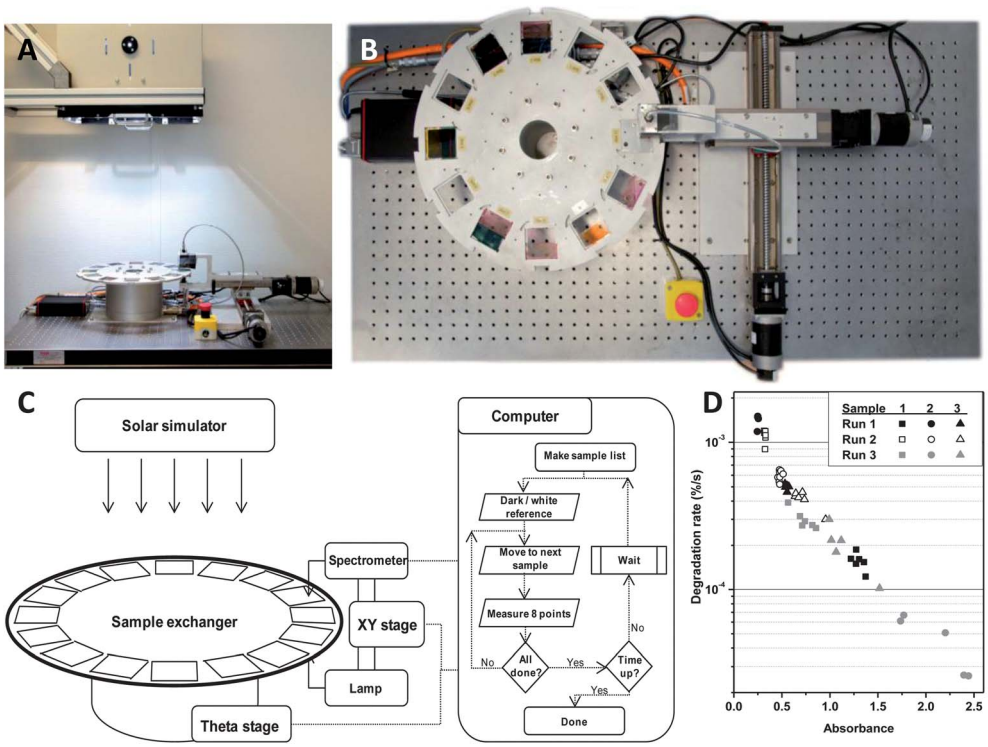

Fig. 3 (A) Side view of the degradation setup. (B) Top view of the sample exchanger. (C) Schematic illustration of the automated degradation setup. A flow chart describes the procedure for the degradations. (D) Absorbance resolved degradation rates for P3HT where data from different samples and different degradation experiments are shown.

estimated to be roughly 4 hours, while a manually operated setup was estimated to a workload of roughly 400 hours, clearly indicating the gain in operator efficiency. Additionally, the precision of the automated setup outperforms any manual handling since measurements are performed with higher frequency, non-interrupted illumination, and with a fixed geometry during the entire degradation as compared to the manual handling where samples are removed from the degradation setup and transported to and from the spectrometer. Finally, in terms of the reliability of the automated setup the timing of the data point acquisition is computer controlled (data are stored with millisecond accuracy), while manual handling involves an attentive operator keeping track of time, introducing a multitude of risks to the data acquisition. We firmly believe that comparative studies on this or larger scales mandatorily require a setup of the complexity described here to enable fast extraction of reliable data.

AFM thickness correlations

A Bruker Neos atomic force microscope (AFM) was used to establish correlations between layer thickness and material absorption for each of the studied materials and material combinations. A minimum of four samples covering a broad thickness range were spin coated. By scratching the sample with a scalpel, AFM measurements across the scratch allowed the determination of film thicknesses with an uncertainty of 5 nm. For all material combinations, linear correlations were found between the peak absorption of the polymer and the thickness. Simulations of the theoretical absorption of the film demonstrate that a linear correlation in the thickness range is indeed expected in accordance with the Lambert–Beers law. Fig. S3† shows an optical simulation in the range of 5 to 200 nm of both P3HT and P3HT:$PC_{60}BM$ demonstrating a clear linear correlation between the polymer peak absorption and the thickness for both the polymer and the blend validating the observed linear AFM correlations. The simulation was based on the refractive index as measured by spectroscopic ellipsometry (Sopra lab GES5E). The refractive index of the P3HT:$PC_{60}BM$ blend was obtained by combination of the refractive indices of the pure phases using an effective media approximation as described in ref. 25.

Results and discussion

Stability of conjugated polymers

In this study six different polymers have been studied (Fig. 1). These have been chosen to cover a wide range of chemical moieties and photochemical stability. Furthermore, all materials are known for their high performance or historical use in PSCs and are therefore highly relevant to the present research. In the discussion of the evaluation of photochemical stabilities of different materials, the basis for comparisons is important. Conventionally, the basis for comparison of different conjugated polymers has been the absorbance peak values in the UV-visible spectrum, where all samples in a comparative study have been adjusted to the same peak absorbance.[14] The absorbance is an easily measurable quantity and intrinsic to the spectroscopic degradation probe. Additionally, it can also be qualitatively estimated by visual inspection of the light attenuation by the film, simplifying sample preparation. Such an *absorbance basis* implies that for a material with low linear attenuation coefficient, a thicker film is needed to achieve the same absorption as for a high linear attenuation coefficient material. The light penetration depth depends on the linear attenuation coefficient, where a low linear attenuation coefficient implies a larger ratio of photons being absorbed deeper into the bulk of the material. To justify an absorbance basis for polymer comparisons, each photon absorbed by the material should thus contribute with equal degradation independent of whether the material is a high or low linear attenuation coefficient material. Since degradation of conjugated polymers in the ambient is governed by oxygen this ideally implies that the oxygen availability is effectively constant within the penetration depth of the light.

Degradation rates of the six polymers are presented in Fig. 4 and resolved in terms of their absorbance. The degradation rate of MEH-PPV is found to exceed the rest of the materials by two orders of magnitude, while the thermocleaved PT is highly stable (Fig. 4). This is in correspondence with the expected stability reported in the literature.[14,22] The absorbance resolved degradation rates additionally show a clear exponential decrease with absorbance for all studied polymers. The degradation rate of regio-regular P3HT is observed to vary from 10^{-3} to 5×10^{-5}% per second with increasing absorbance implying a relative variation of a factor of 20. This observation explains the above described variations of lifetimes of P3HT reported in the literature where degradation rates have been found to range by a factor of 10 for P3HT.[14,16] This clearly demonstrates the high importance of absorbance/film thickness in the discussion of photochemical stabilities of conjugated polymers.

The observed exponential decreases are believed to be an effect of the exponential decay of light into the film. Consequently, an increased degradation in the top layer is expected while the bottom part remains partly shielded. The degradation products in the form of small degradation products, oligomers, *etc.* were found to increase the absorbance in the range of 280–320 nm over the cause of the degradation. This layer may function as a physical barrier toward oxygen or other reactants. Additionally, many other factors come into play such as oxygen solubility, morphology, *etc.* and therefore no simple mechanism for the

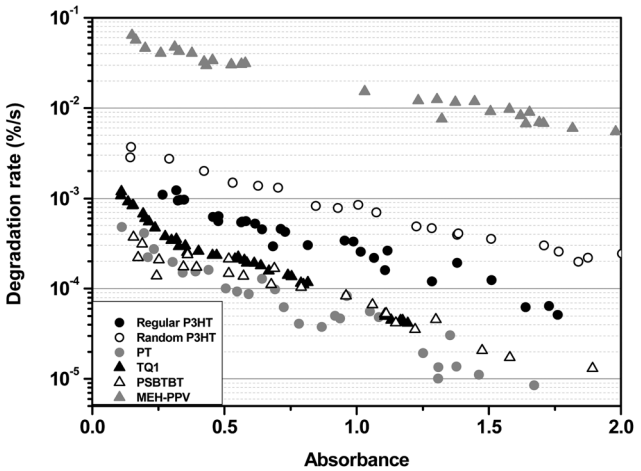

Fig. 4 Absorbance resolved degradation rates for six different polymers.

degradation can be established; see the section *Outlook and Perspectives* for a general discussion on this matter.

Utilizing the absorbance resolved degradation rates, all material stabilities can be evaluated in units of the degradation rates of regio-regular P3HT thus providing a relative stability with regio-regular P3HT as a reference. This unit is advantageously used as a measure of comparative photochemical stabilities of polymers since a reference is needed to compensate for the differences between different degradation setups and environmental factors. All correlations in Fig. 4 were fitted exponentially and their fits divided by the P3HT degradation rate fit to obtain relative stabilities (Fig. 5). Relative stabilities were only evaluated in the range where degradation rates for both the reference and the individual polymer were obtained. Even though not all ranges were covered due to processing difficulties, the strict exponential evolutions observed within the measured ranges are expected to continue if processing were possible. For an ideal basis of comparison for the degradation data, ideally constant relative stabilities for all materials would have been obtained. However, due to the above described assumptions for the absorption basis, constant relative stabilities are not expected. Relative stabilities for all polymers are found to vary within the absorbance range studied with the largest variations being observed for TQ1 where the relative stability increases from 2 to 6 with absorbance. Many parameters are expected to influence the thickness dependent stability of the materials. Specifically, P3HT is known as a highly crystalline material, which may affect the thickness dependence. This effect, in combination with the other issues discussed in the section *Outlook and Perspectives*, may explain the variations.

The slopes of the degradation rate–absorbance (thickness) correlations for the polymers as shown in Fig. 4 are observed to be similar in magnitude and thus the absorption basis seems to provide an acceptable presentation for comparisons of different polymers. The relative stabilities of PT and TQ1 are found to increase slowly with absorbance, while the remaining exhibit a slightly negative slope. This demonstrates that regio-regular P3HT has a degradation rate slope lying in the middle of the remaining polymers and thus serves as a good reference for all polymers. The six different polymers have highly different linear attenuation coefficients which may influence the degradation rate slopes. As a result, the film thicknesses for samples with absorbance of 0.6 attain highly different thicknesses as indicated in Table S2†. A PT film would only be 44 nm thick, while a TQ1 film would be 164 nm, as compared to regio-regular P3HT, which would be 101 nm. No pattern was found between the slopes of the relative stabilities and the linear attenuation coefficient and therefore the use of absorption as a basis seems to successfully allow for comparison of polymers with highly different linear attenuation coefficients.

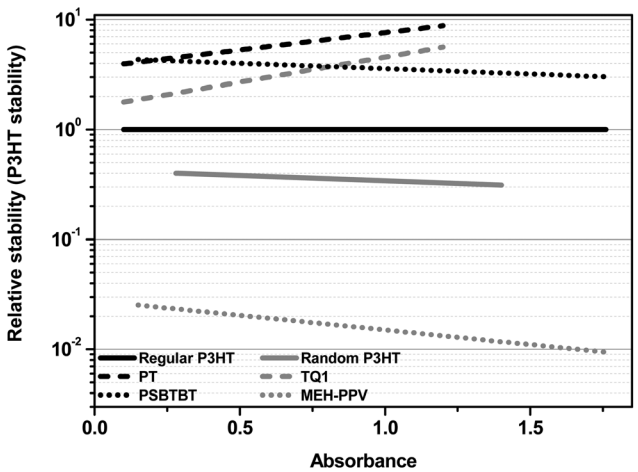

Fig. 5 Absorbance resolved stabilities in units of P3HT stability for the studied polymers.

Regio-Random P3HT was found to exhibit relative stabilities of 0.3–0.4 relative to regio-regular P3HT. This is in correspondence with earlier reports on the photochemical stability of regio-regular and regio-random P3HT stating a relative stability of 0.33 for films of 1.8 absorbance.[13] Likewise, photochemical stabilities of TQ1 at 0.2 absorbance[16] and MEH-PPV and PSBTBT at 0.6 absorbance[14] have been established in combination with regio-regular P3HT. These studies showed a relative TQ1 stability of 5, while we observe a relative stability of 2. MEH-PPV and PSBTBT were found to exhibit relative stabilities of 0.010 and 2 while, with our degradation setup, we observed stabilities of 0.019 and 4, respectively. The reason for these deviations could be one of the following: the degradations reported in the literature were performed with a UV filtered light spectrum by which light below 300 nm was removed. The UV responses of different polymers vary with the different functional groups and will thus introduce differences in relative stabilities. The temperature was kept at 85 °C in the earlier studies, which is known to increase degradation rates differently for different polymers.[15] Additionally, the strong decrease of degradation rates with absorbance has not been reported before and therefore this parameter may not have been given much attention. A small variation between the optical densities of two films being compared can lead to large deviations in the observed relative stabilities. Finally, the automated setup presented here is associated with higher precision of the degradation rates due to the large number of degradations carried out, while the degradation rates evaluated from a single sample are associated with significant uncertainty, which may introduce the observed differences. Generally, the absorbance (thickness) is a parameter which introduces large variations in degradation rates. Therefore this parameter must be given extensive attention for future comparative photochemical studies since large uncertainties can easily be introduced and conclusions may be made on a wrong basis. The precision to which the relative stability of a given polymer can be assessed based on a single thickness is found to be rather low due to the variation in relative stability. Only conservative estimations can be made with validity. It is recommended that conclusions on relative stabilities from a single thickness are not resolved in less than factors of five. More precise conclusions demand for degradations of several optical densities and preferably several independent degradation experiments for each optical density as presented in this work. Only then can a more precise conclusion on relative stabilities be made where the effect of absorbance (thickness) is taken into consideration.

An alternative basis for comparison of materials is the film thickness, which is less reported in the literature.[26] For a *thickness basis* to be sensible, the absorption in the bulk should not

introduce degradation. Two different materials with different linear attenuation coefficient would exhibit highly different absorbances if films of identical thicknesses were compared. Thus for this to represent a physically sound model, only the very top part of the material should degrade. This can be understood as the oxygen availability being very limited below the surface, where the bulk of the film will only suffer from negligible photolysis.[27] In this case initially the light only degrades the very top of the film, and gradually the degradation proceeds into the film as the upper parts photobleach.

As for the degradations presented above with an absorbance basis, an analogous analysis can be made by correlation with the material thickness. For each material, linear correlations between the peak absorption value and the film thickness as determined by AFM were established. The parameters for all thickness correlations are given in Table S2† and the individual thickness correlations in Fig. S4 and S5†. This allowed for a direct comparison of polymer degradation rates as a function of the respective film thicknesses (Fig. S6†). Since the thickness correlates linearly with the absorbances, the evolution of degradation rate with film thickness was found to be exponential as in the case of the absorbance basis. Analogous to the absorbance basis all degradation rate correlations were fitted and by division with the degradation rates of regio-regular P3HT, an expression of the relative stability for each polymer compared to regio-regular P3HT was obtained (Fig. 6).

The effect of changing the basis of comparison to a thickness basis changes both the horizontal and vertical positions of the lines. Generally, the variations in the relative stability evolutions are observed to vary to a higher degree than in the case of the absorbance basis, where *e.g.* an order of magnitude of variations is found for PSBTBT and PT. The theoretical absorbances as deduced by AFM thickness correlations for 100 nm films of each polymer show the large deviations in absorption (Table S2†). While regio-regular P3HT lies in the middle of the distribution with an absorbance of 0.59, a similar PT film would have an absorbance of 1.57 and PSBTBT only 0.31. PT and PSBTBT are the extremes in terms of linear attenuation coefficients and these deviations from the linear attenuation coefficient are obviously not handled well by the thickness basis of comparison, where relative stability of PT is found to increase highly with thickness, while the opposite is the case for PSBTBT. Thus it can be concluded that when comparing individual polymers, an absorption basis is considered the best basis of comparison since this allows for comparisons of materials of highly different linear attenuation coefficients.

Stability of electron acceptors

Stability of the single electron acceptors is expected be a function of the oxidation potential and therefore the HOMO level of the acceptor. A high HOMO level is more readily oxidized than a low level, and thus the high HOMO level acceptors are expected to exhibit lower photochemical stabilities. In this discussion the LUMO levels are not considered due to the negligible population relative to the HOMO levels. Photochemical stabilities of electron acceptors were studied in terms of the decrease of their peak absorption in the range of 300–350 nm (Fig. 7). While the solubility of C_{60} in common organic solvents is rather low, functionalization of the fullerene cage may highly increase the solubility.[28] Thus, all acceptors as shown in Fig. 2 were studied in terms of photochemical stability except for C_{60} due to solution processing complications. All acceptors exhibited exponential increases of degradation rates with decreasing absorbance as in the case of single polymers. The stabilities were found to vary by less than a factor of 3, which is significantly lower than the case of the polymers (Fig. 4). $PC_{60}BM$ and $PC_{70}BM$ were found to be approximately three times more stable than the high HOMO acceptors bisPCBM and ICBA, which is in correspondence with their respective HOMO levels.[29]

The electron acceptors were generally found to be more photochemically stable than the polymers, where $PC_{60}BM$ and $PC_{70}BM$ exhibited stabilities one order of magnitude higher than *e.g.* regio-regular P3HT.

Stability of P3HT:electron acceptor blends

The photochemical stability of blends of conjugated polymers and electron acceptors is a topic that has only been briefly discussed in the literature. Rivaton *et al.* evaluated the stabilities of

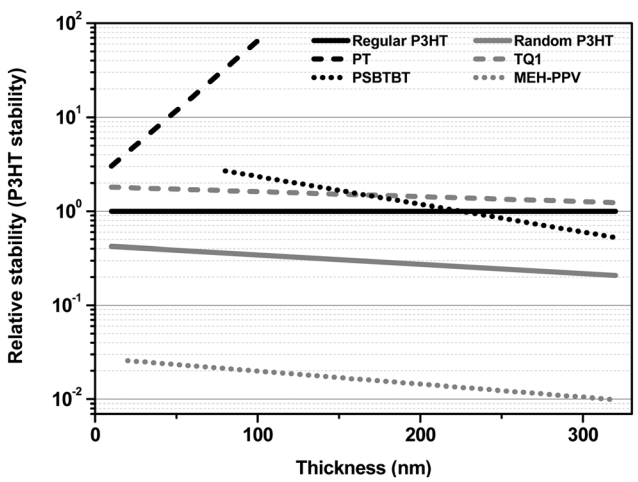

Fig. 6 Thickness resolved degradation rates for different polymers.

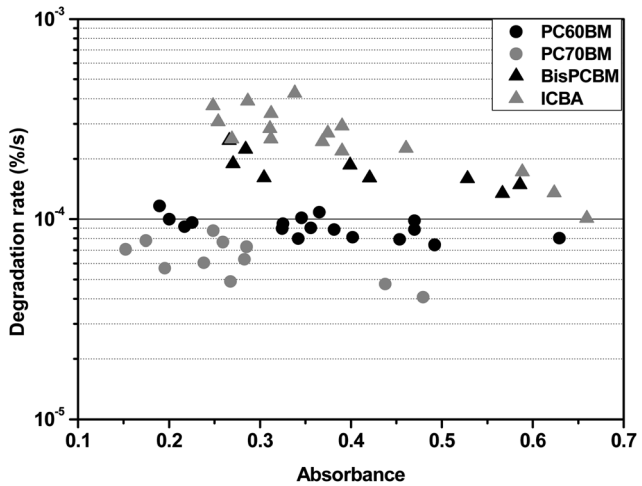

Fig. 7 Absorbance resolved degradation rates of electron acceptors.

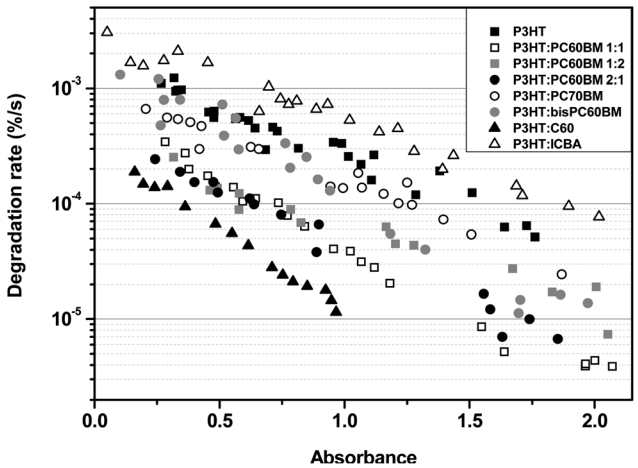

Fig. 8 Absorbance resolved degradation rates for pure regio-regular P3HT blended with different electron acceptors.

regio-regular P3HT and P3HT:$PC_{60}BM$ (1 : 1 ratio) with a thickness basis of comparison, where approximately 200 nm films were compared.[26] In this study a stabilization factor of 8 was found between the polymer and the blend. To make a more thorough comparison of electron acceptors, we have studied five different electron acceptors in conjunction with regio-regular P3HT as well as P3HT:$PC_{60}BM$ in 1 : 1, 1 : 2 and 2 : 1 ratios. Degradation rates were evaluated by integration of the P3HT part of the absorption spectrum (400–600 nm). Degradation of blends generally showed a rapid degradation of the polymer compared to the acceptor as reflected in the respective UV-vis absorption spectra, which is in correspondence with the higher stability of the latter as discussed above.

Degradation rates of all P3HT:electron acceptor combinations as well as pure P3HT compared with an absorbance basis demonstrate a behavior similar to the case for the single polymers and electron acceptors (Fig. 8). All blends show exponential decreases with absorbance (and rather similar slopes on a log scale). Interestingly, the degradation rates are observed to vary with an order of magnitude between the most unstable blend, P3HT:ICBA, and the most stable blend, P3HT:C_{60}. All curves were exponentially fitted and divided by the pure P3HT degradation rate fit to obtain the stabilization of P3HT by incorporation of an electron acceptor (Fig. 9). All relative stability curves were found to increase slightly with absorbance. The reason for this is the steeper slope of the degradation rate correlation with absorbance for P3HT than for the blends. The largest variation in relative stability was observed for P3HT:$PC_{60}BM$ (1 : 1 ratio) where the value increased from 3 to 10 with increasing absorbance. A thickness basis was also applied to the degradation rates (Fig. S7†) and by division of the P3HT degradation rates, the relative stabilities from a thickness basis were evaluated (Fig. S8†). Due to the higher linear attenuation coefficient at the peak absorbance for pure P3HT (approximately 530 nm) when compared to the blends, absorption and thickness bases are expected to provide highly different results. Indeed this is the case for the relative stabilities for the thickness basis, where all relative stabilities are found to decrease with thickness. Generally, larger fluctuations are observed when applying the thickness basis than in the case of the absorbance basis, where *e.g.* for the different blend ratios of P3HT:$PC_{60}BM$ the 2 : 1 ratio displays a significantly higher stability than the 1 : 1 and 1 : 2 ratios, which is counterintuitive. Based on these conclusions, the more suitable basis of comparison of a pure polymer and its respective blends with different electron acceptors is an absorbance basis.

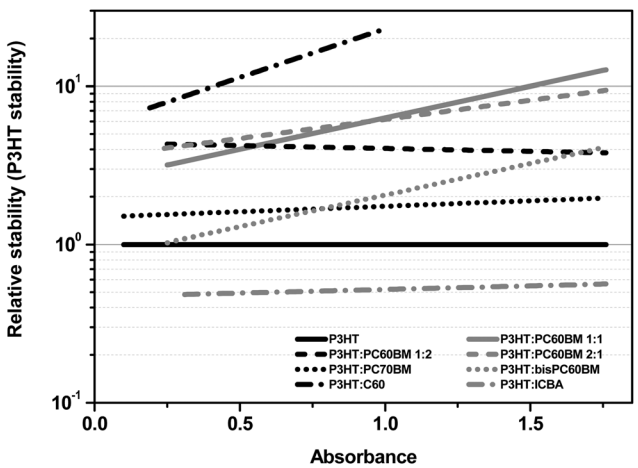

Fig. 9 Absorbance resolved relative stabilities for blends consisting of P3HT and different electrons.

The photochemical stabilities of blends based on a conjugated polymer and different electron acceptors have not been reported in the literature. Nevertheless, significant variations in relative stabilities are observed for the different electron acceptors with C_{60} stabilizing by a factor of approximately 10 while ICBA is observed to destabilize the blend by a factor of 2. The stabilization correlations for the $PC_{60}BM$ blends of different ratios are observed to exhibit intersections in the absorbance range of 0.35–0.8 within which they all exhibit highly similar stabilizations. This is in accordance to expectations, since these blends consist of a highly intimate mixing of the donor and acceptor and therefore no significant variations in acceptor stabilization are expected. However, at higher absorbances, the 1 : 2 blend is less stable, which is counterintuitive since the higher content of $PC_{60}BM$ is expected to induce a higher photochemical stability. Consequently, it appears that sound conclusions on stabilization by electron acceptors should be based on the lower absorbance range (below 0.8). An additional argument for using an absorption basis for the lower absorbance range is that photoactive materials for solar cells are intended to be applied as films that are sufficiently thick to absorb the greater proportion of the incoming light while being sufficiently thin to enable extraction of carriers. For most active layers this equates to film absorptions in this range.

The relative stabilities of the different P3HT:acceptor blends demonstrate the same stability ranking as observed for the pure electron acceptors, however with higher variations. An unstable high HOMO acceptor that degrades significantly within the lifetime of the polymer will decrease the efficiency of the charge transfer of the excited state from the polymer to the acceptor for a given donor–acceptor blend. However, due to the generally higher stabilities of the electron acceptors compared to regio-regular P3HT, this effect is not pronounced. Another effect introduced is the charge transfer efficiency for the different

donor–acceptor blends. It is generally accepted that the excited state of P3HT is efficiently quenched by fullerenes and its derivatives through a charge transfer from the P3HT to the photochemically stable fullerene.[30,31] Extensive attention is directed at developing electron acceptors with lower donor–acceptor LUMO–LUMO gap than for the commonly used $PC_{60}BM$ to increase the open circuit voltage (V_{oc}) of PSC.[32–34] However, the impact of such a decrease in the electron affinity of the acceptor ultimately implies different charge transfer kinetics between the donor and the acceptor. With a higher LUMO level of the acceptor the statistical distribution between excited states on the donor and the acceptor is moved in the direction of the donor. As excited states are prone to photodegradation, the overall effect is a decreased photochemical stability. In the literature there are no reports on the LUMO levels of all the electron acceptors studied in this work. By direct comparison between LUMO levels of the individual electron acceptors, large variations are found, which originate from different cyclic voltammetry setups. An indirect approach to assessment of the LUMO levels is by inspection of the V_{oc} obtained for optimized PSCs applying P3HT and the different electron acceptors.[32] The typical V_{oc} values for regio-regular P3HT and different electron acceptors are (C_{60}) 0.40 V,[35] ($PC_{70}BM$) 0.63 V,[36] ($PC_{60}BM$) 0.65 V,[37] (bisPCBM) 0.73 V,[33] and (ICBA) 0.87.[38] The ranking of the V_{oc} was found to be consistent with individual studies of LUMO levels of typically $PC_{60}BM$ and another fullerene derivative.[33,39,40]

The magnitude of the stabilization of P3HT by the electron acceptor is observed to correlate clearly with the LUMO–LUMO gap in the low absorbance range. A ranking of decreasing stabilization of C_{60}, $PC_{60}BM$, $PC_{70}BM$, bisPCBM, and ICBA is found, which is in clear correspondence with a decreasing LUMO–LUMO gap or increasing V_{oc} of the corresponding PSCs. Only $PC_{60}BM$ and $PC_{70}BM$ do not clearly fulfil this principle since their LUMO–LUMO levels are similar. However, stability of pure $PC_{70}BM$ was found to slightly exceed the one of $PC_{60}BM$, which may explain the deviation from the LUMO–LUMO gap correlation. Additionally, other factors such as morphology and phase segregation may play a role; see the section *Outlook & Perspectives* for further discussion. Overall, this result demonstrates the increasing thermodynamic tendency of increasing the population of excited states on the P3HT relative to the acceptor, thus implying a higher degradation rate. For this reason, the application of ICBA in PSCs to obtain 6.5% efficiency[38] introduces a significant decrease in photochemical stability that in turn will affect the operational device lifetime.

Stability of polymer:$PC_{60}BM$ blends

For each of the studied polymers, their respective blends in a ratio of 1 : 1 with $PC_{60}BM$ were studied. Degradation rates of the decrease of the respective polymer contribution to the UV-visible absorption were evaluated as a function of peak absorbance of the polymer transition (Fig. S9†) and thickness (Fig. S10†). No major differences are observed between the absorbance and the thickness plots, where primarily PT:$PC_{60}BM$ is shifted due to the higher optical density, however to a lesser extent than in the case of the pure polymers due to the $PC_{60}BM$ content. To evaluate the relative stabilities, P3HT:$PC_{60}BM$ is applied as the reference to which remaining blends are compared. The shift of the optically dense PT introduces a difference in relative stability from around 4 with an absorbance basis (Fig. 10) to around 8 with a thickness basis (Fig. S11†), while the low linear attenuation coefficient of blend PSBTBT:$PC_{60}BM$ changes from 3 to 2. This demonstrates the sensitivity of the method toward the basis of comparison where two polymers of similar stability are found to exhibit highly different blend stabilities with the two bases of comparison.

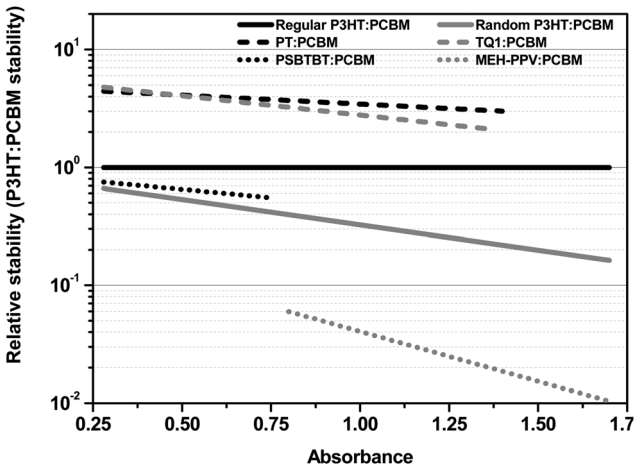

Fig. 10 Absorbance resolved stabilities in units of P3HT:$PC_{60}BM$ stability of blends based on different polymers and $PC_{60}BM$.

The best consistency between the observed polymer and blend relative stabilities is found for the absorbance basis. Additionally, less variation with absorbance/thickness is observed, and thus an absorbance basis is regarded the best basis of comparison for different blends. The relative stabilities of the blends were found to be similar to the case of the single polymers. However PSBTBT demonstrates a deviating behavior, where the material is observed to destabilize by the introduction of $PC_{60}BM$, which is in contradiction to all the other studied polymers. This effect may be attributed to microscopic properties such as morphology,

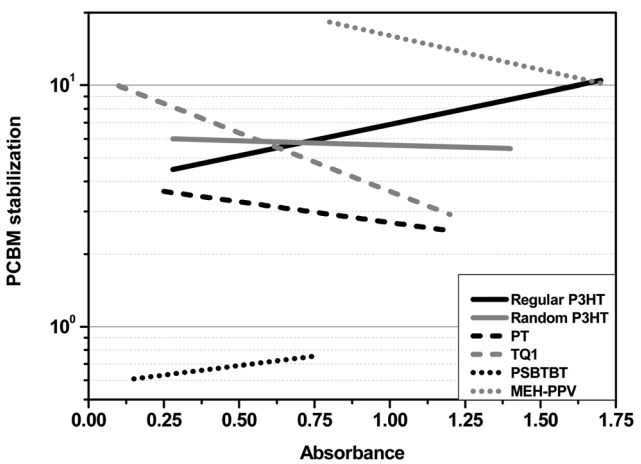

Fig. 11 Absorbance resolved photochemical stabilization of different polymers by introduction of $PC_{60}BM$.

phase segregation, *etc.*, as discussed in the section *Outlook and Perspectives*.

Absorbance resolved $PC_{60}BM$ stabilization of the different polymers was evaluated as the ratio between the degradation rate of the blend and the single polymers (Fig. 11). Fluctuations in the stabilization curves of both positive and negative slopes are observed and both TQ1, regio-regular and regio-random P3HT are observed to intersect around an absorbance of 0.75. However, these results are based on a combination of degradation rates of the single polymers and their respective blends, both of which are affected by uncertainties in the method, and thus their quotient is expected to be further impacted. The general expectation is that a highly unstable material should benefit highly from being blended with $PC_{60}BM$, since each excitation has a large possibility of leading to a degradation event, while for a highly stable material this effect is less pronounced. This is indeed the tendency observed, where the unstable MEH-PPV is highly stabilized by a factor of around 15, while the stable PT is only stabilized by a factor 3. Additionally, PSBTBT is found to destabilize slightly by a factor of 0.3. A destabilization is expected if the polymer is comparable or more photochemically stable than the electron acceptor. This is the case for PSBTBT, where for absorbances above 1, the polymer stability even exceeds the stability of $PC_{60}BM$. For this material combination a charge transfer to $PC_{60}BM$ will induce a larger degradation rate than by keeping the excited electron on the pure polymer. This demonstrates how the photochemical advantage well-known for *e.g.* regio-regular P3HT of blending with $PC_{60}BM$ is found to decrease with more stable polymers, where even destabilizations are introduced.

Outlook and perspectives

This work presents a systematic study of the influence of absorbance and electron acceptor on the photochemical stability of conjugated polymers. It was shown that the relative stabilities of different polymers could only be qualitatively assessed from single thicknesses, since they were found to vary with absorbance. However, attention in the processing was not given to obtain *e.g.* identical morphology, phase segregation, and crystallinity, which are parameters that are expected to influence stability. Photochemical stability testing of polymers appears as a general tool robust enough to establish a stability ranking of the different materials without a specific focus on the control of these parameters. However, in order to understand the mechanisms behind the observed behavior and the variations in relative stabilities with absorbance, detailed studies of several parameters are needed. Parameters that are prone to influence photochemical degradation rates are *e.g.*:

- Morphology
- Kinetics
- Reactant solubility
- Vertical segregation
- Exciton diffusion length

The stability is expected to change as a function of the morphology for both the pure polymers as well as for the blends as a function of solvent, processing method, temperature, humidity, *etc.* Additionally, the impact of these parameters is expected to vary with the material type thus making up a large parameter space. The solubility of the degradation reactant (typically oxygen) and the kinetics of the diffusion of oxygen differ for each material thus influencing the degradation rates for different film thicknesses. Additionally, vertical segregation of P3HT:$PC_{60}BM$ has been observed to vary highly with the processing method and substrate. Finally, the exciton diffusion length may vary for different material systems, which influences the dependence of domain size on photochemical stability. Consequently, obtaining an understanding of the underlying mechanisms demands for further work on *e.g.* regio-regular P3HT where the impact of these above mentioned parameters are studied. Additionally, in order to obtain a higher precision of the relative stabilities of different polymers by photochemical stability testing, a more thorough study of each material and the above described parameters is needed. By this, better estimations of the actual material stabilities can be given thus increasing the precision of the technique.

Conclusions

A novel photochemical stability assessment platform was presented by which degradation of organic materials can be evaluated with high precision. In this work, the technique has been applied to stability studies of electron donors and acceptors relevant to PSC. Photochemical stabilities of six different polymers and 5 different electron acceptors demonstrated a strong increase of degradation rates with film absorbances. This is important for comparative studies where the absorbance has to be kept constant for all materials being studied to provide a basis for valid conclusions on relative stabilities. The validity of estimating a material stability based on a single measurement at a single absorbance is considered doubtful. We believe that only by studying a wide absorbance range for all studied samples can a sound estimation of relative stabilities be obtained. The precision of this estimation was also found to depend on the basis of comparison, where an absorbance basis was considered the best choice for all studied material combinations. Since this model is a simplified version of the real world, uncertainties are introduced into the stability evaluation. Consequently, our conclusion is that only sound relative stabilities are given in no less than factors of five if only a single degradation of each material has been performed. However, with these precautions in mind, photochemical degradation as a stability evaluation tool is found to be a powerful tool to obtain estimates of relative stabilities of conjugated polymers, electron acceptors, and blends relevant to PSCs.

Acknowledgements

This work was supported by the Danish Strategic Research Council (2104-07-0022), EUDP (j. no. 64009-0050) and PV-ERA-NET (project acronym POLYSTAR).

References

1 M. Helgesen, R. Søndergaard and F. C. Krebs, Advanced materials and processes for polymer solar cell devices, *J. Mater. Chem.*, 2010, **20**, 36.
2 G. Dennler, M. C. Scharber and C. J. Brabec, Polymer–fullerene bulk-heterojunction solar cells, *Adv. Mater.*, 2009, **21**, 1323–1338.

3 F. C. Krebs, T. Tromholt and M. Jørgensen, Upscaling of polymer solar cell fabrication using full roll-to-roll processing, *Nanoscale*, 2010, **2**, 873–886.
4 R. F. Service, Outlook brightens for plastic solar cells, *Science News & Analysis*, 2011, **332**, 293.
5 M. Jørgensen, K. Norrman and F. C. Krebs, Stability/degradation of polymer solar cells, *Sol. Energy Mater. Sol. Cells*, 2008, **92**, 686–714.
6 S. Beaupré, P.-L. T. Boudreault and M. Leclerc, Solar-energy production and energy-efficient lighting: photovoltaic devices and white-light-emitting diodes using poly(2,7-fluorene), poly(2,7-carbazole), and poly(2,7-dibenzosilole) derivatives, *Adv. Mater.*, 2010, **22**, E6–E27.
7 P. A. Troshin, *et al.*, Impedance measurements as a simple tool to control the quality of conjugated polymers designed for photovoltaic applications, *Adv. Funct. Mater.*, 2010, **20**, 4351–4357.
8 K. Norrman, M. V. Madsen, S. A. Gevorgyan and F. C. Krebs, Degradation patterns in water and oxygen of an inverted polymer solar cell, *J. Am. Chem. Soc.*, 2010, **132**, 16883–16892.
9 E. Vitoratos, *et al.*, Thermal degradation mechanisms of PEDOT:PSS, *Org. Electron.*, 2009, **10**, 61–66.
10 T. Tromholt, A. Manor, E. A. Katz and F. C. Krebs, Reversible degradation of inverted organic solar cells by concentrated sunlight, *Nanotechnology*, 2011, **22**, 225401.
11 S. Bertho, *et al.*, Effect of temperature on the morphological and photovoltaic stability of bulk heterojunction polymer:fullerene solar cells, *Sol. Energy Mater. Sol. Cells*, 2008, **92**, 753–760.
12 P. J. Goutam, D. K. Singh, P. K. Giri and P. K. Iyer, Enhancing the photostability of poly(3-hexylthiophene) by preparing composites with multiwalled carbon nanotubes, *J. Phys. Chem. B*, 2011, **115**, 919–924.
13 H. Hintz, *et al.*, Photodegradation of P3HT—a systematic study of environmental factors, *Chem. Mater.*, 2010, **23**, 145–154.
14 M. Manceau, *et al.*, Photochemical stability of π-conjugated polymers for polymer solar cells: a rule of thumb, *J. Mater. Chem.*, 2011, **21**, 4132–4141.
15 S. Schuller, P. Schilinsky, J. Hauch and C. J. Brabec, Determination of the degradation constant of bulk heterojunction solar cells by accelerated lifetime measurements, *Appl. Phys. A: Mater. Sci. Process.*, 2004, **79**, 37–40.
16 J. E. Carlé, *et al.*, Fused thiophene/quinoxaline low band gap polymers for photovoltaic's with increased photochemical stability, *Sol. Energy Mater. Sol. Cells*, 2011, **95**, 3222–3226.
17 E. Wang, *et al.*, An easily synthesized blue polymer for high-performance polymer solar cells, *Adv. Mater.*, 2010, **22**, 5240–5244.
18 *Polymer Photovoltaics—A Practical Approach*, Ed. F. C. Krebs, SPIE, Bellingham, 2008.
19 J. Hou, H.-Y. Chen, S. Zhang, G. Li and Y. Yang, Synthesis, characterization, and photovoltaic properties of a low band gap polymer based on silole-containing polythiophenes and 2,1,3-benzothiadiazole, *J. Am. Chem. Soc.*, 2008, **130**, 16144–16145.
20 M. Bjerring, J. S. Nielsen, N. C. Nielsen and F. C. Krebs, Polythiophene by solution processing, *Macromolecules*, 2007, **40**, 6012–6013.
21 T. Tromholt, S. A. Gevorgyan, M. Jørgensen, F. C. Krebs and K. O. Sylvester-Hvid, Thermocleavable materials for polymer solar cells with high open circuit voltage-a comparative study, *ACS Appl. Mater. Interfaces*, 2009, **1**, 2768–2777.
22 M. Manceau, M. Helgesen and F. C. Krebs, Thermo-cleavable polymers: materials with enhanced photochemical stability, *Polym. Degrad. Stab.*, 2010, **95**, 2666–2669.
23 K. O. Sylvester-Hvid, *et al.*, Non-destructive lateral mapping of the thickness of the photoactive layer in polymer based solar cells, *Prog. Photovoltaics*, 2011, DOI: 10.1002/pip.1190.
24 T. Tromholt, M. Manceau, M. Helgesen, J. E. Carlé and F. C. Krebs, Degradation of semiconducting polymers by concentrated sunlight, *Sol. Energy Mater. Sol. Cells*, 2010, **95**, 1308–1314.
25 M. V. Madsen, *et al.*, Ellipsometry as a nondestructive depth profiling tool for roll-to-roll manufactured flexible solar cells, *J. Phys. Chem. C*, 2011, **115**, 10817–10822.
26 A. Rivaton, *et al.*, Light-induced degradation of the active layer of polymer-based solar cells, *Polym. Degrad. Stab.*, 2010, **95**, 278–284.
27 M. Manceau, *et al.*, Effects of long-term UV-visible light irradiation in the absence of oxygen on P3HT and P3HT:PCBM blend, *Sol. Energy Mater. Sol. Cells*, 2010, **94**, 1572–1577.
28 P. A. Troshin, *et al.*, Material solubility-photovoltaic performance relationship in the design of novel fullerene derivatives for bulk heterojunction solar cells, *Adv. Funct. Mater.*, 2009, **19**, 779–788.
29 Y. He, G. Zhao, B. Peng and Y. Li, High-yield synthesis and electrochemical and photovoltaic properties of Indene-C70 bisadduct, *Adv. Funct. Mater.*, 2010, **20**, 3383–3389.
30 M. O. Reese, *et al.*, Photoinduced degradation of polymer and polymer–fullerene active layers: experiment and theory, *Adv. Funct. Mater.*, 2010, **20**, 3476–3483.
31 J. Piris, *et al.*, Photogeneration and ultrafast dynamics of excitons and charges in P3HT/PCBM blends, *J. Phys. Chem. C*, 2009, **113**, 14500–14506.
32 F. B. Kooistra, *et al.*, Increasing the open circuit voltage of bulk-heterojunction solar cells by raising the LUMO level of the acceptor, *Org. Lett.*, 2007, **9**, 551–554.
33 M. Lenes, *et al.*, Fullerene bisadducts for enhanced open-circuit voltages and efficiencies in polymer solar cells, *Adv. Mater.*, 2008, **20**, 2116–2119.
34 Y. He and Y. Li, Fullerene derivative acceptors for high performance polymer solar cells, *Phys. Chem. Chem. Phys.*, 2011, **13**, 1970–1983.
35 I. R. Gearba, C.-Y. Nam, R. Pindak and C. T. Black, Thermal crosslinking of organic semiconducting polythiophene improves transverse hole conductivity, *Appl. Phys. Lett.*, 2009, **95**, 173307.
36 J. Y. Kim, *et al.*, Efficient tandem polymer solar cells fabricated by all-solution processing, *Science*, 2007, **317**, 222–225.
37 M. Reyes-Reyes, K. Kim and D. L. Carroll, High-efficiency photovoltaic devices based on annealed poly(3-hexylthiophene) and 1-(3-methoxycarbonyl)-propyl-1-phenyl-(6,6)C[61] blends, *Appl. Phys. Lett.*, 2005, **87**, 083506.
38 G. Zhao, Y. He and Y. Li, 6.5% Efficiency of polymer solar cells based on poly(3-hexylthiophene) and indene-C(60) bisadduct by device optimization, *Adv. Mater.*, 2010, **22**, 4355–4358.
39 Z.-L. Guan, J. Bok Kim, Y.-L. Loo and A. Kahn, Electronic structure of the poly(3-hexylthiophene):indene-C60 bisadduct bulk heterojunction, *J. Appl. Phys.*, 2011, **110**, 043719.
40 D. Mühlbacher, *et al.*, High photovoltaic performance of a low-bandgap polymer, *Adv. Mater.*, 2006, **18**, 2884–2889.

Supplementary information for

Photochemical stability of conjugated polymers, electron acceptors and blends for polymer solar cells resolved in terms of film thickness and absorbance

Thomas Tromholt*, Morten Vesterager Madsen, Jon E. Carlé, Martin Helgesen, Frederik C. Krebs

Risø National Laboratory for Sustainable Energy, Technical University of Denmark, Frederiksborgvej 399, DK-4000 Roskilde, Denmark

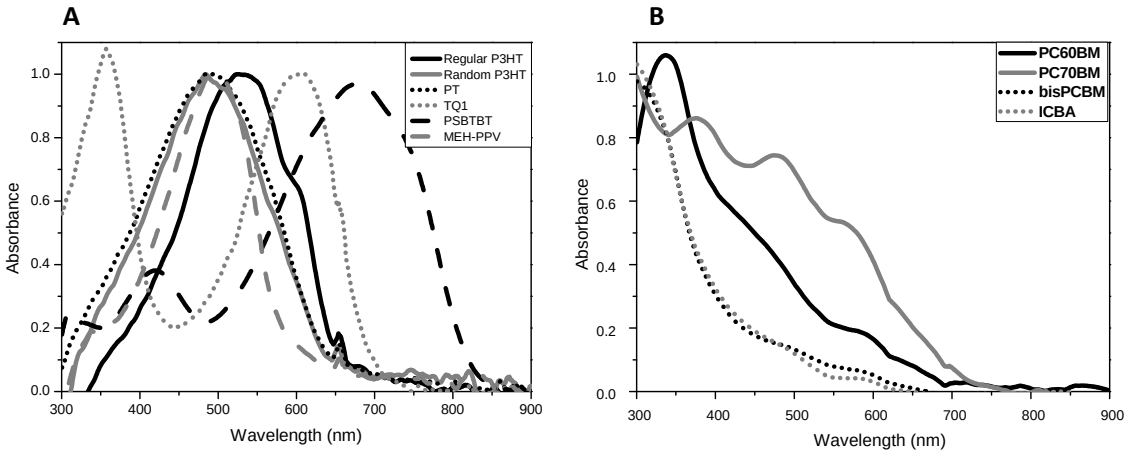

Figure S1: UV-vis absorption spectra of (A) the studied polymers and (B) the studied electron acceptors

Polymer	Molecular weight Mn	Reference
Regio-regular P3HT	50000	Rieke Metals
Regio-random P3HT	40000	[1]
PT	11300	[2]
TQ1	21000	[3]
PSBTBT	10000	[4]
MEH-PPV	45600	[5]

Table S1: Molecular weights of the polymers studied. Reference [1-5] describe synthesis and molecular weight of all polymers.

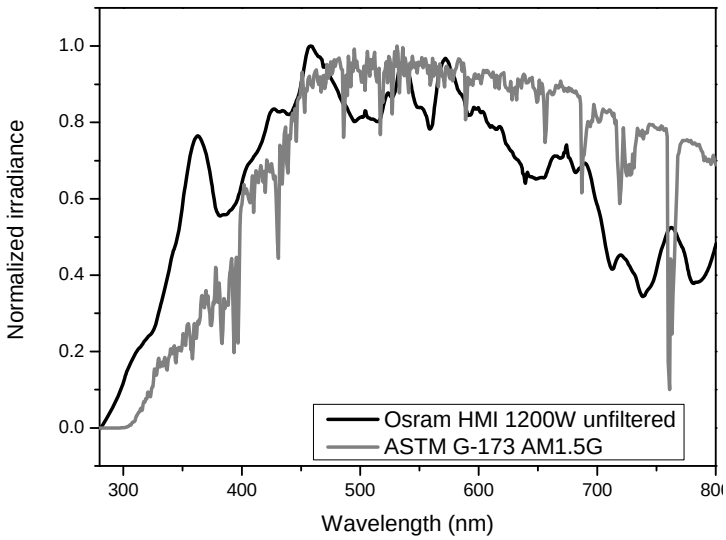

Figure S2: Irradiance of the 1200 W HMI lamp from Osram and the ASTM G-173 AM1.5 reference solar spectrum.

Material	A value in y = ax+b	B value in y=ax+b	Abs for 100 nm	Thickness for 0.6 Abs
Pure polymers				
Regio-regular P3HT	185.3	-9.8	0.59	101
Regio-random P3HT	188.9	2.2	0.52	116
PT	57.7	9.6	1.57	44
MEH-PPV	180.8	-8.3	0.60	100
TQ1	301.8	-17.4	0.39	164
PSBTBT	232.8	27.6	0.31	167
Regio-regular P3HT:Acceptor				
P3HT:PC60BM 1:1	372.9	-7.4	0.29	216
P3HT:PC60BM 1:2	469.2	-24.6	0.27	257
P3HT:PC60BM 2:1				0
P3HT:PC70BM	263.8	35.9	0.24	194
P3HT:C60				0
P3HT:bisPC60BM	306.6	24.0	0.25	208
P3HT:ICBA	310.4	17.5	0.27	204
Blends				
Regio-random P3HT:PC60B	378.6	-11.0	0.29	216
TQ1:PC60BM	443.8	5.3	0.21	272
PT:PC60BM	252.0	-20.6	0.48	131
PSBTBT:PC60BM	430.5	12.8	0.20	271
MEH-PPV:PC60BM	334.1	-22.9	0.37	178

Table S2: Fitting constant for correlations between absorption peaks and film thicknesses as determined by AFM measurements

Appendix 1.2

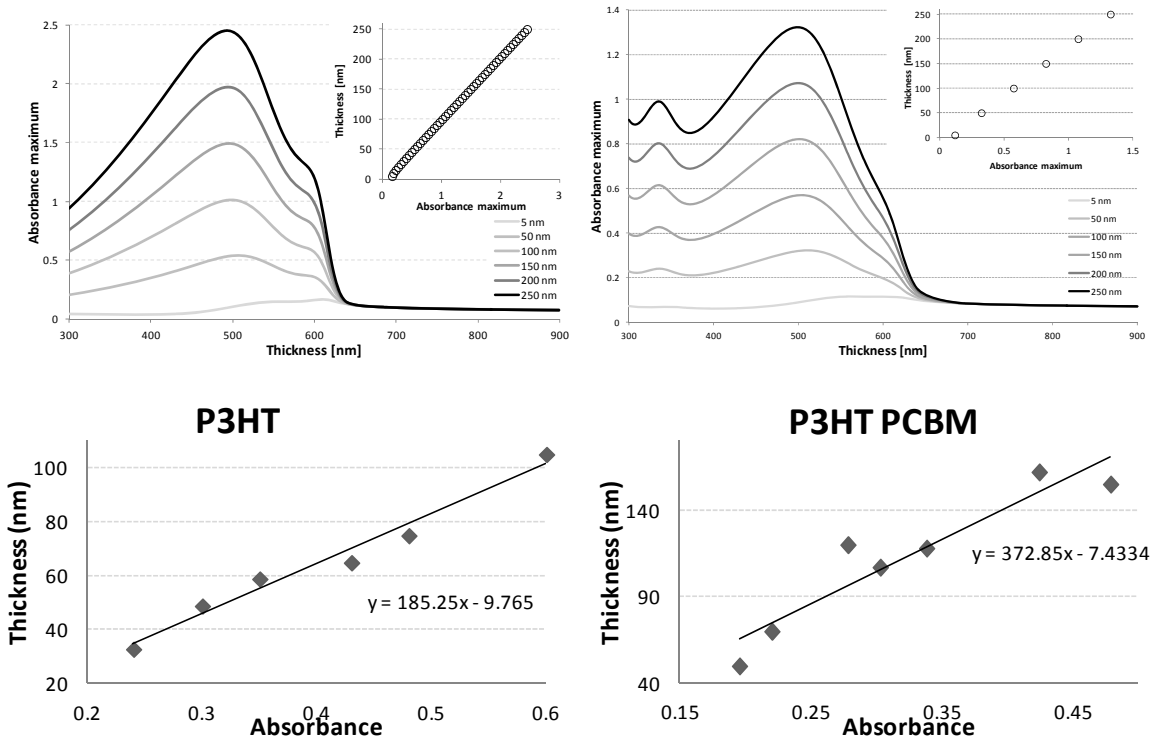

Figure S3: Simulated absorption spectra of (Top left) regio-regular P3HT and (Top right) regio-regular P3HT:PCBM of varying thickness. The insets show the linear relations between absorption maximum and thickness for both the polymer and the blend. (Bottom) The measured AFM thickness / absorbance relations for P3HT and P3HT:PCBM.

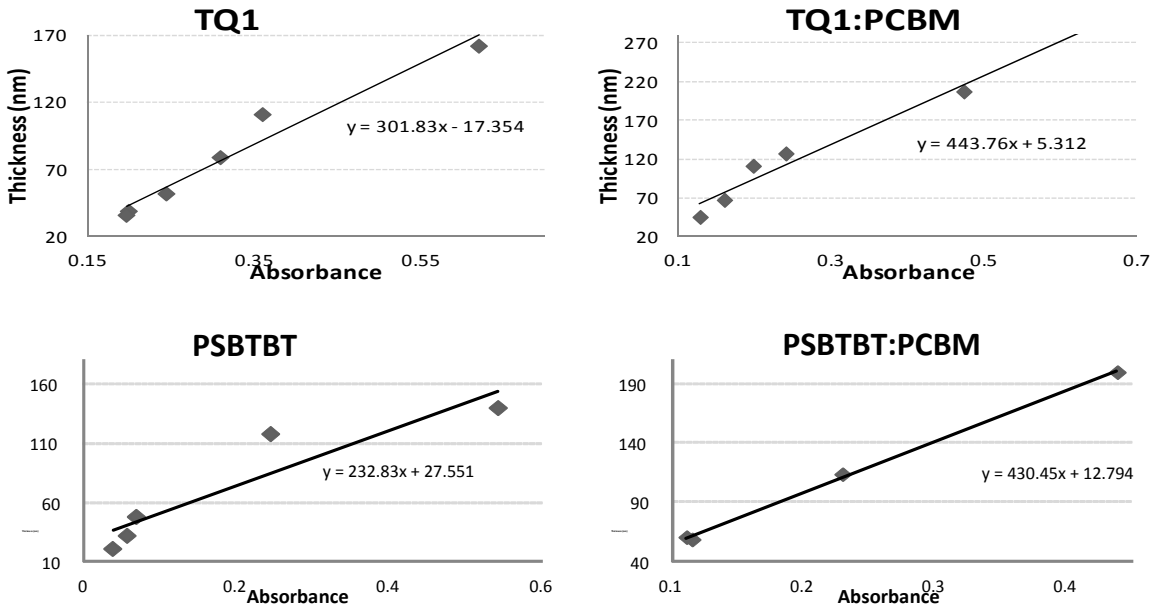

Appendix 1.2

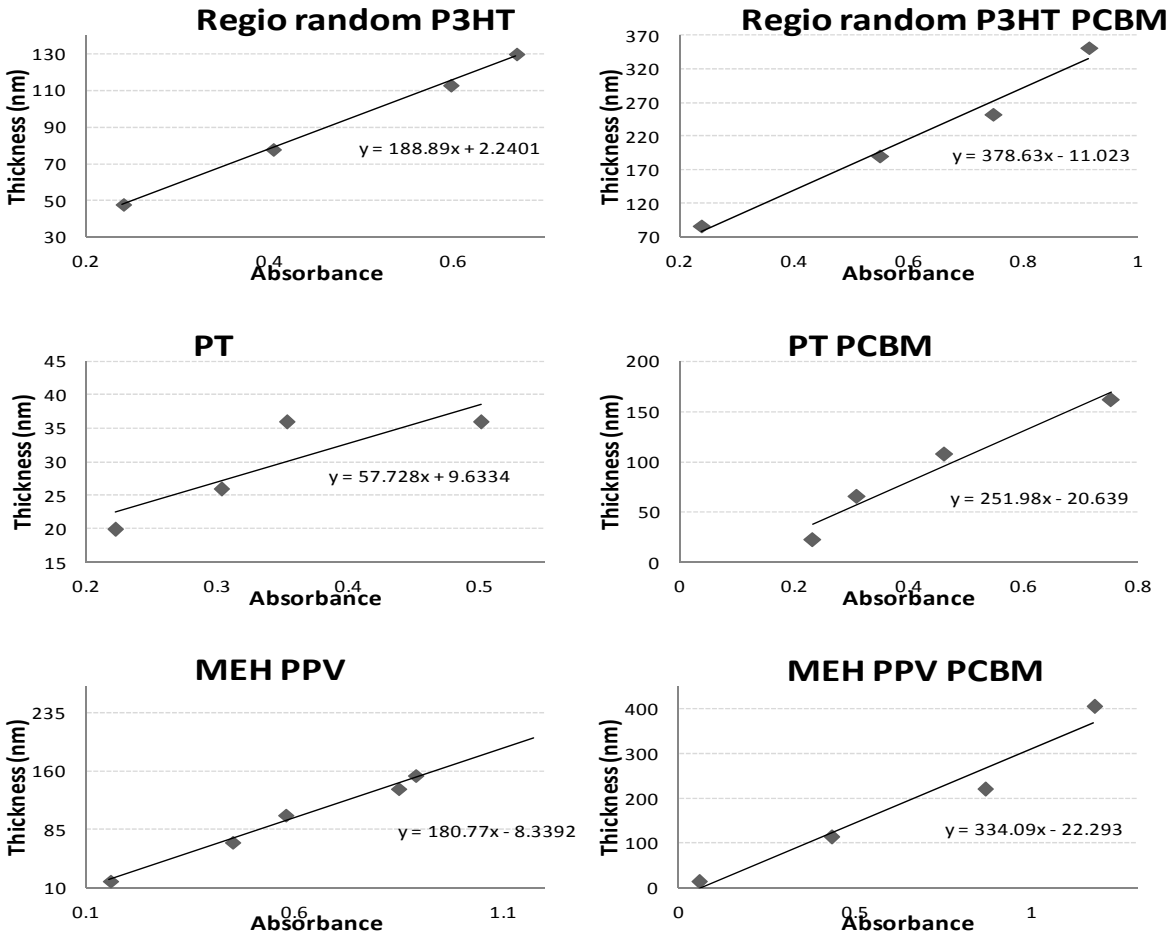

Figure S4: AFM thickness / absorbance relations for the different polymers on the left column and polymers blended with PCBM 1:1 in the right column.

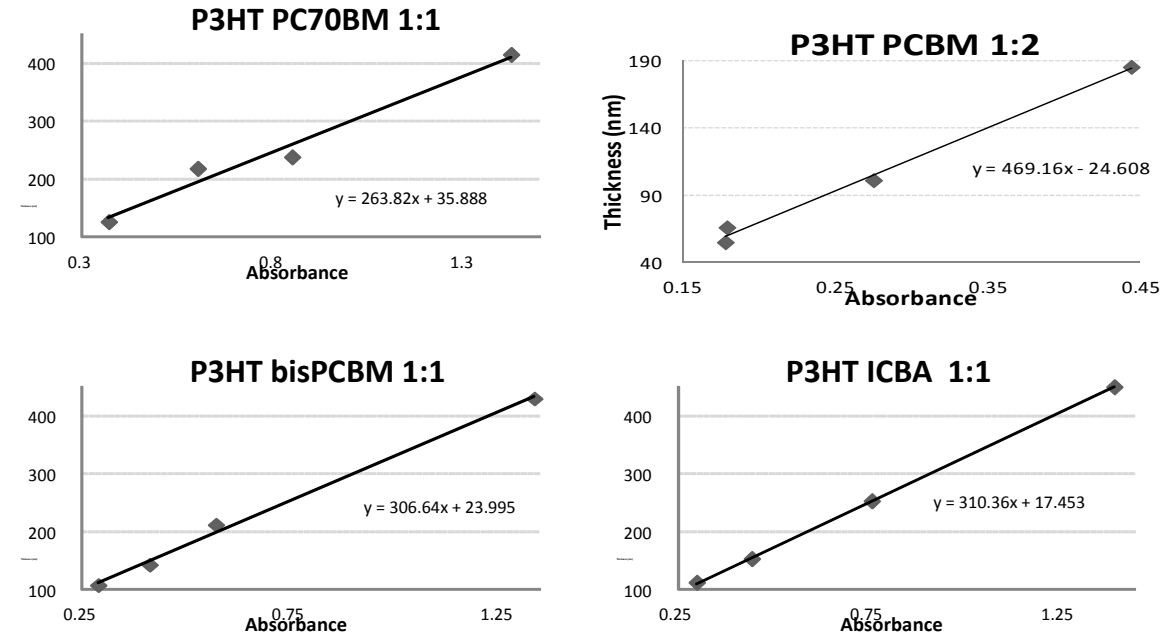

Appendix 1.2

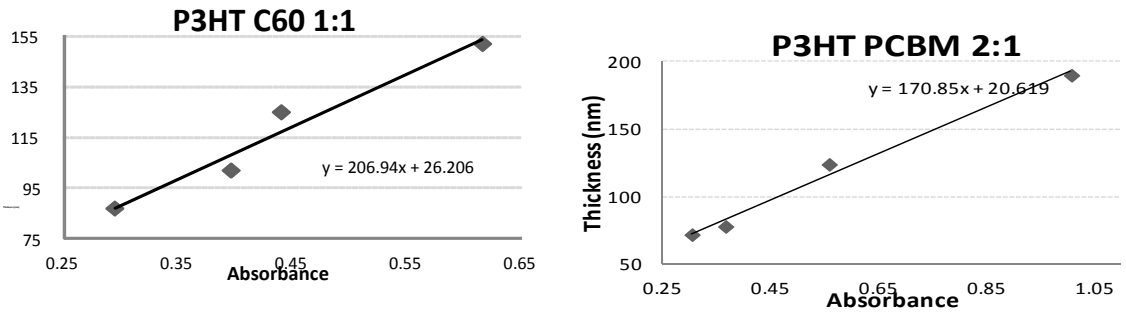

Figure S5: AFM thickness / absorbance relations for the different acceptors blended with P3HT. The ratio is 1:1 for all except for P3HT PCBM 1:2 and P3HT PCBM 2:1.

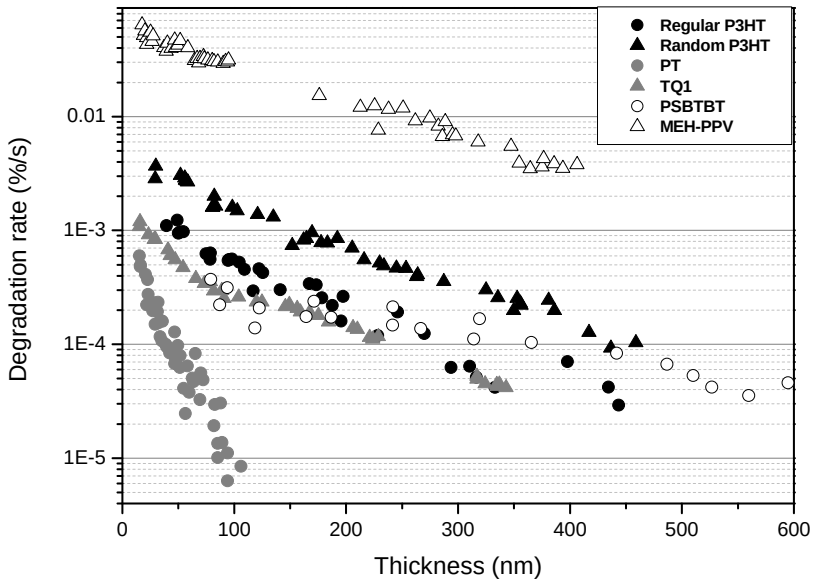

Figure S6: Degradation rates as a function of film thickness for different polymers.

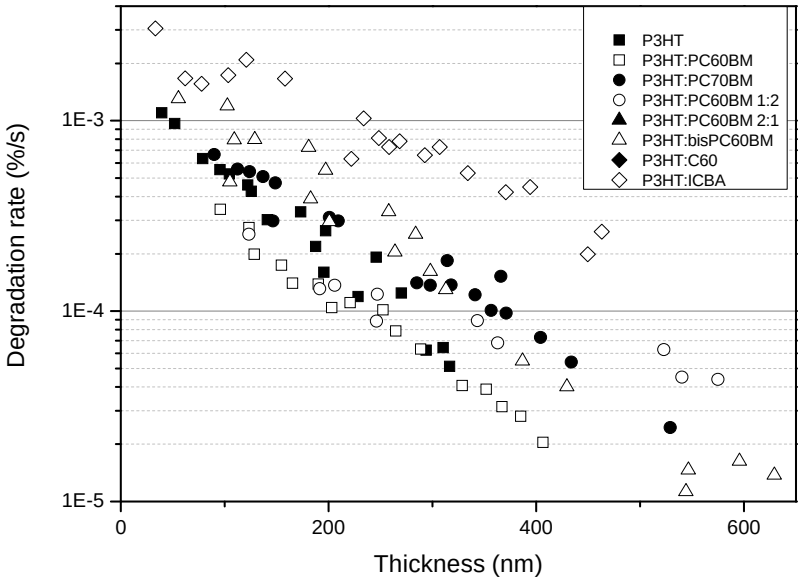

Figure S7: Thickness resolved degradation rates for P3HT blended with different electron acceptors.

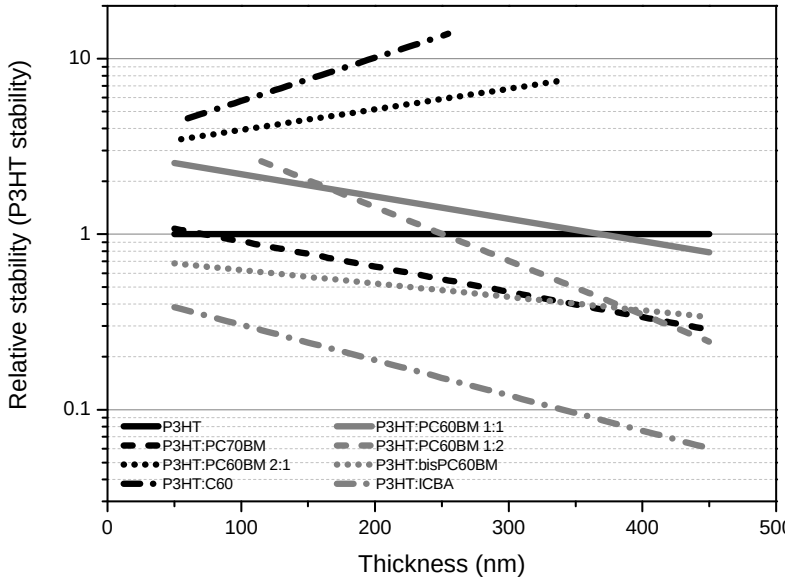

Figure S8: Thickness resolved stabilities in units of P3HT stability for P3HT blended with different electron acceptors.

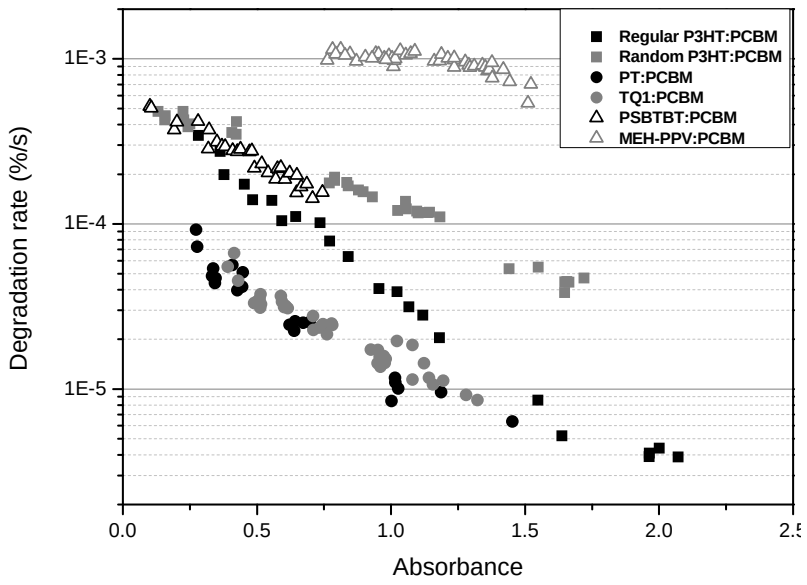

Figure S9 Absorbance resolved degradation rates of bulk hetero junctions based on different polymers and $PC_{60}BM$.

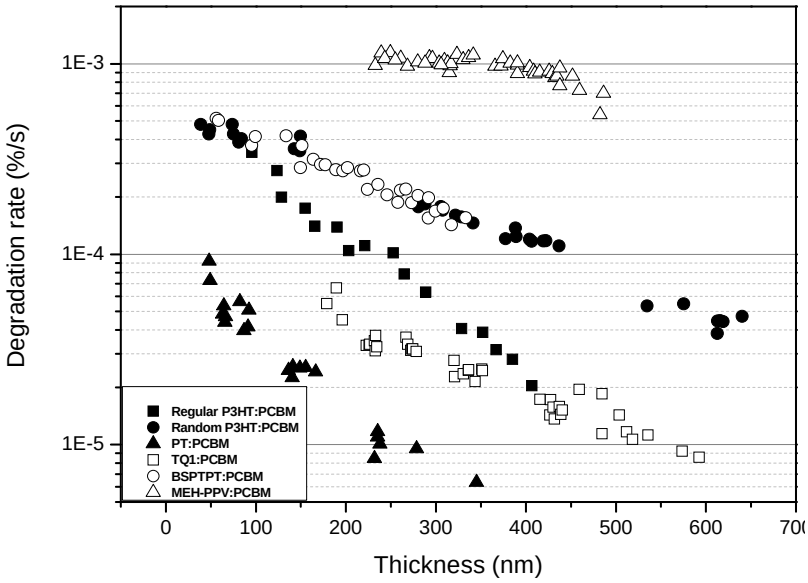

Figure S10: Thickness resolved degradation rates of blends based on different polymers and PC60BM.

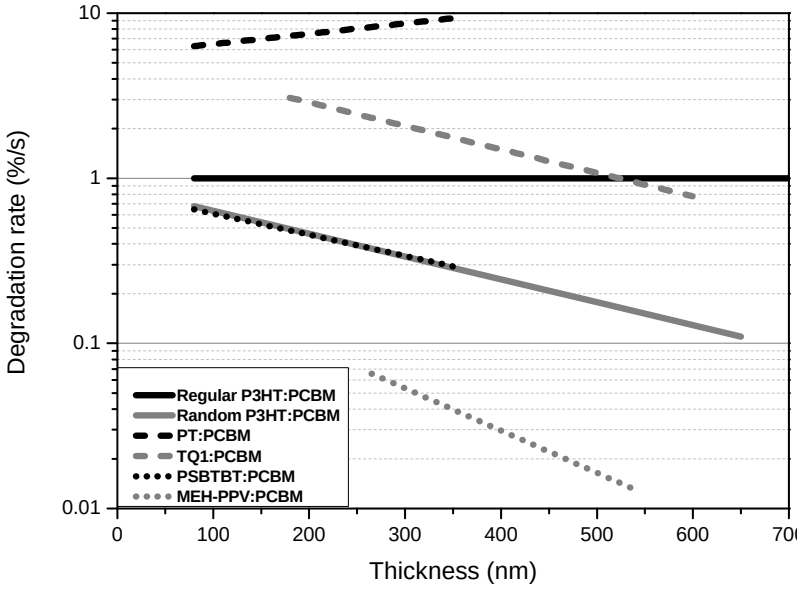

Figure S11: Thickness resolved stabilities in units of P3HT:PC_{60}BM stability of blends based on different polymers and PC_{60}BM.

Bibliography

1. F. C. Krebs, Ed., *Polymer Photovoltaics - A Practical Approach*, SPIE, Bellingham, 2008.

2. F. C. Krebs, M. Jørgensen, K. Norrman, O. Hagemann, J. Alstrup, T. D. Nielsen, J. Fyenbo, K. Larsen, and J. Kristensen, *Solar Energy Materials and Solar Cells*, 2009, **93**, 422-441.

3. J. E. Carlé, M. Jørgensen, M. Manceau, M. Helgesen, O. Hagemann, R. Søndergaard, and F. C. Krebs, *Solar Energy Materials and Solar Cells*, 2011, **95**, 3222-3226.

4. T. R. Andersen, T. T. Larsen-Olsen, B. Andreasen, A. P. L. Böttiger, J. E. Carlé, M. Helgesen, E. Bundgaard, K. Norrman, J. W. Andreasen, M. Jørgensen, and F. C. Krebs, *ACS nano*, 2011, **5**, 4188-96.

5. F. C. Krebs, H. Spanggard, T. Kjær, M. Biancardo, and J. Alstrup, *Materials Science and Engineering: B*, 2007, **138**, 106-111.

Influence of processing and intrinsic polymer parameters on photochemical stability of polythiophene thin films

Morten V. Madsen*, Thomas Tromholt, Arvid Böttiger, Jens W. Andreasen, Kion Norrman and Frederik C. Krebs

Department of Energy Conversion and Storage, Technical University of Denmark, Frederiksborgvej 399, DK-4000 Roskilde, Denmark

*Email: mves@dtu.dk

Abstract

Intrinsic polymer parameters such as regio-regularity, molecular weight, and crystallinity play an important role when studying polymer stability. 18 different batches of poly-3-hexyl-thiophene (P3HT) were degraded in a solar simulator (AM1.5G, 1000 W/m^2) and the degradation kinetics were monitored. The results suggest that the radical reaction responsible for the photodegradation takes place at terminal thiophene rings exposed at points were the conjugation is broken. This proposed mechanism is supported by the fact that stability scales with regio-regularity following the ratio of head-to-tail connected thiophene units. Annealing was found to relax the P3HT films and increase conjugation length and, in turn, increase stability observed as a delayed spectral blueshift caused by photochemical degradation. Crystallinity was found to play a minor role in terms of stability. Oxygen diffusion and light shielding effects were shown to have a negligible effect on the photochemical degradation rate. The results obtained in this work advance the understanding of polymer stability and will help improve the design of materials used for polymer solar cells resulting in longer lifetimes, which will push the technology closer to large-scale applications.

Keywords

P3HT, photooxidation, organic photovoltaics, photo-chemical stability, degradation

Introduction

The field of polymer solar cells (PSC) is growing fast, manifested in an exponential increase in publications.[1] The technology has reached a point where focus has shifted to application, demonstration and commercialization. The technology combines low cost, flexibility, and fast processability well-suited for large scale production that, in turn, will constitute a strong alternative to energy production. State-of-the-art in terms of efficiency has been reported to have increased to above 10% for small area laboratory devices.[2,3] Large scale production based on roll-to-roll techniques is now possible and production of 10.000 units has been demonstrated.[4] However, limited lifetime of the devices is still an issue and it is thus crucial to be able to both characterize and understand the different degradation mechanisms responsible for the performance deterioration of PSCs. It is well-known

that several aspects affect the final lifetime of the device including stability of the morphology, oxygen, and water diffusion, and polymer photo degradation.[5,6] The exact nature of the degradation mechanisms depends on the specific materials used in the multilayer stack of the solar cell. Consequently, when studying the overall PSC device stability, the actual stability of each layer cannot be deduced. Specifically, the stability of the photo-active layer is highly important since this layer accommodates the free charge carrier generation. Evaluation of the stability of this layer is therefore paramount to overcome the issue of lifetime for PSC. The evaluation of polymer photo-chemical stability using primarily UV-vis spectroscopy is an emerging field as documented by a number of recent reports on comparative studies. Manceau et al. reported a study involving 20 different polymers from which relative stabilities of an extensive range of functional groups were established.[7] In an extensive material screening by Tromholt et al. material stabilities were also resolved in terms of the optical density of the samples. [8] Exponential increases of stability were observed for all materials and it was concluded that identical optical densities are needed when comparing stabilities between different materials.

This paper focuses solely on the intrinsic photo-chemical stability of the well-known conjugated polymer poly-3-hexyl-thiophene (P3HT). Degradation of P3HT is well-documented and can be facilitated by exposure to light and molecular oxygen that destroys the π–conjugation and consequently induces loss of absorption. P3HT is degraded under these conditions in solution as well as a solid (e.g. a film). The consequence of degradation is well-established but the mechanism responsible for it has been subject to discussion. Whereas singlet oxygen is known to be the cause of degradation in solution,[9] the degradation mechanism in the solid state is believed to be different. Manceau et al. have proposed a degradation mechanism based on a radical process beginning from an abstraction of an allylic hydrogen, leading to side-chain and sulfur oxidation.[10,11] This process is responsible for breaking the macromolecular backbone resulting in loss of conjugation and consequent bleaching of the sample. This mechanism occurs under both photo- and thermal oxidation enforcing the notion that singlet oxygen is not the main intermediate in the degradation process. Hintz et al. have conjectured that the polymer is mainly attacked at the terminal thiophene rings under photo-oxidation.[12] The authors concluded this from observing the kinetics of the blueshift in the optical absorption. They observed that the blueshift, indicating loss of conjugation (observed for oligomers with less than 20 thiophene units), is not observed until the end of the degradation of the polymer. Hintz et al. have also demonstrated that a strong increase in photon effectiveness is observed for photo-degradation of P3HT films for decreasing irradiation wavelengths.[13] Changing the illumination wavelength from 554 to 335 nm leads to an increase by a factor of 50 in effectiveness of the P3HT photo-oxidation. This observation supports the radical chain mechanism driven by photo-generation of radicals by the photolysis of precursors absorbing in the UV-region.

The absolute stability of polymers is known to be affected by degradation parameters such as light spectrum, room temperature, ozone level, and humidity. Thus, direct comparisons of absolute stabilities assessed with different degradation setups in different laboratories are not straightforward. To reduce influence of different degradation parameters in photo-chemical stability reports, material stabilities are normally expressed in units of

stability of a reference material of well-known stability, typically P3HT. However, this assumes that P3HT presents an intrinsic, constant stability that is independent of synthesis routes, regio-regularity (RR), molecular weight, molecular weight distribution, crystallinity etc. The overall effect is that the material stabilities expressed in units of P3HT stability as reported in the literature may be associated with significant uncertainty. Furthermore, until now, development of stable conjugated polymers for PSCs has been focused on the stability of the different functional groups used for the synthesis. However, understanding the influence of the above described intrinsic polymer properties on the photo-chemical stability is highly appealing, since this will provide a new set of tools when designing novel materials for PSCs.

In this report we describe the influence of the intrinsic polymer properties on the photo-chemical stability of P3HT. This involves 18 different batches of P3HT from different manufacturers and batches made in house. P3HT polymers with significantly different M_w and RR are studied. The effect of inducing crystallinity by thermal annealing is reported by studying stabilities for different annealing temperatures. Furthermore, the degradation kinetics is studied for films of different thicknesses, which allows for studying the influence of light shielding and oxygen availability in the film.

Experimental

Degradation Setup and Data Evaluation

A fully automated, high-throughput photo-chemical degradation setup was used for the degradation of all materials in this study as described elsewhere.[12] The setup utilized a Steuernagel solar simulator with an Osram 1200 W metal halide arc lamp providing an approximate AM1.5G spectrum with an intensity of 1000 W/m^2. The sample exchanger had a capacity of 22 samples and a UV-vis spectroscopic probe based on an optical fiber-based CCD spectrometer (Avantes AvaSpec 1024) and a halogen/deuterium light source (Avantes AvaLight-DHc) are used to measure the evolution in the absorbance of the samples. For this study, the setup was programmed to monitor 28 degradation points per sample. A fully loaded sample exchanger with 22 samples consequently monitors 616 degradation points in parallel. A C# based automated software infrastructure was established to handle the high number of data files. To avoid spectral shielding from the substrate, illumination was always performed from the polymer side.

Degradation rates were extracted from the rate of decrease of the calculated total number of absorbed photons per second as absorbed by the polymer when the recorded absorption spectrum is folded with a theoretical AM1.5G solar spectrum as described in reference 13. We observed that plotting the rate of number of absorbed photons as a function of initial absorption maximum yields a constant value for a broad interval from 0.4 to 1 in absorbance, see Figure 1. The ordinate axis in this plot is dependent on the choice of integration range and therefore the same integration range (400 – 600 nm) has been used for all materials. It was thus possible to run a large number of degradation experiments for different polymers and compare their stablities while the effect of thickness was cancelled. This behaviour has been observed for P3HT, poly(5-methoxy-2-(2-ethyl-hexyloxy)phenylenevinylene] (MEH-PPV), and polythiophene (PT). Normalized degradation rates in all

comparisons are given in units of the stability of the polymer designated R1, see Table 1. Consequently, values below 1 describe polymers more stable than R1 and values above 1 describe polymers less stable.

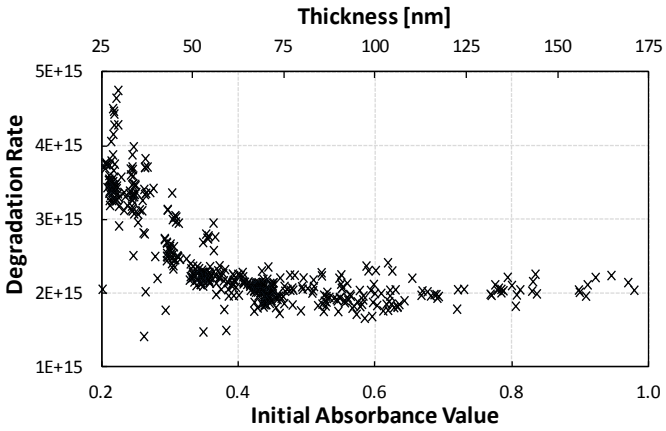

Figure 1. Rate of change in number of absorbed photons as a function of initial absorbance value and thickness.

Using degradation rates based on loss of absorbance directly allows for correlating the degradation state to the number of intact monomer units. The number of monomers scales directly with the absorbance, and thus the degradation state can be written as

$$D_{state} = \frac{N_{Monomer}}{N_{initial}} = \frac{A}{A_{initial}},$$

where $N_{initial}$ is the initial number of monomers, $A_{initial}$ and A is the initial and current absorbance respectively. The number of monomers at a given time during degradation can be expressed by

$$N_{Monomer} = \frac{N_A \rho}{M} t \cdot D_{state},$$

where N_A is Avogadro's number, ρ is the polymer density, M is the molar mass, and t is the film thickness. According to the Lambert-Beer law, the thickness of the film scales with the absorbance. Using the absorption to thickness conversion presented in reference 12 for regio-regular P3HT, the film thickness can be expressed by $t = (A_{\max} - 0.622) \cdot 188.68$ nm, where $A_{\max}$ is the peak absorbance. The density was determined to be $\rho = 1.07\, g/cm^2$ by X-ray reflectometry for polymer R2. The molar mass of the P3HT monomer is $M = 166.3\, g/mol$. The reciprocal rate of monomer loss yields the degradation event interval,

$$\tau = \left(\frac{dN_{Monomer}}{dt} \right)^{-1}.$$

NMR

^{1}H NMR was used to determine the regio-regularity of P3HT in deuterated chloroform solution. For P3HT the regio-regularity is determined as the ratio between the signal at 2.8 ppm, originating from the preferred head-to-tail connected monomers, and the signal at 2.6 ppm being associated with the head-to-head coupled monomers.

X-ray diffraction

X-ray diffraction was used to quantify the crystallinity of annealed films. The position of the P3HT *100* reflection was determined by a specular scan using a dedicated reflectometry setup, with a rotating Cu anode as source, operating at 50 kV, 200 mA. The X-ray beam is monochromatized (λ = 1.5418 Å) and collimated by a 1D multilayer optic and the beam is further collimated by incident and diffracted beam slits.

With a point detector positioned at the diffracted beam angle (2θ) for the *100* reflection, rocking scans were recorded by rotating the sample from incidence angle zero to 2θ. The integrated intensity, less background, was used as a measure of the polymer crystallinity.

Materials

P3HT films were spin-coated on microscopy slides obtained from Menzel from 12 mg/mL chlorobenzene solutions. 18 different batches of P3HT from different manufactures as well as in-house manufactured batches were studied. For each batch the manufacturer, the batch number and an abbreviation have been indicated in Table 1. The regio-regularity was measured by ^{1}H NMR.

Code	**Manufacturer**	**Batch**	**RR**	**Mn [kDa]**
M1	Merck	EE-97802	94.8%	19.6
M2	Merck	EE-99202	94.0%	23.7
M3	Merck	EE-101702	95.8%	29.6
M4	Merck	EE-99120	93.0%	15.7
R1	Rieke Metals	PTL 10-87	91.7%	28.8
R2	Rieke Metals	BS19-60A	-	21.6
R3	Rieke Metals	BS16-24	92.1%	23.3
B1	BASF	GK-2126-108	96.8%	-
B2	BASF	GK-2566/77	93.7%	-
B3	BASF	2010_A6-7	94.6%	-
P1	Plextronics	11-11822	96.0%	-
P2	Plextronics	P04205	96.0%	34.7

P3	Plextronics	PO2122	91.6%	-
P4	Plextronics	PO4054	95.1%	-
D1	DTU (in house)	McCullough route, chloroform fraction[15]	96.1%	17.3
D2	DTU (in house)	McCullough route, hexane fraction[15]	96.0%	2.8
D3	DTU (in house)	Method B, Soxhlet purified[15]	76.2%	40
D4	DTU (in house)	Method A, Soxhlet purified[15]	76.1%	-

Table 1. The 18 different samples of P3HT studied. The manufacturers and their batch numbers have been stated as well as the abbreviations used. The regio-regularity has been determined using ^{1}H NMR. R2 was not measured by NMR as the polymer had been depleted.

Results and discussion

Figure 2 shows the relative stabilities expressed as normalized rate of degradation of the 18 different polymers in units of R1, evaluated as described in the experimental section. The polymers are grouped according to manufacturer; D is DTU in-house synthesized batches of P3HT, M are commercial P3HT polymers from Merck, R from Rieke Metals, B from BASF, and P from Plextronics. The complete list of polymers is shown in Table 1. The polymers D3 and D4 are regio-random P3HT polymers, while the rest are regio-regular to different degrees. While all regio-regular P3HT polymers exhibit relative degradation rates close to 1, the regio-random polymers are significantly less stable exceeding relative degradation rates of 2. This is consistent with the work by Hintz *et al.* where an increase in degradation rate by a factor of five was observed, in fair agreement with the factor of three observed on average in this work.[10]

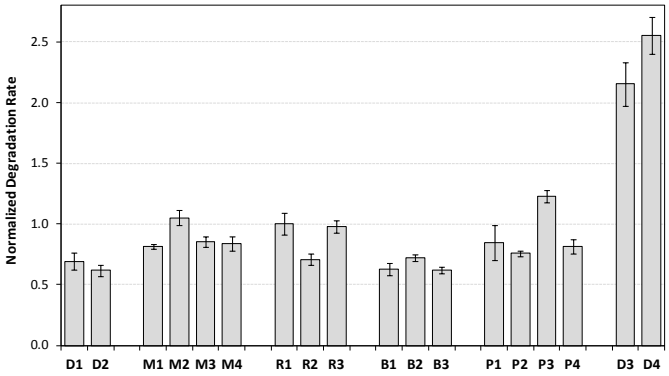

Figure 2 Degradation rates normalized to the value of R1. For each polymer a minimum of three samples with 28 sample points each, were monitored for the full degradation. The error bars indicate the standard deviation.

While the regio-regularity clearly affects the stability of the polymer, the molecular weight seems to have no significant effect in agreement with Dupuis *et al.* When comparing the polymer D2 that has a particularly low molecular weight (M_n = 2.8 kDa), with the polymer D1 that has a significantly higher molecular weight (M_n = 17.3 kDa) it is clearly evident that both polymers have similar regio-regularities close to 96% and clearly have identical degradation rates (Figure 2) if the error bars are considered. This suggests that molecular weight has either no or a negligible influence on the degradation rate. Indeed plotting the normalized degradation rate against the number average molecular weight (not shown) reveals that no correlation is present. It can thus be concluded that the length of the polymer chain is much less important than the conjugation length. However, for very low molecular weights this is probably not true, but is at least valid for polymers with M_n above 2.8 kDa as shown in this work. It therefore seems that the regio-regularity is the major dominating factor on the stability of the polymer. Dupuis *et al.* have reported that regio-regularity is the crucial parameter that controls the photo stability and reported a linearity between degradation rate and regio-regularity in the range from 93% regio-regularity to 98%.[16]

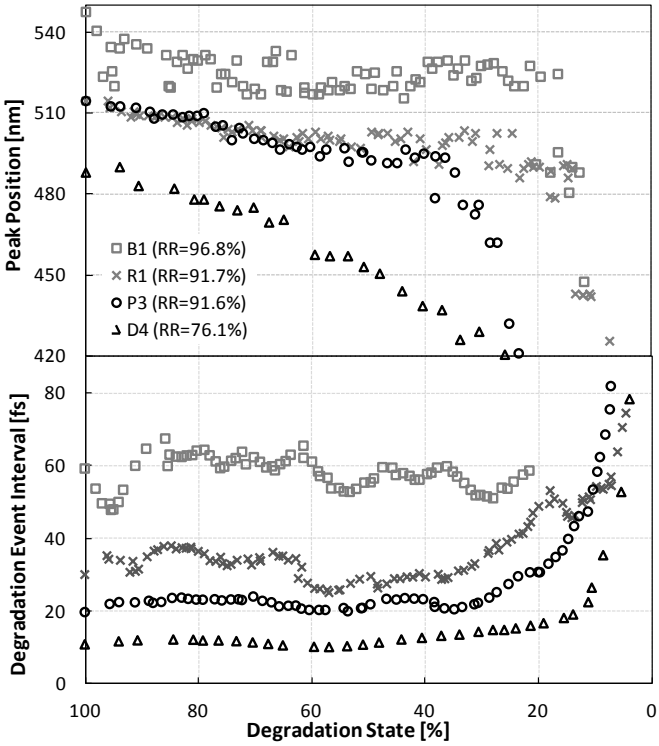

Figure 3. (Top) Absorption peak position as a function of degradation state. (Bottom) Degradation event interval plotted against degradation state. All data is based on polymer films of 140 nm thickness.

Reaction kinetics are indicative of the underlying reaction mechanism determining the rate constants. Figure 3 shows the degradation event interval for selected polymers ranging from a regio-random (D4) to three different degrees of increasing regio-regularity. It is evident that all four polymers follow strict 0^{th} order kinetics for the

first 70% of the degradation as the interval is constant. Furthermore, the degradation event interval is observed to increase with regio-regularity. The timescales of photolysis in the absence of oxygen are many orders of magnitude slower than photo-oxidative degradation.[17] Likewise, thermolysis at moderate temperatures (<400 K) is negligible.[11] Both contributions can therefore be neglected in the analysis of the degradation kinetics. The degradation kinetics of the initial part of the degradation is expected to be 0^{th} order assuming that only terminal thiophene rings are attacked during the photo-oxidation. Preferential surface degradation could possibly explain the 0^{th} order kinetics. However, this possibility can be excluded based on the blue-shift dynamics of the polymers, see Figure 3. Observing the regio-regular B1 it is evident that no significant blueshift occurs in the initial parts of the degradation process. This would not be the case if the top layer was preferentially degraded. The hypothesis is that if only terminal thiophene rings are attacked, there should not be a significant blueshift of the spectrum in the initial part of the degradation process. Figure 3 confirms that B1 (RR=96.8%) only exhibits a limited blueshift for the initial 80% of the degradation process. For the regio-random D4 (RR=76.1%) a strong blueshift is observed during the entire degradation process. R1 (RR=91.7%) and P3 (RR=91.6) show stronger blueshift compared to B1. The strong blueshift observed for regio-random P3HT is ascribed to the shorter initial conjugation length of the chain like morphology in the regio-random polymer. Figure 3 shows that the initial peak position for the regio-random D4 at ~490 nm is close to the value at which the regio-regular polymers initiate their quick peak shift, indicating that the conjugation length of D4 is sufficiently short at the initial stage that every monomer contributes strongly to the size of the bandgab and each monomer loss is thus associated with a peak shift. The observation suggests that breaking the regularity induces attack points for the radical reaction, implying that a regio-random polymer is more susceptible to photo-degradation. If true, the stability of the polymer must scale with regio-regularity.

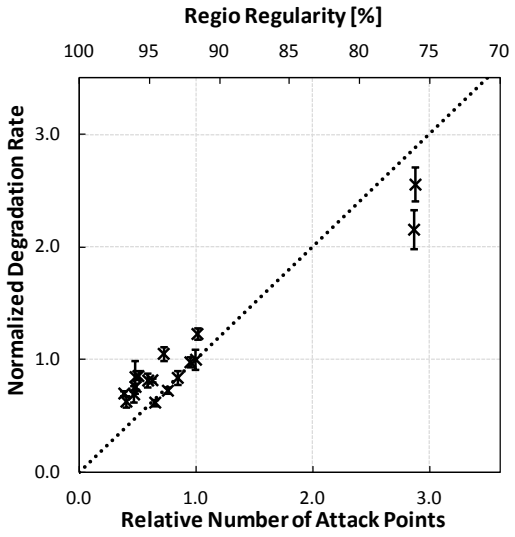

Figure 4. Normalized degradation rate plotted against the calculated relative conjugation length / regio-regularity. The dotted line represents the predicted degradation rate.

Assuming that each breach of regularity introduces two new attack points, it is possible to model the degradation rate as a function of regio-regularity. The relative number of attack points can then be written as

$$N_{ap} = \frac{2(1 - RR_x)}{2(1 - RR_{R1})},$$

where N_{ap} is the number of attack points relative to R1, RR_x is the regio-regularity of the specific polymer, and RR_{R1} is the regio-regularity of R1. Figure 4 shows a plot of the normalized degradation rate as a function of regio-regularity and relative number of attack points. The degradation rate appears to scale with regio-regularity by a linear relationship between regio-regularity and polymer stability. The dotted line in the graph is the theoretical value of degradation rate, calculated from the degradation rate of R1. It is evident that the simple model is capable of explaining the behavior in a convincing manner, suggesting that each breach of regularity induces new attack points that weaken the system. The conjugation length is proportional to the regio-regularity since the conjugation breaks when the polymer is not planar and the π electrons are not in the same plane.

Besides the difference in ratio of head-to-tail connected thiophene units, regio-random and regio-regular P3HT films differ in a more distinct manner. Regio-regular P3HT has been reported to exhibit vanishing intersystem crossing and thereby low triplet yield in contrast to regio-random P3HT.[18] Triplet states are more photochemically active due to their longer lifetime and therefore have been proposed as the cause for the increased degradation rate.[13] It was further implied that the fragmentation of the conjugated π-system in regio-random P3HT takes place on a random basis, while for regio-regular P3HT, terminal thiophene rings are attacked. The results presented in this work, however, demonstrate a strict 0^{th} order degradation rate for both regio-random batches, enforcing the notion that only terminal thiophene rings at points of broken conjugation are attacked. The increase in degradation rate can be explained by an increase in attack points resulting from the lower regularity and the blueshift dynamics is explained by the change in initial conjugation length.

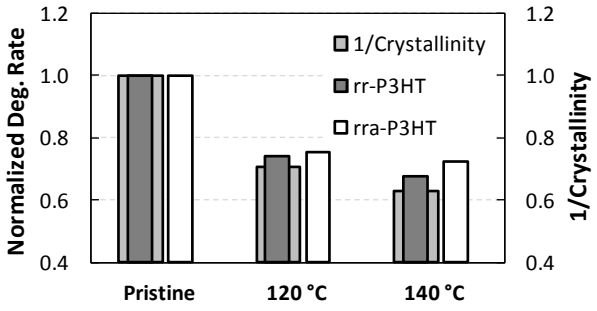

Figure 5. (Left scale) Degradation rate of (dark grey) regio-regular and (white) regio-random P3HT normalized to their respective pristine degradation rates. (Right scale) Reciprocal crystallinity as deduced from X-ray diffraction studies.

Dupuis *et al.* offered an alternative explanation suggesting that difference in degradation rate is related to the fact that oxygen can diffuse more readily through the amorphous zones and is not soluble in the crystal domains amorphous phase of semicrystalline polymers or at the interface amorphous/crystalline phase.[16] Regio-regular P3HT films more readily crystallizes, whereas a regio-random film maintains a more chainlike morphology. Figure 5 shows a plot of the degradation rate superimposed on the reciprocal crystallinity as measured by X-ray diffraction for the regio-regular polymer R2. As is evident from Figure 5 annealing at 120 °C and 140 °C for one hour was found to induce relative degradation rates of 0.75 and 0.68, respectively, relative to the pristine sample. This indicates that the crystallinity of the sample has affected the stability. While an increase in crystallinity is obtained for regio-regular P3HT, annealing is not expected to increase the crystallinity of regio-random P3HT significantly. Indeed, when the regio-random D4 was annealed, no diffraction peaks were observed in the X-ray diffractogram (not shown). This is also consistent with a glass transition temperature of –3 °C reported for regio-random P3HT, indicating that the polymer is indeed amorphous.[19] However, comparable relative stabilizations were observed relative to the regio-regular R2, see Figure 5. Considering that the degradation rate has been shown to scale with the number of kinks in the polymer, it is hypothesized that the main contribution of the annealing step is the relaxation of the polymer leading to an increased conjugation length. Consequently, thermal annealing of P3HT is favorable to the photo-chemical stability. During spin coating the polymers are frozen in a morphology that is not necessarily the lowest energy state. Annealing the films generally relaxes the films, i.e. the chains are stretched and high-energy kinks are avoided. If the annealing effect can be ascribed to an increased conjugation length, a difference in the degradation kinetics as observed in Figure 3 for regio-regularity is expected. This was indeed observed when the regio-regular R1 batch was studied by comparing the pristine polymer to films annealed for two hours at 80 °C and 120 °C. The samples were allowed to cool at a slow rate for 48 hours prior to the degradation experiment. Based on 200 degradation points for each sample type, the degradation state for which the absorption peak reaches 480 nm was 20.85, 18.85, and 17.5% for the pristine, 80 °C and 120 °C annealed samples, respectively. Consequently, annealing the polymer introduces the same delay of the blueshift as observed for higher regio-regular samples. This is in accordance with the hypothesis that the relaxation of the film to a lower energy state increases the conjugation length, which in turn increases film stability.

As a final validation of the hypothesis, the stabilization of the amorphous polymer poly (2-methoxy-5-(2'-ethyl)hexoxy-phenylenevinylene) (MEH-PPV) was assessed as a function of annealing temperature (not shown). For this polymer, stabilization by a factor of 3.5 was observed. The strong stabilization of the MEH-PPV film supports the hypothesis that the relaxation of the polymer is the main contributing factor in the stabilization.

Effect of Thickness on Degradation Kinetics

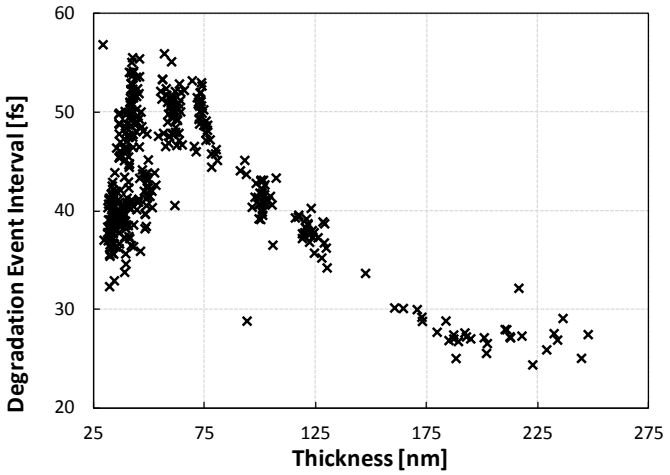

Figure 6. Degradation event interval plotted against the thickness of a film of R1 polymer.

Studying films of different thicknesses gives insight into oxygen availability in the film and effects of light shielding. Assuming that oxygen diffusion is not limited and that light shielding from the top layer of the film is insignificant, the concentration of oxidized thiophene rings is independent of film thickness. No significant spatial reaction gradient is observed in the top 10 nm of a degraded P3HT film, as deduced from angle dependent X-ray photoelectron spectroscopy measurements.[12] This suggests that there is no shielding effect in at least the top layer of the film. Figure 6 shows a plot of degradation event interval against film thickness. It is clear from Figure 6 that a peak is observed around 60 nm. Thin films (below 60 nm) are less stable and very sensitive to changes in film thickness (i.e. steep slope in Figure 6). Thicker films are also less stable manifested in decreasing intervals between degradation events for increasing film thickness, which is close to being a linear correlation between 75 and 175 nm. The decrease in the time between degradation events for thicker films is expected since the thicker film contains a higher number of monomers, and thus more reaction sites. Figure 7 shows the film lifetime plotted against thickness, and it is evident that in the range 125 to 175 nm the film lifetime is constant. The plot is constructed by multiplying the event interval by the initial number of monomers. The existence of a constant lifetime region implies that the degradation takes place in parallel for the entire depth of the film. This means that for this region light shielding is negligible and oxygen is equally available for all depths in accordance with the findings of Hintz *et al*.[13] For films thicker than 175 nm, either light shielding or lack of oxygen sets the bottom part of the film apart from rest of the film with a lower degradation rate. The event interval is therefore observed to stabilize in this region.

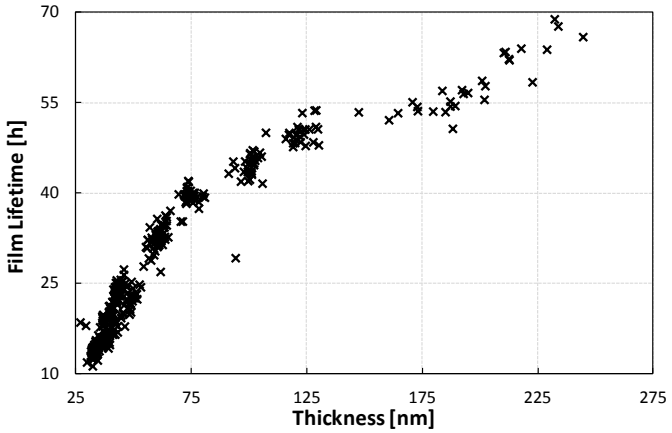

Figure 7. The film lifetime as calculated from the time between degradation events and the initial number of monomers. Thereby the film lifetime is extrapolated from the initial 50% of the degradation.

In Figure 8 the degradation state at which the blueshift reaches 480 nm is plotted. For films in the stable region of 125–175 nm, the blueshift occurs late near the last 20% of the degradation. For films thicker than 175 nm the blueshift appears earlier. This is consistent with the fact that parts of the film degrade later than the top part of the film, thereby extending the degradation. A key point of Figure 8 is the fact that thin films (<75 nm) blueshift rather quickly. This indicates that another mechanism is involved. Ozone has been shown to cause 1^{th} order degradation kinetics and to attack the polymer at random sites.[12] It is conceivable that the relatively high ozone content of the laboratory environment affects the degradation for thin films. This would explain the decrease in degradation interval seen in Figure 6 and also the strong blueshift in Figure 8. However, the kinetics of the degradation remained 0^{th} order. Another likely candidate for the increase in reaction rate is the higher surface to volume ratio. If the reactions are more likely on the surface the rate may easily be different. The polymers in the top layer can be expected to have a higher density of kinks, introducing more attack points for the reaction. This would also explain the fast blueshift observed for thin films.

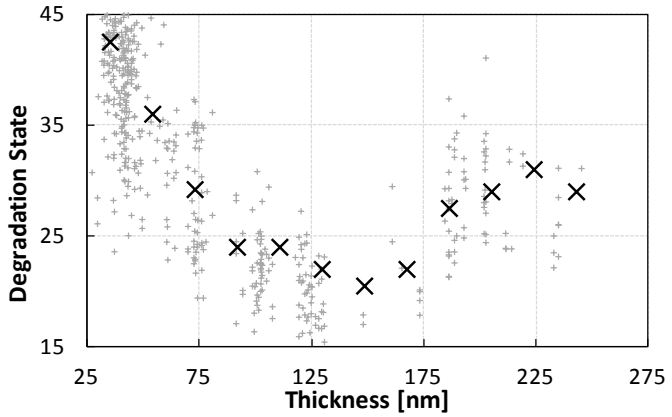

Figure 8. Wavelength shift observed for different thicknesses of P3HT films. The black crosses represent data bins of a width of 40 nm.

Conclusion

18 different batches of P3HT were degraded under simulated sunlight (AM1.5G, 1000 W/m^2) and the respective stabilities were evaluated from the decrease in optical absorption. A highly automated setup allowed for monitoring hundreds of degradation points in parallel to allow for statistically sound investigations of degradation kinetics. It was shown to be evident that the polymer degradation follows strict 0th order degradation kinetics for the initial part of degradation. The typical blueshift of the absorption peak observed during degradation was found to appear later for the more regio-regular films. This indicates that the radical reaction responsible for the photo-degradation attacks terminal thiophene rings exposed at points where the conjugation is broken. Stability was found to increase with regio-regularity following the ratio of head-to-tail connected thiophene units, demonstrating that the polymer is indeed attacked at points of broken conjugation. Annealing relaxes the films and increases conjugation length. This, in turn, increases stability and delays spectral blueshift. For films of different thicknesses, the interval between degradation events is observed to scale linearly with the initial number of thiophene rings for medium thick films (75–175 nm) indicating that oxygen diffusion and light shielding effects have negligible or no effect for medium thickness films.

Acknowledgements

This work was supported by the Danish Strategic Research Council (2104-07-0022), EUDP (j. no. 64009-0050) and PVERA-NET (project acronym POLYSTAR).

References

[1] M. Jørgensen, K. Norrman, S.A. Gevorgyan, T. Tromholt, B. Andreasen, F.C. Krebs, Stability of polymer solar cells, Adv. Mater. 2012;24:580-612.

[2] UCLA, UCLA engineers create tandem polymer solar cells that set record for energy-conversion, Http://newsroom.ucla.edu/portal/ucla/ucla-engineers-create-tandem-polymer-228468.aspx, Accesssed 5/5-2012.

[3] Heliatek, Heliatek sets new record efficiency of 10.7% for its organic tandem cell, Http://www.heliatek.com/?p=1923&lang=en, Accessed 5/5-2012.

[4] F.C. Krebs, J. Fyenbo, D.M. Tanenbaum, S.A. Gevorgyan, R. Andriessen, B. van Remoortere, Y. Galagan, M. Jørgensen, The OE-A OPV demonstrator anno domini 2011, Energy Environ. Sci. 2011;4:4116-4123.

[5] M. Jørgensen, K. Norrman, F.C. Krebs, Stability/degradation of polymer solar cells, Sol. Energy Mater. Sol. Cells. 2008;92:686-714.

[6] K. Norrman, M.V. Madsen, S.A. Gevorgyan, F.C. Krebs, Degradation patterns in water and oxygen of an inverted polymer solar cell, J. Am. Chem. Soc. 2010;132:16883-16892.

[7] M. Manceau, E. Bundgaard, J.E. Carlé, O. Hagemann, M. Helgesen, S. Roar, M. Jørgensen, F. C. Krebs, Photochemical stability of π-conjugated polymers for polymer solar cells a rule of thumb, J. Mater. Chem. 2011;21:4132-4141.

[8] T. Tromholt, M.V. Madsen, J.E. Carlé, M. Helgesen, F.C. Krebs, Photochemical stability of conjugated polymers, electron acceptors and blends for polymer solar cells resolved in terms of film thickness and absorbance, J. Mater. Chem. 2012;22:7592-7601.

[9] M. Koch, R. Nicolaescu, P.V. Kamat, Photodegradation of Polythiophene-Based Polymers : Excited State Properties and Radical, J. Phys. Chem. C. 2009;113:11507-11513.

[10] M. Manceau, A. Rivaton, J.-L. Gardette, Involvement of Singlet Oxygen in the Solid-State Photochemistry of P3HT, Macromol. Rapid Commun. 2008;29:1823-1827.

[11] M. Manceau, A. Rivaton, J.-L. Gardette, S. Guillerez, N. Lemaître, The mechanism of photo- and thermooxidation of poly(3-hexylthiophene) (P3HT) reconsidered, Polym. Degrad. Stab. 2009;94:898-907.

[12] H. Hintz, H. J. Egelhaaf, H. Peisert, T. Chassé, Photo-oxidation and ozonization of poly(3-hexylthiophene) thin films as studied by UV/VIS and photoelectron spectroscopy, Polym. Degrad. Stab. 95 (2010) 818-825.

[13] H. Hintz, H. J. Egelhaaf, L. Lüer, J. Hauch, H. Peisert, T. Chassé, Photodegradation of P3HT−A Systematic Study of Environmental Factors, Chem. Mater. 2010;23:145-154.

[14] T. Tromholt, M. Manceau, M. Helgesen, J.E. Carlé, F.C. Krebs, Degradation of semiconducting polymers by concentrated sunlight, Sol. Energy Mater. Sol. Cells. 2010;95:1308-1314.

[15] F.C. Krebs, Polymer Photovoltaics A Practical Approach, SPIE, 2008.

[16] A. Dupuis, P. Wong-Wah-Chung, A. Rivaton, J.-L. Gardette, Influence of the microstructure on the photooxidative degradation of poly(3-heaxylthiophene), Polym. Degrad. Stab. 2012;97:366-374.

[17] M. Manceau, S. Chambon, A. Rivaton, J.-L. Gardette, S. Guillerez, N. Lemaître, Effects of long-term UV–visible light irradiation in the absence of oxygen on P3HT and P3HT:PCBM blend, Sol. Energy Mater. Sol. Cells. 2010;94:1572-1577.

[18] O. Korovyanko, R. Österbacka, X. Jiang, Z. Vardeny, R. Janssen, Photoexcitation dynamics in regioregular and regiorandom polythiophene films, Phys. Rev. B: Condens. Matter. 2001;64:235122(1-6).

[19] S. Hugger, R. Thomann, T. Heinzel, T.-A. T., Semicrystalline morphology in thin films of poly(3-hexylthiophene), Colloid. Polym. Sci. 2004;282:932-938.

Submitted to ADVANCED ENERGY MATERIALS

DOI: 10.1002/aenm.((please add manuscript number))
Article type: Communication

Concentrated light for accelerated photo degradation of polymer materials

Morten V. Madsen, Thomas Tromholt, Kion Norrman, and Frederik C. Krebs*

Mr. Morten V. Madsen, Mr. Thomas Tromholt, Dr. Kion Norrman, and Prof. Frederik C. Krebs
Department of Energy Conversion and Storage, Technical University of Denmark, DK-4000 Roskilde, Denmark
E-mail: mves@dtu.dk

Keywords: Concentrated light, P3HT, Photo oxidation, organic photovoltaics, degradation

The field of polymer solar cells (PSCs) is maturing fast manifested in an ever increasing number of publications covering the subject. Over the last decade, reported efficiencies have risen to exceed 10%, and several companies have entered the field.[1,2] While efficiencies and production scalability are high interest areas, the Achilles' heel of polymer solar cells has long remained the operational lifetime of the devices. When organic matter is illuminated, the materials react via photochemical and photolytic processes, making it essential to utilize materials where the yield and rate of photochemical degradation is minimized. Outdoor tests of PSCs with lifetime exceeding one year have been demonstrated[3] and materials such as polythiophene (PT) have been shown to have degradation rates of 0.029% / h under ambient 1 sun conditions[4]. With this level of stability, fast material screening under accelerated conditions is an appealing prospect. Acceleration methods utilizing atmosphere and temperature control have been used to increase degradation rates by a factor of 20.[5] It has been demonstrated that increasing the temperature accelerates the degradation according to the Arrhenius equation for both PSCs and single polymer layers.[5,6] Concentrated light is another novel direct acceleration condition, which accelerates the rate of photo oxidation of the polymer. Due to the multitude of degradation mechanisms that are accelerated by concentrated light, the PSC response to concentrated light is complex,[7] and even effects such

as reversible degradation have been observed.[8] For the simplified system of pure polymer in the ambient, accelerated degradation has been performed up to 200 suns.[9] This study demonstrated that degradation of polymers can serve as a standard tool for rapid polymer stability evaluation. However, the validity of using concentrated light to accelerate the degradation process still remains to be studied.

This paper focuses on the use of concentrated light as a deterministic method of polymer degradation. For this, films of pure regio-regular poly-(3-hexyl-thiophene) (P3HT) were studied and their degradation rates compared. A novel fully automated lamp-based light concentrator (**Figure 1**) was constructed to allow for precise evaluation of degradation rates at high light intensities ranging from 0.1 to 150 suns. The evaluated degradation rates were, in turn, compared to the degradation rates of 1 sun degradation, with equivalent light spectra at all intensities. The degradation state is deduced by monitoring the changes in the optical spectrum of the sample during the illumination.[4] The artificial solar concentrator had the advantage of long term stability and precision in comparison with solar collector setups.[9] Automated sample exchangers were employed to ensure that no errors were introduced when handling samples. The full details of the experiments and the setups are provided in the Supporting Information.

Degradation of P3HT films at 1 sun is a well described phenomenon, known to proceed *via* a mechanism based on a radical process initiated by an abstraction of an allylic hydrogen, leading to side-chain and sulfur oxidation.[10,11] This process is responsible for breaking the macromolecular backbone resulting in loss of conjugation and consequent bleaching of the sample. It has been demonstrated that the P3HT polymer is attacked at terminal thiophene rings at points of broken conjugation, and that degradation is both thickness and regio-regularity dependent.[4,12] A strong increase in photon effectiveness is observed for photo degradation of P3HT films for decreasing irradiation wavelengths, and it has been

demonstrated that oxygen diffusion is not a rate limiting factor under 1 sun conditions.[6] For concentrated light conditions it is unknown if this remains true. Concentrated light might introduce degradation mechanisms that are not observed at 1 sun, which could change the degradation rates. The thermal equilibrium of the sample is expected to change with intensity convoluting the degradation rates. A single study by Tromholt *et al.* reports accelerated photochemical degradation by concentrated sunlight. They observed an acceleration factor of 55 for P3HT by comparing the degradation rate at 1 sun (0.1 W/cm^2) and at 100 suns (10 W/cm^2).[9] This suggests that at 100 suns, each photon has roughly half the effectiveness that a photon has at 1 sun. The spectrum at 1 sun in that particular work was an artificial light source, while the 100 sun spectrum was natural sunlight focused through a concentrating lens setup. The spectra thus had vastly different UV content and a decrease in photon effectiveness was consequently expected. The question, however, remains: are the photons equally destructive at all intensities or do some higher order degradation mechanisms become prevalent at higher intensities. The gradual decrease of absorbance during degradation of P3HT is linear in the initial part of the degradation process at 1 sun.[6] In **Figure 2** the black line represents degradation of a 110 nm P3HT film at 1 sun. The degree of degradation is observed to increase linearly with dose and is completely degraded after roughly 50 hours in agreement with the literature.[4] For concentrated light at 50, 100, and 150 suns, the dose-corrected degradation rate is observed to be higher as shown in Figure 2. Furthermore, the linearity is observed to be lost for concentrated light conditions. The degradation rate is decelerating with time, making it impossible to establish a single degradation rate for polymers degraded under concentrated light. The dose-corrected degradation rates, expressed as degradation rate per solar intensity, for concentrated conditions, have been determined for the initial 10 percent of the degradation process and compared (Figure S1). The dose-corrected acceleration factor, calculated by the ratio of the dose-corrected concentrated degradation rates and the

corresponding value for 1 sun, is shown in **Figure 3** for degradations at 50, 100, and 150 suns for film thicknesses between10 and 115 nm. The degradation rate corresponding to 1 sun, depicted as the dashed line in Figure 3, represents a polynomial fit of 526 separate degradation experiments covering the entire film thickness range with an r-squared value of 0.93. The dose-corrected acceleration factor of 8 observed for 150 suns at the largest film thickness indicates an absolute acceleration factor of 1,200, which is the highest acceleration factor reported in literature. It is evident that increasing light intensity implies increasing dose-corrected degradation rates when compared to the 1 sun data. Additionally, the effect is observed to increase with film thickness, suggesting that the photon effectiveness increases with higher light intensities and film thicknesses.

The concentrated light will induce a temperature increase in the material, and we thus hypothesize that the rise in effectiveness observed in our data is purely a consequence of the induced temperature increase during experiments. The extent of the induced temperature increase depends on the absorption of the sample, and thus the hypothesis explains the decelerating degradation rates observed in Figure 2. It was technically not possible to measure the temperature in the material during light exposure, so an estimate was done based on a simple approximation. By assuming that the temperature can be modeled by the absorbed energy Q_{in}, a radiative loss, and a loss associated with the thermal conductivity through the glass, the steady state can be written as $Q_{rl} + Q_{TC} = Q_{in} + Q_0$,where Q_{rl} is the radiative loss given as $Q_{rl} = 2\sigma e T^4 a$, $Q_0 = 2\sigma e T_0^4 a$ is the room temperature energy, and $Q_{TC} = ka|dT/dx|$ is the thermal conductivity. The emissivity is set to $e = 0.92$ equal to the emissivity for glass, and in the interval given for poly-vinyl-chloride. The room temperature energy is set to $T_0 = 30\,°C$. For the thermal conductivity it is assumed that the glass is coupled to a perfect heat reservoir, the glass has a thickness of 1 mm, and a thermal conductivity of $k = 0.8$. The area *a* is given by the area of the incoming light. The input energy is calculated as the number of photons absorbed

at each wavelength ($A(\lambda)$) multiplied by the energy at that given wavelength ($E(\lambda)$) by $Q_{in} = \sum\left[A(\lambda)\overline{N} \cdot E(\lambda)\right]$. The absorption is measured for each thickness and the number of photons is calculated from the spectrum of the light source. By solving the equation for each thickness, it is possible to calculate the temperature (Figure S2). For a film of 100 nm, a temperature of 65 °C is predicted for 150 suns. It is important to emphasize that this temperature will be a lower limit estimate since the model assumes an instant thermalisation between the polymer and the glass substrate. Furthermore, the model assumes that the substrate is coupled to a perfect heat reservoir.

In an attempt to obtain an experimental value for the temperature, a glass /polymer / silver sample with a thickness of 50 nm was constructed by evaporating silver on a P3HT covered glass substrate. By illuminating the sample from the glass side, the temperature could be measured by coupling a thermocouple to the silver layer, thereby avoiding the temperature increase due to the absorption of the thermocouple. At 150 suns a temperature of 175 °C was measured. Since the reflection from the silver interface is not perfect, the silver will induce a temperature increase by itself, so the measured value can be considered as an upper limit for the temperature of the polymer. As the light passes the film twice, the effective thickness is 100 nm. Consequently, a film with a thickness of 100 nm will have a temperature in the range between 65 °C and 175 °C.

Assuming that the temperature dependence of the reaction can be described by an Arrhenius model, it is possible to model the temperature based on the observed acceleration factor. The acceleration observed during degradation at two different temperatures *T'* and *T* can be described by

$$K = Be^{\frac{E_A}{R}T'} \Big/ Be^{\frac{E_A}{R}T} = e^{\frac{E_A}{R}\left(\frac{1}{T}-\frac{1}{T'}\right)},$$

where R is the gas constant, E_A is the activation energy, and B is the pre-factor. The activation energy for P3HT has been reported by Hintz *et al.* to be $E_A = 26.5\,kJ$ and thereby it is possible to calculate the temperature of the material for a given acceleration factor (Figure S2).[6] The temperature for a film of 100 nm is thus predicted to be 100 °C at 150 suns, which is within the established upper and lower limit.

The hypothesis implies that materials with different activation energies will yield different acceleration factors. In order to investigate this further, polythiophene (PT) with an activation energy of $E_A = 16.0\,kJ$ was tested.[13] It is assumed that the temperature of PT is equal to the temperature of P3HT at equal absorption level since the absorption spectrum of P3HT and PT are similar. At an optical density of 0.5, PT is predicted to have a dose-corrected acceleration factor of 2.2. The experimentally determined dose-corrected acceleration factor for PT was 2.0 in fair agreement with the prediction. This implies that the degradation rate based on concentrated light is deterministic given the sample temperature and the activation energy.

The thermal activation is expected only for samples where photo oxidation is dominant. The increased energy associated with the temperature increase is insignificant in comparison to the energy of the light. At 100 °C, the thermal energy equates to 32 meV, which is significantly lower than the photon energy (1 - 4.5 eV). **Figure 4** shows the degradation of six samples under ambient and nitrogen atmospheres. It is evident that the photolysis of P3HT is not thermally activated as the degradation at 1 sun, 50 suns, and 150 suns overlap in degradation time. Reference 11 has documented that thermo oxidation takes place on a time scale of 10,000 hours while photo oxidation takes place in the time frame of 100 hours. It thus follows that for all practical purposes thermal activation only occurs when oxygen is present. Under ambient atmosphere, acceleration is observed for increasing intensity. The sample exposed to 1 sun and a nitrogen atmosphere was stopped at 96% of the initial absorbance. In order to degrade the 1 sun sample to 50 percent, a timeframe of 1 month was needed, far

exceeding the capacity of nitrogen available. This study represents the first degradation experiment described in the literature where P3HT under photolysis has reached T50.

The hypothesis of thermal activation as the only major contributing factor to the dose-corrected acceleration factor also implies that the reaction mechanism remains unchanged. This is in agreement with the findings described in reference 9 where IR spectra of degraded polymers were compared at 1 sun and 100 suns for poly-(phenylene-vinylene) (PPV). **Figure 5** shows a plot describing the evolution of the peak shift in the optical absorption spectrum for 1 sun and concentrated light. The values represent the degradation state at which the absorption peak has shifted from the initial value to 480 nm. It is clearly evident that the peak shift occurs at the same degradation state for all light concentrations. This supports the fact that the reaction mechanics remain unchanged for all intensities.

In an attempt to prevent heating of the samples, an air ventilation setup was installed. The samples were continuously ventilated by a dry air flow at a flow rate of 25 liters per minute at ambient temperature directed at the polymer surface, effectively cooling the samples. As is evident from **Figure 6** the degradation rates from the cooled samples overlay the 1 sun degradation rates. It was further observed that the degradation rates exhibited a linear behavior with dose, suggesting that no temperature change took place. The fact that the temperature influence can be eliminated by effective cooling proves the hypothesis of thermal activation and demonstrates that the degradation mechanism remains constant for all intensities between 1 and 150 suns. This also implies that concentrated light can be used to determine the degradation rates for polymer films with proper cooling, leading to the opportunity of using concentrated light as a rapid evaluation tool in the pursuit of stable materials.

By studying degradation rates at different light intensities of conjugated polymers, it has been clearly established that the degradation rate scales linearly with light intensity. Any observed

deviations from this behavior can be ascribed to an induced temperature increase leading to a thermal acceleration factor. The degradation mechanism and kinetic have been demonstrated to remain unchanged in the range between 1 and 150 suns, and oxygen diffusion rates are not a limiting factor, even at 150 suns. This documents that the photon effectiveness towards degradation is fundamentally independent of the light intensity for films of P3HT. If the temperature of the sample and activation energy is known, it is possible to compensate for the temperature induced acceleration and use concentrated studies deterministically. This can lead to extremely high acceleration factors, and an acceleration factor of 1,200 has been reported in this paper for P3HT. Photolysis has been shown to be unaffected by temperature and degradation experiments have been performed to T50 at 50 and 150 suns. Concentrated light for accelerated polymer degradation thus constitutes a practical approach by which the time frame of polymer stability evaluation can be severely reduced and the 1 sun stability can be precisely calculated. This allows for rapid, routine stability studies of even very air-stable polymers, which will prove valuable to the development of commercial PSCs with stability exceeding years.

Supporting Information
Please see the Supporting Information for experimental details and supporting results.

Acknowledgements
This work was supported by the Danish Strategic Research Council (2104-07-0022), EUDP (j. no. 64009-0050) and PVERA-NET (project acronym POLYSTAR). The authors would like to express gratitude to Kristian Larsen valuable in building the solar concentrator, the sample exchanger robot, and the atmosphere chambers.

Received: ((will be filled in by the editorial staff))
Revised: ((will be filled in by the editorial staff))
Published online: ((will be filled in by the editorial staff))

[1] UCLA, *Http://newsroom.ucla.edu/portal/ucla/ucla-engineers-create-tandem-polymer-228468.aspx, Accesssed 5/5-12* **2012**.

[2] Heliatek, *Http://www.heliatek.com/?p=1923&lang=en, Accessed 5/5-12* **2012**.

[3] J.A. Hauch, P. Schilinsky, S.A. Choulis, R. Childers, M. Biele, C.J. Brabec, *Sol. Energy Mater. Sol. Cells* **2008**, *92*, 727-731.

[4] T. Tromholt, M.V. Madsen, J.E. Carlé, M. Helgesen, F.C. Krebs, *J. Mater. Chem.* **2012**, *22*, 7592-7601.

[5] S. Schuller, P. Schilinsky, J. Hauch, C.J. Brabec, *Appl. Phys. A-Mater.* **2004**, *79*, 37-40.

[6] H. Hintz, H.-J. Egelhaaf, L. Lüer, J. Hauch, H. Peisert, T. Chassé, *Chem. Mater.* **2010**, *23*, 145-154.

[7] T. Tromholt, E.A. Katz, B. Hirsch, A. Vossier, F.C. Krebs, *Appl. Phys. Lett.* **2010**, *96*, 073501.

[8] T. Tromholt, A. Manor, E.A. Katz, F.C. Krebs, *Nanotechnology* **2011**, *22*, 225401.

[9] T. Tromholt, M. Manceau, M. Helgesen, J.E. Carlé, F.C. Krebs, *Sol. Energy Mater. Sol. Cells* **2010**, *95*, 1308-1314.

[10] M. Manceau, A. Rivaton, J.-L. Gardette, *Macromol. Rapid Commun.* **2008**, *29*, 1823-1827.

[11] M. Manceau, A. Rivaton, J.-L. Gardette, S. Guillerez, N. Lemaître, *Polym. Degrad. Stab.* **2009**, *94*, 898-907.

[12] H. Hintz, H.-J. Egelhaaf, H. Peisert, T. Chassé, *Polym. Degrad. Stab.* **2010**, *95*, 818-825.

[13] T.F. Otero, F. Santos, *Electrochim. Acta* **2008**, *53*, 3166-3174.

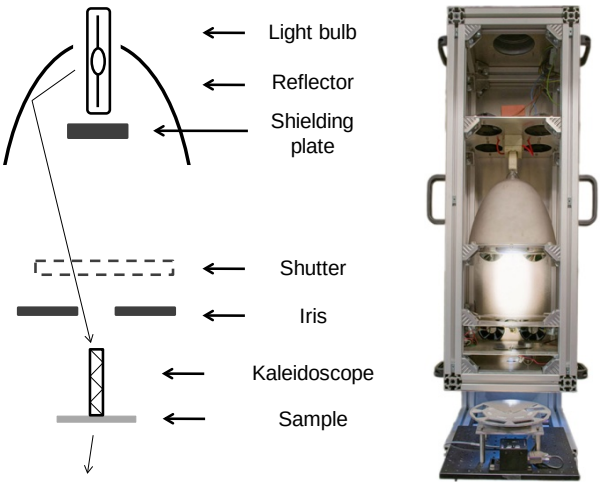

Figure 1. Schematic representation and photo of the concentrator setup.

Submitted to ADVANCED ENERGY MATERIALS

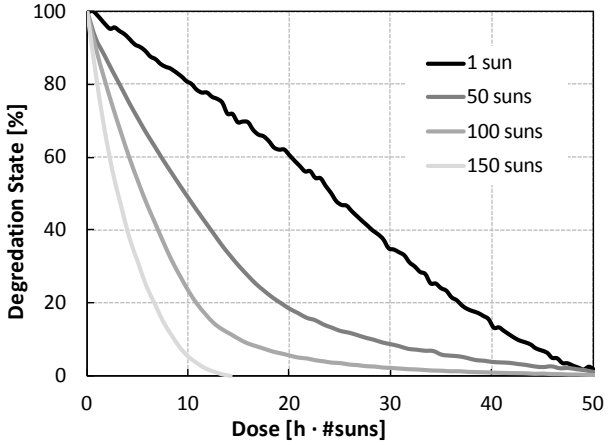

Figure 2. Degradation state *versus* dose for 110 nm P3HT films performed at 1, 50, 100, and 150 suns.

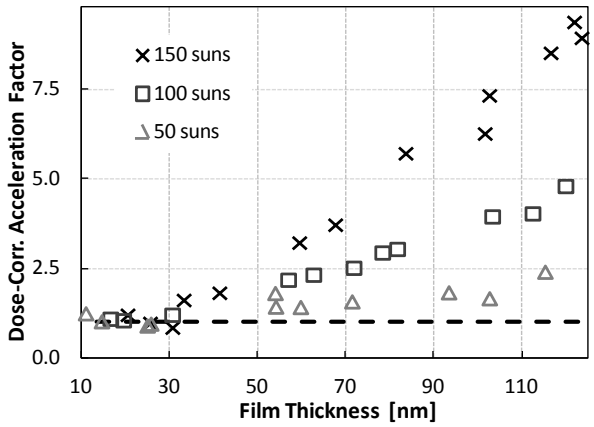

Figure 3. Dose-corrected acceleration factors for films degraded at 50, 100, and 150 suns as a function of film thickness.

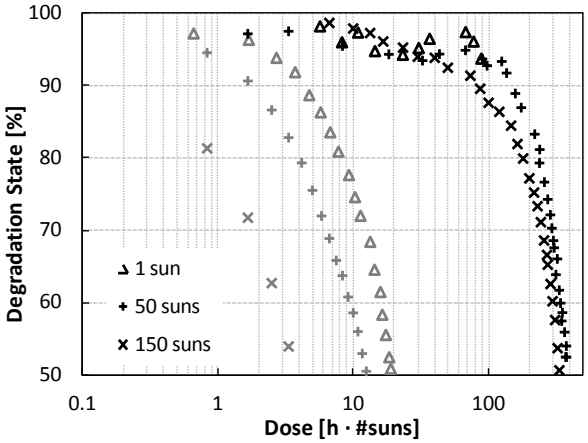

Figure 4. Degradation of P3HT in nitrogen atmosphere (black markers) and degradation in ambient atmosphere (grey markers).

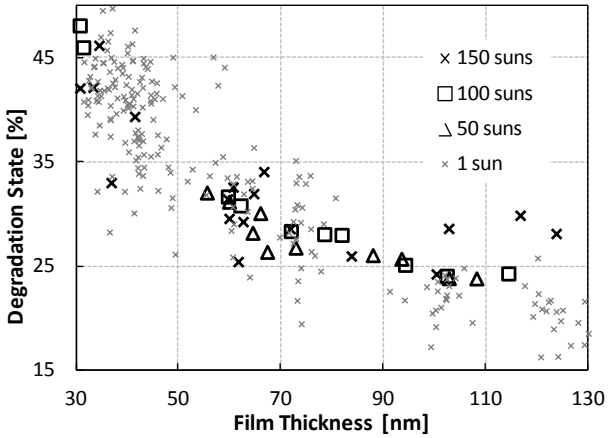

Figure 5. Degradation state for which the film absorbance has shifted to 480 nm as observed for different thicknesses of P3HT films and at different light intensities.

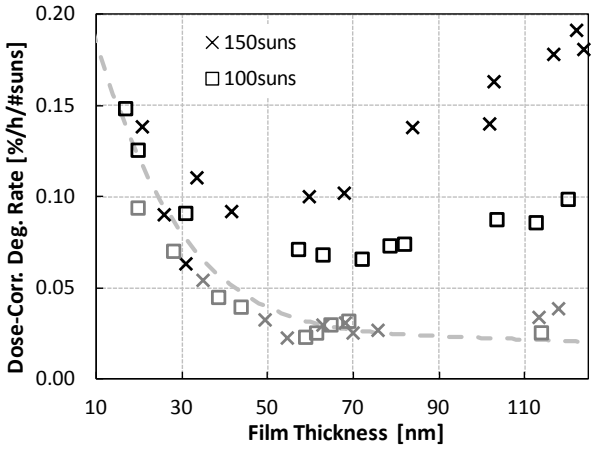

Figure 6. Dose-corrected degradation rates for cooled (grey markers) and non-cooled samples (black markers).

Submitted to ADVANCED ENERGY MATERIALS

Concentrated light is used to perform photochemical degradation of polymer solar cell materials with acceleration factors up to 1,200. With proper cooling the photon efficiency in regards to photo degradation is constant for 1–150 suns and oxygen diffusion rates is not a limiting factor. The reaction is temperature activated and the induced temperature increases the reaction rate.

Keyword Concentrated light, P3HT, Photo oxidation, organic photovoltaics, degradation

Morten V. Madsen*, Thomas Tromholt, Kion Norrman, and Frederik C. Krebs

Concentrated light for accelerated photo degradation of polymer materials

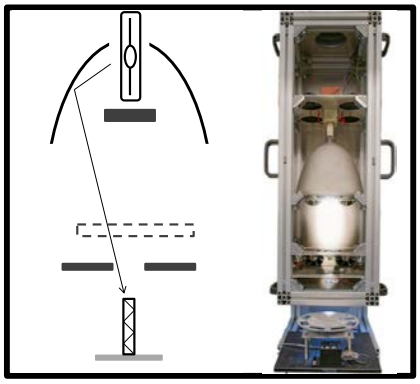

Submitted to ADVANCED ENERGY MATERIALS

Supporting Information

for *Adv. Energy Mater.*, DOI: 10.1002/aenm.((please add manuscript number))

Concentrated light for accelerated photo degradation of polymer materials

Morten V. Madsen, Thomas Tromholt, Kion Norrman, and Frederik C. Krebs*

S1 - Experimental

A fully automated, high-throughput photo-chemical degradation setup was used for the degradation of all materials at 1 sun.[1] The setup utilizes a Steuernagel solar simulator with an Osram 1200 W metal halide arc lamp powered by a Schiederwerk 12-12 AC SL power supply providing an approximate AM1.5G spectrum with an intensity of 1000 W/m^2. A sample exchanger with a capacity of 22 samples was used in conjunction with a UV-vis spectroscopic probe based on an optical fiber-based CCD spectrometer (Avantes AvaSpec 1024) and a halogen/deuterium light source (Avantes AvaLight-DHc) to measure the optical evolution of the samples. The setup is further documented in reference 1.

The light concentrator setup is based on the same type of light bulb used in the 1 sun degradation setup. A rhodium coated elliptical reflector made by Optiforms (focal length 509 mm, diameter 260 mm, height 206 mm) focuses the light from the light bulb into at the second focal point of the ellipse, as shown in Figure 1 in the article. At this focal point a fused silica kaleidoscope (10 x 10 x 75 mm^3) obtained from Quartz Plus is positioned, homogenizing the spatial light distribution of the outgoing light, providing a square 1 cm^2 illuminated area. A shielding plate was used to avoid direct light from the bulb to reach the kaleidoscope and induce poor light distribution. Light intensity is controllable by a custom-made, thermally resistant automated two blade iris, optimized to provide a high spatial

conservation of the light intensity distribution on the illumination area at different light intensities. Light intensities in discrete steps from 0.1 to 150 suns are obtainable with the setup and a shutter allowed for controllable periods of illumination. The light intensity was calibrated with a S314C thermopile from Thorlabs. A custom automated sample exchanger similar to the one used for 1 sun degradation tests was used to ensure precise sample handling. UV-visible absorbance spectra were recorded in transmission mode with an Avantes Avaspec 3648 CCD fiber spectrometer and an Avantes Avalight DHc deuterium-halogen light source. It was found that a higher degree of light blocking by the iris introduced a higher inhomogeneity of the light intensity. Going from a free light passage at 150 suns to higher degrees of blocking, up to 10% higher intensity was observed in the corners of the kaleidoscope. At all intensities, symmetry around the center of the kaleidoscope was observed, which indicated a good alignment of the optical elements in the setup in terms of projection of the light onto the kaleidoscope. For all samples, a 3 mm pinhole was used over the sample to avoid the reduced homogeneity of light distribution. The outgoing light from the kaleidoscope was found to be slightly diverging, implying that the distance between sample and kaleidoscope had to be kept constant for all experiments. No spectral variance could be observed for different intensity settings. The spectrum of the concentrated light is approximately identical to the spectrum of the solar simulator with a UV cutoff at 280 nm since no filters are applied. The temporal stability of the intensity was found to be <5% for both setups, and thus on a level comparable to standard HMI based solar simulators. Degradation rates were extracted from the loss of absorption normalized to the initial value as described in reference 1.

Two atmosphere chambers were constructed with double quartz windows to allow absorption spectra to be recorded without the need of removing the sample from the chamber. Both chambers were designed to be mounted on the sample exchanger robot and thereby

measurements of four samples under controlled atmospheres could be conducted simultaneously under one sun conditions and serially under concentrated light.

S2 - Materials

Regio-regular P3HT from Rieke Metals (Lot: PTL 10-87) was spin-coated on microscopy slides obtained from Menzel from 12 mg / mL chlorobenzene solutions. The film thickness is expressed by $t = (A_{\max} - 0.622) \cdot 188.68$ nm, where $A_{\max}$ is the peak absorbance in accordance with Reference 1.

S3 – Supporting Data

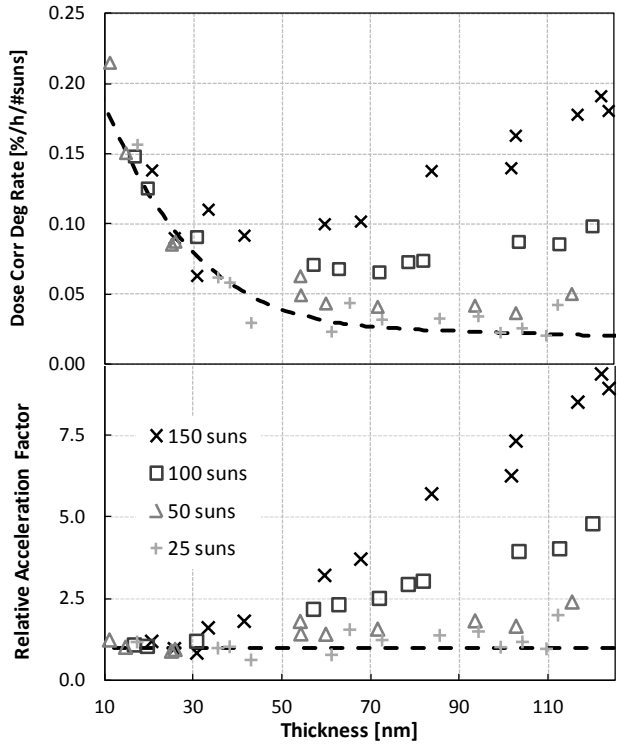

Figure S7. The degradation rate of the initial 10 percent of the degradation at 1, 25, 50, 100, and 150 suns is shown in the top graph. The degradation rate under 1 sun is depicted as a dashed line and represents a polynomial fit of 526 separate degradations in the thickness range with an r-squared value of 0.93. Overlaying this data is the degradation rates for 25, 50, 100, and 150 suns divided by the number of suns. The relative acceleration factor is depicted below.

Submitted to ADVANCED ENERGY MATERIALS

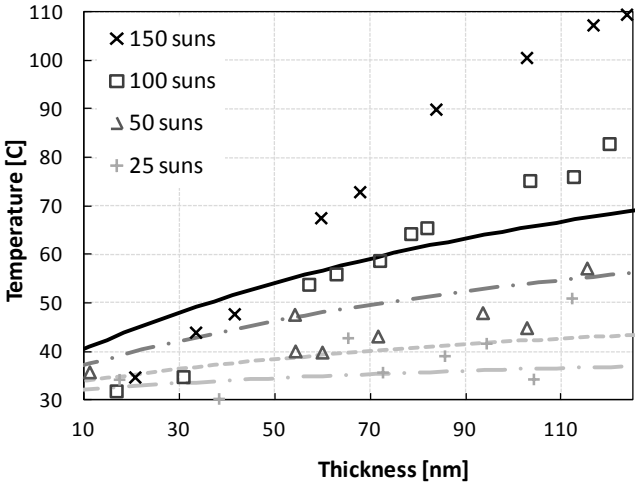

Figure S8. Assuming that the temperature dependence of the reaction can be described by an Arrhenius model, the sample temperature is plotted for 25, 50, 100 and 150 suns (markers). The lines represent the calculated temperatures for the films based upon their absorption.

References

[1] Tromholt, T.; Madsen, M. V.; Carlé, J. E.; Helgesen, M.; Krebs, F. C., *J. Mater. Chem.* **2012**, *22*

Oxygen- and water-induced degradation of an inverted polymer solar cell: the barrier effect

Morten V. Madsen, Kion Norrman, and Frederik C. Krebs
Technical University of Denmark, Risø National Laboratory for Sustainable Energy,
Frederiksborgvej 399, DK-4000 Roskilde, Denmark
kino@risoe.dtu.dk

Abstract. The work focuses on the degradation of performance induced by both water and oxygen in an inverted geometry organic photovoltaic device with emphasis on the accumulated barrier effect of the layers comprising the layer stack. By studying the exchange of oxygen in the zinc oxide (ZnO) layer, the barrier effect is reported in both a dry oxygen atmosphere and an oxygen-free humid atmosphere. The devices under study are comprised of a bulk heterojunction formed by poly(3-hexylthiophene) and [6,6]-phenyl-C61-butyric acid methyl ester sandwiched between a layer of zinc oxide (electron transporting layer) and a layer of poly(3,4-ethylenedioxythiophene) poly(styrenesulfonate) (hole transport layer) and the two electrodes indium tin oxide and silver. Time-of-flight secondary ion mass spectrometry is employed to characterize the accumulated barrier effect. A pronounced barrier effect is observed in the humid atmosphere, correlating well with a long observed lifetime in the same atmosphere. [DOI: 10.1117/1.3544010]

Keywords: barrier effect; isotopic labeling; TOF-SIMS; degradation; inverted geometry; organic photovoltaics.

Paper 10155SSPR received Aug. 30, 2010; revised manuscript received Nov. 24, 2010; accepted for publication Dec. 14, 2010; published online Feb. 7, 2011.

1 Introduction

In recent years polymer solar cells have presented themselves as an upcoming technology in the commercial photovoltaic market. The existence of companies developing and marketing polymer solar cells is evidence that the technology is maturing rapidly. The main driver behind the commercialization of polymer solar cells is the production scalability. Production involving only printing techniques have been demonstrated, either without any vacuum steps involved[1–3] or starting from an indium tin oxide (ITO) covered substrate.[4,5] Performance issues with polymer solar cells include the limited efficiency and lifetime. Efficiencies are typically in the region of 5% with a few reports of efficiencies approaching higher values in the 6 to 8% range.[6,7] Polymer solar cells have been produced on a pilot scale and demonstrated in real world situations[8] with an inferior efficiency, which suggests that efficiency is not a significant obstacle for the technology to reach a production stage. In this regard stability and lifetime is a more pressing issue. Today, lifetimes on the order of a few years are being recorded with good stability for air stable devices, encapsulated devices, and devices exposed to outdoor conditions.[9–14] An effective encapsulation is in many cases the enabling technology for stable polymer solar cells. However, the use of expensive barrier materials is not desirable from a production point of view. Characterizing the performance of the solar cell under different atmosphere conditions can experimentally determine the stability of the cell toward a specific atmosphere,[15] but do not in any way quantify the degree of oxidation caused by the atmosphere. Furthermore, as each layer in the cell acts as a barrier, changing a layer may change the overall need for encapsulation. In this study the

1947-7988/2011/$25.00 © 2011 SPIE

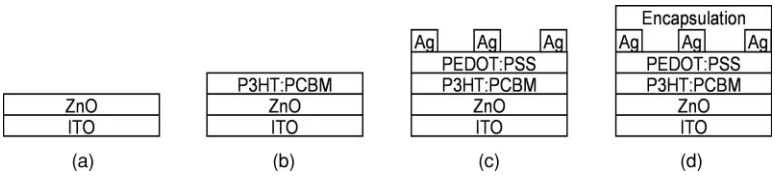

Fig. 1 Schematic illustration of partial (a)–(c) and complete (d) solar cell devices.

barrier effect was determined by studying the oxygen exchange inside the solar cell caused by an isotopically labeled dry oxygen ($^{18}O_2$) atmosphere or an oxygen-free humid ($H_2{}^{18}O$) atmosphere by employing time-of-flight secondary ion mass spectrometry (TOF-SIMS).

2 Experimental

A series of four partial and complete solar cells of inverted geometry were prepared, see Fig. 1. The solar cell is comprised of an ITO electrode, an electron transporting layer (ZnO), an active layer poly(3-hexylthiophene):[6,6]-phenyl-C61-butyric acid methyl ester (P3HT:PCBM), a hole transport layer poly(3,4-ethylenedioxythiophene) poly(styrenesulfonate) (PEDOT:PSS), silver electrode stripes, and an Alcan encapsulation. One set of complete and partial devices were subjected to an isotopically labeled dry oxygen ($^{18}O_2$) atmosphere and another set was subjected to an oxygen-free isotopically labeled humid ($H_2{}^{18}O$) atmosphere. The atmosphere exposure time was set to 21 days (504 h) where the devices were subjected to 330 W m^{-2} of illumination at 65 $\pm$ 2°C. The accumulated barrier effect was measured by TOF-SIMS at the ZnO surface inside the solar cell (after layer removal).

2.1 *Photovoltaic Preparation*

Complete and partial solar cell devices were prepared on ITO coated glass substrates. ZnO nanoparticles were prepared by a method similar to the one described earlier, however, with the ink prepared in acetone instead of o-xylene/WS-1.[4] The ZnO particles were stabilized with 10% methoxyethoxyacetic acid and filtered (0.45 μm) prior to use. The final concentration of the ZnO solution was 42.5 mg mL^{-1}. The ZnO solution was spin-coated using a rotational speed of 1000 rpm and subsequently annealed for 5 min at 140°C. The P3HT:PCBM ink was prepared by dissolving P3HT (Sepiolid P200 from BASF) and PCBM (99%, Solenne BV) in half the required volume of 1,2-dichlorobenzene at 110°C for 2 h followed by the addition of one volume of chloroform. The final concentrations were 24 mg mL^{-1} for P3HT and 22 mg mL^{-1} for PCBM. The P3HT:PCBM solution was spin-coated using a spin speed of 1000 rpm and subsequently annealed for 2 min at 140°C. The PEDOT:PSS was (EL-P 5010 from Agfa with a conductivity of ~30 Ohm $square^{-1}$) diluted with isopropanol (10:5 w/w) to give a final viscosity of 270 mPa · s. The PEDOT:PSS solution was spin-coated using a rotational speed of 1000 rpm and subsequently annealed for 5 min at 140°C. The silver ink was from Dupont (PV410) and printed on without modification in a stripe pattern with stripes being 0.2 mm wide and spaced by 0.8 mm. A stripe pattern was used to mimic the conditions used for R2R fabricated devices, where a stripe pattern is employed to reduce cost. The active areas of the devices were ~3 cm^2.

2.2 *Control of Atmosphere*

The influence of the atmosphere was established by illumination (330 W m^{-2}, 65 $\pm$ 2°C) in chambers equipped with a quartz window allowing for control of the atmosphere.[15] Prior to the experiment a pressure of $\sim 10^{-4}$ mbar was established and the entire system was purged with nitrogen (99.9%) and pumped back down to $\sim 10^{-4}$ mbar. One chamber was then injected

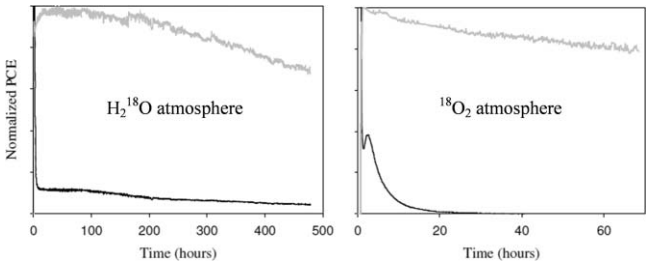

Fig. 2 Normalized PCE describing the degradation in performance of encapsulated (gray) and nonencapsulated (black) devices under continuous illumination (330 W m^{-2}, AM1.5G, 65 $\pm$ 2 $^{\circ}$C).

via a septum with $H_2{}^{18}O$ (97%, 5 mL, ~20 mmol). The entire system has a volume of 2.5 L resulting in a saturated isotopically labeled atmosphere. Another chamber was filled with 1 atm of $^{18}O_2$:N_2 (20:80).

2.3 *Accessing the ZnO Layer*

In order to study the ZnO surface the preceding layers need to be removed. Since the layers comprised the cell where the solution was processed, the organic layers can subsequently be re-dissolved and removed. The PEDOT:PSS layers were removed by either delamination in the case of the encapsulated device or by gently swiping the surface with a cotton stick soaked in pure water. The underlying P3HT:PCBM layers were removed using the same procedure by substituting water with chloroform. Delamination of encapsulated devices is accomplished by peeling off the encapsulation. The delamination occurs at the PEDOT:PSS-P3HT:PCBM interface as verified by TOF-SIMS mass spectra (not shown).

2.4 *Chemical Characterization*

Analysis of the ZnO surface was performed using a TOF-SIMS IV (ION-TOF GmbH, Münster, Germany) with 25-ns pulses of 25-keV Bi^+ (primary ions), bunched to form ion packets with a nominal temporal extent of $<$0.9 ns at a repetition rate of 10 kHz yielding a target current of 0.9 pA. These primary ion conditions were used to obtain 10 mass spectra for each sample acquired on a 100×100 μm^2 surface area for 20 s. The intensity of the ^{18}O signal describes the oxygen exchange that has taken place in accordance with the reaction shown below.

$$Zn^{16}O + {}^1\!/_2{}^{18}O_2 \rightarrow Zn^{18}O + {}^{16}O. \quad (1)$$

By comparing the ^{18}O signal intensities for the different surfaces (Fig. 1), semiquantitative information on the barrier effect was extracted.

3 Results and Discussion

Two functional solar cells were produced, as depicted in Fig. 1(c) and Fig. 1(d). Both were performance tested prior to the degradation experiments. This was done in both an oxygen-free humid atmosphere and a dry oxygen atmosphere.

3.1 *Cell Performance*

Figure 2 depicts a comparison of the degradation of the solar cell performance in a dry oxygen atmosphere and an oxygen-free humid atmosphere. Both encapsulated and unencapsulated

devices, corresponding to Fig. 1(c) and Fig. 1(d), were tested. The mounting process took 1 h. Power conversion efficiency (PCE) was measured before and after the mounting process, which revealed a small insignificant drop in the PCE. Figure 2 shows the temporal development of PCE after the mounting process and exchange of the atmospheres.

It is observed that both atmospheres lead to fast degradation of the initial response for the unencapsulated devices. However, a clear difference is seen in device stability in the two atmospheres. The dry oxygen atmosphere led to complete degradation of the solar cell properties in roughly 20 h with all parameters showing fast decay. On the contrary the device in the oxygen-free humid atmosphere remained nearly constant after the initial performance drop. During the 480 h time frame of the experiment the cell had not reached the end of its functional lifetime.

3.2 *Barrier Effect*

Complete and partial devices were placed in the atmosphere chambers for 504 h (21 days) and subjected to light for the entire duration. After the exposure to the atmosphere the devices were removed from the atmosphere chamber, the ZnO layer was exposed, and TOF-SIMS mass spectra were obtained. Figure 3 shows a plot of the degree of oxygen exchange that took place during the experiment at the ZnO surface inside the cell. The normalized intensities are based on the integrated ^{18}O signal normalized to the largest degree of oxygen exchange. TOF-SIMS is not directly quantitative, however, since the substrate is the same in each case the intensities can be compared semiquantitatively.

At the directly exposed ZnO surface [Figs. 3(a) and 1(a)] a higher degree of oxygen exchange (roughly a factor of 2) is observed in an oxygen-free humid atmosphere as compared to a dry oxygen atmosphere. ZnO is expected to exchange oxygen easily; hence the oxygen uptake at the ZnO surface cannot directly be correlated to degradation. However, it can be used to determine the accumulated barrier effect of the preceding layers. The explanation for the difference in oxygen uptake at the directly exposed ZnO surface can be found in the different trapping mechanisms for oxygen and water. The exchange with $^{18}O_2$ is expected to take place through trapping of superoxide radicals at the surface of the ZnO nanoparticles, whereas the exchange with $H_2{}^{18}O$ is expected to take place through the exchange of hydroxide on the surface of the ZnO nanoparticles.

In the dry oxygen atmosphere a clear barrier effect is observed for all layers [Figs. 3(b)–3(d), white columns]. It is seen that each layer has a distinctive effect as a barrier. An accumulated effect is therefore seen. In the oxygen-free humid atmosphere the active layer is observed to have a pronounced barrier effect [Fig. 3(a) and 3(b), striped columns] to such an extent that

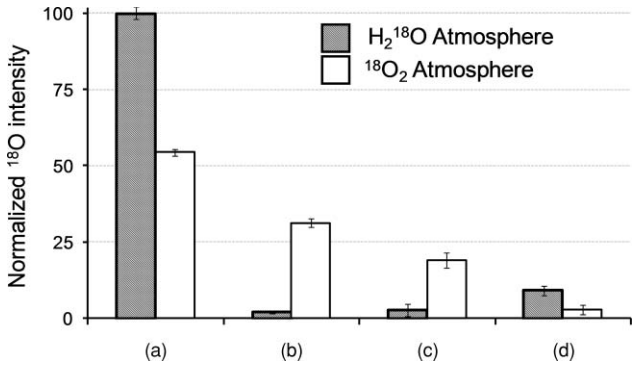

Fig. 3 Normalized ^{18}O intensities for partial (a)–(c) and complete (d) solar cells. The values have been normalized to the largest degree of oxygen exchange seen in the oxygen-free humid atmosphere. (c) The functional cell without encapsulation, (d) the same cell with encapsulation, and (a) and (b) partial devices (see Fig. 1).

the active layer effectively shields the effect of the preceding layers as the difference between B and C lies within the error bars (i.e., a bottleneck effect). The elevated ^{18}O intensity for the encapsulated device [Fig. 3(d), striped column] can seem puzzling as it intuitively was expected to show the lowest value. One possible explanation could be that the adhesive used for the Alcan encapsulation is hygroscopic, i.e., the adhesive acts as a reservoir for water.

4 Conclusion

Barrier effects against molecular oxygen and water in an inverted geometry polymer solar cell (Alcan-Ag-PEDOT:PSS-P3HT:PCBM-ZnO-ITO) were determined using TOF-SIMS in conjunction with isotopic labeling. In an oxygen-free humid atmosphere the barrier effect of the active layer (P3HT:PCBM) is demonstrated to be very pronounced. The barrier effect of the active layer effectively overshadows the effect of the preceding layers (i.e., a bottleneck effect). In a dry oxygen, atmosphere barrier effects of similar magnitudes are observed for the various layers giving rise to a steady increase in the accumulated barrier effect. These results provide information on how much of the atmosphere reached the ZnO surface during the experiment, it does not directly provide information on the degree of oxidation/degradation in the organic materials, and does not provide information on where oxidation/degradation took place. It is therefore not possible to relate these results to the relative lifetime in molecular oxygen and water.

Acknowledgments

This work was supported by the Danish Strategic Research Council (DSF 2104–05-0052 and 2104–07-0022), EUDP (j. nr. 64009–0050) and PV ERA-NET transnational POLYMOL project PolyStaR.

References

1. F. C. Krebs, M. Jørgensen, K. Norrman, O. Hagemann, J. Alstrup, T. D. Nielsen, J. Fyenbo, K. Larsen, and J. Kristensen, "A complete process for production of flexible large area polymer solar cells entirely using screen printing—First public demonstration," *Sol. Energy Mater. Sol. Cells* **93**, 422–441 (2009).
2. F. C. Krebs, "All solution roll-to-roll processed polymer solar cells free from indium-tin-oxide and vacuum coating steps," *Org. Electron.* **10**, 761–768 (2009).
3. F. C. Krebs, "Roll-to-roll fabrication of monolithic large-area polymer solar cells free from indium-tin-oxide," *Sol. Energy Mater. Sol. Cells* **93**, 1636–1641 (2009).
4. F. C. Krebs, S. A. Gevorgyan, and J. Alstrup, "A roll-to-roll process to flexible polymer solar cells: model studies, manufacture and operational stability studies," *J. Mater. Chem.* **19**, 5442–5451 (2009).
5. F. C. Krebs, H. Spanggard, T. Kjaer, M. Biancardo, and J. Alstrup, "Large area plastic solar cell modules," *Mater. Sci. Eng., B* **138**, 106–111 (2007).
6. S. H. Park, A. Roy, S. Beaupré, S. Cho, N. Coates, J. S. Moon, D. Moses, M. Leclerc, K. Lee, and A. J. Heeger, "Bulk heterojunction solar cells with internal quantum efficiency approaching 100%," *Nature Photonics* **3**, 297–303 (2009).
7. H. Y. Chen, J. Hou, S. Zhang, Y. Liang, G. Yang, Y. Yang, L. Yu, Y. Wu, and G. Li, "Polymer solar cells with enhanced open-circuit voltage and efficiency," *Nature Photonics* **3**, 649–653 (2009).
8. F. C. Krebs, T. D. Nielsen, J. Fyenbo, M. Wadstrøm, and M. S. Pedersen, "Manufacture, integration and demonstration of polymer solar cells in a lamp for the Lighting Africa initiative," *Energy Environ. Sci.* **3**, 512–525 (2010).
9. E. A. Katz, S. Gevorgyan, M. S. Orynbayev, and F. C. Krebs, "Out-door testing and long-term stability of plastic solar cells," *Eur. Phys. J. Appl. Phys.* **36**, 307–311 (2006).

10. J. A. Hauch, P. Schilinsky, S. A. Choulis, R. Childers, M. Biele, and C. J. Brabec, "Flexible organic P3HT:PCBM bulk-heterojunction modules with more than 1 year outdoor lifetime," *Sol. Energy Mater. Sol. Cells* **92**, 727–731 (2008).
11. F. C. Krebs and K. Norrman, "Analysis of the failure mechanism for a stable organic photovoltaic during 10 000 h of testing," *Prog. Photovoltaics* **15**, 697–712 (2007).
12. F. C. Krebs, "Air stable polymer photovoltaics based on a process free from vacuum steps and fullerenes," *Sol. Energy Mater. Sol. Cells* **92**, 715–726 (2008).
13. F. C. Krebs, Y. Thomann, R. Thomann, and J. W. Andreasen, "A simple nanostructured polymer/ZnO hybrid solar cell–preparation and operation in air," *Nanotechnology* **19**, 424013–434025 (2008).
14. B. Zimmermann, U. Würfel, and M. Niggemann, "Longterm stability of efficient inverted P3HT:PCBM solar cells," *Sol. Energy Mater. Sol. Cells* **93**, 491–496 (2009).
15. S. A. Gevorgyan, M. Jørgensen, and F. C. Krebs, "A setup for studying stability and degradation of polymer solar cells," *Sol. Energy Mater. Sol. Cells* **92**, 736–745 (2008).

Morten V. Madsen is a PhD student at Risø National Laboratory for Sustainable Energy, Technical University of Denmark. He received his BS and MS degrees in nanotechnology from the University of Aalborg in 2007 and 2009, respectively, with the main focus on physics and materials. His PhD project is focused around degradation and stability of polymer solar cells.

Kion Norrman is a senior scientist at Risø National Laboratory for Sustainable Energy, Technical University of Denmark. He received his BS, MS, and PhD degrees in chemistry from the University of Copenhagen in 1991, 1993, and 1996, respectively. He is the author of more than 40 peer reviewed papers and has written three book chapters. His current research interests include chemical characterization and modification of materials with focus on mapping degradation mechanisms in organic solar cells.

Frederik C. Krebs is a professor at Risø National Laboratory for Sustainable Energy, Technical University of Denmark. He received his BS in chemistry (1993) and biochemistry/immunology (1994) at the University of Abberdeen (Scotland) and obtained a DEA (1995) at Université de Nantes (France). He received his PhD degree in chemistry (2000) at the Technical University of Denmark. Since then he worked at Risø National Laboratory for Sustainable Energy, Technical University of Denmark, where he is now professor (2010). He is currently working in the field of organic photovoltaics. His group covers all aspects within organic photovoltaics with emphasis on large scale roll-to-roll printing of polymer solar cells. He and his group have contributed extensively to the literature: more than 200 peer reviewed papers, conference proceedings, editorials, books, patents, and reports. He is currently an associate editor for the international journal Solar Energy Materials and Solar Cells.